ASSEMBLY OF ORGANIC LAYERS ONTO CARBON SURFACES

A thesis

submitted in partial fulfilment

of the requirements for the Degree of

Doctor of Philosophy in Chemistry

in the

University of Canterbury

by

Emelyn S. Q. Tan

University of Canterbury

2006

Work in this thesis has been published in the following articles:

Invited publication: Downard, A. J.; Jackson, S. L. and Tan, E. S. Q. Fluorescence microscopy study of protein adsorption at modified glassy carbon surfaces, *Australian Journal of Chemistry, in the Electrochemistry Special Issue*, **2005**, 58, 275 – 279.

Cover featured article: Downard, A. J.; Tan, E. S. Q. and Yu, S. S. C. Controlled assembly of gold nanoparticles on carbon surfaces, *New Journal of Chemistry*, **2006**, 30, 1283 – 1288.

Invited publication: Downard, A. J.; Garrett, D. J. and Tan, E. S. Q. Microscale patterning of organic films on carbon surfaces using electrochemistry and soft lithography, *Langmuir, in the Special Issue on Electrochemistry*, accepted for publication.

Other publications:

Pietak, A.; Korte, S.; Tan, E.; Downard, A. and Staiger, M. P. A novel technique for characterizing the surface of natural fibres, *Applied Surface Science*, in press.

Norén, L.; Tan, E. S. Q.; Withers, R. L.; Sterns, M. and Rundlof, H. A neutron, x-ray and electron diffraction study of the structures of $Pb_3O_2X_2$ (X = Cl, Br), *Materials Research Bulletin*, **2002**, 37(8), 1431 – 1442.

Acknowledgements

I am very grateful to the people pictured below:

Firstly, Jesus thanks for everything.

Many thanks goes to my supervisor Assoc. Prof. Alison Downard for her enthusiasm, expert guidance and invaluable wisdom. I would like to thank Dr. Paula Brooksby for her extensive knowledge and ability to solve problems. Also, thanks to Amy, Sam and Jared for being good workmates and for being around to share the frustrations.

I am also indebted to BJ, Audrey, Fiona and my family for their love and support.

Finally, I would like to thank the MacDiarmid Institute for scholarship funding.

Alison

Paula

Amy

Sam

Jared

BJ

Audrey

Fiona

Family

Table of Contents

Abstract

This thesis presents the study of organic layers covalently assembled onto carbon surfaces. As a result of their attachment, the properties of carbon surfaces were controllably adjusted so that these surfaces could be used for desired applications. In order that a wide range of properties were imparted onto the carbon surface, many different modifiers were attached and thoroughly characterised. Three applications that the modified carbon surfaces were used for were the subsequent coupling of molecular species, adsorption of protein and assembly of aldehyde/sulfate-functionalised polystyrene (PS) and citrate-capped gold nanoparticles (NPs). Finally, patterning of different organic layers at pre-determined spatially defined locations on the one carbon surface was also investigated.

The carbon surfaces used in this work were glassy carbon (GC) and pyrolysed photoresist film (PPF) surfaces. For PPF, methods for the reproducible fabrication of electrochemically suitable surfaces were investigated. The properties of GC and PPF surfaces are very similar apart from the surface roughness. PPF has near atomic smoothness and has RMS roughness values that are approximately four times smaller than GC.

The first series of modifier layers attached to the carbon surfaces was via the oxidation of seven different primary amines. The different layers allowed the modulation of the wettability of the surface. Both *n*-tridecylamine (TDA, monoamine) and 1,12-diaminododecane (DAD, diamine) are able to form multilayers. The stability of TDA and DAD layers were tested by scanning, soaking and sonicating the layers in different media. Changes in the layer were monitored by the probe response of ferrocene monocarboxylic acid (FCA). However, atomic force microscope (AFM) depth profiling experiments showed that changes in the probe response did not indicate cleavage of the covalently attached layer and mechanisms are proposed to account for the changes in the response of the probe.

Surface concentrations of the amine modifiers were estimated by the coupling of an electrochemically active species, FCA and nitrobenzoyl chloride (NBC). The electrochemical reduction of the 4-nitrophenylethylamine (NPEA) layer in acid caused the layer to 'shrink'. Surface concentration estimates of NPEA from acid reduction of layers with different thicknesses suggested that only a limited fraction of the *p*-nitro groups were reduced in acid. However, in ACN (acetonitrile)/0.1 M $[Bu_4N]BF_4$ (tetrabutyl ammonium fluoroborate) the relationship between the concentration of electroactive surface groups and layer thickness was linear.

The other series of modifiers that was attached to alter the surface properties was performed by the reduction of aryl diazonium salts. Subsequent coupling reactions of tetraethylene glycol diamine (TGD) to *para* methyl benzene (*p*-MCA) and NBC to electrochemically reduced *para* nitro benzene (*p*-NB) layers were carried out. Surface concentrations of *p*-NB as estimated from reduction scans was higher when reduction was performed in ethanol/water compared to acid. Four peaks at N_{1s} binding energies were observed in x-ray photoelectron spectroscopy (XPS) spectra for both acid and ethanol/water reduced layers.

The ability of attached amine and aryl layers to modulate the adsorption of protein was investigated using fluorescently labelled protein, bovine serum albumin-fluorescein isothiocynate (BSA-FITC) and fluorescence microscopy. TGD, *para* methyl benzene (*p*-MB), *para* hexyl benzene (*p*-HB) and *para* polyethylene glycol (*p*-PEG)-modified GC surfaces promoted protein adsorption relative to as-prepared GC, whereas *n*-hexylamine (HA) and polyethylene glycol diamine (PGD) layers reduced protein adsorption.

The assembly of two types of NPs, aldehyde/sulfate-functionalised PS and citrate-capped gold NPs, onto amine-containing modifiers layers was examined. Citrate-capped gold NPs were synthesised and characterised. The surface coverage of the gold NPs was

controlled by using different modifiers of different chemical compositions, tuning the modification conditions and adjusting the immersion time, concentration and pH of gold NP solution.

Approaches to creating patterns of modifiers in pre-determined spatially defined locations on GC and PPF surfaces using poly(dimethyl)siloxane (PDMS), poly(vinyl)alcohol (PVA) and thin metal films were investigated. With the "fill-in" approach using PDMS, the smallest pattern of modifiers was the *parallel lines* with a line width of 20 μm and straight edges and was created by performing electrochemistry in PDMS microchannels which has not been previously investigated. Visualisation techniques, based on optical and scanning electron microscopy, were demonstrated for the molecular patterns.

Abbreviations and Symbols

ACN	Acetonitrile
AFM	Atomic force microscope
AlBS	Aluminium coated on backside
AOI	Area of interest
Ar	Aryl ring
BSA-FITC	Bovine serum albumin-fluorescein isothiocynate
CV	Cyclic voltammetry
DAD	1,12-diaminododecane
DCC	1,3-dicyclohexylcarbodiimide
DCM	Dichloromethane
DIPEA	Diisopropylethylamine
DMF	Dimethylformamide
DMSO	Dimethylsulfoxide
EDCI	1-ethyl-3-(3'-dimethylaminopropyl)carbodiimide hydrochloride
E	Potential
$E°'$	Formal potential for a redox couple (Formal mid potential between oxidation and reduction peaks for a reversible process)
$E_{1/2}$	Observed mid potential between oxidation and reduction peaks for a

	reversible process
E_i	Initial potential
E_f	Final/applied or chosen modification potential
E_p	Peak potential
ΔE_p	Peak separation between oxidation and reduction peaks for a reversible process
E_{pa}	Potential of anodic/oxidation peak
E_{pc}	Potential of cathodic/reduction peak
ESCA	Electron spectroscopy for chemical analysis
Fc	Ferrocene
Fc^+	Ferrocenium
FCA	Ferrocene monocarboxylic acid
GC	Glassy carbon
HA	*n*-hexylamine
HATU	O-(7-azobenzotriazol-1-yl)-1,1,3,3-tetramethyluronium hexfluorophosphate
HOPG	Highly oriented pyrolytic graphite
HP	*para* hexyl phenyl
HRTEM	High resolution transmission electron microscope
IPA	Isopropyl alcohol

IR	Infrared
ITO	Indium tin oxide
i	Current
i_p	Peak current
i_{pa}	Anodic/oxidation peak current
i_{pc}	Cathodic/reduction peak current
MQ	MilliQ
MCA	*para* methylene carboxylic acid phenyl
MES	4-morpholineethanesulfonic acid
MP	*para* methyl phenyl
NB	Nitrobenzoyl
NBC	Nitrobenzoyl chloride
NHS	*N*-hydroxysuccinimide
NiCr	Nichrome
NMP	*N*-methylpyrrolidone
NMR	Nuclear magnetic resonance
NP	Nanoparticle
NPEA	4-nitrophenylethylamine
NPh	*para* nitro phenyl

p-HB	*para* hexyl benzene diazonium tetrafluoroborate
p-MB	*para* methyl benzene diazonium tetrafluoroborate
p-MCA	*para* methylene carboxylic acid benzene diazonium tetrafluoroborate
p-NA	*para* nitro aniline
p-NB	*para* nitro benzene diazonium tetrafluoroborate
p-PEG	*para* polyethylene glycol benzene diazonium tetrafluoroborate
PB	Phosphate buffer
PBS	Phosphate buffered saline
PEG	*para* polyethylene glycol phenyl
PDMS	Poly(dimethyl)siloxane
PGD	Polyethylene glycol diamine (Mr ≈ 2003 $g.mol^{-1}$)
PPF	Pyrolysed photoresist film
PS	Polystyrene
PVA	Poly(vinyl)alcohol
RMS	Root-mean-squared
rpm	Rotations per minute
SAM	Self-assembled monolayer
SCE	Saturated calomel electrode

SEM	Scanning electron microscope
$[Bu_4N]BF_4$	Tetrabutyl ammonium fluoroborate
TDA	*n*-tridecylamine
TEM	Transmission electron microscope
TGD	Tetraethylene glycol diamine
THF	Tetrahydrofuran
UV	Ultraviolet
UV-VIS	Ultraviolet-visible
v	Scan rate
XPS	X-ray photoelectron spectroscopy

1.1. Introduction

Assembly of organic layers onto surfaces has vast applications in biological and chemical sensing and in molecular electronics. The focus of the work covered in this thesis is to controllably alter the properties of carbon surfaces by the covalent assembly of organic layers, so that the surfaces are useful for desired applications. Other surfaces that are commonly used are gold and silicon. Self-assembled monolayers (SAMs) of alkanethiols form on gold surfaces via a spontaneous, covalent Au-S linkage. The SAMs are well-defined and close-packed with tilting (*ca.* 30°) of the assembled alkanethiols that is driven by hydrophobic and van der Waals interactions between non-polar segments of the modifiers.[1] However, the disadvantages with the SAMs on gold approach are the gold surface degrades structurally and the alkanethiols desorb over a period of days.[2] Assembly of silanes onto silicon surfaces via Si-O-Si bonds can be messy and lead to polymerisation of silanes at the surface. Consideration of the issues of stability and control over surface modification led to the investigation of carbon as a substrate.

Carbon is the chosen surface in this work as it is highly conducting with a wide potential window, structurally stable, relatively inexpensive and stable layers of organic modifiers can attach to the surface in a controllable manner via covalent bonds such as C-C and C-N.[3,4] There are many different forms of conducting carbon materials including glassy carbon (GC), highly orientated pyrolytic graphite (HOPG), pyrolysed photoresist film (PPF), carbon nanotubes, carbon powder, screen printed carbon, carbon fibres, carbon nanocapsules, fullerene and carbon composites.[5] In this work, the two carbon materials that are used are planar PPF and GC surfaces and their properties are reviewed in Chapter 3.

1.2. Modification methods for carbon surfaces

Recently, methods involving radical-based mechanisms have been developed for the modification of carbon surfaces with covalently attached layers of organic species. This section outlines the modification of planar carbon surfaces rather than other forms of carbon. With the other forms of carbon materials, there are a large number of methods involving various mechanisms. For example, for the chemical modification of carbon nanotubes alone there are more than ten reported reactions.

The radical-based methods involve covalent attachment of modifier species to carbon surfaces without extensively altering the underlying carbon surface. In contrast, earlier procedures occurred via oxidation of the carbon surface that produced a variety of carboxyl and oxygenated functionalities, such as carboxylic acid, carbonyl and hydroxy groups. These groups were subsequently used as precursors for further modification.[6,7] Oxidative treatments include abrasive polishing, heating at 400 – 500 °C in air, oxygen plasma treatment, electrochemical oxidation and chemical oxidation in acid.[6-11] The disadvantage with these approaches is that oxidative conditions tend to have degrading effects on the polyaromatic carbon framework. Moreover, the functional groups generated at the surface required further conversion or coupling agents for the groups to undergo the subsequent attachment of modifiers.[6] These procedures were typically used for the attachment of amine modifiers to the carboxylic acid groups at the surface.[6]

Covalent attachment of modifier species to planar carbon surfaces through radical reactions has mainly used electrochemical routes. Electrochemically-assisted covalent modification of carbon electrodes has been performed by the oxidation of amines,[12]

alcohols[13] and aryl acetates[14] and the reduction of iodinium salts[15] and the widely used aryl diazonium salts[4,16]. All of these modifications, apart from the oxidation of alcohols, proceed via generation of solution-based radicals at the surface as a result of a one-electron oxidation or reduction. The radical then reacts with sp^2 and sp^3-hybridised carbon atoms on the electrode forming stable organic layers.[3]

For the oxidation of amines at the carbon surface, the most commonly proposed mechanism has the reaction proceeding via an amine cation radical (Figure 1.1.(i).).[12,17-25] Figure 1.1.(ii). shows the reaction for the oxidation of an alcohol.[13] It has been proposed that during oxidation, radicals generated at the carbon electrode react with the alcohol to yield an ether linkage.[13] The oxidation of aryl acetates occurs via the formation of the aryl methylene radical (Figure 1.1.(iii).).[14] This reaction is known as the Kolbe reaction, which is the oldest electroorganic reaction.[14] Recently, the reduction of iodonium salts has been shown to modify carbon surfaces via the mechanism shown in Figure 1.1.(iv).[15] Currently, this is the only electrochemical route for the attachment of alkynyl groups to carbon surfaces.[15] The reduction of aryl diazonium salts for the covalent modification of carbon surfaces has been the most established route. The mechanism for attachment is shown in Figure 1.1.(v).[4,16] Comparing the different routes, the oxidation of aryl acetates and the reduction of aryl diazonium salts have the limitation of only derivatising the carbon surface with aromatic groups whereas the other routes permit both aliphatic and aromatic functionalities to be attached.

The oxidation of amines and the reduction of aryl diazonium salts routes for electrode modification are used for much of the work described in this thesis. The

electrochemical oxidation of amines for the covalent modification of carbon surfaces is reviewed in a later section and more detailed descriptions for the reduction of aryl diazonium salts are given in Chapter 5.

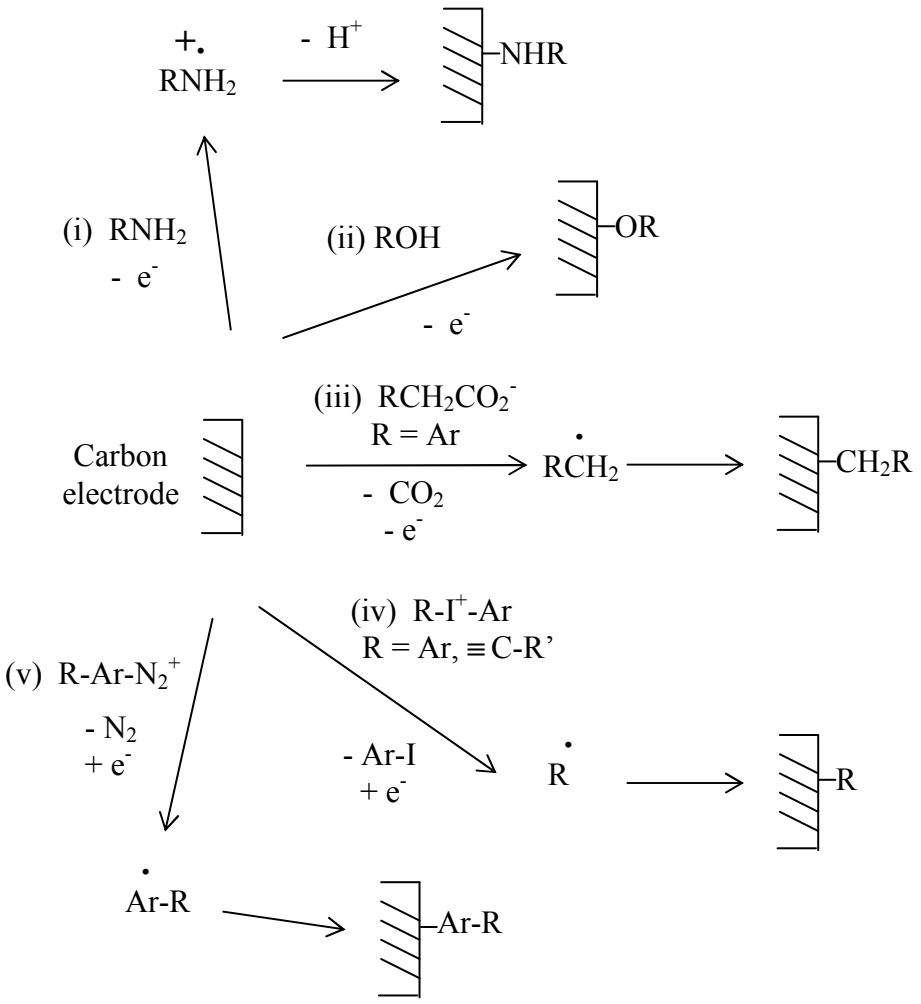

Figure 1.1. Electrochemical-assisted routes for the covalent modification of carbon surfaces. (i) oxidation of amines; (ii) oxidation of alcohols; (iii) oxidation of aryl acetates; (iv) reduction of iodonium salts and (v) reduction of aryl diazonium salts. Ar is the abbreviation for aryl ring.

Less common routes for covalent attachment of modifier species via radical-based mechanisms to planar carbon surfaces are photochemical and thermal. Some examples of these modification routes are outlined here. Photobiotin, a nitro(aryl) azide derivative of biotin was covalently immobilised on GC surfaces using ultraviolet (UV) photolysis.[26] During photolysis, a nitrogen atom of the azide is eliminated generating a singlet or triplet nitrene which inserts into O-H and C-H groups of GC.[26]

Aliphatic and aromatic alkynes and alkenes (5-(4-ethynylphenyl)-10,15,20-trimesitylporphinatozinc(II) (alkyne linker), 5,10,15-trimesityl-20-(4-vinylphenyl)porphinatozinc(II) (alkene linker), ethynylferrocene, 4-ethynyl-α,α,α-trifluorotoluene and 5-chloro-1-pentyne) were covalently attached to PPF surfaces after heat treatments (175 – 480 °C) in an argon atmosphere.[27] It has been proposed that the mechanism for the reaction is either via the formation of surface radicals during heat treatment which attacks the alkyne and alkene groups of the modifiers or by Diels-Alder [4 + 2]- and [2 + 2]-cycloaddition reactions.[27] Aryl diazonium salts have also been used for solvent-free modification of carbon rods. The carbon rods were soaked in *p*-butylbenzenediazonium bis(trifluoromethanesulfonyl)amidate and heated overnight at 85 °C. A covalently bonded organic layer formed on the carbon surface.[28]

1,6-aminohexane, didecylamine and 2-aminoanthraquinone have been attached to carbon fibres by prolonged exposure to the neat or concentrated amine liquids at elevated temperatures (120 – 350 °C for 15 hours – 4 days) in a nitrogen atmosphere.[29] The proposed mechanism for the modification involves the nucleophilic attack of the amine at

electrophilic C=C bonds at the carbon fibre surface and the subsequent formation of C-N bonds.[29]

Spontaneous attachment has also been observed when carbon fibres were exposed to a neat liquid of (dimethylamino)methyl-ferrocene at room temperature for five days. The proposed mechanism for the spontaneous attachment is also a nucleophilic attack of the amine at electrophilic C=C bonds at the carbon fibre surface and the subsequent formation of C-N bonds.[29]

1.3. Electrochemical oxidation of amines for the covalent modification of carbon surfaces

The oxidation of primary amines at GC surfaces and carbon fibres has been shown to result in the formation of surface attached layers.[3] During the electrochemically-assisted oxidation, the amine loses one of its lone pair of electrons at the surface and the generated radical reacts with the surface. The amine is attached via the formation of a stable, covalent C-N bond (Figure 1.2).[3,12,17-25,30,31] The secondary amine that is formed at the surface does not undergo further oxidation.[12]

Several radical-based mechanisms for primary amine oxidation have been proposed in the literature and are shown in Figure 1.3.[3,12,17-25,30,31] Figure 1.3.(i). has the reaction proceeding via an amine cation radical in a concerted manner.[12,17-25] Figure 1.3.(ii). also involves an amine cation radical, however, the reaction is step-wise where the loss of the proton occurs after the amine is attached to the surface.[12] A recent mechanistic study has suggested that it is an amine radical that attaches to the surface rather than an amine cation

radical (Figure 1.3.(iii).).[30] Figure 1.3.(iii). involves the formation of an amine radical and the generation of a proton, followed by the amine radical attaching to the surface.[3,30,31]

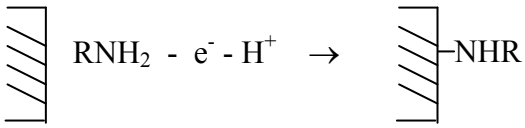

Figure 1.2. The electrochemical oxidation of a primary amine at a carbon surface.

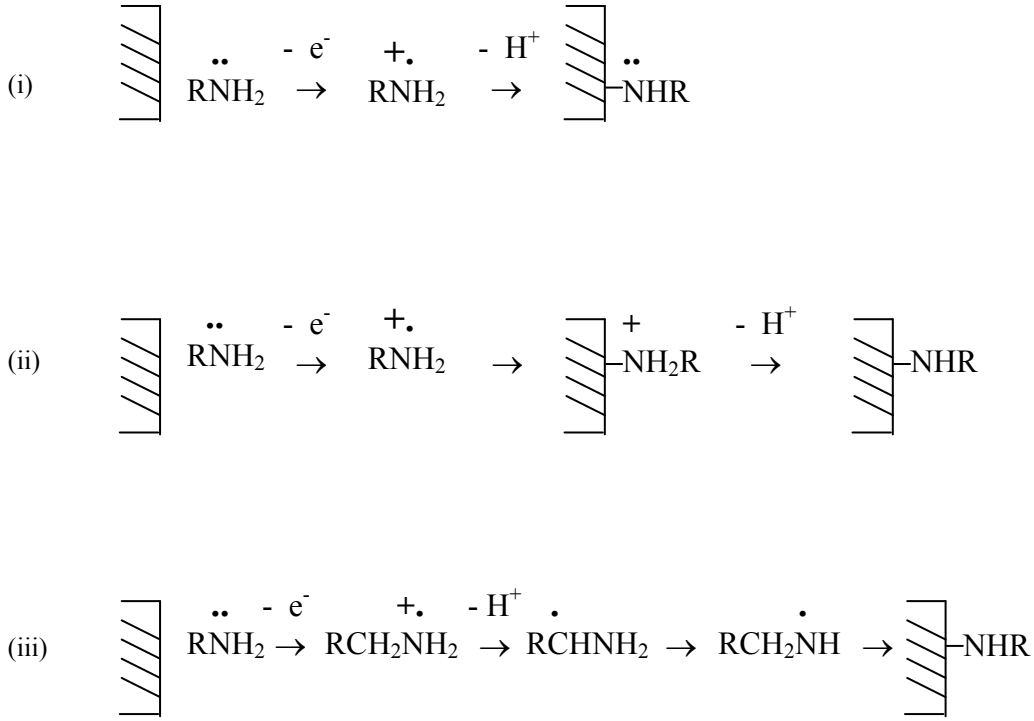

Figure 1.3. Radical-based mechanisms for the electrochemical oxidation of a primary amine at a carbon surface.

A wide range of primary amines (Table 1.1.) have been covalently attached onto carbon surfaces. Modifiers include monoamines, diamines and aromatic amines.

Table 1.1. Primary amines that have been used for the electrochemically-assisted covalent modification of carbon surfaces.

Amine	Surfaces	References
Butylamine	GC	17,30,32
Isobutylamine	Carbon fibre	12
Hexylamine	GC	30
Octylamine	GC	23
Decylamine	GC	32
Dodecylamine	GC	23
Octadecylamine	GC	23,32
6-aminohexanol	GC	32
Triethylene tetramine	Carbon fibre	12,33
Hexamethylene tetramine	Carbon fibre	12
Ethylene diamine	GC, carbon fibre	12,34 35 33
N-(2-aminoethyl)-4-fluorobenzamine	Carbon fibre	12
N-acetylethylenediamine	GC	17
2-amino-2-methylpropane	GC	30
2-amino-4-methyl thiazole	Carbon fibre	12
1,7-diaminoheptane	GC, carbon fibre, graphite electrode	20,36,37
1,10-diaminodecane	GC, carbon fibre, graphite electrode	20,36
1,12-diaminododecane	GC, carbon fibre, graphite electrode	20,36
4-aminobenzoic acid	GC	18,38-41 19,42-49
4-nitrobenzylamine	GC, carbon fibre	12,30
3-nitrobenzylamine	GC	30
4-aminobenzylphosphonic acid	GC	31
4-aminomethylphenylboronic acid	GC	25
4-aminopyridine	GC, carbon fibre, graphite electrode	36
4-aminobutyl-H_3PO_4	GC, carbon fibre, graphite electrode	36
3,4-dihydroxylbenzylamine	GC, carbon fibre, graphite electrode	36
2-aminoanthraquinone	Carbon fibre	29
Aminomethyl-9-anthracene	GC	12
4-aminopyridine	GC	24
4-aminoethylpyridine	GC	24
Imidazole	GC	24
Cysteine	GC	50
β-alanine	GC	21

Dopamine	GC	17
Aspartic acid	GC	22
Di(n-aminopropyl)viologen	GC	34
N-(5-aminopentyl)biotinamide	GC	17

Studies have also been performed with secondary and tertiary amines. Comparing the oxidation of primary, secondary and tertiary amines, the irreversible oxidation peak was the sharpest and occurred at least positive potentials (i.e. more easily oxidised) for tertiary amines, followed by secondary amines, and was less well-defined and at most positive potentials for primary amines.[17,30] This is due to the stabilisation of the amine cation radical by the alkyl subsituents.[17] The lifetimes of the radical cation increased from primary, secondary to tertiary amines.[30] Although the ease of amine oxidation decreased from tertiary, secondary and primary, primary amines were found to give the highest modifier surface concentration in comparison to secondary amines, whereas attachment of tertiary amines was not detectable.[17,30] This behaviour was attributed to steric hindrance of the bulky substituents at the nitrogen atom that prevents the tertiary amine cation radical to access the surface.[17] Attachment of primary amines was supported by the observation that the irreversible oxidation peak disappeared and the current decreased significantly with repeat cyclic voltammetry (CV) modification scans whereas for secondary and tertiary amines the height of the oxidation peak remained relatively unchanged.[30] In summary, for attachment of amine modifiers to carbon surfaces via amine oxidation, the amines have to be primary or secondary.[17,24,30] The amine oxidation mechanism in Figure 1.2. has a H group eliminated during the oxidation process, which is not possible with tertiary amines.

Additionally, the nitrogen has to be sp^3. For example, pyridine where the nitrogen is in the sp^2 state did not appear to form the cation radical and attachment did not occur.[24]

With a monoamine modifier, the reaction occurs as in Figure 1.2, however, when diamine modifiers are attached, it is possible that both amines attach to the surface. In one study that investigated the attachment of ethylene diamine to carbon fibres, it was proposed that the single oxidation peak observed accounted for two single electron processes. The two identical and electronically independent amines were oxidised at closely spaced potentials.[12] From the coupling of 4-fluorobenzoyl chloride, the conformation of the ethylene diamine monolayer attached to carbon fibres was suggested to be 75% in the looped arrangement where both amines were surface-bound and the remaining 25% were attached via one amine.[12] In another study, two irreversible oxidation peaks were observed for modification of carbon fibres with ethylene diamine.[35] The peaks were attributed to the corresponding mono- and dication radicals, respectively. From potentiometric titrations of modified carbon fibres with HCl, it was found that the majority of the ethylene diamine modifiers were attached to the carbon fibres by oxidation of the two amines which led to mainly a polymeric multilayer chain and also a looped configuration.[35] For longer diamines, 1,7-diaminoheptane, 1,10-diaminodecane and 1,12-diaminododecane, it has been proposed that only one amine of the diamine was covalently attached to the GC surface whereas the other is not surface-bound.[20]

Monolayers of amines have been shown to be formed by the oxidation of primary amines, as indicated by x-ray photoelectron spectroscopy (XPS) data.[19-23,25] Electrochemical reduction of surface-attached aminomethyl-9-anthracene and

aminomethyl-nitrophenyl layers has also shown with monolayer concentrations, assuming the attached groups were perpendicular to the surface.[12,30] In contrast, oxidation of ethylene diamine at carbon fibres has been proposed to lead to amine multilayers.[35]

Factors that have been examined that influence the amount of modifiers at the surface have been the scan rate during the modification scans,[17,20] applied potential,[12,17] the modifier length[20] and the concentration of the amine modifier[12,32]. Using a decreased scan rate, more positive applied potentials, longer modifier length and increased modifier concentration has been shown to increase the amount of modifier attached. Increasing the electrolysis time and temperature has led to more homogenous modifier surface concentrations.[12] The carbon surface was also important as immobilisation of amines did not occur at the basal plane of HOPG and thus was suggested to only occur at edge plane of the GC electrodes.[17]

The electrochemical oxidation has been commonly carried out in anhydrous ethanol and acetonitrile (ACN) electrolyte solutions.[3,12,17] However, the process has also been performed in 0.1 M KCl aqueous solution where 4-aminobenzoic acid[49] and 4-aminobenzylphosphonic acid[31] were attached to GC electrodes. The 4-aminobenzoic acid was proposed to attach via the amine cation radical mechanism.[49] With the 4-aminobenzylphosphonic acid, two irreversible oxidation peaks were observed in CV modification scans and XPS data showed two types of N_{1s} environments. It was proposed that the oxidation of the primary amine was occurring in turn with the oxidation of the benzylphosphonic acid group (via a Kolbe-like reaction where the phosphonic acid group

was cleaved).[31] The attachment of di(n-aminopropyl)viologen onto GC was also carried out in aqueous solution, which resulted in multilayer formation.[34]

1.3.1. Stability of the amine layers

The stability of amine layers on carbon surface has not been thoroughly studied. In one report, the XPS spectra of *N*-acetyl-ethylenediamine layers on GC electrodes were found to be similar after sonication in water, ethanol and pH 7 phosphate buffer.[17] Butylamine layers were unchanged after soaking in 0.1 M H_2SO_4 for 24 hours which supported the formation of a hydrolytically stable C-N bond. However, 100 cyclic scans in 0.1 $HClO_4$ between 0.2 and 0.8 V vs. Ag/AgCl/saturated $LiClO_4$ gave a ~10% decrease in N : C ratio.[17] Another report showed that a dodecylamine monolayer was stable after sonication in phosphate buffer for 15 minutes by XPS.[23] 1,7-diaminoheptane, 1,10-diaminodecane and 1,12-diaminododecane-modified GC electrodes were stable to sonication in ethanol or water for 20 minutes as confirmed by XPS and the CV scans of the redox probe.[20] Sonication of aspartic acid-modified[22] and *β*-alanine-modified[21] GC electrodes for 15 minutes in water, ethanol and pH 6.0 phosphate buffered saline (PBS), followed by thermal treatment for 40 minutes at 110 °C under high vacuum (10^{-9} Torr), led to no change in the XPS spectra when compared to the as-prepared layers. The XPS spectra of ethylene diamine or 2-amino-4-methyl thiazole-modified carbon fibres thermal treated for 1 hour at 110 °C under high vacuum (10^{-9} Torr) were unchanged indicating the stability of the layer to the treatment.[12] In summary, these stability tests confirm that the modifiers were not only physisorbed on the surface but attached with stable covalent linkages.

1.3.2. Characterisation of the amine layers

Characterisation of the amine layers on carbon materials has been commonly carried out using electrochemical (CV modification scans of amine oxidations and CV scans of solution-based redox probes at surface-attached amine layers) and spectroscopic (XPS) techniques.[3,12,17,19-22,25,29,30,32,35,51,52]

Amine oxidation gave an irreversible CV scan which was attributed to the attachment of the amine modifier to the carbon electrode via a C-N bond.[12,20-23] On repeat scanning, the peak disappeared and the current decreased significantly which also supported the formation of a layer at the surface, that led to the passivation of the electrode.[12,20-22,30]

The decrease of the redox probe response at modified carbon surfaces has been reported to depend on the length of the modifier,[23,32] probe[19,20] and the modification conditions used for amine attachment. Modifiers with longer chains led to slower electron kinetics of redox probe species.[23,32] At GC surfaces modified with 4-aminobenzoic acid using identical modification conditions, the electron transfer of $Fe(CN)_6^{3-}$ probe species was completely blocked, however, the response of $Ru(NH_3)_6^{3+}$ was comparable to the unmodified GC. The difference in the redox responses was ascribed to electrostatic interactions between the modified surface and the probe. At a pH where the acid of the modifier was deprotonated, the response was decreased when there were electrostatic repulsions between the modified surface and the probe ($Fe(CN)_6^{3-}$) and unchanged when the modified surface and probe ($Ru(NH_3)_6^{3+}$) were oppositely charged.[19] Electrostatic

interactions between 1,7-diaminoheptane-modified GC surfaces and the $Fe(CN)_6^{3-}$ and $Ru(NH_3)_6^{3+}$ probes at selected pH values also influenced the probe responses.[20]

Using XPS, the indications for amine attachment were the characteristic N_{1s} peak at approximately 400 eV and the increase in N : C ratio compared to the unmodified carbon.[12,17,19-23,25,30,32]

1.3.3. Assembly of species onto amine-modified carbon surfaces

Characterisation of amine layers

Instead of using direct methods (refer above) to characterise the modifier layer at a carbon surface, selected species have been assembled onto already attached modifiers with the sole intention of gaining information about the modifier layers. The characterisation of the assembled species provided useful information about the modifier layer. The other reason for subsequent assembly was to investigate the versatility of the surface-bound modifiers as tethers.

Assembly of electroactive species onto amine-modified carbon surfaces has been widely studied. Metal complexes were assembled onto the ethylene diamine-modified carbon fibres via electrostatic interactions. The positive charge on the protonated amine groups of the ethylene diamine-modified carbon fibres was initially compensated by chloride ions when immersed in concentrated HCl. The chloride anions were then exchanged with noble metal complexes such as $[Au(III)Cl_4]^-$, $[PtCl_4]^{2-}$ and $[PdCl_4]^{2-}$, as determined from the electrochemical behaviour of the noble metals in the presence of the anionic components when attached to the carbon fibres.[35] 3,5-dinitrobenzoyl chloride was

also covalently coupled to the ethylene diamine-modified carbon fibres.[35] Other examples of electroactive species that have been assembled onto terminal amines of diamine-modified GC surfaces are the heteropolyanion, $P_2W_{18}O_{62}^{6-}$, which was attached to 1,7-diaminododecane via electrostatic interactions with the protonated amines of the modifier layer and ferrocene acetic acid which was covalently coupled to 1,10-diaminododecane via amide bond formation.[20]

Instead of subsequent assembly to already attached modifiers, amine modifiers with electroactive functionalities have been attached to the surface and their electrochemistry analysed to determine surface concentrations. For example, the reductions of 4-nitrobenzylamine and aminomethyl-9-anthracene attached onto GC and carbon fibres have been observed.[12] From the CV scans, the reduction of these surface-bound species in ACN/electrolyte solution was not fully reversible and upon repeat scans the response slowly disappeared. This was accounted for by the protonation of the radical anion by residual water.[12] GC surfaces have also been modified with 3-nitrobenzylamine and 4-nitrobenzylamine and from their electrochemical behaviours in DMF and ACN/electrolyte solutions, their estimated surface concentrations were found to be close to those for a calculated compact layer.[30]

Rather than using electroactive species to gain information about the amine layers, using functionalities that can be observed by XPS was also a useful strategy for analysis of the layers. 4-fluorobenzoyl chloride was coupled to ethylene diamine attached to carbon fibres. The fluorine group was easily detected by XPS and it was suggested from the F : N ratio that 75% of the modifiers were in a looped arrangement where both amines were

surface-bound and the remaining 25% were attached via one amine.[12] Epichlorohydrin was also subsequently attached to ethylene diamine and hexamethylene tetramine-modified carbon fibres and the chlorine group was detected by XPS.[12] 2-amino-4-methyl thiazole-modified carbon fibres were also analysed using XPS before and after electrooxidation treatment. No cleavage of the layer was observed.[12]

Catalytic surfaces and sensors

Amine-modified surfaces have been used for the assembly of species that have good catalytic ability and are useful for the fabrication of sensor devices. The strategy commonly utilised for assembly has been the layer-by-layer deposition involving electrostatic interactions, where alternating layers were assembled on top of each other until the multilayers were formed. The deposition of zirconium-phosphonate multilayers was carried out on amine-modified GC surfaces. Zirconium-1,10-decanediylbis(phosphonic acid) multilayers were attached by firstly modifying surface attached butylamine, decylamine, octadecylamine and 6-aminohexanol with phosphoryl chloride. The resulting phosphate sites were subsequent reacted with zirconium acetylacetonate followed by alkylbis(phosphonic acid) and these two adsorption steps were repeated as desired.[32] 1,7-diaminoheptane-modified GC surfaces were used for assembly of Dawson-type tungstodiphosphate anion $P_2W_{18}O_{62}^{6-}$ and $Ru(NH_3)_6^{3+}$ multilayers, and the resulting surface allowed for the detection of trace amounts of iodate.[37]

Another related example is the immobilisation of polyoxometalates (inorganic metal-oxygen cluster anionic compounds) onto a GC surface modified with 4-

aminobenzoic acid. Alternating combinations of species have been assembled on the 4-aminobenzoic acid-modified surface where one layer was quaternised poly(4-vinylpyridine) complexed with $[Os(bpy)_2Cl]^{2+/+}$ (QPVP-Os) and the other layer were polyoxometalates such as $Pr(SiMo_7W_4O_{39})_2^{13-}$ [19] and $SiW_{12}O_{40}^{4-}$,[18] giving multilayers. The $SiW_{12}O_{40}^{4-}$/QPVP-Os/4-aminobenzoic acid/GC surface showed to have electrocatalytic abilities for the reductions of HNO_2, BrO_3^- and H_2O_2. Instead of polyoxometalates, $P_2W_{15}V_3O_{62}^{9-}$,[48] a sandwich-type compound $Fe_4(H_2O)_2(As_2W_{15}O_{56})_2^{12-}$ [47] and $PdCl_4^{2-}$ [43] were also attached using an identical strategy. The $P_2W_{15}V_3O_{62}^{9-}$/QPVP-Os/4-aminobenzoic acid/GC electrode possessed high catalytic ability for the electroreduction of BrO_3^- and NO_2^- and the electrooxidation of ascorbic acid[48] and the $Fe_4(H_2O)_2(As_2W_{15}O_{56})_2^{12-}$/QPVP-Os/4-aminobenzoic acid/GC surface was able to catalyse the electroreduction of NO_2^- and H_2O_2.[47] The sandwiched $PdCl_4^{2-}$ anions were then electrochemically reduced to give palladium nanoparticles (NPs) and the resulting NP surface was able to enhance the electroreduction of dissolved oxygen and the electrooxidation of hydrazine compounds in aqueous solutions.[43] The layer-by-layer method has also been used to assemble platinum NPs to 4-aminobenzoic acid-modified GC electrodes. The [tetrakis(*N*-methylpyridyl)porphyrinato]cobalt cation and $PtCl_6^{2-}$ were alternately assembled by electrostatic interactions, forming multilayers. The sandwiched $PtCl_6^{2-}$ ion was electrochemically reduced to yield the platinum NPs and the NP surface was able to catalyse the electroreduction of oxygen.[38,39] Instead of the $PtCl_6^{2-}$ anion, $SiW_{12}O_{40}^{4-}$ [40,41] and $P_2W_{18}O_{62}^{6-}$ [40,41] were also attached using an identical approach. The resulting layers

demonstrated catalytic activity for the hydrogen evolution reaction and the electroreduction of oxygen.[40,41]

Transition metal substituted polyoxometalates $ZnW_{11}M(H_2O)O_{39}^{n-}$ (M = Mn, Cu, Fe, Co, Cr, Ni, Zn)[42] and bis-Keggin-type heteropolyanion $Nd(SiMo_7W_4O_{39})_2^{13-}$ [45] were assembled directly onto 4-aminobenzoic acid-modified GC surfaces. These surfaces were shown to have electrocatalytic behaviour for the reduction of H_2O_2 and BrO_3^- and/or HNO_2.[42,45] Copper hexacyanoferrate multilayers[49] were also assembled onto 4-aminobenzoic acid-modified GC surfaces.

The *p*-benzoquinone-modified electrode which was fabricated by subsequent coupling of *p*-benzoquinone to an ethylene diamine-modified GC surface was used for the detection of hydrogen peroxide in a flow injection system.[34] Aminopyridyl compounds, 4-aminopyridine, 4-aminoethylpyridine and imidazole, acted as tethers for the attachment of cobalt(II) tetraphenylporphyrin. The nitrogen on the pyridyl group was the fifth ligand of the complex. The efficiency for the electroreduction of carbon dioxide was enhanced by having a tether group between the complex and electrode.[24]

Biosensors

Many different biological molecules have been immobilised onto amine-modified surfaces. The applications of the immobilised lipids, enzymes, protein and DNA as biosensors have typically been investigated. Potential biosensors, for the detection of K^+ for example, were fabricated from the construction of a hybrid bilayer membrane on a GC surface by the interaction of the lipid monolayer with the hydrophobic surface. A

hydrophobic carbon surface was achieved by electrochemical modification with octylamine, dodecylamine and octadecylamine.[23] One method for immobilising enzymes such as glucose oxidase, horseradish peroxide and dehyrogenase at a GC surface was using a 4-aminomethylphenylboronic acid tether.[25] The immobilised enzymes maintained good catalytic activity, as demonstrated by the electrocatalytic reduction of H_2O_2.[25] The protein avidin was immobilised onto *N*-(5-aminopentyl)biotinamide-modified GC surfaces which have potential uses in biosensing platforms.[17]

Calf thymus DNA was deposited onto 4-aminobenzoic acid-modified GC surfaces by layer-by-layer deposition using poly(diallyldimethylammonium chloride)[46] or QPVP-Os [44] as the alternating layer. Noradrenaline and *β*-nicotinamide adenine dinucleotide have been coupled to ethylene diamine-modified GC surfaces using glutaraldehyde.[34]

The activities of biological molecules have also been shown to be increased at amine-modified electrode. The electrochemical oxidation of uric acid has been shown to be catalysed at a cysteine-modified GC electrode compared to an unmodified electrode.[50] Di(n-aminopropyl)viologen and *p*-benzoquinone-modified GC electrodes mediated the electron transfer of the enzymes, *desulfovibrio vulgaris* hydrogenase and horseradish peroxidase.[34] The *p*-benzoquinone-modified electrode was fabricated by subsequent coupling of *p*-benzoquinone to an ethylene diamine-modified GC surface.[34] Oxidation of *β*-nicotinamide adenine dinucleotide was facilitated by dopamine immobilised at a GC electrode.[17]

Attachment of modifiers with selective capabilities for different analytes has shown to be useful for sensing devices. Examples included the ability of the aspartic acid-[22] or *β*-

alanine-modified[21] GC electrodes to differentiate between dopamine and ascorbic acid, due to charge discrimination of the negatively charged carboxyl groups of the surface-bound modifiers for protonated dopamine over ascorbic acid.

1.4. Assembly of species onto non-amine modified carbon surfaces

In this section, a few examples of species assembled to modified carbon surfaces, apart from amine-modified surfaces, are outlined.

For characterisation purposes, epichlorohydrin was subsequently attached to 4-aminophenyl groups generated by the electrochemical reduction of *para* nitro phenyl (NPh) layers or by hydrolysis of 4-acetamidophenyl groups. The presence of chlorine at the GC surfaces was detected by XPS and showed that the reduction and hydrolysis were successful, giving amine functionalities.[16,53] Gold NPs were covalently attached to a GC surface modified with 4-mercaptophenyl, which had been prepared by the reduction of its corresponding aryl diazonium salt.[54] The sensitivity and selectivity for catecholamines was increased by using 4-sulfophenyl-modified carbon fibre microelectrodes.[55]

One example for the immobilisation of biological molecules onto modified carbon surfaces is the attachment of glucose oxidase to a GC surface which was carried out via a cinnamic acid linker. The cinnamic acid tether was attached by the reduction of its corresponding aryl diazonium salt.[56] In another example, rabbit and human immunoglobulins were chemically coupled to 4-carboxylmethylaniline. The diazonium salt of 4-carboxylmethylaniline-protein was then formed and electrochemically attached to the screen-printed graphite electrode microarrays and used for biosensing.[57] Viral DNA sensing

platforms were prepared by attachment of oligonucleotides onto 4-aminophenyl-modified carbon screen printed electrodes, which was used for the detection of an amplified herpes virus DNA sequence in an electrochemical hybridisation assay. The 4-aminophenyl linker was attached by the reduction of an aryl diazonium salt.[58]

In this work, subsequent assembly of molecular species, protein, aldehyde/sulfate-functionalised polystyrene (PS) and citrate-capped gold NPs to different modifier layers on carbon surfaces are carried out.

1.5. Patterning of surfaces

In the context of this work, patterning of substrates involves covalently attaching modifiers in pre-determined locations on the surface. A great deal of work has been put into developing techniques for patterning gold and silicon surfaces with SAMs on the micro- and nano-scale. Several methods are available for molecular patterning on gold and silicon surfaces.

One of the more common patterning techniques has been micro-contact printing (or stamping) of SAMs onto gold surfaces using a poly(dimethyl)siloxane (PDMS) stamp. This method involved firstly fabricating a stamp which is a piece of PDMS with raised features. The stamp was then inked with molecules which were transferred onto a surface when the stamp was brought into contact with the surface. The pattern of the PDMS features determined the molecular pattern on the surface. This method was introduced by

Whitesides' group where in the original work alkanethiol SAMs were patterned onto gold surfaces with feature sizes down to 200 nm.[59]

Since then resolutions down to < 50 nm have been achieved with V-shaped stamps[60] and various organic molecules,[61-64] silanes,[65] dendrimers,[60] polymers,[66] metal films[67-69] and NPs[70,71] have been patterned on surfaces. Biological components including protein,[60,72,73] antibodies,[74] and DNA[75] have also been transferred onto surfaces in patterns. Apart from gold substrates, silicon based,[60,63-65,76] glass,[62,72-75] gallium arsenide,[67-69] aluminium based,[63,65] polystyrene[72] and mica[61] surfaces have been patterned.

Surfaces for micro-contact printing were selected or pre-modified by attaching molecules so that the surface-'ink' interaction was stronger than the PDMS stamp-'ink' association. This ensured that transfer of the 'ink' occurred. Due to the hydrophobicity of PDMS, non-polar molecules have been generally used as the 'ink'. However, PDMS has also been rendered hydrophilic for patterning polar molecules, by various methods, the most common of which was oxygen plasma treatment.[75,77,78] The resulting PDMS has a higher oxygen content and a lower carbon content, and it has been suggested that a silicon atom was bonded to three or four oxygen atoms.[77]

In this work, alternative approaches to patterning using PDMS are investigated.

1.6. Characterisation techniques

The presence of a modifier layer at a conducting surface has been most commonly shown by the diminishing of the electrochemical response of a redox probe species and by

XPS. Also, when an electroactive functionality was present in the modifier, the electrochemistry of the group was observed by CV and the surface coverage estimated.

1.6.1. CV

The cyclic voltammetric responses of electroactive species are measured in the work described in this thesis. A brief description of CV is given below.

CV is a potential sweep technique. It involves sweeping the electrode potential between potential limits E_1 and E_2 at a known sweep rate (also called scan rate). On reaching limit E_2 the sweep is reversed to E_1, to obtain a cyclic scan. The CV scan is a plot of current vs. potential and indicates the potentials at which redox process occur. The potential axis is also a time axis that is related to scan rate.[79]

To carry out an oxidation process, a positive potential ramp is applied and the electroactive species loses an electron at the electrode giving rise to an anodic current (i_{pa}) which usually gives an oxidation peak at a given potential (E_{pa}). Cathodic currents (i_{pc}) are observed when the potential is applied in the negative direction leading to a reduction process, typically giving a reduction peak at a given potential (E_{pc}). The CV scan is usually initiated at a potential where species are not electroactive.

The redox processes can be reversible, quasi-reversible or irreversible process. Reversibility can be defined as electrochemical or chemical. In an electrochemically reversible process, the electron transfer is not rate limiting. In contrast, the electron transfer is rate limiting in an electrochemically irreversible process. For a chemically reversible process, both forms of the redox couple (O for the oxidised form and R for the reduced

form) are stable in the time scale of the measurement, whereas in a chemically irreversible process the product of the redox reaction undergoes a chemical transformation faster than the time scale of the measurement.

The peak current (i_p) for an electrochemically and chemically reversible system is defined by the Equation 1.1. at 25 °C.[80]

1.1. $$i_p = (2.69 \times 10^5) n^{3/2} A D_o^{1/2} C_o^* v^{1/2}$$

where n is the stoichiometric number of electrons involved in an electrode reaction, A is the area of the electrode in cm^2, D_o is the diffusion coefficient of species O in $cm^2.s^{-1}$, C_o^* is the concentration of species O in $mol.cm^{-3}$ and v is the scan rate in Vs^{-1}.

The observed mid potential between the oxidation and reduction peaks ($E_{1/2}$) is very close to the formal potential for a redox couple ($E°'$) for an electrochemically reversible process. The peak separation between the oxidation and reduction peaks (ΔE_p) provides a measure of the rate of electron transfer between an electroactive species and the electrode. Slow electron transfer gives rise to an increased ΔE_p. For an electrochemically reversible redox process, the peak positions for the redox processes (E_p) are independent of scan rate (v). For an electrochemically irreversible or quasi-reversible redox process, E_{pa} moves positive with increasing v for an oxidation process and E_{pc} moves negative with increasing v for a reduction process. There is no peak on the return scan for an electrochemically irreversible redox process.

It is possible to determine if a redox process is reversible, quasi-reversible or irreversible process from the shape of the CV. Table 1.2. lists the observed relationships between electrochemically reversible, quasi-reversible and irreversible processes when the electroactive species are solution-based.[79] When the electroactive species are immobilised on the electrode surface and the electron transfer is reversible, then $i_{pa}/i_{pc} = 1$, $i_p \alpha v$ and $\Delta E_p \approx 0$ V. In practice, $\Delta E_p \neq 0$ V due to many factors that may include the environment the electroactive species are in and the electrolyte solution used.

Table 1.2. Observed relationships between electrochemically reversible, quasi-reversible and irreversible processes for solution-based electroactive species.[79]

Reversible: the rate of electron transfer is fast compared to the rate of mass transport and does not control the overall rate.

- $i_{pa}/i_{pc} = 1$
- $i_p \alpha v^{1/2}$
- $E_{1/2} \approx E°'$
- $\Delta E_p = 59/n$ mV, where n is the stoichiometric number of electrons involved in an electrode reaction
- E_p is independent of v

Quasi-reversible: the rate of electron transfer and mass transport are similar and both control the overall rate.

- $\Delta E_p > 59/n$ mV and increases with v

Irreversible: the rate of electron transfer is slow compared to the rate of mass transport and controls the overall rate.

- no reverse peak
- $i_p \alpha v^{1/2}$
- E_{pa} moves positive with increasing v and E_{pc} moves negative with increasing v

The contribution of ohmic (*iR*) drop must also be considered. When a current flows, the resistance from the electrode and solution causes the potential experienced by the electroactive species to be less positive for an oxidation process or less negative for a reduction process, than the applied potential.

Surface concentrations

The surface concentrations of surface-immobilised electroactive species can be estimated from CV scans. Surface concentration is calculated according to Equation 1.2.

1.2. $$\Gamma = Q / nFA$$

where Γ is surface concentration in mol.cm^{-2}, Q is charge in Coulombs, n is the number of electrons, F is Faraday's constant (96485 C.mol^{-1}) and A is the geometric area of electrode in cm^2. The charge ($Q = i \times t$) associated with the redox process is determined from the peak area in the CV, where i is current in A and t is time in s.

Probe response at modified surfaces

When solution-based electroactive species with well-characterised reversible electrochemistry (redox probes) are present at a modified electrode, the CV of the probe can occur via several processes.[80] Assuming a neutral insulating modifier layer, two processes and hence two distinguishable types of probe responses can be identified.

(i) Electron transfer across a compact homogeneous layer

The electrochemical response of the probe is affected by the presence of a modifier layer which decreases the rate of electron transfer between the probe species and electrode. Electron transfer rates can be slowed at even extremely thin modifier layers.[81] Increasing the thickness of the layer may result in the electron transfer being completely inhibited. The layer increases the distance of closest approach between the probe species and the electrode, and the electron transfer occurs via an electron tunnelling (non-adiabatic) mechanism,[82] as depicted in Figure 1.4. The effect of tunnelling on the electron transfer rate constant can be written as Equation 1.3.[80]

1.3. $$k^0(x) = k^0(x = 0) \exp(-\beta x)$$

where k^0 is the standard heterogeneous rate constant in cm.s^{-1}, x is the distance from the electrode in cm and β is the tunnelling barrier coefficient in Å^{-1}. There is an exponential decrease in electron transfer rate from tunnelling with distance as shown by Equation 1.3.[80] Typical reported β values for SAMs on gold surfaces are approximately 0.8 Å^{-1}.[83,84] Therefore, x can be very small for $k^0(x) \neq k^0(x = 0)$, resulting in the probe response at the modified electrode to differ from the unmodified electrode.

The probe response (Figure 1.5.(ii).) when electron transfer is slowed across a compact homogeneous layer shows firstly an increase in ΔE_p and secondly a decrease in peak current compared to the unmodified electrode (Figure 1.5.(i).). To quantify the changes of the probe response at a modified electrode, peak current ratios relative to the

unmodified electrode can be used, for example, the ratio (i_{pa} after modification)/(i_{pa} at as-prepared GC electrode). The probe response at a modified electrode is typically quasi-reversible or the probe response is not observed (i.e. scan is featureless at the same current range used to record the CV scan at the unmodified electrode) when the electron transfer is strongly inhibited by the layer.

When the layer contains charged groups and the probe is charged, electrostatic interactions will also influence the CV probe response. For example, when the reduced form of the probe is oppositely charged to the modifier layer, the oxidation peak is usually larger than the reduction peak. This is due to electrostatic attractions between the probe and the layer causing accumulation of the probe at the surface. After its oxidation, the charge is decreased causing it to diffuse away from the electrode giving a smaller reduction peak. At times, due to electrostatic attractions increasing the probe concentration at the surface, the response of a probe at a modified electrode may be similar to that at the unmodified electrode suggesting that a modifier layer is not present. However, when a probe is used with the same charge as the modifier layer, electrostatic repulsions reduce the probe concentration at the surface and it is indicative that a layer is present.[19]

A similar probe response as in Figure 1.5.(ii). would also be observed in the presence of a 'loosely packed' layer or a layer consisting of holes and/or thin patches. A reduced number of the probe species diffuses through the layer to the electrode giving a decreased response compared to at the unmodified electrode.

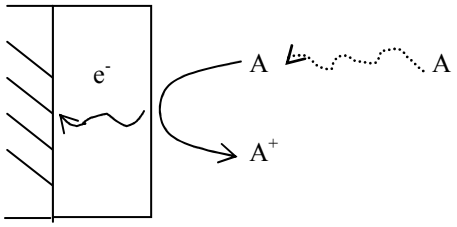

Figure 1.4. Electron tunnelling through a modifier layer for a one-electron oxidation process.

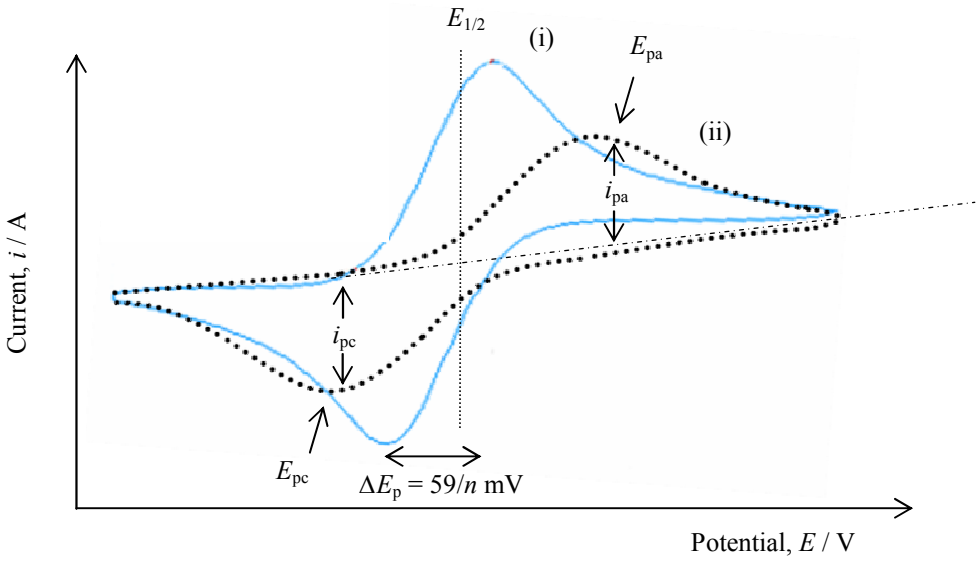

Figure 1.5. A typical CV scan for a solution-based probe species at (i) an unmodified electrode and (ii) a modified electrode, where the reduced form of the probe is initially present.

(ii) Electron transfer across a layer incorporating pinholes

When small widely-spaced pinholes are present in an otherwise compact homogeneous modifier layer, the probe species approaches the electrode by radial diffusion to the pinholes and electron transfer occurs at the surface as depicted in Figure 1.6. The probe response depends upon the fractional coverage of the electrode by the layer, size of

the pinholes, distribution of the pinholes, standard rate of electron transfer and time scale of the measurement.[80,85] This situation is complicated as the size and distribution can vary across the layer. The probe response that is observed (Figure 1.7.) is typical of microelectrode behaviour.[80] However, the probe response can be similar to Figure 1.5.(ii). when pinholes are present but closely-spaced because radial diffusion fields overlap giving an essentially linear diffusion field.[80]

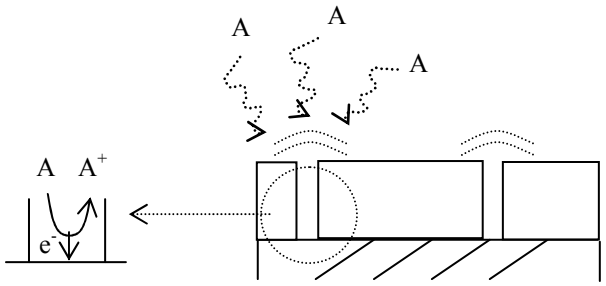

Figure 1.6. Radial diffusion to small, widely-spaced pinholes in the modifier layer, for a one-electron oxidation process.

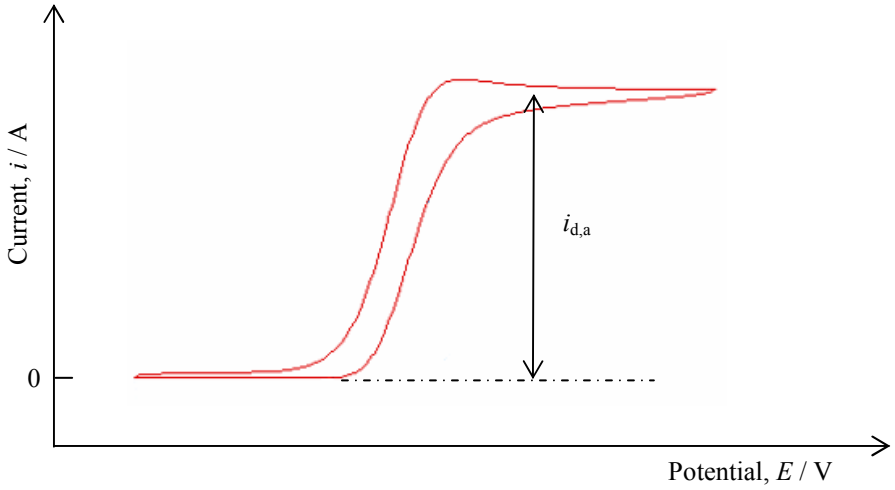

Figure 1.7. A typical CV scan for a solution-based probe species at a modified layer where pinholes are present and where the reduced form of the probe is initially present. $i_{d,a}$ is the diffusion-limited anodic current and $E_{1/2} = E_{3/4} - E_{1/4}$.

In summary, the probe CV recorded at a modified surface provides some indication of the blocking behaviour and morphology of the layer. The observed probe response is typically a combination of the processes which arise from mixed linear and radial diffusion. The blocking behaviour provides some indication of surface concentration per monolayer (compactness) and the thickness of the layer. With electrochemically-assisted surface modification, for a given modifier and surface, the blocking behaviour of the layer is a result of a series of factors that include the concentration of the modifier, scan rate, number of modification scans or electrolysis time and applied potential.[12,16,17,20,32,53,86]

1.6.2. Contact angle measurements

Contact angle measurements provide a straightforward and useful indication of the wettability of a surface. Water is the most common solvent used for these types of measurements. In this work, the wettability of modified surfaces is measured by water contact angles from sessile drops.

Two types of contact angle measurements are commonly made: sessile (or static) and dynamic contact angles. For sessile drop measurements, a deposited drop lies on the surface and forms a contact angle that depends on the properties of three phases: solid (modified surface), liquid (water drop) and gas (surrounding atmosphere). Measurements are taken from the drop as shown in Figure 1.8.(i). A surface is generally considered hydrophobic when the angle is > 65°.[87] For example, the sessile water contact angle on teflon was measured to be 100 ± 3°.

With dynamic contact angles, the advancing and receding angles can give useful information about the surface. When measuring advancing angles, the size of the drop is constantly increased and the wetting line is fresh (Figure 1.8.(ii).), whereas with receding angles the drop is deposited and then retracted (Figure 1.8.(iii).). Advancing angles are used as they eliminate time-based effects due to evaporation of sessile drops and receding angles provide information about the dewetting properties of the surface. By tilting the surface, dynamic angles can also be measured to offer indications on the roughness and rolling resistant properties of the surface.

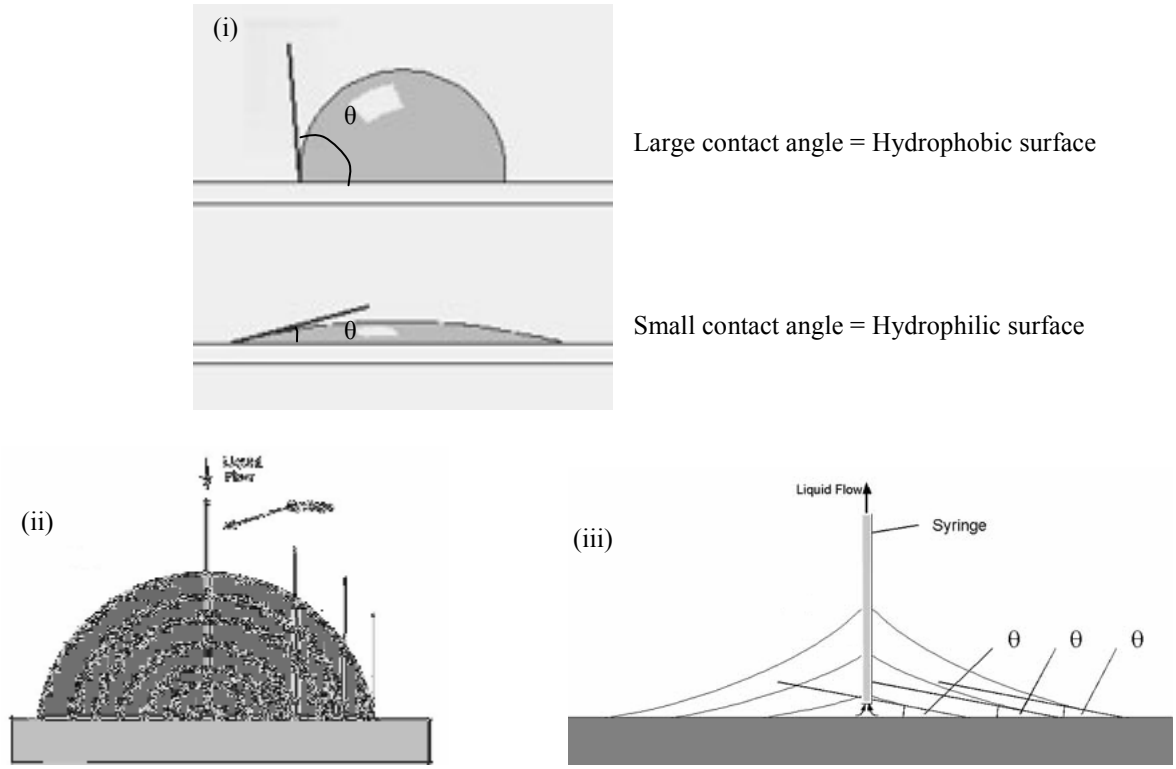

Figure 1.8. Schematic diagrams depicting the measurement of (i) sessile contact angles and dynamic contact angles. Dynamic contact angles can be measured by (ii) advancing angles or (iii) receding angles. θ is the contact angle measured. Images are from www.kruss.info.

1.6.3. XPS

XPS, also known as electron spectroscopy for chemical analysis (ESCA), can provide information about the atomic composition and functional groups present in the sample. In this work, the N : C atomic ratios and the N functionalities are identified for certain samples. The sample is subjected to a beam of monoenergetic X-ray photons of known energy ($h\nu$) causing an inner-shell electron to be emitted from the sample,[88] as shown in Figure 1.9. The kinetic energy of the emitted electron (E_k) is measured and its binding energy calculated (E_b) as $E_b = h\nu - E_k - w$, where w is the work function of the spectrometer that corrects for the electrostatic environment in which the electron is observed.[88] The binding energy is characteristic of the atom and orbital for a given bond. XPS provides a plot of emission intensity and binding energy. From wide scans, elemental analysis can be carried out. From narrow scans of peaks assigned to a given atom, functional groups containing the atom can be assigned from peak positions at different binding energies.

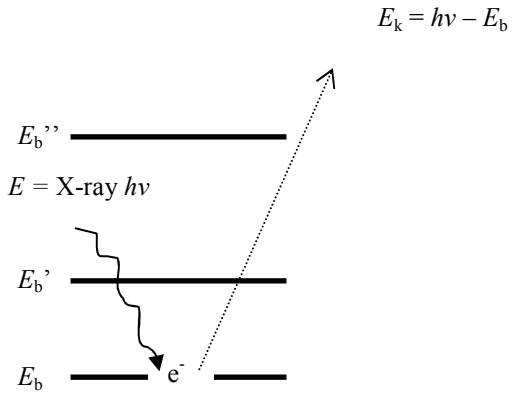

Figure 1.9. Schematic representation of XPS. E is quantum energy, h is Planck's constant, ν is the frequency, E_b is the binding energy and E_k is the kinetic energy of the emitted electron.

1.6.4. Raman spectroscopy

Raman spectroscopy can be used to determine the functional groups present in the sample. In this work, Raman spectroscopy is used to characterise the carbon surfaces. Incident photons from an intense beam of monochromatic electromagnetic radiation ($h\nu_i$, where h is Planck's constant, ν_i is the incident frequency) is directed at the sample causing the vibrations and/or rotational motions of the molecule to be altered by ΔE (change in quantum energy),[89] as shown in Figure 1.10. According to quantum theory, a molecular motion can only have certain discrete energy states.[90] Therefore, depending on ΔE and hence $h\nu_s$ (where ν_s is the scattering frequency), specific Raman bands are obtained from which functional groups in the sample can be identified. The position of the bands are expressed in $\bar{\nu}$ (wavenumber in cm^{-1}) which is given by ν/c (where ν is frequency in s^{-1} and c is the velocity of light in $cm.s^{-1}$).[89,90] When ΔE is positive, energy is absorbed by the molecule and Stokes Raman scattering is observed whereas anti-Stokes Raman scattering is achieved when the energy of the resulting photon is higher than that of the laser hence occurring at a high Raman frequencies and ΔE is negative.[89,90]

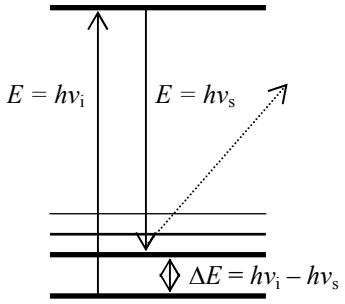

Figure 1.10. Schematic representation of Raman spectroscopy showing Stokes Raman scattering. E is quantum energy, h is Planck's constant, ν_i is the incident frequency, ν_s is the scattering frequency and ΔE is change in quantum energy.

1.6.5. Atomic force microscope (AFM)

The AFM is typically used for measuring surface topography. It provides an excellent contrast that allows for direct quantitative height measurements of surface features. The horizontal field of view can be larger than 125 μm and the vertical range is from the nano-scale up to 8 – 10 μm.[91] In this work, the AFM is mainly used in tapping mode for topographical measurements of modified surfaces. Contact mode is used briefly and discussed in Chapter 9a. As shown in Figure 1.11, the tip at the end of the cantilever is brought into closest contact with the sample (contacts the surface when in contact mode) and is scanned across the surface by the scanner moving the sample under the tip. The changes in horizontal (x, y) and vertical (z) planes of the flexible cantilever alter the deflection of the laser which is detected by the quadrapole photodetector. The laser positions are recorded and converted to an image.

The distance between the cantilever and detector is generally three orders of magnitude greater than the length of the cantilever (mm compared to μm), therefore, tiny movements in the cantilever can be detected giving rise to high sensitivity.[91] The scanner is an extremely accurate positioning platform. The scanner moves across the first line of the scan and back and then steps in the perpendicular direction to the second scan line and so on. The equally spaced samples (or image points) per line are usually identical to the number of lines, in order to obtain a cube grid of data points in the x, y and z directions.[91] Apart from the samples per line, the scan rate can also affect the resolution of the image. Faster scan rates tend to reduce the sharpness of the image.

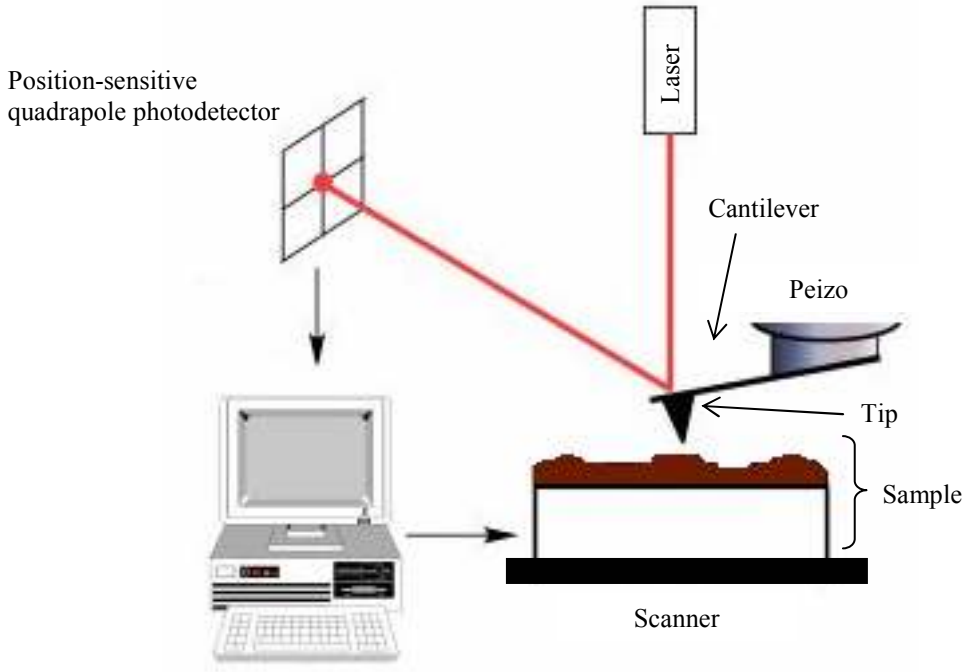

Figure 1.11. Schematic representation of the AFM.
Image is from www.spectroscopynow.com.

A sharper tip will provide more detailed images. Two cantilever designs are common, a single beam or a "V" shaped beam (triangular). The length, width, thickness of the beam(s), the resonance frequency and force constant of the cantilever are selected depending on the mode of operation and the sample properties. Stiff cantilevers with high resonance frequencies and high force constants are more suitable for tapping mode on a hard surface, for example.[91]

Tapping mode, which is a non-contact mode, uses an oscillating cantilever that is brought into close proximity to the surface (Figure 1.12.). The tip "bounces" along a path above the surface and senses the forces, usually van der Waals, exerted by the surface, altering its resonance frequency.[91] Good vertical resolution can be achieved with tapping

mode but lateral resolution is poorer compared to contact mode where the tip contacts the surface during imaging.[91]

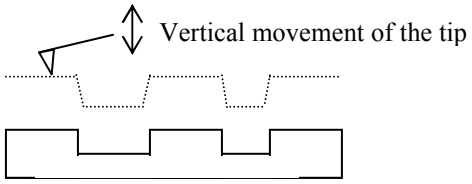

Figure 1.12. Schematic showing the path of the tip (dotted line) when using the AFM in tapping mode.

1.6.6. Scanning electron microscope (SEM) and transmission electron microscope (TEM)

Both the SEM and TEM are very powerful imaging techniques. Using high resolution instruments, the best resolution achievable using the SEM is *ca.* 1 nm[92] and for the TEM it is *ca.* 0.06 nm[93]. In this work, the SEM and TEM are used for visualisation of NPs and SEM is also used to image patterns of modifiers.

Briefly, the SEM works by a beam of high speed electrons "hitting" the sample, interacting with the electrons in the atoms of the sample and generating secondary electrons. Because of their low energy (3 – 5 eV), the majority of the secondary electrons are absorbed by the sample and only those produced near the surface of the sample (~1%) escape and are detected, contributing to image formation.[94] Raised features on the sample appear brighter than the flat background as there is a shorter path length for the escape of electrons.[94]

With the TEM, the electron beam must be able to penetrate and be transmitted through the sample. The transmitted electrons are captured giving rise to the image. Based on De Broglie's equation that states $\lambda = h/mv$ (where λ is wavelength, h is Planck's constant, m is mass of the particle and v is the velocity of the particle), as the accelerating voltage for the electron beam is increased, the wavelength decreases and the resolvable size decreases (i.e. resolution increases).[94] The high resolution transmission electron microscope (HRTEM) uses a higher accelerating voltage to obtain higher resolution images compared to TEM.

1.7. Scope of this work

This work aims to controllably modulate the surface properties of carbon (PPF and GC) by the attachment of different modifiers. Modifiers are assembled via the oxidation of amines and the reduction of aryl diazonium salts. The modified surfaces are then used for the subsequent coupling of molecular species, adsorption of protein and assembly of aldehyde/sulfate-functionalised PS and citrate-capped gold NPs. Patterning of different modifiers at pre-determined spatially defined locations on the one carbon surface is also investigated.

In *Chapter 2*, the experimental details used in this work are provided. In *Chapter 3*, the preparation and characterisation of the GC and PPF surfaces are detailed. Thorough characterisation of the carbon surfaces is necessary before organic layers are attached. The resistivity, electrochemical properties, carbon composition, wettability and surface roughness of both surfaces are examined.

In *Chapter 4*, seven different primary amine modifiers are attached to GC and PPF surfaces via covalent C-N linkages. Apart from fabricating layers that are used for various applications, this part of the work is also aimed at gaining information about amine layers which have not been well-studied. In *Chapter 5*, five different aryl diazonium salt modifiers are attached to the carbon surfaces via covalent C-C bonds. Aryl layers have been well-characterised in comparison to amine layers and attaching these layers broadens the range of surface properties that is achieved. The subsequent coupling of various molecular species to already attached amine and aryl layers are discussed in *Chapter 4* and *5*.

In *Chapter 6*, amine and aryl layers are treated with fluorescently labelled protein and surfaces that increase or resist the adsorption of protein are identified. Also, the capability of fluorescence microscopy as a semi-quantitative method to estimate protein adhesion is assessed.

In *Chapter 7*, the assembly of aldehyde/sulfate-functionalised PS and citrate-capped gold NPs are carried out on amine and aryl surfaces. The assembly of NPs provides information about the modifier layers and can be useful for further applications such as sensing.

In *Chapter 8*, the experimental methods and preliminary experiments for using PDMS in molecular patterning on carbon surfaces are discussed. PDMS is one of the three materials used to block part of the surface for patterning. The other two materials are poly(vinyl)alcohol (PVA) and thin metal films. In *Chapter 9*, these three materials are used in five patterning approaches to fabricate carbon surfaces with two different chemical

moieties on the one surface. Explorations into visualisation methods for the molecular patterns are also carried out.

Chapter 10 provides the final conclusions and discussions of further work arising from this study.

1.8. References

(1) Bard, A. J.; Abruna, H. D.; Chidsey, C. E.; Faulkner, L. R.; Feldberg, S. W.; Itaya, K.; Majda, M.; Melroy, O.; Murray, R. W.; et al. *Journal of Physical Chemistry* **1993**, *97*, 7147-7173.

(2) Flynn, N. T.; Tran, T. N. T.; Cima, M. J.; Langer, R. *Langmuir* **2003**, *19*, 10909-10915.

(3) Downard, A. J. *Electroanalysis* **2000**, *12*, 1085-1096.

(4) Pinson, J.; Podvorica, F. *Chemical Society Reviews* **2005**, *34*, 429-439.

(5) McCreery, R. L.; Callstrom, M.; Neenan, T.; Alsmeyer, D.; Wang, Y. *Frontiers of Chemistry* **1990**, *2*, 27-29.

(6) Murray, R. W. *Electroanalytical Chemistry*; Marcel Dekker, **1984**.

(7) McCreery, R. L. *Electroanalytical Chemistry*; Marcel Dekker, **1991**.

(8) Otero, L.; Vettorazzi, N.; Barbero, C.; Miras, M. C.; Silber, J. J.; Sereno, L. *Journal of Electroanalytical Chemistry* **1993**, *350*, 251-265.

(9) Silva, A. R.; Martins, M.; Freitas, M. M. A.; Valente, A.; Freire, C.; de Castro, B.; Figueiredo, J. L. *Microporous and Mesoporous Materials* **2002**, *55*, 275-284.

(10) Jarrais, B.; Silva, A. R.; Freire, C. *European Journal of Inorganic Chemistry* **2005**, 4582-4589.

(11) Fujihira, M.; Osa, T. *Progress in Batteries & Solar Cells* **1979**, *2*, 244-248.

(12) Barbier, B.; Pinson, J.; Desarmot, G.; Sanchez, M. *Journal of the Electrochemical Society* **1990**, *137*, 1757-1764.

(13) Maeda, H.; Yamauchi, Y.; Hosoe, M.; Li, T.-X.; Yamaguchi, E.; Kasamatsu, M.; Ohmori, H. *Chemical & Pharmaceutical Bulletin* **1994**, *42*, 1870-1873.

(14) Andrieux, C. P.; Gonzalez, F.; Saveant, J.-M. *Journal of the American Chemical Society* **1997**, *119*, 4292-4300.

(15) Vase, K. H.; Holm, A. H.; Pedersen, S. U.; Daasbjerg, K. *Langmuir* **2005**, *21*, 8085-8089.

(16) Delamar, M.; Hitmi, R.; Pinson, J.; Saveant, J. M. *Journal of the American Chemical Society* **1992**, *114*, 5883-5884.

(17) Deinhammer, R. S.; Ho, M.; Anderegg, J. W.; Porter, M. D. *Langmuir* **1994**, *10*, 1306-1313.

(18) Cheng, L.; Liu, J.; Dong, S. *Analytica Chimica Acta* **2000**, *417*, 133-142.

(19) Liu, J.; Cheng, L.; Liu, B.; Dong, S. *Langmuir* **2000**, *16*, 7471-7476.

(20) Liu, J.; Dong, S. *Electrochemistry Communications* **2000**, *2*, 707-712.

(21) Zhang, L.; Sun, Y.-G. *Analytical Sciences* **2001**, *17*, 939-943.

(22) Zhang, L.; Lin, X. *Analytical and Bioanalytical Chemistry* **2005**, *382*, 1669-1677.

(23) Han, X.; Wang, L.; Qi, B.; Yang, X.; Wang, E. *Analytical Chemistry* **2003**, *75*, 6566-6570.

(24) Tanaka, H.; Aramata, A. *Journal of Electroanalytical Chemistry* **1997**, *437*, 29-35.

(25) Ma, Y.; Gao, Q.; Yang, X. *Microchimica Acta* **2005**, *150*, 21-26.

(26) Brooks, S. A.; Ambrose, W. P.; Kuhr, W. G. *Analytical Chemistry* **1999**, *71*, 2558-2563.

(27) Ssenyange, S.; Anariba, F.; Bocian, D. F.; McCreery, R. L. *Langmuir* **2005**, *21*, 11105-11112.

(28) Liang, C.; Huang, J.-F.; Li, Z.; Luo, H.; Dai, S. *European Journal of Organic Chemistry* **2006**, 586-589.

(29) Buttry, D. A.; Peng, J. C. M.; Donnet, J.-B.; Rebouillat, S. *Carbon* **1999**, *37*, 1929-1940.

(30) Adenier, A.; Chehimi, M. M.; Gallardo, I.; Pinson, J.; Vila, N. *Langmuir* **2004**, *20*, 8243-8253.

(31) Yang, G.; Liu, B.; Dong, S. *Journal of Electroanalytical Chemistry* **2005**, *585*, 301-305.

(32) Hoekstra, K. J.; Bein, T. *Chemical Materials* **1996**, *8*, 1865-1870.

(33) Park, S.-J.; Donnet, J.-B. *Journal of Colloid and Interface Science* **1998**, *206*, 29-32.

(34) Hoogvliet, J. C.; Van Os, P. J. H. J.; Van der Mark, E. J.; Van Bennekom, W. P. *Biosensors & Bioelectronics* **1991**, *6*, 413-423.

(35) Antoniadou, S.; Jannakoudakis, A. D.; Jannakoudakis, P. D.; Theodoridou, E. *Journal of Applied Electrochemistry* **1992**, *22*, 1060-1064.

(36) Liu, J.; Cheng, L.; Dong, S.; Liu, B. In *Faming Zhuanli Shenqing Gongkai Shuomingshu* **2001**, p 6 pp.

(37) Liu, J.; Cheng, L.; Liu, B.; Dong, S. *Electroanalysis* **2001**, *13*, 993-998.

(38) Shen, Y.; Liu, J.; Wu, A.; Jiang, J.; Bi, L.; Liu, B.; Li, Z.; Dong, S. *Langmuir* **2003**, *19*, 5397-5401.

(39) Shen, Y.; Liu, J.; Wu, A.; Jiang, J.; Bi, L.; Liu, B.; Li, Z.; Dong, S. *Chemistry Letters* **2002**, 550-551.

(40) Shen, Y.; Liu, J.; Jiang, J.; Liu, B.; Dong, S. *Journal of Physical Chemistry B* **2003**, *107*, 9744-9748.

(41) Shen, Y.; Liu, J.; Jiang, J.; Liu, B.; Dong, S. *Electroanalysis* **2002**, *14*, 1557-1563.

(42) Liu, J.; Cheng, L.; Dong, S. *Electroanalysis* **2002**, *14*, 569-574.

(43) Liu, J.; Cheng, L.; Song, Y.; Liu, B.; Dong, S. *Langmuir* **2001**, *17*, 6747-6750.

(44) Liu, J.; Jin, Y.; Wu, A.; Li, Z.; Dong, S. *Electroanalysis* **2004**, *16*, 1931-1937.

(45) Liu, J.; Liu, B.; Dong, S. *Fenxi Huaxue* **2002**, *30*, 129-133.

(46) Luo, L.; Liu, J.; Wang, Z.; Yang, X.; Dong, S.; Wang, E. *Biophysical Chemistry* **2001**, *94*, 11-22.

(47) Bi, L.; Liu, J.; Shen, Y.; Jiang, J.; Dong, S. *New Journal of Chemistry* **2003**, *27*, 756-764.

(48) Zhai, S.; Liu, J.; Jiang, J.; Dong, S. *Electroanalysis* **2003**, *15*, 1165-1170.

(49) Yang, G.; Shen, Y.; Wang, M.; Chen, H.; Liu, B.; Dong, S. *Talanta* **2006**, *68*, 741-747.

(50) Yan, Z.; Zhang, J.-R.; Fang, H.-Q. *Analytical Letters* **1999**, *32*, 223-234.

(51) Liu, A.; Anzai, J. *Langmuir* **2003**, *19*, 4043-4046.

(52) Jansen, R. J. J.; van Bekkum, H. *Carbon* **1995**, *33*, 1021-1027.

(53) Allongue, P.; Delamar, M.; Desbat, B.; Fagebaume, O.; Hitmi, R.; Pinson, J.; Saveant, J.-M. *Journal of the American Chemical Society* **1997**, *119*, 201-207.

(54) Harnisch, J. A.; Pris, A. D.; Porter, M. D. *Journal of the American Chemical Society* **2001**, *123*, 5829-5830.

(55) Hermans, A.; Seipel, A. T.; Miller, C. E.; Wightman, R. M. *Langmuir* **2006**, *22*, 1964-1969.

(56) Hall, S. B.; Yang, X.; Officer, D. L.; Belcher, W. J.; Burrell, A. K. *Synthetic Metals* **2003**, *137*, 1429-1430.

(57) Corgier, B. P.; Marquette Christophe, A.; Blum Loic, J. *Journal of the American Chemical Society* **2005**, *127*, 18328-18332.

(58) Ruffien, A.; Dequaire, M.; Brossier, P. *Chemical Communications* **2003**, 912-913.

(59) Kumar, A.; Biebuyck, H. A.; Whitesides, G. M. *Langmuir* **1994**, *10*, 1498-1511.

(60) Li, H.-W.; Muir, B. V. O.; Fichet, G.; Huck, W. T. S. *Langmuir* **2003**, *19*, 1963-1965.

(61) Workman, R. K.; Manne, S. *Langmuir* **2004**, *20*, 805-815.

(62) Carmichael, T. B.; Vella, S. J.; Afzali, A. *Langmuir* **2004**, *20*, 5593-5598.

(63) Goetting, L. B.; Deng, T.; Whitesides, G. M. *Langmuir* **1999**, *15*, 1182-1191.

(64) Andersson, H.; Jonsson, C.; Moberg, C.; Stemme, G. *Sensors and Actuators, B: Chemical* **2001**, *B79*, 78-84.

(65) Jeon, N. L.; Finnie, K.; Branshaw, K.; Nuzzo, R. G. *Langmuir* **1997**, *13*, 3382-3391.

(66) Liang, Z.; Li, K.; Wang, Q. *Langmuir* **2003**, *19*, 5555-5558.

(67) Zaumseil, J.; Meitl, M. A.; Hsu, J. W. P.; Acharya, B. R.; Baldwin, K. W.; Loo, Y.-L.; Rogers, J. A. *Nano Letters* **2003**, *3*, 1223-1227.

(68) Menard, E.; Bilhaut, L.; Zaumseil, J.; Rogers, J. A. *Langmuir* **2004**, *20*, 6871-6878.

(69) Felmet, K.; Loo, Y.-L.; Sun, Y. *Applied Physics Letters* **2004**, *85*, 3316-3318.

(70) Santhanam, V.; Andres, R. P. *Nano Letters* **2004**, *4*, 41-44.

(71) Guo, Q.; Teng, X.; Yang, H. *Nano Letters* **2004**, *4*, 1657-1662.

(72) Bernard, A.; Delamarche, E.; Schmid, H.; Michel, B.; Bosshard, H. R.; Biebuyck, H. *Langmuir* **1998**, *14*, 2225-2229.

(73) Renault, J. P.; Bernard, A.; Bietsch, A.; Michel, B.; Bosshard, H. R.; Delamarche, E.; Kreiter, M.; Hecht, B.; Wild, U. P. *Journal of Physical Chemistry B* **2003**, *107*, 703-711.

(74) Graber, D. J.; Zieziulewicz, T. J.; Lawrence, D. A.; Shain, W.; Turner, J. N. *Langmuir* **2003**, *19*, 5431-5434.

(75) Lange, S. A.; Benes, V.; Kern, D. P.; Hoerber, J. K. H.; Bernard, A. *Analytical Chemistry* **2004**, *76*, 1641-1647.

(76) Rozkiewicz, D., I.; Ravoo Bart, J.; Reinhoudt David, N. *Langmuir* **2005**, *21*, 6337-6343.

(77) Makamba, H.; Kim, J. H.; Lim, K.; Park, N.; Hahn, J. H. *Electrophoresis* **2003**, *24*, 3607-3619.

(78) Trimbach, D. C.; Al-Hussein, M.; De Jeu, W. H.; Decre, M.; Broer, D. J.; Bastiaansen, C. W. M. *Langmuir* **2004**, *20*, 4738-4742.

(79) Southampton Electrochemistry Group *Instrumental methods in electrochemistry*; Ellis Horwood Limited, **1985**.

(80) Bard, A. J.; Faulkner, L. R. *Electrochemical methods: fundamentals and applications*; Second ed.; John Wiley & Sons, **2001**.

(81) Cheng, Q.; Brajter-Toth, A. *Analytical Chemistry* **1995**, *67*, 2767-2775.

(82) Becka, A. M.; Miller, C. J. *Journal of Physical Chemistry* **1992**, *96*, 2657-2668.

(83) Wang, W.; Lee, T.; Reed, M. A. *Physical Review B* **2003**, *68*, 035416.

(84) Tran, E.; Grave, C.; Whitesides, G. M.; Rampi, M. A. *Electrochemica Acta* **2005**, *50*, 4850-4856.

(85) Amatore, C.; Saveant, J. M.; Tessier, D. *Journal of Electroanalytical Chemistry and Interfacial Electrochemistry* **1983**, *147*, 39-51.

(86) Brooksby, P. A.; Downard, A. J. *Langmuir* **2004**, *20*, 5038-5045.

(87) Vogler, E. A. *Advances in colloid and interface science* **1998**, *74*, 69-117.

(88) http://www.chemistry.adelaide.edu.au/external/soc-rel/content/xps.htm.

(89) Colthup, N. B.; Daly, L. H.; Wiberley, S. E. *Introduction to infrared and Raman spectroscopy*; Academic Press, **1975**.

(90) Turrell, G.; Corset, J. *Raman microscopy: developments and applications*; Academic Press, **1996**.

(91) Braga, P. C.; Ricci, D. *Atomic force microscopy: biomedical methods and applications*; Humana Press, **2004**.

(92) Goldstein, J.; Newbury, D.; Joy, D.; Lyman, C.; Echlin, P.; Lifshin, E.; Sawyer, L.; Michael, J. *Scanning electron microscopy and X-ray microanalysis*; Third ed.; Kluwer Academic/Plenum Publishers, **2003**.

(93) De Graef, M. *Introduction to conventional transmission electron microscopy*; Cambridge University Press, **2003**.

(94) Flegler, S. L.; Heckman, J. W., Jr.; Klomparens, K. L. *Scanning and transmission electron microscopy: an introduction*; W. H. Freeman and Company, **1993**.

2.1. Introduction

This chapter includes general methods that are used in the work described in more than one chapter. Specific methods relevant to work in only one chapter are outlined in that chapter. Full experimental details are given in Chapter 3 for the preparation and characterisation of pyrolysed photoresist film (PPF) and glassy carbon (GC) surfaces, Chapter 4 for the attachment and characterisation of amine layers on carbon surfaces, Chapter 5 for the attachment and characterisation of aryl layers on carbon surfaces, Chapter 6 for the adsorption of protein onto modified GC surfaces, Chapter 7 for assembly of nanoparticles (NPs) onto modified PPF and GC surfaces, Chapter 8 for using poly(dimethyl)siloxane (PDMS) in molecular patterning on PPF surfaces and Chapter 9 for using poly(vinyl)alcohol (PVA) and metal films in molecular patterning on PPF and GC surfaces.

2.2. Experimental methods

2.2.1. General solutions and materials

General solutions

MilliQ (MQ) water (Millipore), > 18 MΩ.cm, was used for all aqueous solutions. Phosphate buffered saline (PBS) is phosphate buffer (PB, 0.04 M, pH 7.4) with added 0.1 M NaCl. PB (0.04 M, pH 7.4) was made by dissolving KH_2PO_4 (1.179 g) and Na_2HPO_4 (4.302 g), both dried in a 45 °C oven for at least a day, in 1 L of MQ water. NaOH was added to obtain the desired pH. The pH meter was calibrated with two standard buffers of pH 6.86 (phosphate) and 10.01 (carbonate). Tween 20 (polyoxyethylenesorbitan

monolaurate, Bio-Rad) detergent was used as a 5% aqueous solution dissolved in MQ water. Acetonitrile (ACN) was HPLC grade (Ajax Finechem) and other common organic solvents were analytical reagent grade.

Redox probe solutions

Redox probe solutions were:

1. Ferrocene monocarboxylic acid (FCA, ≈ 0.5 mM) in PBS;
2. $Ru(NH_3)_6^{3+}$ (variable concentration) in PBS;
3. Ferrocene (Fc, ≈ 0.5 mM) in ACN/0.1 M $[Bu_4N]BF_4$ (tetrabutylammonium fluoroborate)

These compounds were used as purchased from Sigma.

Solutions for electrode modification

Modifier solutions were prepared in anhydrous ACN with 0.1 M $[Bu_4N]BF_4$. ACN was dried over CaH_2 for 7 days and refluxed under $N_{2(g)}$ for 2 hours. Immediately prior to distillation in a $N_{2(g)}$ atmosphere, the ACN was refluxed for at least another 30 minutes.

The electrolyte, $[Bu_4N]BF_4$, was prepared from tetrabutylammonium hydroxide (40%, Acros Organics) and fluoroboric acid (40%, BDH). 5 mL of the acid diluted to 25 mL with MQ water was added with constant stirring to 20 mL of the hydroxide diluted to 100 mL with MQ water. The white precipitate was collected under vacuum and thoroughly washed with MQ water. The three step drying process involved air-drying under suction for 30 minutes, followed by 2 days in a 45 °C oven and then drying under reduced pressure at

80 °C for 2 days. When drying under reduced pressure with heating, the electrolyte was placed in a round bottomed flask and immersed in a silicon oil bath that was heated to 80 °C and high vacuum suction was applied to the flask. The dried electrolyte was stored under vacuum.

Modifier solutions were freshly prepared each day and used at most for three modifications.

2.2.2. Electrochemistry

Instruments

Electrochemical measurements were performed using either a computer-controlled EG & G PAR model 173 potentiostat coupled to a Powerlab 4SP (ADInstruments) or a computer-controlled EG & G PAR model 273A instrument.

Cell set-ups and electrodes

Electrochemistry was carried out in a three-electrode cell, with the working electrode being a carbon surface. For aqueous electrochemistry, potentials were referenced against a saturated calomel electrode (SCE, $Hg/HgCl_2$, KCl saturated). The reference electrode in non-aqueous solutions was usually $Ag/10^{-2}$ M $AgNO_3$ (10^{-2} M $AgNO_3$ in ACN/0.1 M $[Bu_4N]BF_4$) or at times a Ag wire pseudo-reference (as stated). The $Fc^{0/+}$ couple appeared at $E_{1/2}$ = 0.01 V vs. $Ag/10^{-2}$ M $AgNO_3$ and 0.38 V vs. Ag wire. A platinum wire was used as the auxiliary electrode.

All electrochemical cells were rinsed with 0.1 M HNO_3, washed with MQ water and then dried at 45 °C before use. Figure 2.1. shows the three different electrochemical cell set-ups used. Table 2.1. lists the carbon surfaces and their geometric areas when in the various cell set-ups.

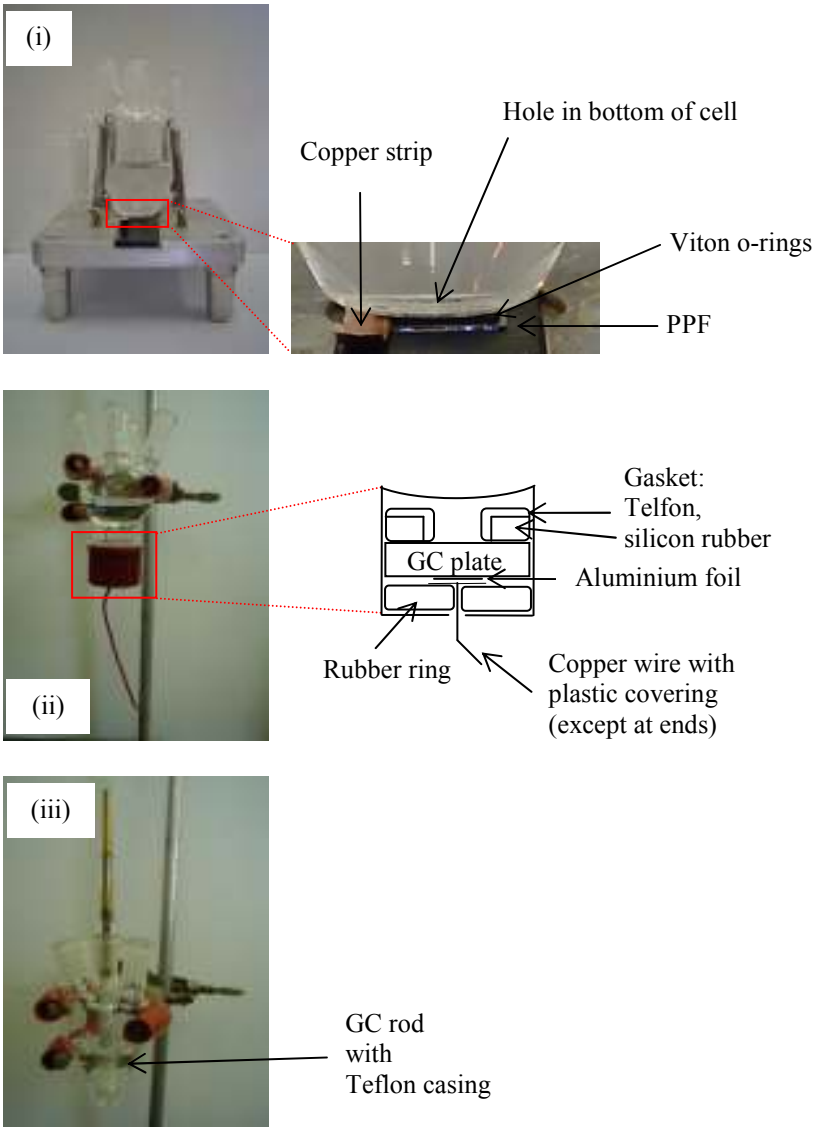

Figure 2.1. Photographs of the electrochemical cell set-ups. Set-ups for different carbon surfaces were (i) PPF and GC plates; (ii) GC plates and (iii) GC rods.

Table 2.1. Table summarising the different carbon surfaces used and their geometric areas.

Electrode		Electrode diameter (o-ring or gasket)	Electrode geometric area
PPF		5.5 mm (008 viton o-ring)	0.24 cm^2
GC plate		In cell set up (ii): 9.0 mm (Teflon/silicon rubber circular gasket), or In cell set-up (i): 5.5 mm (008 viton o-ring) [a]	In cell set-up (ii): 0.64 cm^2, or In cell set-up (i): 0.24 cm^2 [a]
GC rod		3.0 mm	0.07 cm^2

[a] Only used in this set-up for the modification of *p*-NB.

Set-up (i) was used for PPF surfaces and only for GC plates for modification with *para* nitro benzene diazonium tetrafluoroborate (*p*-NB), set-up (ii) was for GC plates and set-up (iii) was used for GC rods. With set-up (i) the PPF or GC plates were mounted face-up on an insulated metal stage under a glass cell held down by four springs. A 008 viton o-ring placed on the centre of the square surface sealed the solution above the surface. A slightly larger o-ring was placed around the 008 o-ring to help support the cell. Electrical contact was by a copper strip placed on the PPF or under the GC plate and not exposed to

solution. In this set-up the solution was initially introduced into the cell using a dropper to prevent trapping of air bubbles on the surface. The remaining solution was poured into the cell.

The 008 o-ring gave a geometric surface area of 0.24 cm^2. The diameter of the 008 viton o-ring (5.5 mm) was measured by inking the o-ring with a marker. The o-ring was then assembled in the electrochemical cell set-up with a piece of paper rather than a carbon surface. The mark on the piece of paper was measured with a ruler. The electrode area was also calculated from the diameter of the modifier layer measured under a magnifying lens with electronic callipers (specifications described later). The height of all the o-rings used in this work (when out of the cell) was 1.8 ± 0.2 mm as measured by electronic callipers.

Set-up (ii) has the GC plate mounted face-up horizontally at the bottom of the glass cell between a Teflon/silicon rubber circular gasket and a rubber ring for cushioning. The gasket sealed the solution above the centre of the plate defining the electrode geometric area as 0.64 cm^2. The diameter of the gasket was measured using electronic callipers (specifications described later). Aluminium foil and copper wire provided electrical contact to the GC plate and were external to the solution.

In set-up (iii) the GC rod (electrode geometric area of 0.07 cm^2) was suspended face-down in the solution. In this work, this electrode is referred to as a GC rod rather than a disk electrode in order to distinguish between the GC plate and PPF surfaces which also have disk shaped electrode areas.

Electrochemical methods

In this work, cyclic voltammetry (CV) and controlled potential electrolysis were used. The standard modification procedure entailed an initial CV scan from 0 V to the chosen modification potential (E_f) and back, at 100 mV s^{-1}, followed by a potential step from 0 V to E_f for 10 minutes. A final scan was then recorded in the modifier solution. For non-standard modifications, electrolysis times varied between 1 and 25 minutes. In the text, the modification procedure is denoted as *modifier (concentration of modifier, electrolysis time in minutes or number of scans to E_f).* The initial potential CV scan served the purpose of confirming that electrical connections to the surfaces were intact and the final scan confirmed that the modification had proceeded as expected. All electrochemical measurements were performed at room temperature in a $N_{2(g)}$ atmosphere.

Accompanying the modification procedure was a single CV scan in a redox probe solution prior to and after the modification step. The probe scan before modification was to determine the suitability of the carbon surface for electrochemistry and the scan after provided a qualitative estimate of the blocking properties of the resulting attached modifier layer. Probe scans were recorded with scan rate of 100 mVs^{-1}. Table 2.2. gives the potential ranges for the CV scans of the redox probe species.

Table 2.2. Potential ranges for CV scans of the various redox probe species

Probe species	**Potential range / V**
FCA	-0.2 to 0.5
$Ru(NH_3)_6^{3+}$	0.3 to -0.6
Fc	-0.4 to 0.3

The whole modification procedure including washing involved the following steps:

1. Probe scan at as-prepared PPF or GC
2. Wash with MQ water (omitted when Fc probe was used)
3. Wash with ACN
4. Dry with $N_{2(g)}$ (omitted when GC rod was used)
5. Modification
6. Wash with ACN
7. Washed with MQ water (omitted when Fc probe was used)
8. Probe scan at modified PPF or GC
9. Remove from cell
10. Wash with ACN (only carried out when Fc probe was used)
11. Wash with MQ water
12. Dry with $N_{2(g)}$ (omitted when GC rod was used)

For PPF and GC plates where the geometric area was defined by an o-ring or gasket, the whole modification procedure was carried out without removing the electrode from the cell. GC rods were moved between cells containing the different solutions.

2.2.3. AFM

The atomic force microscope (AFM) consisted of a Nanoscope® Dimension™ 3100 controller coupled with a Nanoscope® IIIa scanning probe microscope controller from

Digital Instruments, a subdivision of Veeco. All AFM data were collected in ambient air conditions (temperature 21 °C and relative humidity of approximately 60%). AFM measurements were mainly made in tapping mode. The AFM was also used in contact mode. The experimental details are given in Chapter 9.

Tapping mode cantilevers were purchased from Ultrasharp. Rectangular, non-contact NSC 14/AlBS (aluminium coated on backside) or NSC 15/AlBS cantilevers, or triangular, non-contact NSC 21/AlBS cantilevers were used for root-mean-squared (RMS) roughness measurements or for profiling scratches in the AFM depth profiling experiments. Cantilevers, NSC 12/AlBS, with three rectangular tips were used for making scratches in the AFM depth profiling experiments. Table 2.3. lists the specifications of the AFM cantilevers and tips.

Table 2.3. Specifications of the tapping mode AFM cantilevers and tips used.

Specifications	**NSC 14/AlBS**	**NSC 15/AlBS**	**NSC 21/AlBS**	**Cantilevers used for AFM depth profiling experiments: NSC 12/AlBS also known as NSC 37/AlBS**	
	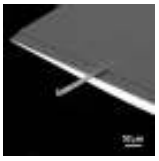		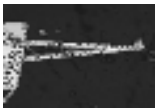		
				Longest	**Shortest**
Cantilever length	125 ± 5 µm	125 ± 5 µm	290 ± 5 µm	350 ± 5 µm	250 ± 5 µm
Cantilever width	35 ± 3 µm	35 ± 3 µm	40 ± 3 µm	35 ± 3 µm	35 ± 3 µm
Cantilever thickness	2.0 ± 0.5 µm	4.0 ± 0.5 µm	2.0 ± 0.3 µm	2.0 ± 0.3 µm	2.0 ± 0.3 µm
Resonance frequency	110 – 220 kHz	265 – 400 kHz	20 – 30 kHz	17 – 21 kHz	33 – 49 kHz
Force constant, k	1.8 – 12.5 N/m	20 – 75 N/m	0.5 – 1.5 N/m	0.1 – 0.4 N/m	0.35 – 1.2 N/m
Tip curvature radius	< 10 nm	< 10 nm	< 10 nm	< 10 nm	< 10 nm
Tip Height	20 – 25 µm	15 – 20 µm	20 – 25 µm	15 – 20 µm	15 – 20 µm
Full tip cone angle	30°	< 30°	< 30°	< 20°	< 20°

In tapping mode, the typical settings were as follows – scan rate: 1 Hz; samples per line: 512; realtime plane fit: line; offline plane fit: full; integral gain: 0.4; proportional gain: 0.7 and z-limit: 3 μm.

The topography of the surface was imaged by scanning over a desired area. Processing the images firstly required the images to be flattened with a flattened order of 1. Following that, RMS roughness measurements could be extracted from the image. Imaging and processing details and roughness values are given in the relevant chapters.

AFM depth profiling experiments were carried out on PPF surfaces. The strategy was to mechanically scratch away a small section of the modifier layer. The depth of the scratch is then measured to give the thickness of the attached layer. Two of the three tips on NSC 12/AlBS (the longest and shortest tips) were used. When in the tip holder, the cantilever was angled at 10˚ and the vertical height between the two tips was 8 μm, as shown in Figure 2.2.

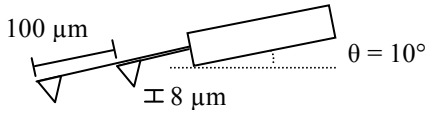

Figure 2.2. Dimensions of NSC 12/AlBS shortest and longest tip, when in tip holder. Not drawn to scale.

For scratching, the laser on the AFM was focussed on the shortest tip which was lowered to the surface. The camera and vision system was directed at the longest tip as it approached and engaged the surface for scratching. The longest tip was bent slightly

backward and appeared under stress when the shortest tip engaged the surface. When the shortest tip was engaged with the surface, the longest tip was embedded in the modifier layer with constant force of 0.7μN.[1] As the shortest tip scanned, the longest tip physically removed a portion of the modifier layer, as depicted in Figure 2.3.(a). The scratch was made by scanning to and fro along the x-axis and up the y-axis of the AFM image (Figure 2.3.(b).). The scan starts in the middle of the y-axis, moves to the top of the scan, scans back to the bottom and then back to the top. This resulted in the top half of the scratch being scratched three times and the bottom half of the scratch being scratched twice. Figure 2.3.(b). shows the movement of the longest tip during the first part of three for scratch formation (dotted arrows). This also relates to the movement of the shortest tip during the first part of the scan, starting at the middle of the y-axis and moving to the top of the scan. The length of the scratch was typically 10 μm and the aspect ratio was either 4:1 (i.e. a 10 μm by 2.5 μm scratch) or 8:1 (i.e. a 10 μm by 1.25 μm scratch). Generally, if the layer thickness was more than 4 nm, the scratch could be observed on the AFM camera and vision system.

Two tips (longest and medium) that could scratch the modifier layer were present on the cantilever. It was unimportant which of the two scratches was profiled as the thicknesses measured from scratches made by both tips were similar. The force exerted by the medium tip was 0.4 μN compared to 0.7 μN for the longest tip.[1]

The cross-sectional profile across the resulting scratch enabled the layer thickness to be determined. The scratch was scanned with either a new tip (NSC 15/AlBS or NSC 21/AlBS), or more commonly, with the longest tip used for scratching which required

refocusing of the laser from the shortest tip to the longest tip. When imaging the scratch, the scan angle was 90° to the x-axis of the scratch i.e. along the y-axis of the scratch. The length of the image captured of the scratch was usually 10 µm, with aspect ratio of 1:1 (i.e. a 10 µm by 10 µm image), 4:1 (i.e. a 10 µm by 2.5 µm image) or most commonly, 8:1 (i.e. a 10 µm by 1.25 µm image). When the aspect ratio was 4:1 or 8:1, two images were taken at different locations along the scratch, as shown by the dotted lines in Figure 2.3.(b).

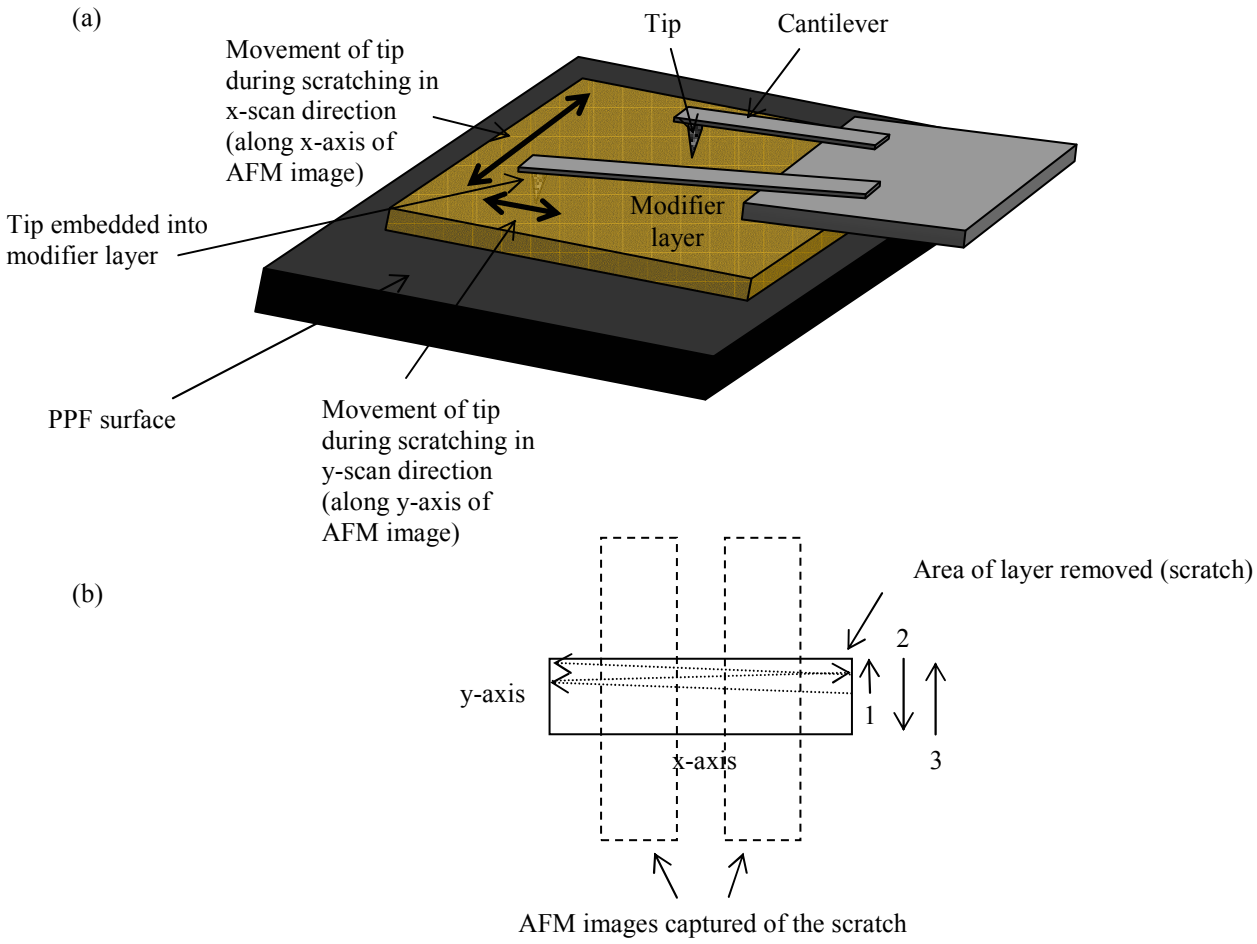

Figure 2.3. (a) Schematic of an AFM depth profiling experiment. (b) Schematic showing the movement of the longest tip during formation of the scratch and the two AFM images captured of the scratch (dotted rectangles) from which the layer thickness was measured.

For some experiments, it was important that the same scratch could be relocated, for example, after the layer underwent some treatment or when the scratch was imaged with a different tip. In these cases, prior to AFM depth profiling experiments, the PPF surface was scratched using a scalpel on either side of the modifier layer as shown in Figure 2.4.

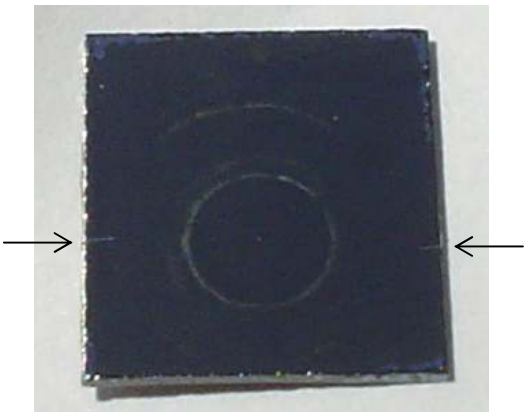

Figure 2.4. Scratches made by scalpel when relocating scratches made during the AFM depth profiling experiment. Circle in the middle is the modified area.

To scratch through the modifier layer at a known location, the camera focussed first on the right scalpel scratch and a sketch of the scratch was made. The cursor was then positioned on a distinctive point in the scalpel scratch and the origin (0,0) was set at that point. The cursor was then moved to the left scalpel scratch and a sketch of that scratch was made. The cursor was then positioned at a point and the coordinates at that point were recorded. The third position of the cursor was in the modified area on a distinctive pit in the modified surface (defect in the PPF) and the coordinates were recorded. The cursor was then moved a precise distance (> 20 μm) away from the defect and the longest tip engaged the modified layer at the position of the cursor, as seen on the camera and vision system. To

find the scratch after removal and replacement of the sample on the AFM stage, the three coordinates (1. right scratch – origin (0,0), 2. left scratch and 3. defect in PPF) were relocated in the same manner as when scratching, and the cursor was moved from the pit coordinates.

The thickness of the underlying PPF surface that was removed when scratching the modifier layer was measured by scratching as-prepared PPF surfaces prepared in various batches. The thickness of PPF removed during scratching was 0.3 nm and this was subtracted from the thicknesses of the modifier layers.

For each surface, two scratches were usually made and two scans (each with aspect ratio either 4:1 or 8:1) were taken of each scratch to achieve a statistical average of layer thickness. Processing the images of the scratch involved firstly flattening the image with flatten order of 1. The four images were then analysed by section analysis or localised depth to give thickness values. Figure 2.5. is an example of an image analysed by section analysis. The cross-section (top image) is an average of points in the y-axis of the image (bottom image). From the average cross-section for each of the four images, 10 thickness measurements were taken at random positions on the layer by moving one cursor with the other cursor positioned at the bottom of the scratch (top image shows one out of 10 positions). 5 positions were taken on each side of the scratch. The vertical difference in cursor position was the thickness of the modifier layer. A localised depth measurement was also recorded as shown in Figure 2.6. This was carried out by selecting an area in the scratch and an area on one side of the scratch. The vertical difference between the selected areas gave one measurement. This was repeated by selecting an area on the other side of the

scratch. The two measurements were averaged to give the localised depth measurement. The average and the standard deviation of the 11 values were calculated. The final thickness measurement for a sample was the average of 44 values and the error was the standard deviation of the values. The error was an indication of the roughness of the layer. However, the instrumental inaccuracy is ± 0.3 nm. Hence, if the standard deviation was smaller than or equal to the instrumental inaccuracy, ± 0.3 nm was the reported error and if it was larger than the instrumental inaccuracy, the error was the standard deviation. For scans that were bowed where edges of the scans were higher than actual due to the fault in the instrument or with a significant amount of debris, less than 44 measurements were taken. Table 2.4. is the statistical analysis used to calculate thickness of the modifier layer for one sample. Tables for all samples where thickness was measured are included in the Appendix. Samples prepared in work detailed in Chapter 4 where thicknesses were measured have their thickness tables given in Appendix 4, and this is similarly carried out for samples prepared in the other chapters.

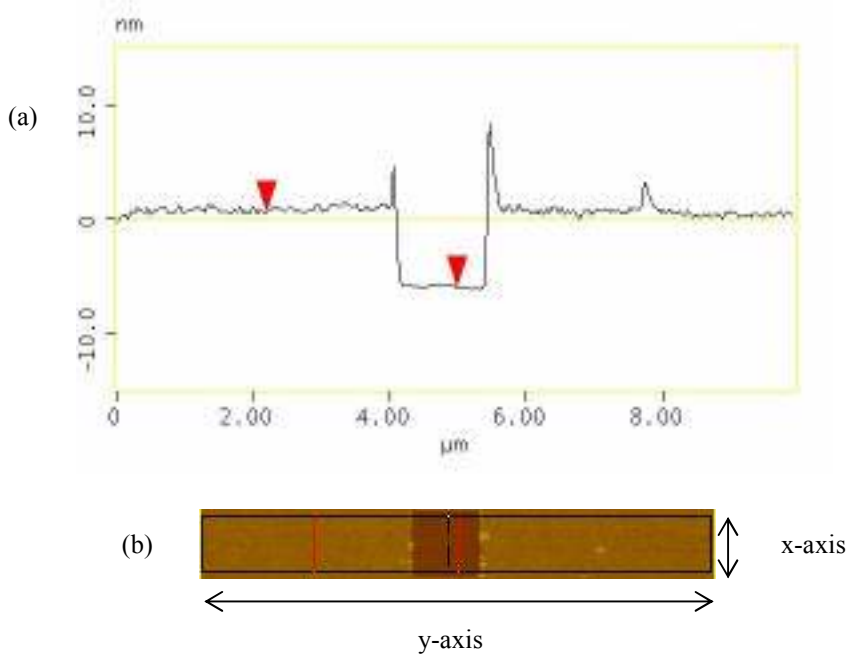

Figure 2.5. (a) AFM image analysed by section analysis to give layer thickness. The AFM image (b) was averaged along the x-axis to give the image (a). The vertical difference between the cursors in the top image was one thickness measurement out of ten obtained. The cursor on the layer was moved to five different positions along the layer on each side of the scratch to give ten thickness measurements.

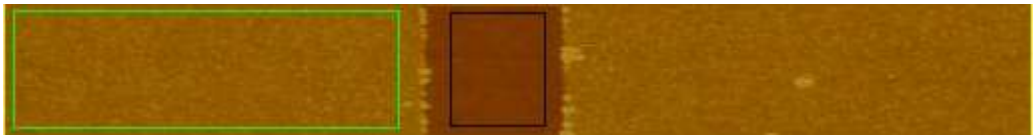

Figure 2.6. AFM image analysed by localised depth to give layer thickness. The vertical difference between the areas in the rectangles was one thickness measurement out of two obtained. The other was measured by moving the left rectangle to the right side of the scratch. The rectangle would be reduced in size to avoid the debris from the scratch.

Table 2.4. Statistical analysis used to calculate thickness of the modifier layer for one sample. [a]

Scratch no.	Scan no.	Thickness values	Scan			Scratch			Sample	
1	1	11	Av. of scan minus 0.3 nm	s of scan	s^2 of scan					
	2	11	Av. of scan minus 0.3 nm	s of scan	s^2 of scan	Av. of scratch = ($\sum$av. of scan)/2	s of scratch = $\sqrt{\sum s^2}$ of scan	s^2 of scratch = ($\sqrt{\sum s^2}$ of scan)^2		
2	3	11	Av. of scan minus 0.3 nm	s of scan	s^2 of scan					
	4	11	Av. of scan minus 0.3 nm	s of scan	s^2 of scan	Av. of scratch = ($\sum$av. of scan)/2	s of scratch = $\sqrt{\sum s^2}$ of scan	s^2 of scratch = ($\sqrt{\sum s^2}$ of scan)^2	**Av. of sample = ($\sum$av. of scratch)/2**	**s of sample = $\sqrt{\sum s^2}$ of scratch**

[a] Av. = average, s = standard deviation, s^2 = variance

2.2.4. Microscopy: optical, fluorescence and SEM

An Olympus BX60 (inverted light microscope) with digital image capture using an Olympus DP10 camera was used for optical microscopy. There was a polariser and diffusion interference contrast settings on the optical microscope which allowed viewing of the black carbon surfaces. The optical microscope provided magnification from 5 to 100 x. Fluorescence measurements were obtained by means of an Hg arc lamp fitted with a 470 – 500 nm filter and an inverted epifluorescence microscope (Olympus 1X70) equipped with a Photometrics CoolSNAP colour camera. Images were taken at 10 x magnification. Scales on the optical and fluorescence images were determined by imaging micron-sized rulers under the microscope at the various magnifications.

Two scanning electron microscopes (SEMs) were used in this work. The majority of the images were taken on a Raith 150 e-beam lithography system operating with the

accelerating voltage set at 10 kV, aperture at 30 and $I_{filament}$ of 2.39. The aperture and stigmation were carefully altered to focus the images prior to capture. Optimisation of the images was carried out by adjusting the brightness and contrast. Magnification of images ranged from 29 x to 200 kx (200,000 x). A small number of images were taken on the SEM (Leica 440) at the School of Biological Sciences, University of Canterbury, with the help of Neil Andrews.

2.2.5. Water contact angle measurements

Water contact angle measurements provided straightforward analysis of the wettability of the attached modifier layers. Contact angles of water were measured from sessile drops. The surface was placed on a stage controlled by a goniometer and the water droplet image was captured by an Edmund Scientific camera with Video for Windows NT software.

1 μL of MQ water was dispensed onto a horizontal surface that was carefully aligned perpendicular to the capturing device. At least two identical surfaces were prepared for these measurements. Two drops were sequentially placed onto each surface and three measurements were taken from each side of the drop. For each drop, six angles were recorded. The average water contact angle of two separate samples i.e. of 24 measurements, was calculated with an error that included all the measurements taken. With PPF samples, only one drop was placed on the layer at one time due to the smaller modified area compared to GC plate modified in cell set-up (ii). The sample was rinsed with MQ water and dried with $N_{2(g)}$ between drops. Raw data are detailed in the Appendix 3, 4 and 5.

2.2.6. Other instruments and methods

Spectroscopy:

- Nuclear magnetic resonance (NMR) spectra were obtained with either a Varian Inova operating at 500 MHz for ^{1}H or a Varian Unity 300 operating at 75 MHz for ^{13}C. NMR spectra were recorded in a variety of solvents depending mainly on sample solubility. Samples were run by Rewi Thompson at the Department of Chemistry, University of Canterbury.

- Raman scattering spectroscopy was either carried out in the Department of Physics and Astronomy, University of Canterbury, with the help of Dr. Roger Reeves or at the Department of Chemistry, University of Otago, by Penny Walsh. The Canterbury instrument is a Spex 1403 spectrometer with a liquid N_2 cooled charge-coupled device detector (Jobin-Yvon 3000). The Ar^{+} ion laser source was 50 mW laser power and had the excitation wavelength of 488 nm. Spectra were recorded with an integration time of 60 seconds and a slit width of 0.3 μm on the detector. The Otago instrument is a Bruker IFS-55 interferometer with an FRA/106S attachment. A liquid N_2 cooled Ge detector (D-418 Bruker Optics) was used. The excitation source is a Nd : Yttrium-Aluminium-Garnet laser with laser power of 240 mW and an excitation wavelength of 1064 nm. Spectra were collected with a resolution of 4 cm^{-1} and using 256 scans where each scan takes 2 seconds.

- X-ray photoelectron spectroscopy (XPS) analyses were carried out by Dr. Byrony James, Department of Chemical and Materials Engineering at the University of Auckland. The instrument is a Kratos Axis Ultra DLD. The X-ray source is a monochromatic aluminium K-alpha source, energy 1486.6 eV, operated at 150 W power. Wide scans were conducted

from 1100 to 0 eV with a step size of 1 eV and pass energy of 160 eV. Most narrow scans were conducted with a step size of 0.1 eV and a pass energy of 20 eV. All peak positions were referenced to aromatic carbon at 284.7 eV.

Profilometer: A Sloan Dektak II profilometer was used for profiling large topographies (> 5 μm). The scan rate was set at medium and the scan distance varied according to the size of feature to be analysed. Vertical measurements were recorded by positioning the right and left cursors at appropriate positions; for example for a depth profile, the left cursor was at the bottom of the scratch and the right cursor at the surface.

Photographing: Photographs were captured by a 3.2 megapixel digital camera.

Callipers: Measurements of o-ring dimensions and other objects (as stated) were taken with a Preisser® vernier (electronic callipers).

Orbital shaker: The orbital shaker was from Edwards Instruments Co.

Ultrasonicator: The ultrasonicator used was a 125 W Branson, a Smith Kline Company instrument.

pH meter: The pH meter was from Hanna Instruments and was calibrated before use against at least two standard buffers on either side of the expected pH of the sample solution.

2.3. Software

For the instruments in the previous sections, the instruments' associated software was used where available.

Quantification of fluorescence

The fluorescence of images captured on the fluorescence microscope was measured using Image Pro Plus software. An area of interest (AOI) of an appropriate size was defined and positioned on the desired area of the image. The program measured the proportion of green pixels within the AOI, using the intensity histogram analysis.

Calculation of surface concentration

LinkFit was used for curve fitting electrochemical data to find the peak area for a redox process arising from a surface-immobilised species.[2] From the peak area, the surface concentration of the electroactive species was calculated. Mixed Lorentzian-Gaussian curves were fitted to the voltammetric peaks via the Levenberg-Marquardt algorithm and the curves areas were calculated by integration to give the peak area. The number of curves used to fit the peak was varied so as to best accommodate and represent the peak. When the peak area was not curve fitted, the area was calculated by integration. Baselines were best fit or linear. To determine the most suitable baseline, a series of peak areas were calculated using each of the baselines. The baseline that gave the most reasonable data was used. For the same series of experiments, the same baseline was used in order to compare the surface

concentration values. Surface concentration was calculated according to Equation 2.1. Raw data and calculations are detailed in the Appendix 4 and 5.

2.1. $$\Gamma = Q / nFA;$$

where Γ is surface concentration in mol.cm^{-2}, Q is charge in Coulombs, n is the number of electrons, F is Faraday's constant (96485 C.mol^{-1}) and A is the geometric area of electrode in cm^2. $Q = i$ x t, where i is current in A and t is time in s.

Calculation of modifier length

Spartan was used for calculating the length of the different modifiers. The modifiers were drawn as attached to a sp^3 carbon (in the carbon surface) with the atoms having the outermost radii. Structures were drawn in the extended conformation and to give the maximum length which was taken as the length of the modifier.

2.4. References

(1) Brooksby, P. A.; Downard, A. J. *Journal of Physical Chemistry B* **2005**, *109*, 8791-8798.

(2) Loring, J. S. *LinkFit* **2004**.

3.1. Introduction

Fabrication of thin film carbon surfaces by pyrolysing photoresist applied onto a silicon wafer was initially carried out and used for electrochemical measurements by Kim and co-workers.[1] The fabrication and characterisation of PPF have also been of interest to other workers.[2-4] According to their studies,[2-4] the carbon composition, physiochemical and electrochemical properties of PPF are strongly dependent on pyrolysis temperature (600 – 1200 °C). As the temperature increases, these properties become more similar to those of GC. The following is a brief review of the characteristics of PPF, fabricated with pyrolysis temperature ≥ 1000 °C.

Pyrolysis of the photoresist involves step-wise increments of temperature until the pyrolysis temperature is reached. At initial temperatures between 150 and 300 °C, decomposition of the resin in the photoresist and the initial release of water, carbon dioxide (from decarboxylation) and carbon monoxide (from decarbonylation) occurs. This is followed by the evolution of aromatic species above 350 °C.[1] The weight of the film decreases sharply between 0 and 500 °C and a plateau is observed after 500 °C.[1,2] The weight loss that is associated with the loss of these species results in the final film being between 13 and 31% of the initial weight, as measured by thermogravimetric analysis.[2,4] The shrinkage of the photoresist with pyrolysis is also observed with profilometry and scanning electron microscopy (SEM). When the initial photoresist thickness is between 5 and 8 μm it reduces to a PPF thickness between 1 and 2 μm.[1-3] The weight loss is consistent with the decrease in thickness.

Characterisation of PPF surface properties has been carried out using various methods detailed as follows: resistivity using four-point probe measurements and current-sensing atomic force microscopy (AFM); electrochemical properties using cyclic voltammetry (CV); O : C ratios using x-ray photoelectron spectroscopy (XPS); chemical composition using XPS, Raman spectroscopy and the transmission electron microscope (TEM) and root-mean-squared (RMS) roughness from AFM measurements.

The resistivity of PPF is reported as (5.1 – 5.7) x 10^{-3} Ω.cm, which is only slightly larger than the resistivity of GC which is (4.5 – 5.0) x 10^{-3} Ω.cm.[2,4] There is relatively homogeneous resistivity across the surface as measured by current-sensing AFM.[3] PPF surfaces appear to have similar electrochemical behaviour to GC electrodes. This is tested by observing the electron transfer kinetics of redox probe couples at varied scan rates. The potential windows of the surfaces are also similar to GC.[1,2]

The O : C ratios of the PPF surface are found to range from 1 – 6% depending on the period the surface is exposed to air (up to 4 days).[2-4] At GC, the O : C ratio ranges from 7 – 8% over the same period of air exposure.[4] From XPS data, two different oxygen species with peak positions at 531.9 and 533.1 eV are reported to be present at the PPF surface. The earlier peak is assigned to C=O and/or C-O-C groups and the latter to C-O and/or C-OH groups.[3] Oxide groups, heterogeneously distributed, including C-O-C, COOH, and Ar-OH (phenol) are also present at GC.[5] Raman spectroscopy is used for characterisation as graphitic carbon is a relatively strong Raman scatterer with two E_{2g} modes predicted to be Raman active at ~42 and ~1600 cm^{-1}.[3] Raman spectra shows two broad bands at ~1360 and ~1600 cm^{-1} (the peak at ~42 cm^{-1} is not measured.).[2-4] The 1360 band is assigned to D or

A_{1g} vibration modes (disorder) and the 1600 to the E_{2g} mode (graphitic). The bands have contributions from sp^2 and sp^3 carbon and also aromatic rings.[2,3] As the 1360/1600 integrated peak intensity ratio increases, the crystallite size is found to decrease and greater disorder is indicated. The relative intensity is dependent on the preparation method, for example, type of photoresist used and pyrolysis temperature. Bands are present at the same Raman shifts for GC. The 1360/1600 peak intensity is larger than 1 for GC.[2,6]

TEM investigations of PPF reveal a graphite-like structure in a predominantly amorphous carbon film where the lattice image of the (002) plane is evident.[1,2] The crystallite size for a PPF surfaces is reported to be 2.8 nm, which depends on the type of photoresist and pyrolysis temperature used for fabrication.[1,2] The chemical composition of PPF appears to be similar to GC which is described as a tangled mass of graphitic ribbons with small crystallite regions of 4 – 10 nm.[7] In the manufactured form, GC is a rough surface with pores of 50 – 300 nm in diameter[8] and GC has a roughness of 1.3 nm when it is polished with 0.5 μm alumina.[9] The RMS roughness of the PPF surface is reported to be 0.2 – 0.5 nm (near atomic smoothness).[3,4] The difference in roughness is the only important difference between the two surfaces in terms of the work reported in this thesis.

PPF and GC are the two carbon surfaces used in this work and this chapter is dedicated to the preparation and characterisation of the surfaces. GC is a commonly used electrode, commercially available product and a highly conducting, mechanically stable, impermeable and reusable material (after polishing). PPF surfaces have similar properties to GC and have the advantages of being significantly smoother and are disposable. Many

methods are utilised for their characterisation as it is important to understand their properties in order to use them for attaching layers and subsequently other materials.

3.2. Experimental methods

3.2.1. Fabrication and preparation of PPF surfaces

Instruments and materials

Two spin coaters were used in the fabrication of PPF surfaces: a spin coater from EMS Limited and the single wafer spin processor model WS-400A-6NPP from Laurell Technologies Corporation.

Pyrolyses were carried out in a Gallenkamp furnace with a silicon glass tube or a Radatherm's model 2216e tube furnace. The Gallenkamp furnace was used for the initial 15 firings and the majority of firings were carried out on the Radatherm furnace.

Silicon wafers were purchased from Silicon Quest and Micro Materials and Research Consumables. *n*-type/phosphorous doped, 4", Si (100), prime and monitor grade, 475 – 575 μm thick with resistivity 1 – 20 Ω.cm were purchased from Silicon Quest. *n*-type/phosphorous doped, 4", Si (100), prime and monitor grade, 500 – 550 μm thick with resistivity 2 – 50 Ω.cm were purchased from Micro Materials and Research Consumables. All the wafers were single side polished with 2 semi standard flats. Photoresists AZ 4620, S 1813 and S 1518 were purchased from Clariant.

Procedure

PPF preparation in this work was based on procedures previously described.[1-4] The standard, optimised protocol for fabrication of suitable PPF is described here.

n-type/phosphorous doped, 4", Si (100) wafers used as the base substrate for the film were either: (i) prime grade, 500 – 550 μm thick with resistivity 2 – 50 Ω.cm; (ii) monitor grade, 500 – 550 μm thick with resistivity 2 – 50 Ω.cm; (iii) prime grade, 475 – 575 μm thick with resistivity 1 – 20 Ω.cm or (iv) monitor grade, 475 – 575 μm thick with resistivity 1 – 20 Ω.cm. In the first step of the PPF fabrication process, a wafer was placed under a stream of $N_{2(g)}$ to remove dust and then a thin layer of photoresist was spin coated onto it. Any type of photoresist was suitable for this step. The wafer was baked in a 95 °C oven for 10 minutes and then cooled to touch prior to cutting with a diamond cutter. The photoresist provided "cushioning" and allowed for smooth cutting of the wafer and also prevented damage of the surface by debris generated from cutting. The wafer was cut into squares of dimensions 14 mm by 14 mm, using a diamond cutter attached to a device that allowed millimetre range motion of the cutter and held the wafer in position using vacuum suction. The photoresist was then removed from the silicon chips by sonicating for 1 – 2 minutes in acetone, methanol then isopropyl alcohol (IPA). The chips were dried with $N_{2(g)}$ and put into a 95 °C oven for 10 minutes to remove any remaining solvent.

Prior to the application of photoresist the silicon chips were rotated on the spin coater at 3000 rotations per minute (rpm) for about 10 seconds or blown with $N_{2(g)}$, to remove dust. 3 – 4 drops of AZ 4620 photoresist was dispensed from a plastic dropper and the spin coater was started immediately. Care was taken to ensure there were no air bubbles

in the photoresist when it was dispensed. The silicon chips were spin coated with one coat at 3000 rpm for 30 seconds. The acceleration and deceleration were at the lowest setting on the spin coater and with the selected acceleration setting, the spin coater took 7 seconds to reach 3000 rpm. The samples were soft baked in a 95 – 120 °C oven for at least 20 minutes and cooled at room temperature for 10 minutes prior to pyrolysis. The thickness of the photoresist prior to pyrolysis was measured to be 7 – 8 μm (refer later).

Approximately 30 – 35 samples were positioned side by side in a fused silica and quartz boat which was inserted into the tube of the furnace. The boat was pushed a set distance of 22 cm into the tube in order to position the samples in the middle of the furnace. Samples pyrolysed in the middle of the furnace exhibited better properties than those pyrolysed at the ends of the furnace, presumably because the temperature was not even throughout the tube.

The temperature increments were 500 °C for 20 minutes, 750 °C for another 20 minutes and finally at the pyrolysis temperature of 1050 °C for 1 hour. The furnace was cooled to room temperature before the samples were removed. Both the pyrolysis and cooling phases were performed in a forming gas (95% $N_{2(g)}$ + 5% $H_{2(g)}$, with flow rate = 6 L min^{-1}) atmosphere to minimise the oxidation of carbon.

The samples were briefly sonicated for 3 seconds in successive baths of acetone, methanol and IPA, dried with $N_{2(g)}$ and put into a 45 °C oven for 5 – 10 minutes. The surfaces were then used for electrochemistry or stored under vacuum. Each PPF surface was only used once.

3.2.2. Preparation of GC rods and plates

The GC rods (Atomergic) were fabricated at the mechanical workshop, Department of Chemistry, University of Canterbury, by sealing a small piece of 3 mm diameter GC rod in teflon and electrical contact to the GC was with a brass rod. The rods were initially polished with a series of wet sandpapers of decreasing coarseness, beginning with 1000, 1200, 2/0 then 4/0. Following that, the electrodes were polished with 9, 6 then 3 μm synthetic diamond paste/diamond lapping oil slurry on a polishing cloth. The paste, oil and cloth were from Leco. After polishing in each of the diamond paste slurries, the diamond paste was removed from the electrode with a tissue saturated with acetone. The electrode was then finally polished in a 1 μm alumina/water slurry, which is removed by holding the electrode under a stream of water and then wiping the electrode with a piece of tissue, to give to smooth mirror finish. At times, the rod was also sonicated in MilliQ (MQ) water for 1 – 3 minutes to help remove the adsorbed alumina prior to electrochemistry. All polishing was carried out in a figure 8 motion to achieve even flatness over the whole electrode.

Square GC plates (Tokai Carbon) with dimensions of 15 mm, 15 mm by 3 mm were obtained by dividing the bulk plate using a diamond saw blade. The GC plates were initially polished in a similar process as the GC rods. After polishing in diamond paste, the further preparation of the GC plates was dependent on the subsequent uses for the modified GC plates. The preparation was either identical to the rods (as above) or as described in the relevant chapters.

3.2.3. Characterisation of PPF surfaces and GC plates

Resistance was measured using a home-made device designed by Dr. Paula Brooksby, Department of Chemistry, University of Canterbury. Resistance was measured by placing two parallel gold contacts of equal length on the carbon surface and recording the resistance between the two contacts using a standard voltmeter with copper pins. The length of the gold contacts was equal to the width between them. A spring tension device provided reproducible downward pressure of the gold wires onto the surface. Four measurements were taken on each sample and were averaged. For each measurement, the gold contacts were rotated slightly.

3.3. Results and discussion

3.3.1. Fabrication and preparation of PPF surfaces

Many difficulties were initially encounted. There were many problems with the fabrication of these PPF surfaces especially with regards to the adhesion of the pyrolysed photoresist film to the silicon wafers. The optimised method detailed in the Experimental section was derived after procedures detailed in Appendix 3. Factors which strongly influenced the quality of the PPF samples were found to be:

(i) *Si (100) wafer*: *p*-type Si (100) is boron-doped and its conducting properties affected the electrochemistry of the PPF. The poor adhesion of PPF prevented SiO_2 wafers from being used.

(ii) *Photoresist and spin-coating*: three types of photoresists were used – AZ 4620, S 1813 and S 1518. AZ 4620 was the easiest to use and gave the best quality PPF surfaces. With the latter two photoresists, four coats were required to be applied by spin coating in order to achieve a suitable thickness for pyrolysis (7 – 8 μm (refer later)). Between coats, the surfaces were soft baked in a 95 °C oven for at least 10 minutes and were cooled to room temperature. Multicoating was labour intensive and very time consuming. Additionally, having multiple coats increased the number of defects and sometimes led to cracking of the existing layer of photoresist on application of the next layer. Applying multiple coats on different days and spin coating longer than 12 hours before pyrolysis also resulted in poor quality PPF surfaces.

(iii) *Pyrolysis temperature*: The Gallenkamp furnace was used at the beginning of this work and at times gave poor quality PPF samples. This was due to the furnace not reaching the set temperature during pyrolysis.

3.3.2. Characterisation of PPF surfaces

All PPF samples were initially inspected visually. If the samples appeared homogeneously black and were free of obvious defects, then other types of characterisations were performed. A representative number of surfaces from each batch were analysed for their electrochemical suitability by measuring resistivity and recording a CV scan of a well-known redox couple (probe). The electrochemical properties of those

samples were assumed to be representative of the other surfaces from the same pyrolysis batch.

Visual inspection

Poor quality PPF surfaces could be frequently identified by visual inspection. The most common problem was peeling of the films off the silicon wafer. Other observable defects were pits caused by air bubbles in the photoresist introduced during spin coating and white spots indicating the surface had been oxidised. Oxidation may occur due to oxygen present during pyrolysis or taking out the samples from the furnace when they are not sufficiently cooled. PPF which appeared silver or patchy black were also found to be unsuitable for electrochemistry. PPF surfaces suitable for electrochemistry appeared shiny black.

Thickness and resistivity

The thickness of applied photoresist was measured after soft baking but prior to pyrolysis. After scratching with a pin (silicon wafer not scratched), the scratch was profiled using the profilometer, giving a photoresist layer thickness of approximately 7.2 μm. After pyrolysis, the thickness of the PPF was approximately 1.5 μm. The thickness of the photoresist film shrinks by a factor of five during pyrolysis. Thus, it is important to apply a layer of photoresist between 7 – 8 μm (the thickness of the resulting PPF affects its electrochemical performance).[10]

The resistivity of the surface reflects the conductivity of the surface and hence its electrochemical properties. Equation 3.1. was used to calculate the resistivity of the surface from the measured resistance. PPF surfaces with resistivity lower than 4.4 x 10^{-3} Ω.cm ($R_{PPF\,\square}$ < 30 Ω) were used for electrochemistry. The samples with higher resistivity were not used for electrochemistry.

3.1. $$\frac{\rho\, l}{w\, h} = R_{PPF\,\square} - R_{Cu}$$

since $l = w$ for the device used

$$\rho = (R_{PPF\,\square} - R_{Cu}) \times h$$

ρ = resistivity in Ω.cm
l = length of gold contact in cm
w = width between gold contacts in cm
h = thickness of PPF = 1.5 x 10^{-4} cm
$R_{PPF\,\square}$ = resistance of PPF in Ω
R_{Cu} = resistance of copper pins of voltmeter in Ω (≈ 0.5 Ω)

Electrochemical properties

CV scans of redox probe molecules, ferrocene monocarboxylic acid (FCA), ferrocene (Fc) and $Ru(NH_3)_6^{3+}$, and blank scans in phosphate buffered saline (PBS) and ACN (acetonitrile)/0.1 M $[Bu_4N]BF_4$ (tetrabutylammonium fluoroborate) were recorded at as-prepared PPF. A typical CV scan of the most commonly used probe FCA is shown in Figure 3.1. The peak separation between oxidation and reduction peaks (ΔE_p) for the redox couples $FCA^{0/+}$, $Fc^{0/+}$ and $Ru(NH_3)_6^{3+/2+}$ are 90 ± 10 mV, 80 ± 10 mV and 130 ± 10 mV, respectively. Ferrocenes are well-known to exhibit fast electron kinetics with ΔE_p values close to the theoretical of 59 mV for the one-electron process. Therefore, the larger than expected ΔE_p value for both ferrocene redox couples at PPF is attributed to uncompensated

solution resistance together with the relatively high currents generated at the electrode with a relatively large surface area.

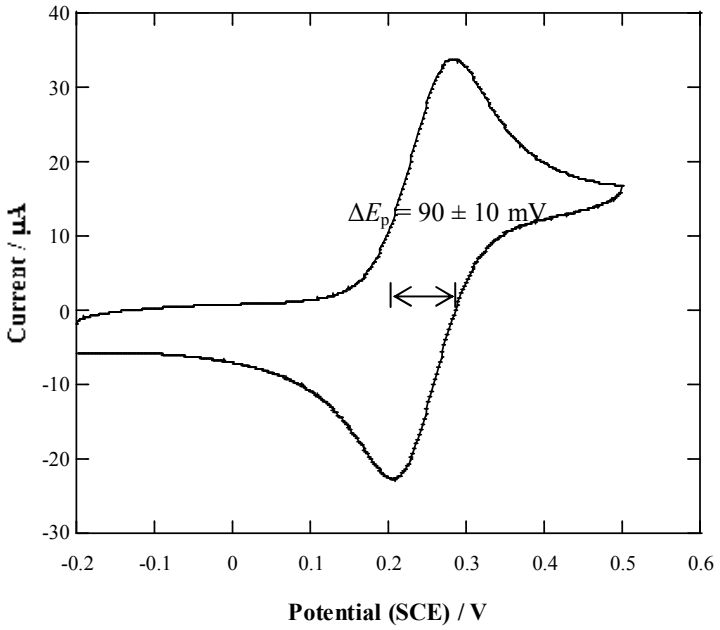

Figure 3.1. CV scan of FCA probe recorded at an as-prepared PPF surface. Scan rate = 100 mVs^{-1}.

PPF surfaces were scanned in thoroughly degassed PBS and ACN/0.1 M $[Bu_4N]BF_4$ in both positive and negative directions beginning at 0 V to determine the potential window of PPF and its stability toward electrochemical oxidation. The potential window is taken as the section of the CV scan that has very low currents.

In aqueous or non-aqueous solutions where trace amounts of H_2O are present such as ACN/0.1 M $[Bu_4N]BF_4$, the oxidation of H_2O and/or surface C in the presence of H_2O (Equation 3.2.) is observed when scanning positive. A steep rise in anodic current indicates that these processes are taking place. Scanning negative in these solutions causes the

reduction of H^+ (Equation 3.2.) which is indicated by a sharp increase in cathodic current. The processes in Equation 3.2. are pH and kinetically dependent.

	Oxidation of H_2O:	$2H_2O$	$\rightarrow$	$4H^+ + O_2 + 4e^-$
3.2.	Oxidation of surface C:	surface-C + H_2O	$\rightarrow$	surface-CO_x + $2H^+ + 2e^-$
	Reduction of H^+:	$2H^+ + 2e^-$	$\rightarrow$	H_2

The potential windows for PPF were established to be -1.5 to 1.5 V in PBS and -2 to 1.5 V in ACN/0.1 M $[Bu_4N]BF_4$. These ranges are consistent with reported values.[11]

When the solutions were not thoroughly degassed, the reduction of O_2 was observed between -0.9 and -1.4 V vs. saturated calomel electrode (SCE) or $Ag/10^{-2}$ $AgNO_3$. The variation of potential of the reduction peak (E_{pc}) was assumed to be due to variable amounts of H_2O in ACN/0.1 M $[Bu_4N]BF_4$.

Characterisation by Raman spectroscopy

Figure 3.2. shows a Raman spectrum of a PPF surface prepared in this work, obtained at the University of Canterbury. The assignment of the two characteristic carbon bands at ~1360 and ~1600 cm^{-1} has been discussed in the Introduction section of this chapter. The spectrum matches those reported by other workers for PPF prepared under optimum conditions. The 1360/1600 peak intensity for PPF surfaces prepared in this work is less than 1.

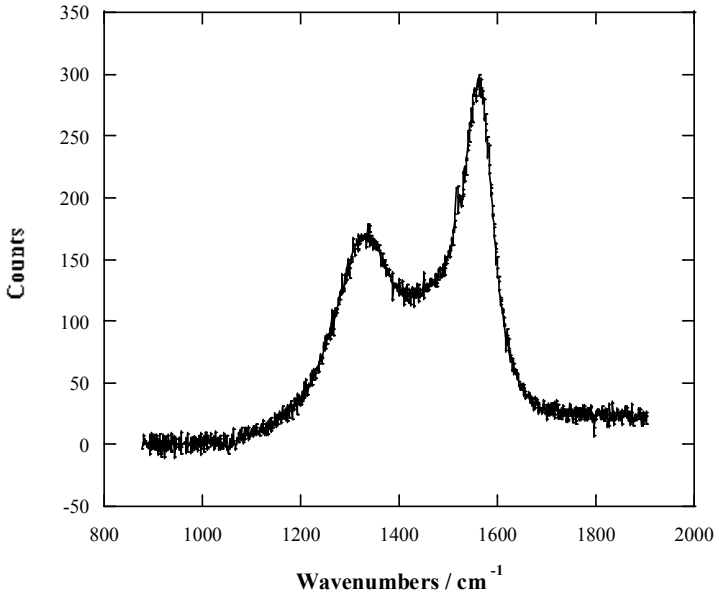

Figure 3.2. Raman scattering spectrum of an as-prepared PPF surface.

Characterisation by AFM and SEM

Figure 3.3. depicts an AFM image and a line profile taken across the image. RMS surface roughness of as-prepared PPF was averaged from eleven 4 μm x 4 μm AFM images, taken from two surfaces from different batches. For each of the eleven images, three line profiles (two horizontal, one vertical) were drawn and for each line profile in the image a RMS roughness value was recorded. The variation in the line profile is the RMS roughness. The RMS surface roughness is calculated to be 0.2 nm with a range from 0.2 – 0.4 nm (Appendix 3.). This is the same as the roughness reported by other workers as outlined in the Introduction of this chapter.

RMS surface roughness values are commonly reported over a range of areas. The scan area 4 μm x 4 μm was selected after RMS surface roughness was measured for scan

distances of 0.5, 1, 1.5, 2, 4, 6, 8 and 10 µm. The RMS roughness increased with increasing scan distance reaching a plateau at 4 – 10 µm.

SEM images of as-prepared PPF are shown in Figure 3.4. The images show some surface structure.

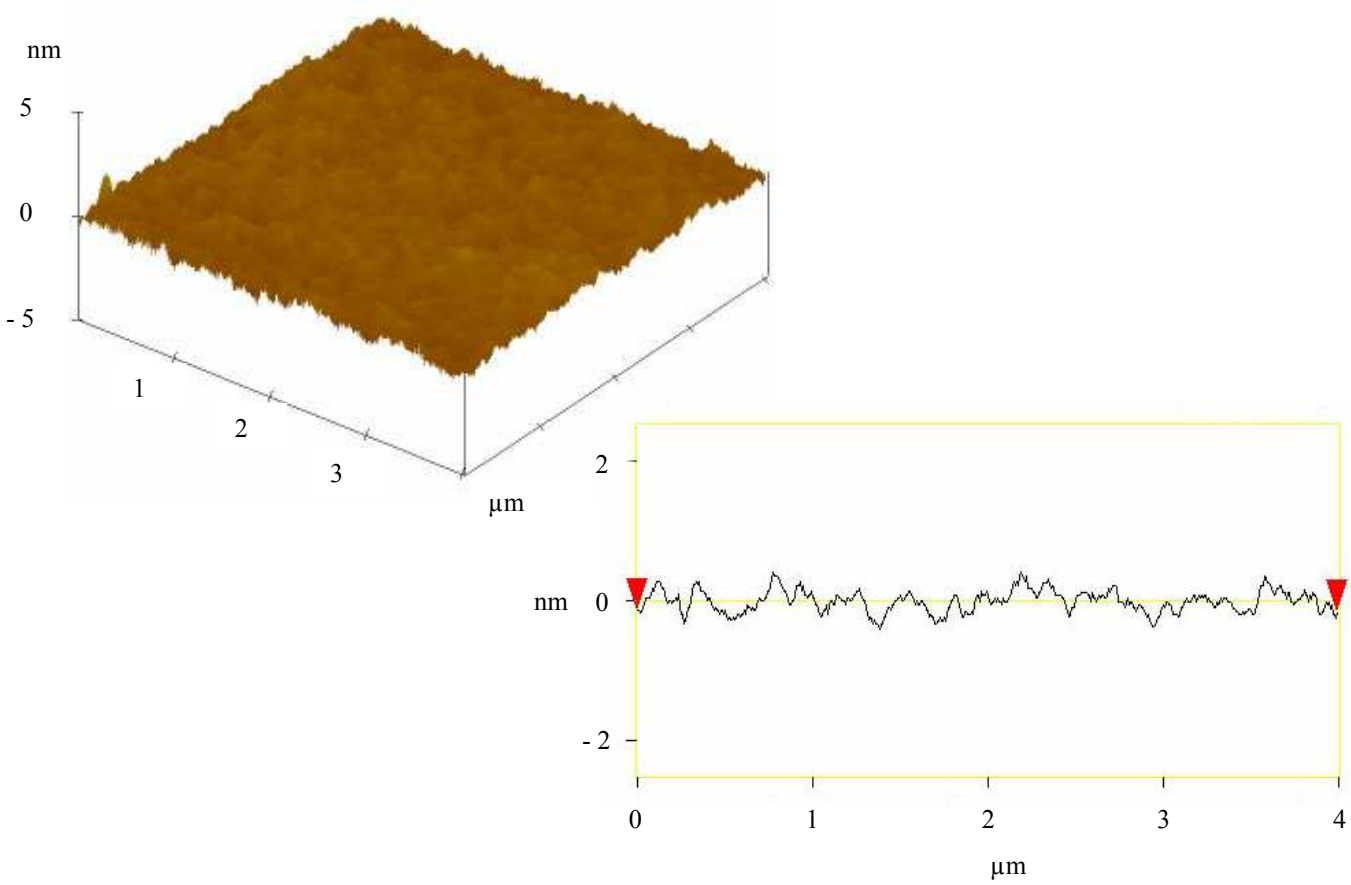

Figure 3.3. A 4 µm x 4 µm tapping mode AFM image of an as-prepared PPF surface (left). Line profile across AFM image where the RMS roughness is the variation between the arrows (right).

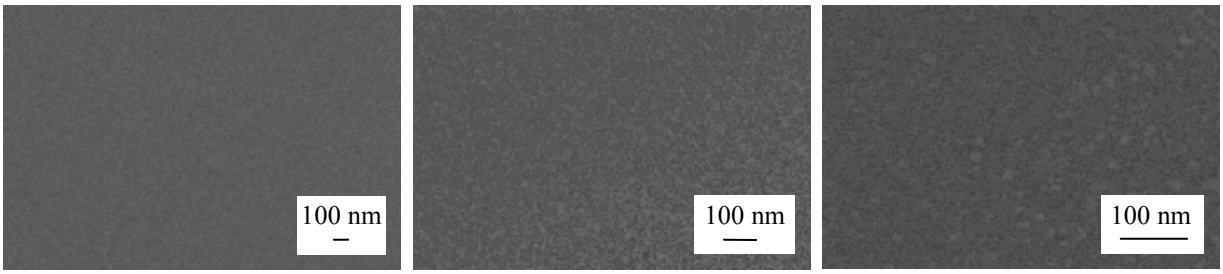

Figure 3.4. SEM images of an as-prepared PPF surface.

Wettability

The average water contact angle of two PPF surfaces is 72 ± 3°. Figure 3.5. shows one of the water drops on an as-prepared PPF surface. The water contact angle of 72 ± 3° indicates that PPF surfaces can be described as hydrophobic according to the definition that hydrophobic surfaces have $\theta > 65°$.[12]

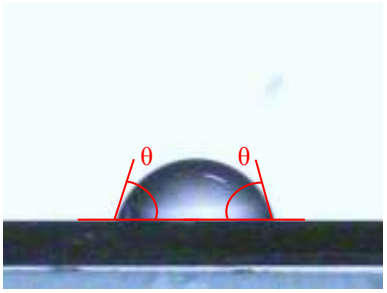

Figure 3.5. Image of a 1 μL water droplet on an as-prepared PPF surface from which water contact angles were measured (as shown) to be $\theta = 72 \pm 3°$.

3.2.3. Characterisation of GC rods and plates

Resistivity and electrochemical properties

The resistivity of a GC plate was measured as 4.0 x 10^{-3} Ω.cm using the same method as for PPF (ρ = 4.4 x 10^{-3} Ω.cm). FCA and $Ru(NH_3)_6^{3+}$ redox responses at GC rods and plates had similar ΔE_p as at PPF after adjusting for the geometric sizes of the electrodes.

The potential window for GC is identical to PPF, i.e. -1.5 to 1.5 V in PBS and -2 to 1.5 V in ACN/0.1 M $[Bu_4N]BF_4$. When scanning in the positive direction in PBS or ACN/0.1 M $[Bu_4N]BF_4$, there is a sudden steep increase in current at approximately 1.5 V in both solutions, as shown in Figure 3.6.(i). and Figure 3.6.(ii), respectively. With PBS, there is a small peak at approximately 1.2 V. Significant amount of effort was put into assigning this peak. PBS contained $K_2H_2PO_4$, Na_2HPO_4 and NaCl and so GC rods were scanned in various electrolytes including 0.1 M NaCl, $NaNO_3$, Na_3PO_4 dissolved in MQ water. No peaks were observed in both NaCl and $NaNO_3$. However, in Na_3PO_4, there was a broad peak centred at 0.9 V and another peak at 1.4 V. This suggests that the peak at 1.2 V is from PO_4^{3-} groups associating with the GC electrode. After the peak, the current increases sharply. As expected, the rise is more significant in PBS compared to ACN/0.1 M $[Bu_4N]BF_4$ due to the amount of H_2O present. The current at the positive potential limit in both solutions decreases with repeat scans becoming constant after seven scans.

Additionally, due to the lesser amount of H_2O present, the positive potential limit in ACN/0.1 M $[Bu_4N]BF_4$ is expected to be higher than for PBS. It is assumed that traces of H_2O in the non-aqueous solvent and/or electrolyte give the low potential limit. Therefore, attempts were made to increase the potential limit by further drying of ACN and the

electrolyte $[Bu_4N]BF_4$ as an addition to the standard drying procedures described in Chapter 2. Additional drying of ACN was by (i) refluxing under $Ar_{(g)}$ rather than $N_{2(g)}$ ($N_{2(g)}$ may have been a source of H_2O); (ii) refluxing over fresh CaH_2 for an additional few hours; (iii) refluxing over phosphorous pentaoxide for two hours and then again over CaH_2 for another half hour or (iv) filtering through activated alumina. The electrolyte was re-dried for another day under reduced pressure at 80 °C. Other changes including flushing all rubber tubing used in the reflux apparatus and degassing tubes with $Ar_{(g)}$ prior to use, and polishing the GC rods with 1 μm diamond paste/lapping oil rather than alumina. However, these attempts did not improve the potential limit beyond 1.5 V.

As for PPF, if the solutions were not thoroughly degassed with $N_{2(g)}$, O_2 redox peaks were observed. These occurred at similar potentials to those at PPF.

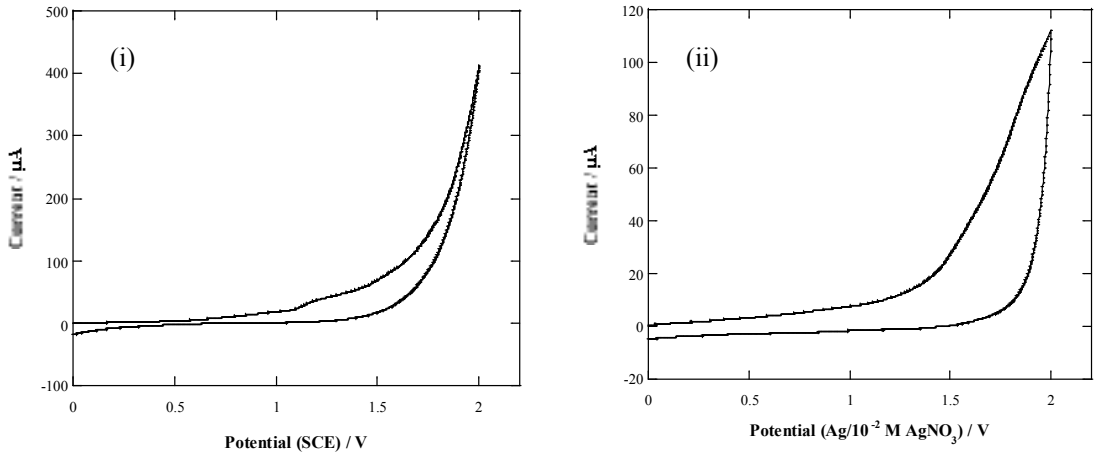

Figure 3.6. CV scans of as-prepared GC rod recorded in (i) PBS and (ii) ACN/0.1 M $[Bu_4N]BF_4$ to determine positive potential limits. Scan rate = 100 mVs^{-1}.

Characterisation by spectroscopy and AFM

The Raman spectrum of an as-prepared GC plate, recorded at the University of Otago, showed two peaks at similar positions to those observed for the PPF surface. The relative magnitudes of the peaks for GC were the opposite to those observed for PPF with the 1360/1600 peak intensity being greater than 1. This suggests that a smaller crystallite size and greater disorder is present in GC compared to PPF for the preparation procedures used in this work.[2,3]

RMS roughness for a GC plate, polished with 1 μm alumina, was measured in a similar fashion to PPF. The RMS roughness over 4 μm scan distances was measured for a 20 μm x 20 μm image. For each of the three 20 μm line profiles drawn on the image, the RMS roughness of five different 4 μm scan distances was measured, giving a total of 15 measurements per image. The average RMS roughness is 0.8 nm and the range of the 15 values is 0.6 – 1.2 nm (Appendix 3.). These values are approximately four times larger than for PPF and are lower than previously reported values as detailed in the Introduction of this chapter. The roughness of GC is similar to that observed for organic layers grafted onto PPF; therefore layers grafted onto GC could not be analysed with the AFM.

Wettability

The water contact angle for GC was measured using a similar procedure to that for PPF. The water contact angle on a GC plate is 71 ± 4°. The water contact angles on PPF and GC surfaces are essentially the same although PPF surfaces have RMS roughness values that are approximately four times smaller than GC surfaces. This is somewhat

surprising as nano-scale differences in surface features have been shown to influence contact angles.[13]

3.4. Conclusions

PPF surfaces were successfully fabricated with an optimised process after a significant amount of method development. The resistivity, electrochemical properties in particular redox probe scans and potential windows, carbon bands in the Raman spectra and wettability for both PPF and GC surfaces were very similar. These results indicated that the PPF surfaces are suitable for use as electrodes and it is indeed a carbon-based surface that has very similar properties to GC. The only major difference between the surfaces is the roughness, as characterised by the AFM. GC is significantly rougher than PPF. This is an advantage for PPF over GC because the organic layers attached to PPF can be analysed using the AFM to gain additional information about the layers. On the other hand, an advantage of GC over PPF is the reusability of the electrode and ease of preparation.

The properties of both PPF and GC surfaces that were prepared and used in this work are similar to reported properties in the literature for the two surfaces. The thickness of the PPF, resistivity, electrochemical properties, carbon composition from Raman spectra and surface roughness are similar to surfaces prepared by other workers.

3.5. References

(1) Kim, J.; Song, X.; Kinoshita, K.; Madou, M.; White, R. *Journal of the Electrochemical Society* **1998**, *145*, 2314-2319.

(2) Ranganathan, S.; McCreery, R.; Majji, S. M.; Madou, M. *Journal of the Electrochemical Society* **2000**, *147*, 277-282.

(3) Kostecki, R.; Schnyder, B.; Alliata, D.; Song, X.; Kinoshita, K.; Kotz, R. *Thin Solid Films* **2001**, *396*, 36-43.

(4) Ranganathan, S.; McCreery, R. L. *Analytical Chemistry* **2001**, *73*, 893-900.

(5) Hoekstra, K. J.; Bein, T. *Chemistry of Materials* **1996**, *8*, 1865-1870.

(6) Liu, Y.-C.; McCreery, R. L. *Journal of the American Chemical Society* **1995**, *117*, 11254-11259.

(7) Jenkins, G. M.; Kawamura, K. *Nature* **1971**, *231*, 175-176.

(8) Kissinger, P. T.; Heineman, W. R. *Laboratory Techniques in Electroanalytical Chemistry*; 2nd edition ed.; Marcel Dekker, **1996**.

(9) Kariuki, J. K.; McDermott, M. T. *Langmuir* **2001**, *17*, 5947-5951.

(10) Donner, S.; Li, H.-W.; Yeung, E. S.; Porter, M. D. *Analytical Chemistry* **2006**, *78*, 2816-2822.

(11) Bard, A. J.; Faulkner, L. R. *Electrochemical Methods: Fundamentals and Applications*; Second ed.; John Wiley & Sons, 2001.

(12) Vogler, E. A. *Advances in Colloid and Interface Science* **1998**, *74*, 69-117.

(13) Martines, E.; Seunarine, K.; Morgan, H.; Gadegaard, N.; Wilkinson, C. D. W.; Riehle, M. O. *Nano Letters* **2005**, *5*, 2097-2103.

4.1. Introduction

The electrochemical oxidation of amines for the modification of carbon surfaces has been reviewed in Chapter 1. As described in Chapter 1, multilayer formation is possible with the amine modifiers but the mechanism for multilayer formation of amines on carbon surfaces has not been investigated. However, the oxidation of amines at metal electrodes has been the subject of several studies. The electrochemical polymerisation of ethylene diamine, 1,2-diaminopropane, 1,3-diaminopropane and diethylenetriamine at platinum and gold electrodes using neat liquid amines with inert supporting electrolyte has been examined in detail.[1-3] Spectroscopic examination of the surface layers shows the presence of linear polymers (no branching) with repeating CH_2-CH_2-N units and no detectable N-N, N=N, C=O or C=N bonds. A tentative mechanism consistent with these observations is proposed and involves C-N bond cleavage, elimination of amine from the growing polymer and the attachment of another amine modifier to already attached modifiers, as detailed in Figure 4.1.[2,3] Similar studies were also carried out with *p*-phenylenediamine and the same mechanism is proposed for its polymerisation.[4] The alternative mechanism where the amine of the modifier in solution is oxidised rather than the surface-bound modifier is not proposed in these studies.

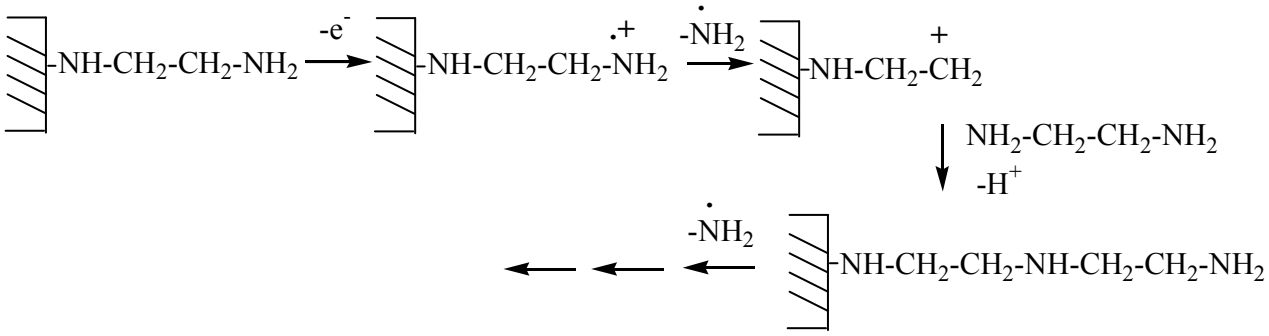

Figure 4.1. Mechanism for multilayer formation of diamines by C-N bond cleavage, elimination of amine from the growing polymer and the attachment of another amine modifier to already attached modifiers to yield a linear structure.[2,3]

In this work, one of the electroactive species that is coupled to the amine-modified carbon surfaces is ferrocene monocarboxylic acid (FCA) where the electroactive centre is the ferrocene (Fc). The coupling of Fc species to already attached modifiers and the electrochemistry of the coupled Fc have been well studied.[5-9] Rather than coupling, the factors affecting the Fc response have also typically been investigated with Fc-terminated self-assembled monolayers (SAMs) assembled onto gold surfaces where the Fc is attached to the thiol prior to assembly.[10-15] The latter approach has an advantage that it does not depend on the yield of the amide bond formation at the surface.

Major factors that control the potential, peak width and peak separation of the redox response of surface-bound Fc species are the environment surrounding the Fc group and the electrochemical solution in which the response is observed. The electrochemical response of the Fc has been shown to be varied when the Fc groups are exposed or buried within the layer[10,11] and when the groups are surrounded by other Fc groups or isolated[12-14]. Poorly or highly hydrated electrolytes in the electrochemical solution also influence the response.[13,15]

The phenomenon of "ion-gated mediated electron transfer" is where the redox process is critically dependent on the rate of counterion transport to the ferrocenium (Fc^+). The oxidation peak is observed up to 300 mV more positive[10] and the width and separation of the peaks increase when the rate of the anion transfer is slowed to the buried Fc^+ site.[11] Moreover, the Fc^+ ion is destabilised when buried in an alkane, non-polar environment, contributing to a shift to a more positive potential for the redox process.[10]

Splitting of the peaks is observed when there is partial aggregation of the Fc groups into domains with different local or electrochemical microenvironments.[12,13] This results in isolated areas of Fc oxidising at various times or repulsive interactions between neighbouring groups of Fc during oxidation. An Fc^+ ion increases the oxidation potential of the neighbouring Fc and even weakly affects the next nearest Fc, via electron hopping between groups.[14]

When the electrochemical solution contains poorly hydrated (hydrophobic) anions that are able to form ion pairs with the Fc^+ groups, symmetrical and more distinct cyclic voltammetry (CV) scans are observed for the coupled Fc redox response.[13,15]

The aim of this work is to prepare and characterise layers formed by the electrochemical oxidation of seven selected primary amine modifiers. Atomic force microscope (AFM) depth profiling is used to determine whether the amine modifiers form layers exceeding thicknesses calculated for a monolayer. Amine multilayers have not been previously detected by the direct method of AFM depth profiling. The stability of two amine layers is examined in this study. *n*-tridecylamine (TDA) and 1,12-diaminododecane (DAD) layers attached with significantly more prolonged modification conditions are

subjected to extensive scanning, soaking and sonicating experiments. The changes are monitored by the redox response of a probe. Apart from monitoring the stability of amine layers, these experiments are intended to provide insights into the difference between layers formed by diamines compared to monoamine modifiers.

The versatility of these amine modifiers for subsequent coupling reactions is also investigated. Various molecules with carboxylic acid and acid chloride functionalities are used for coupling via amide bond formation. These molecules included FCA and nitrobenzoyl chloride (NBC). From analysis of the coupled species, information about the amine layers such as modifier surface concentration can be gained.

4.2. General experimental methods

4.2.1. Preparation of GC plates or rods

Glassy carbon (GC) plates or rods were prepared in three different ways. The preparation method was as detailed in Chapter 3 except when the modified plates are used for the adsorption of protein (Chapter 6) or assembly of aldehyde/sulfate-functionalised polystyrene (PS) nanoparticles (NPs) (Chapter 7). All three methods used 1 μm alumina as the polishing material and so were assumed to give similar surfaces.

Experiments involving adsorption of protein: GC plates were polished with a 1 μm alumina/water slurry on a Leco polishing cloth in a figure 8 motion and rinsed in distilled water. Plates were then sonicated in MilliQ (MQ) water for 10 minutes and in IPA (isopropyl alcohol) /ACN (acetonitrile) (1:1) and activated carbon slurry (50:50 by volume)

for another 10 minutes.[16] The plates were then rinsed in ACN, followed by MQ water and dried with $N_{2(g)}$ before electrochemistry was carried out.

Experiments involving the assembly of PS NPs: GC plates were polished on a 1 μm alumina/water slurry in a figure 8 motion and then sonicated briefly in distilled water. Plates were then sonicated in MQ water for 10 minutes and dried with $N_{2(g)}$ before electrochemistry was carried out.

4.2.2. Materials

The amine modifiers, TDA (Acros Organics), DAD (Aldrich), *n*-hexylamine (HA, Sigma), tetraethylene glycol diamine (TGD, Molecular Biosciences), polyethylene glycol diamine (PGD, Huntsman) and *para* nitro aniline (*p*-NA, Aldrich) were used as purchased with the exception of 4-nitrophenylethylamine (NPEA). NPEA was purchased as the ammonium chloride salt (Aldrich) and was neutralised following a reported method.[17] 0.09 mL of 40% NaOH was added to 0.25 $molL^{-1}$ aqueous solution of the commercial salt. The NPEA was extracted from the aqueous phase using 3 x 10 mL aliquots of toluene. Excess amounts of sodium sulphate were added to remove traces of water and the sodium sulphate was then removed by filtering under vacuum. Toluene was removed on the rotary evaporator under vacuum. The yellow oil product was kept below 0 °C in salted ice and used immediately.

The neutralisation of the amine chloride salt of NPEA was confirmed by ^{1}H nuclear magnetic resonance (NMR). ^{1}H NMR for NPEA was as follows (ACN, 500 MHz) δ 1.95 ppm (s(br), 2H, $N\mathbf{H_2}CH_2CH_2$-Ar-NO_2), 2.86 ppm (t, 2H, $NH_2C\mathbf{H_2}CH_2$-Ar-NO_2), 2.95 ppm

(t, 2H, $NH_2CH_2C\mathbf{H_2}$-Ar-NO_2), 7.50 ppm (d, 2H, $NH_2CH_2CH_2$-Ar**H**-NO_2), 8.18 ppm (d, 2H, $NH_2CH_2CH_2$-Ar**H**-NO_2).

NMR and mass spectroscopy were used to analyse the purity of the purchased TDA and DAD. Mass spectroscopy was performed on a Waters Alliance 2795 instrument by Bruce Clark, Department of Chemistry, University of Canterbury.

^{1}H NMR for TDA was as follows ($CDCl_3$, 500 MHz) δ 0.88 ppm (t, 3H, $NH_2(CH_2)_{12}C\mathbf{H_3}$), 1.26 ppm (s, 20H, $NH_2CH_2(C\mathbf{H_2})_{\mathbf{10}}CH_2CH_3$), 1.44 ppm (m, 2H, $NH_2(CH_2)_{11}C\mathbf{H_2}CH_3$), 1.53 ppm (s(br), 2H, $N\mathbf{H_2}(CH_2)_{12}CH_3$), 2.68 ppm (t, 2H, $NH_2C\mathbf{H_2}(CH_2)_{11}CH_3$). ^{1}H NMR for DAD was as follows ($CDCl_3$, 500 MHz) δ 1.17 ppm (s(br), 4H, $N\mathbf{H_2}(CH_2)_{12}N\mathbf{H_2}$), 1.27 ppm (s) and 1.42 ppm (m) (20H, $NH_2CH_2(C\mathbf{H_2})_{\mathbf{10}}CH_2NH_2$), 2.68 ppm (t, 4H, $NH_2C\mathbf{H_2}(CH_2)_{10}C\mathbf{H_2}NH_2$). ^{1}H NMR for TDA was run with a delay time of 10 seconds, integration time of 8 and zero filling of 128,000 to optimise the integrals.

Table 4.1. lists the physical appearance of the amine modifiers used.

Table 4.1. Physical appearances of the amine modifiers

Amine modifiers	Physical appearance
TDA	Waxy white solid
DAD	White solid
HA	Colourless liquid
TGD	Colourless liquid
PGD	Waxy white solid
NPEA	Yellow viscous liquid
p-NA	Yellow solid

4.2.3. Electrochemistry

The CV of the FCA probe response was recorded before and after each modification to assess the blocking properties of the resulting layer. Modification solutions were sonicated to aid solubility of some of the amine modifiers in ACN. A range of concentrations of amine modifiers was used as shown in Table 4.2.

To determine the oxidation potential of each amine modifier, the potential was scanned to 1.5 V. The applied potential for modification was $E_f = E_{pa} + E'$. E_f values for all the amine modifiers were between 1.2 and 1.3 V (Table 4.2.) and E' ranged from 100 – 300 mV. The scan rate for the initial and final modification scans was 100 mVs^{-1} which was used for all modifiers except PGD for which the scan rate was 50 mVs^{-1}.

The electrolysis time at final/applied potential (E_f) was varied in order to tailor the surface concentration of modifier and thickness of the layer. It was anticipated that an electrolysis time of 10 minutes would yield a compact and blocking amine layer of 'limiting' thickness.

For some electrochemical experiments with GC rods, stirring was carried out at a constant speed using a magnetic flea at the bottom of the cell which did not contact the electrode.

Table 4.2. Concentrations of amine modifiers and E_f values used for the electrochemical attachments of the amine modifiers.

Amine modifier	[amine] / mM	E_f / V
TDA	5	1.3
DAD	5	1.2
HA	5, 10, 200	1.3
TGD	5, 200	1.2
PGD	20, 50, 100	1.3
NPEA	5	1.3
p-NA	5	1.2

4.2.4. Coupling of FCA to amine layers

FCA was coupled to TDA and DAD layers (5 mM, electrolysis time 1 minute) on PPF by a 24 hour immersion in either (i) 40 mM EDCI and 8 mM NHS with 1 mM of FCA in PB or (ii) 1:2:1 molar ratio of DCC/DIPEA/FCA (183 mM DCC, 366 mM DIPEA and 166 mM FCA) in DCM. In addition, a 24 hour coupling of FCA (1 mM) to TGD layers (5 mM, electrolysis time 10 minutes) was carried out in aqueous PB with coupling agent EDCI (20 mM) and activating agent NHS (4 mM). During the 24 hour immersions, all samples were agitated gently using an orbital shaker.

4.2.5. Estimation of surface concentration

The minimum surface concentrations of TDA, DAD and TGD modifiers was estimated by coupling FCA to the amine layer and observing the electrochemistry of the electroactive species Fc. The peak areas of the Fc response allowed the estimation of surface concentration. The surface concentration of NPEA was estimated from the electrochemical response of the *p*-nitrophenyl group recorded in ACN/0.1 M $[Bu_4N]BF_4$

(tetrabutyl ammonium fluoroborate) and/or 0.1 M H_2SO_4. Errors given with the surface concentration values included all the samples measured.

4.3. Results and discussion

The amines modifiers selected in this work all consist of only primary amines, as listed in Table 4.3. The seven amine-containing molecules were specifically chosen with the intentions of comparing: (i) mono- and diamines, (ii) amines of different hydrophobicity and thus wettability and (iii) amines of varied length. The conformation of the attached modifiers is of interest firstly with regards to whether both (looped conformation) or only one of the amines in the diamine modifiers forms a C-N bond and secondly whether multilayer formation is observed with not only the diamine molecules (as observed by other workers) but also the monoamines. The aromatic amine modifier, NPEA, has an electrochemically active *p*-nitrophenyl group from which the surface concentration of amine modifiers attached can be estimated.

The calculated lengths of the modifiers are also given in Table 4.3. These values were used to calculate the minimum number of modifiers attached to the PPF surfaces for a given layer thickness assuming that modifiers were perpendicularly stacked relative to the surface.

Table 4.3. Amine modifiers attached to carbon surfaces and their calculated lengths.

Amine modifier	Abbreviation	Structure Ar = aryl ring	Calculated length of modifier / nm
n-tridecylamine	TDA	$H_2N(CH_2)_{12}CH_3$	1.8
1,12-diaminododecane	DAD	$H_2N(CH_2)_{12}NH_2$	1.8
n-hexylamine	HA	$H_2N(CH_2)_5CH_3$	1.0
Tetraethylene glycol diamine	TGD	$H_2NCH_2CH_2(OCH_2CH_2)_3NH_2$	1.5
Polyethylene glycol diamine Mr ≈ 2003 g.mol^{-1}	PGD	$H_2NCH(CH_3)CH_2(OCH(CH_3)CH_2)_a$- $(OCH_2CH_2)_b(OCH(CH_3)CH_2)_cNH_2$ a + c = 2.5, b = 40.5; a, b and c being average values	Not calculated, estimated as > 15 nm
4-nitrophenylethylamine	NPEA	$H_2NCH_2CH_2ArNO_2$	0.8
Reduced 4-nitrophenylethylamine	Reduced NPEA	$H_2NCH_2CH_2ArNH_2$	0.8
p-nitro aniline	*p*-NA	H_2NArNO_2	0.7

4.3.1. Electrochemistry and attachment

Amine oxidation

The initial and final modification scans for the amine modifiers are shown in Figure 4.2. The oxidation peaks for the amine modifiers are chemically irreversible, as expected for a modification process. Consistent with other reports, it is assumed that the generated primary amine cation radical from the one-electron oxidation has formed a covalent attachment via a C-N to the carbon surface, yielding a secondary amine at the surface. The final CV scans recorded after the electrolysis time show no peaks and the currents are very low. The current of the final CV scans decreases with longer electrolysis times. When amines were attached with repeated scanning to E_f, the oxidation peak was not present after the first scan and the current at E_f gradually decreased with number of scans. Table 4.4. gives the potential of anodic/oxidation peak (E_{pa}) values extracted from the CV scans. The peaks are broad possibly because the initially attached modifiers block the surface and

slowed further oxidation as the CV scan proceeds and/or the oxidation processes of these amines are inherently slow.

Figure 4.2. Initial (a) and final (b) CV scans of the oxidation of amine modifiers. The [amine] = 5 mM (unless otherwise stated) in ACN/0.1 M $[Bu_4N]BF_4$ and scan rate = 100 mVs^{-1}. Data were observed at PPF (unless otherwise stated) and electrolysis times are as stated.

TDA, electrolysis time 1 minute at 1.3 V

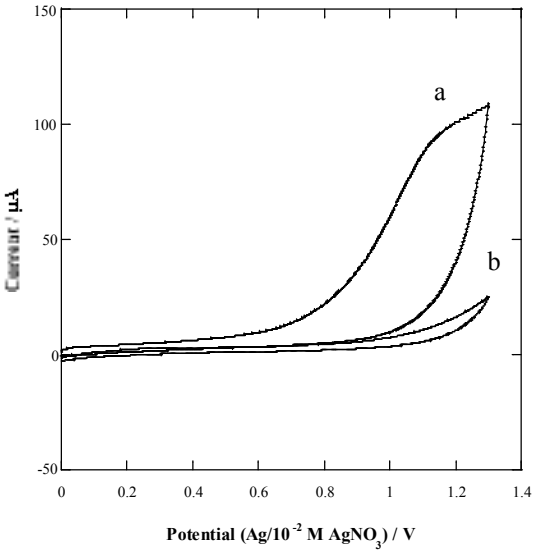

DAD, electrolysis time 1 minute at 1.2 V

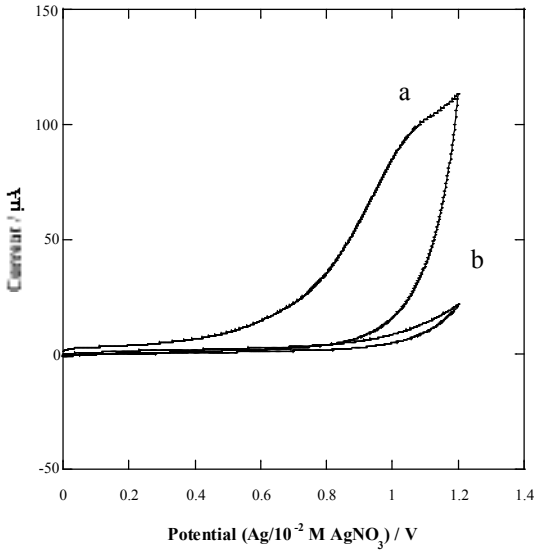

HA, electrolysis time 10 minute at 1.3 V

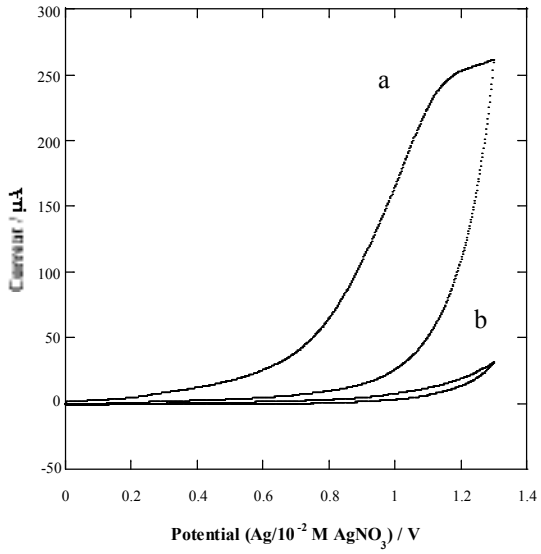

TGD, electrolysis time 10 minute at 1.2 V

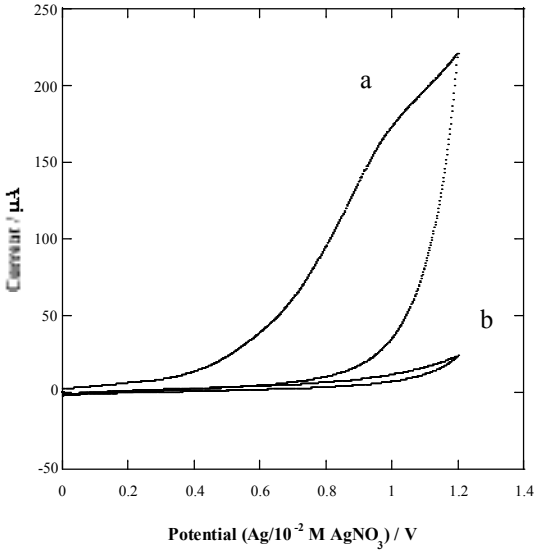

PGD, electrolysis time 10 minutes at 1.3 V, at GC plate (in cell set-up (ii) i.e. electrode geometric area = 0.64 cm^2) Final scan not recorded and [amine] = 50 mM

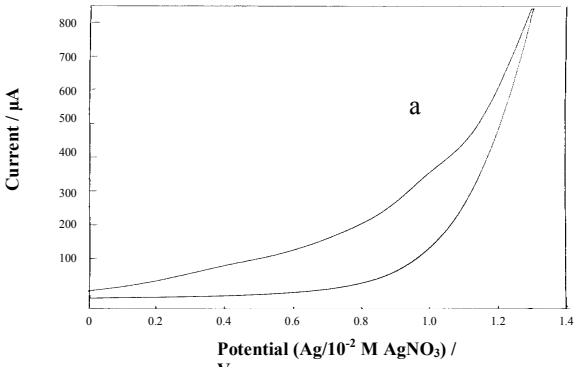

NPEA, electrolysis time 10 minute at 1.3 V

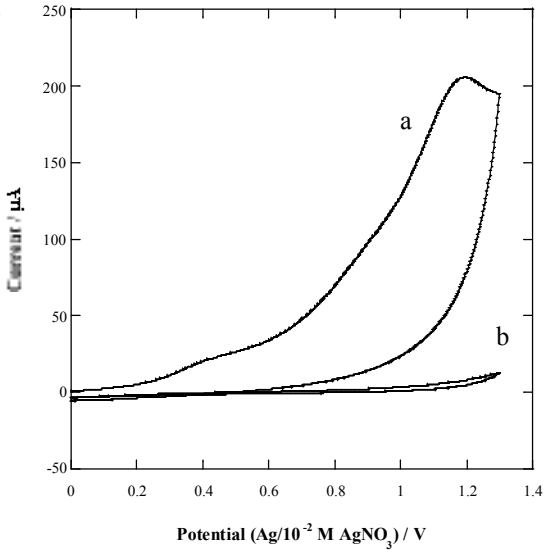

Table 4.4. E_{pa} values from the CV scans of amine modifiers at carbon surfaces.

Amine modifier	E_{pa} / V
TDA	1.1
DAD	1.0
HA	1.1
TGD	1.0
PGD	1.1
NPEA	1.2 (0.4 impurity)
p-NA	1.0

The oxidation peak potentials for all seven modifiers are similar, occurring between 1.0 – 1.2 V. Comparison of the CV scans of modifiers with similar structure and/or length, (TDA compared to DAD and HA compared to TGD) are detailed in the separate sections on these modifiers.

Control experiments were carried out to investigate the effect of applied potential used for amine oxidation on the carbon surfaces. GC and PPF surfaces were subjected to the modification process where E_f was 1.3 V, which was maintained for 10 minutes in a solution of ACN/0.1 M $[Bu_4N]BF_4$ without the amine modifier present. The FCA probe CV

scans before and after the carbon electrode was held at 1.3 V showed a maximum increase in background current of 48 ± 5% for a GC rod, 44 ± 5% for a GC plate and 59 ± 5% for a PPF surface. The increase in background current indicates that there could be some surface degradation during the modification process. This change was similar for electrolysis times of 2, 5 and 8 minutes and suggested that surface degradation occurs within 2 minutes of electrolysis. There was no peak present in scans to 1.3 V in ACN/0.1 M $[Bu_4N]BF_4$ without the amine modifier present.

4.3.2. Water contact angle measurements

The contact angle of water on the various amine layers attached to carbon surfaces provides an indication of the wettability of the amine layer. Figure 4.3.(i). and Figure 4.3.(ii). shows a water droplet on the HA-modified layer and the TGD-modified layer, respectively. Table 4.5. lists the water contact angles for layers prepared with selected modifying conditions and also literature values of other surfaces.

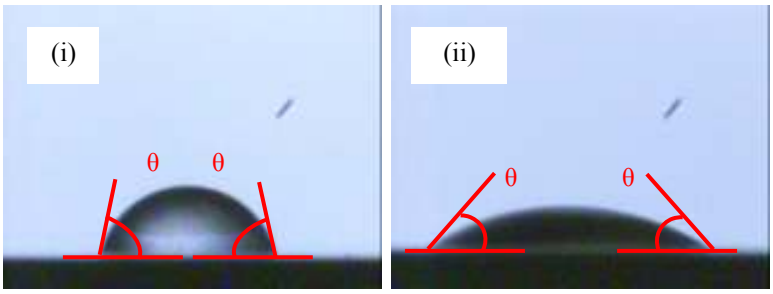

Figure 4.3. Images of 1 µL water droplets on the (i) HA layer and (ii) TGD layer. Both layers were attached onto GC plates using 5 mM solutions and an electrolysis time of 10 minutes. Water contact angles were measured (as shown), giving a value of 77 ± 2° for the HA layer (i) and 45 ± 3° for TGD layer (ii).

From the data in Table 4.5, the order of wettability (from most to least wettable) of the amine layers is TGD > PGD > DAD > HA > TDA. It is possible to explain the order from the hydrophobicity of the amine modifiers as deduced from their structures. Both TDA and HA are hydrocarbon modifiers with an amine via which the modifiers are attached to the surface. Hence, the resulting layer would be hydrophobic. TDA has a longer chain than HA thus increasing its hydrophobicity. In comparison to TDA, DAD has an additional amine which would reduce its hydrophobicity. PGD although longer than TGD has a higher C : O ratio rendering it more hydrophobic compared to TGD.

TDA, HA, DAD layers are considered hydrophobic ($\theta > 65°$) and the PGD and TGD layers are considered hydrophilic ($\theta < 65°$).[18] For the TGD layers on PPF, the water contact angle for both electrolysis times of 2 and 10 minutes were identical considering experimental uncertainty. This suggests that water contact angle is not sufficiently sensitive to detect subtle differences in the TGD layers. The layers attached with varied electrolysis times are different as discussed in a later section.

Compared to the literature values in Table 4.5, the TDA and HA layers are significantly less hydrophobic compared to octadecanethiol SAMs assembled on gold surfaces. This suggests that the amine layers are more 'loosely packed' compared to the SAMs and the water contact angles are influenced by the hydrophilic amines within the layers or by the underlying carbon surface. DAD layers have higher water contact angles than the amine-terminated silane, 11-aminoundecyldimethylsilane. This suggests that DAD does not form well-organised amine-terminated layers. It is more likely that with these 'loosely packed' amine-terminated DAD layers, the hydrocarbon chains and the carbon

surface influence the hydrophobicity. Similar arguments can be used for TGD compared to aminodi(ethyleneglycol)decanethiol assembled on a gold surface, where the hydrophilic chains of the 'loosely packed' TGD layer decreases the water contact angles.

As noted in Table 4.5, two of the three TGD (5 mM, electrolysis time 2 minutes) samples were prepared as part of experiments in Chapter 9a. As part of these experiments, NBC was coupled to TGD-modified PPF surfaces and the influence of the head group on water contact angles was examined. Additionally, water contact angles provided a quick and straightforward way to determine whether coupling of NBC to TGD was successful. Coupling was carried out by immersing the TGD-modified surface into the 0.1 M NBC dissolved in dimethylsulfoxide (DMSO), for 2 hours. The first out of the two TGD samples was immersed into DMSO (without NBC) for 2 hours and the contact angle was 47 ± 1° indicating that the TGD layer was not affected. NBC was coupled to the second TGD sample. The water contact angle increased to 56 ± 2° indicating that coupling of NBC to TGD had occurred. This angle is identical to that measured at a *para* nitro benzene (*p*-NB) layer (0.6 mM, electrolysis time 10 minutes) as detailed in Chapter 5.

Table 4.5. Water contact angles of amine layers attached onto carbon surfaces. These layers were attached with electrolysis times of 10 minutes (unless otherwise stated).

Layer	Structure Ar = aryl ring] = surface	Surface	[modifier] / mM and electrolysis time	Water contact angle / °
TDA	$H_2N(CH_2)_{12}CH_3$	PPF	5	79 ± 3
DAD	$H_2N(CH_2)_{12}NH_2$	PPF	5	74 ± 2
HA	$H_2N(CH_2)_5CH_3$	GC plate	5	77 ± 2
TGD	$H_2NCH_2CH_2(OCH_2CH_2)_3NH_2$	PPF	5, 2 minutes	47 ± 2 [a,b], 47 ± 2 [a,b], 45 ± 2 [b]
		PPF	5	46 ± 3
		GC plate	200	45 ± 3
PGD	$H_2NCH(CH_3)CH_2(OCH(CH_3)CH_2)_a$-$(OCH_2CH_2)_b(OCH(CH_3)CH_2)_cNH_2$ a + c = 2.5, b = 40.5; a, b and c being average values	GC plate	20	59 ± 3
As-prepared		PPF		72 ± 3
As-prepared		GC plate		71 ± 4
Literature values				
Octadecanethiol [19]	Au]-S-$(CH_2)_{17}CH_3$	Gold surface	Not applicable	105 – 110
11-aminoundecyl dimethylsilane [20]	Si]-Si$(CH_3)_2$-$(CH_2)_{11}NH_2$	Silicon or glass surface	Not applicable	58 ± 10 [c]
Amino di(ethyleneglycol) decanethiol [21]	Au]-S-$(CH_2)_{10}$-$(OCH_2CH_2)_2NH_2$	Gold surface	Not applicable	53 ± 2 [c]
Di(ethyleneglycol) decanethiol [21]	Au]-S-$(CH_2)_{10}$-$(OCH_2CH_2)_2OH$	Gold surface	Not applicable	35 ± 2 [c]
p-nitro benzenethiol [19]	Au]-S-Ar-NO_2	Gold surface	Not applicable	65 – 70

[a] Samples prepared as part of experiments in Chapter 9a.
[b] Water contact angles measured from two droplets on a single surface i.e. average of 12 values, instead of the standard procedure using two droplets on two separate surfaces i.e. average of 24 values.
[c] The water contact angles are advancing angles instead of sessile.

These values are lower than those reported for the *p*-nitrophenylthiol SAMs assembled on a gold surface (Table 4.5.). Nonetheless, the difference in contact angles before and after coupling indicated that the NBC molecules attached to the TGD layer dominates the control over the water contact angle. The *p*-nitrophenyl group of the attached nitrobenzoyl (NB) influences the water contact angle. In Chapter 5, the water contact angles on the aryl layers appear to be influenced by the hydrophobicity of the *para* substituent of the modifier. The impact of the head group on the water contact angles is seen with aminodi(ethyleneglycol)decanethiol and di(ethyleneglycol)decanethiol SAMs on gold surfaces, where the amine and hydroxyl head groups give largely different contact angles (Table 4.5.).[21]

In summary, the water contact angle data suggests that the combination of the hydrophobicity of the modifier chain (e.g. TDA compared to HA and DAD compared to TGD) and/or the head group (e.g. TDA compared to DAD and TGD compared to TGD-NB) determines the contact angle.

4.3.3. Visual analysis and optical microscopy

The modified layer which is only of nano-scale thickness could be visualised by eye and optical microscopy. The modifier layer alters the reflectivity of the surface causing the modifier area to appear darker than the as-prepared PPF or GC plate, on the optical microscope images as well as to the eye.

4.3.4. TDA and DAD

The modification of carbon surface with TDA and DAD modifiers and the characterisation of the resulting layers are interesting as the only difference between these modifiers is that TDA is a monoamine and DAD a diamine.

Purity

For these studies, it was important to determine the purity of each modifier especially to assess whether there was any DAD in TDA. Using NMR proved difficult because DAD was symmetrical and its half fragment is present in TDA. However, the relative integrals for the signals occurring at 0.88 and 2.68 were 3 to 2 thus indicating that no DAD was present in the TDA modifier. ^{13}C NMR for both TDA and DAD obtained was consistent with the manufacturer's data.

Attachment

Amine oxidation

Figure 4.2. shows similar CV scans for the modification of TDA and DAD. The oxidation peak of DAD occurs at 100 mV less positive potential than that for TDA. The difference in E_{pa} for the two amines of only 100 mV is not considered significant as the amine oxidation process is chemically irreversible and hence accurate thermodynamic information cannot be gained from the CVs.

Considering the CV scans (Figure 4.2.) obtained using the same electrode area, modifier concentration and scan rate, the peak height of the first CV scan is determined by

the number of electrons in the redox reaction, the diffusion coefficient, the extent to which the surface is blocked by the attached layer as it forms during the scan and the electrode kinetics. Despite this complexity, it seems surprising that the peak currents are similar for the monoamine (TDA) and the diamine (DAD).

Due to the similarity in the oxidation peak current, the peak observed for DAD was assigned to the oxidation of only one of the two primary amines. Oxidation of the other amine was not observed when scanned out to 2 V. This suggests that the two electrochemically equivalent amines of DAD, 12 carbons apart, are interacting and the oxidation of one shifted the oxidation of the other to a more positive potential that is larger than 2 V. The two amines of DAD have different protonation constant values (10.16 and 10.97) supporting the notion that the two amines have some interaction. Oxidation of one of the two interacting electroactive groups has shown to shift the oxidation of the other group to a more positive potential.[22] In this study, the redox response of the two ferrocene groups, separated by a aliphatic linker 12 carbons apart, had observed mid potential between oxidation and reduction peaks for a reversible process ($E_{1/2}$) values 300 mV apart.[22] Thus, the oxidation of DAD, using 1.2 V as the applied potential, presumably formed a C-N bond at surface and the other amine was not surface-bound. The attachment of one amine of the diamine modifier to the surface is consistent with other reports.[23,24]

Probe scans after modification procedure

The surface concentrations of amines and thicknesses of the TDA and DAD layers attached with various electrolysis times were monitored using the voltammetry of the FCA

probe. The blocking properties of the resulting layer is expressed as a current ratio of (anodic/oxidation peak current (i_{pa}) after modification)/(i_{pa} as-prepared PPF or as-prepared GC rod). When a featureless probe scan (i.e. the peak current ratio was close to 0) was observed when the modified surface was scanned within the standard potential range (-0.2 to 0.5 V), a compact, blocking and non-conducting layer of 'limiting' thickness is assumed to be present at the electrode. Layers were then scanned out to 0.8 V to ensure that the layer inhibited the probe redox response over the wider potential range.

CV scans of the FCA probe at TDA and DAD-modified PPF surfaces are shown in Figure 4.4. and 4.5, respectively. Table 4.6. shows the E_{pa} and current ratios of the FCA probe CV scans at TDA and DAD layers on PPF surfaces, prepared using different modification times. The E_{pa} and current ratios were averaged from at least two different samples. Similar results were obtained at GC surfaces.

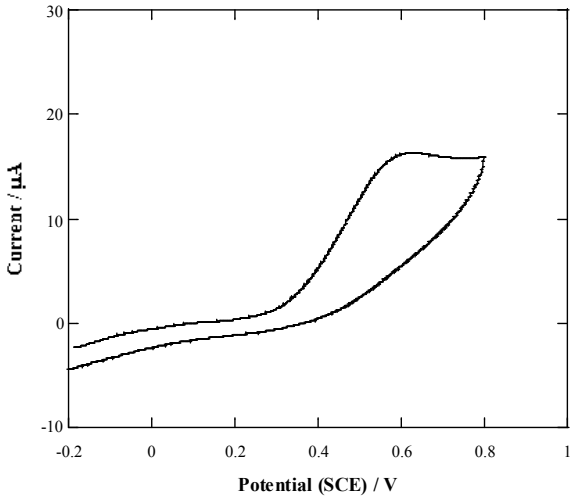

Figure 4.4. FCA CV scans after modification of a PPF surface with TDA. Layers were attached using a 5 mM modifier solution and an electrolysis time of 2 minutes. Scan rate = 100 mVs^{-1}.

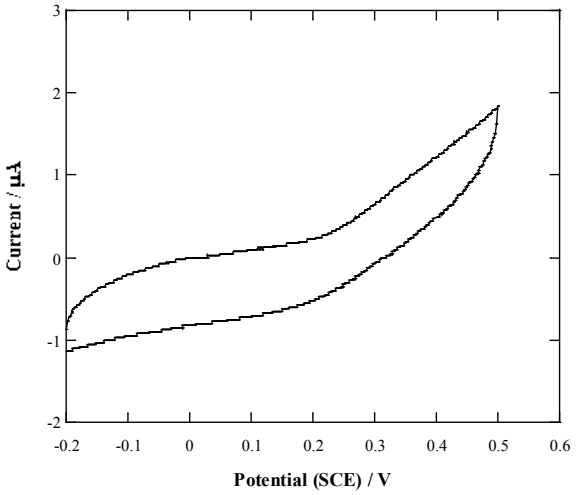

Figure 4.5. FCA CV scans after modification of a PPF surface with DAD. Layers were attached using a 5 mM modifier solution and an electrolysis time of 2 minutes. Scan rate = 100 mVs^{-1}.

Table 4.6. E_{pa} and current ratios of FCA CV scans obtained at TDA- and DAD-modified PPF prepared using different modification times.

Amine layer	Electrolysis time or no. of scans	E_{pa} of probe after modification [a] / V	Current ratio [b] at peak [c] or at 0.35 V	Thickness / nm [d]
None [e]	none	0.30	-	none
TDA	1 minute	0.57	0.43 [c]	1.1
	2 minutes	0.60	0.43 [c]	1.0
	5 minutes	No peak	0	2.5
DAD	1 scan	0.42	0.68 [c]	1.3
	1 minute	No peak	0.09	1.6
	2 minutes	No peak	0.03	1.6
	3 minutes	No peak	0.03	3.3
	5 minutes	No peak	0.06	4.0
	8 minutes	No peak	0.03	Not measured
	10 minutes	No peak	0	5.4

[a] Uncertainty on E_{pa} is ± 0.02 V.
[b] Uncertainty on current ratios of (i_{pa} after modification)/(i_{pa} as-prepared PPF) is ± 0.05.
[d] Thickness values were averaged from samples prepared (Figure 4.7. and Table 4.7.).
[e] i_{pa} of the FCA probe response at an as-prepared PPF surface was ~35 µA.

The E_{pa} of the probe and current ratio of (i_{pa} after modification)/(i_{pa} as-prepared PPF) are related to the electrolysis time or number of scans used in the modification process and the thickness of layer (as measured by AFM depth profiling as detailed in a later section). For both TDA and DAD layers, with increasing modification times, the current ratios decrease and the thicknesses of the layers increase. This observation suggests that the layers grow laterally, i.e. a compact monolayer of modifiers attach to the PPF, before the layer grows vertically where modifiers attach to an existing layer of surface-bound modifiers. If vertical growth preceded lateral growth giving a very 'loosely packed' layer of oligomers, then the current ratios would not decrease as significantly with electrolysis times as observed.

Comparing TDA and DAD layers, a completely blocking layer of TDA was obtained using a shorter electrolysis time compared to DAD. For TDA, with electrolysis times of 1 and 2 minutes, the layers formed decrease the rate of the electron transfer and hence redox process of the FCA probe. This causes the E_{pa} of the probe to occur outside the standard range. After 5 minutes, the resulting layer is completely blocking suggesting that a compact layer was present at the PPF surface. Vertical growth had also occurred as observed by the increase in layer thickness, which could have contributed to the blocking behaviour. With DAD, between electrolysis times of 1 and 8 minutes, small current ratios are observed although the thickness increases. The small currents are probably due to pinholes present within the layer or may be attributed to the additional amines in the DAD layer allowing increased electrostatic interactions with the anionic FCA probe.[25] In the probe solution of pH 7.4, the carboxylic acid of FCA species are partially deprotonated

(pK_a FCA (Fe^{2+}) = 6.44)[26] and the amines are largely protonated (protonation constant 9 – 10). At 10 minutes, the response of the probe is not observed.

However, for the electrolysis times of 1 and 2 minutes, the DAD layers are more blocking compared to TDA even though both layers are of similar thicknesses. This indicates that a more compact layer is initially formed with the diamine compared to the monoamine.

Analysis by AFM depth profiling

Figure 4.6. is an AFM image of part of a scratch made in a TDA layer (5 mM, electrolysis time 10 minutes). The layer has a uniform appearance apart from a few higher features of debris. The debris is either a result of scratching or from handling the sample in air (dust) and can be removed if the sample is washed or exposed to a stream of gas. The lower panel is an average cross-sectional profile of the scratch from which vertical distance measurements are taken to determine layer thickness. Figure 4.7. and Table 4.7. show the increase of thickness of TDA and DAD layers with increasing period of electrolysis. After an electrolysis time of 10 minutes, maximum layer thicknesses of approximately 5 nm and 6 nm for TDA and DAD, respectively, is achieved. This indicates that electron transport is inhibited or significantly slowed over such a distance that no further growth of the layer could occur. For DAD, there is an increase in the spread of layer thickness data with thicker layers, possibly due to the increased disorganisation within the layer contributing to its roughness.

The calculated lengths of the amine modifiers are 1.8 nm for both TDA and DAD. Hence, for the thickest layers obtained, assuming an orientation perpendicular to the surface, the minimum number of molecular layers is estimated as three for TDA and four for DAD. It should be stressed that only a minimum number of layers can be determined from AFM depth profile measurements and no information can be gained concerning the orientation or organisation of the modifiers.[27] It is possible that a greater number of layers are incorporated in a tilted or collapsed structure. Despite the lack of information on the structure of the layers, it is significant that AFM depth profiling provides direct evidence for the formation of amine layers which have thicknesses greater than a monolayer. It is also useful to note that to obtain a modifier layer of monolayer thickness, an electrolysis time of 5 minutes or less should be used for TDA and 2 minutes or less for DAD. These times only apply for the modifier concentrations and E_f values used for these experiments. As the layer thickness increases with electrolysis time, it is possible to tailor thicknesses of the layers by modulating the period of electrolysis. The thicknesses of layers are larger than the calculated length of TDA and DAD modifiers when the electrolysis time is > 5 minutes for TDA and > 2 minutes for DAD. A shorter electrolysis time is required to form multilayers for the DAD modifier compared to the TDA modifier.

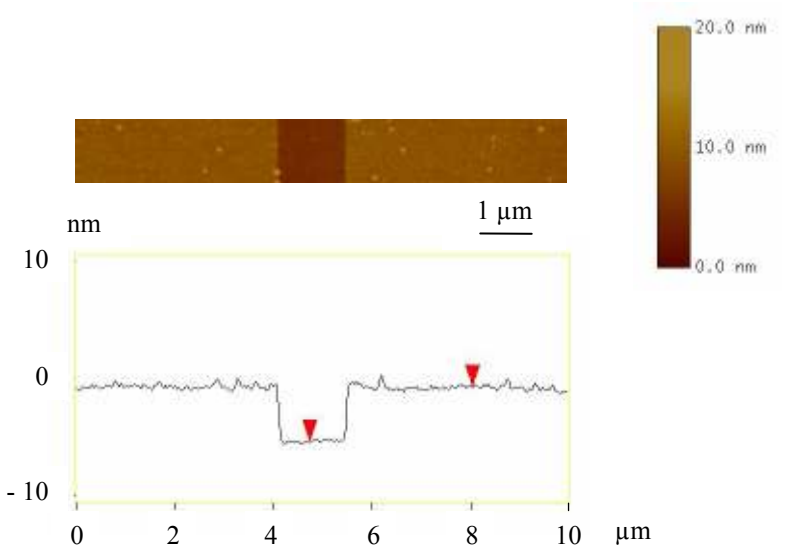

Figure 4.6. Top: AFM image of a scratched TDA layer (5 mM, electrolysis time 10 minutes). Bottom: Average cross-sectional profile of the scratch shown in the top image. The difference in height of the cursors gives one measurement of the layer thickness.

Figure 4.7. and Table 4.7. Plots of thicknesses of TDA and DAD layers against period of electrolysis. Dotted lines are only a visual guide. The minimum number of monolayers was calculated using the calculated length of both TDA and DAD as 1.8 nm, assuming perpendicular attachment to surface.

TDA

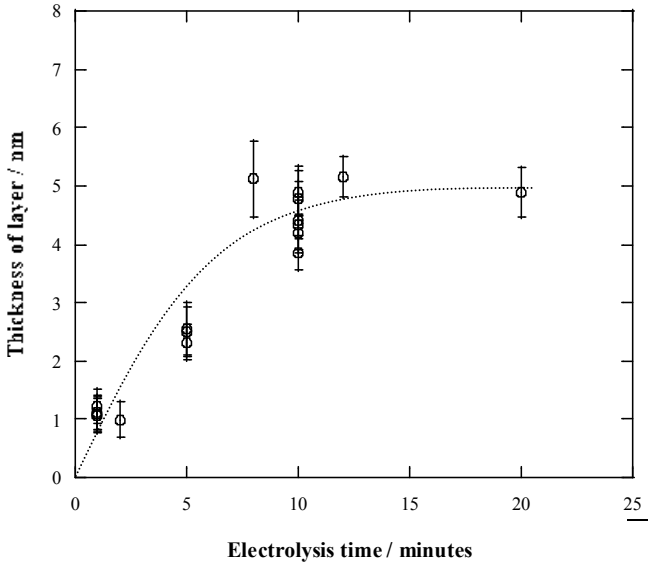

Electrolysis time / minutes	Thickness of layer / nm	Uncertainty / nm [a]	Min. no. of monolayers
1	1.1	0.3	1
1	1.1	0.3	1
1	1.2	0.3	1
1	1.1	0.3	1
2	1.0	0.3	1
5	2.5	0.5	1
5	2.3	0.3	1
5	2.5	0.4	1
8	5.1	0.6	3
10	4.8	0.3	3
10	4.4	0.3	2
10	4.2	0.3	2
10	3.9	0.3	2
10	4.9	0.5	3
10	4.9	0.4	3
10	4.3	0.5	2
12	5.2	0.4	3
20	4.9	0.4	3

[a] Uncertainty includes instrumental inaccuracy and the standard deviation of the measured layer thicknesses.

DAD

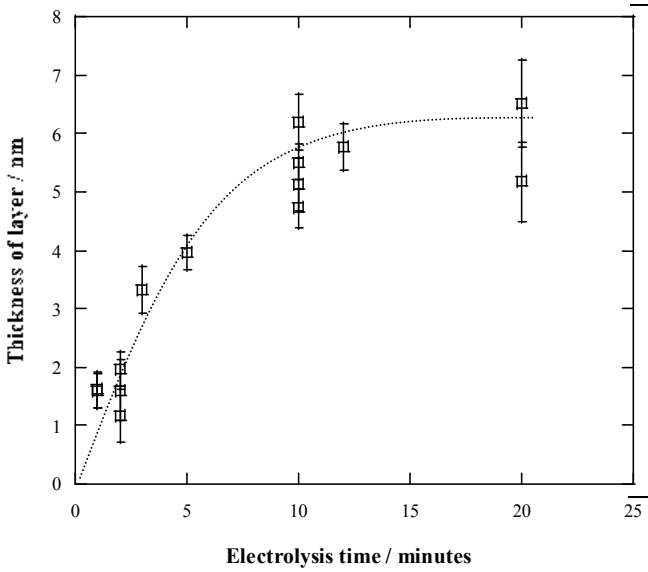

Electrolysis time or no. of scans	Thickness of layer / nm	Uncertainty / nm [a]	Min. no. of monolayers
1 scan [b]	1.0	0.3	1
1 scan [b]	1.5	0.3	1
1 minute	1.6	0.3	1
1 minute	1.6	0.3	1
2 minutes	1.2	0.5	1
2 minutes	1.6	0.5	1
2 minutes	2.0	0.3	1
3 minutes	3.3	0.4	2
5 minutes	4.0	0.3	2
10 minutes	5.5	0.3	3
10 minutes	6.2	0.5	3
10 minutes	5.1	0.4	3
10 minutes	4.7	0.3	3
12 minutes	5.8	0.4	3
20 minutes	6.5	0.7	4
20 minutes	5.2	0.7	3

[a] Uncertainty includes instrumental inaccuracy and the standard deviation of the measured layer thicknesses.
[b] Not included in plot as scans are considered to be not comparable to electrolysis.

A similar mechanism as that detailed in the Introduction for ethylene diamine may be operative for the oxidation of DAD at carbon surfaces. However, as detailed in the above section, only one amine of the DAD modifier is oxidised when the E_f is 1.2 V. Thus, considering the mechanism, it seems more likely that the alternative mechanism where a solution-based modifier is oxidised and attaches to the already attached modifier, to give a multilayer structure, is occurring (Figure 4.8.). For a monoamine, the observation of multilayer formation is very intriguing and has not been previously reported. However, this is not completely unexpected as the electrochemical oxidation process involves the generation of highly reactive solution-based radical species that can attach to surface-bound modifiers. A probable mechanism for the radicals to attach to the already attached TDA modifiers is via H-abstraction from the alkyl chain of the modifier.

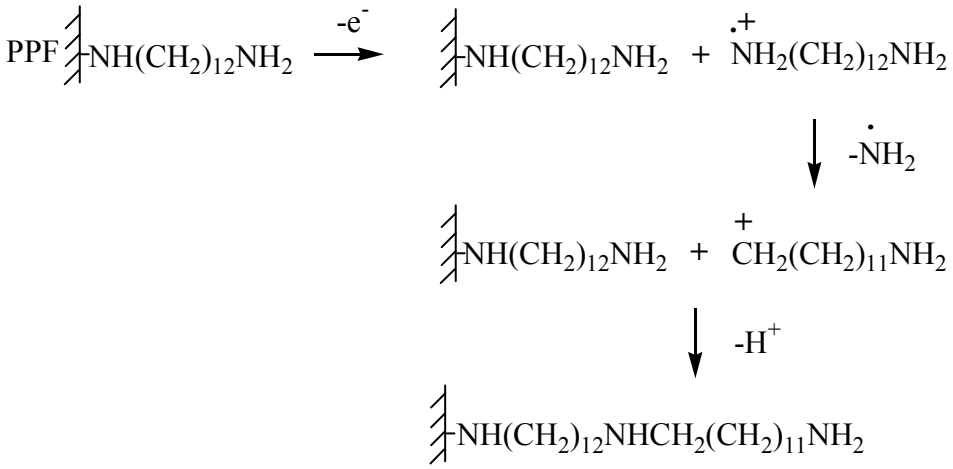

Figure 4.8. Proposed mechanism for multilayer formation of DAD by C-N bond cleavage and elimination of amine from another DAD modifier followed by its attachment to already attached modifiers to yield a linear structure.

Stability of TDA and DAD layers

The experiments described below were aimed at examining the stability of the layers and at providing insights into the structure, orientation and organisation of the layers. The stability of the TDA and DAD layers to 6 months storage and to scanning, soaking and sonicating in various media was examined. The effect of each treatment was determined by recording a FCA CV scan before and after the treatment.

At least three samples of each modifier attached with different electrolysis times were examined before and after 6 months storage in air. The FCA probe scans were similar considering the usual experimental variation and also variation from replacement of the o-ring. This indicates the layers are stable for at least 6 months storage in air.

To examine the effect of applied potential on TDA and DAD layers, modified GC surfaces were subjected to potential scans to progressively more positive or more negative potentials. After each potential scan, the effect on the modifier layer was assessed by obtaining a FCA CV scan. Changes in the TDA or DAD layer were indicated by an increase in the FCA peak currents or an increase in the current at the switching potential (0.5 V) of more than 3 μA. The i_{pa} of the FCA probe response at an as-prepared GC rod was 10 μA, thus an increase of 3 μA was considered large enough to indicate changes had occurred in the layer. All the CV scans obtained after treatment when changes were observed had the appearance of linear diffusion of the probe to the electrode rather than radial diffusion.

GC rods were modified with TDA and DAD by the standard modification procedure with electrolysis time of 10 minutes. The effect of potential was tested in two media:

phosphate buffered saline (PBS) and ACN/0.1 M $[Bu_4N]BF_4$. The TDA or DAD modified GC rod was scanned at 100 mVs^{-1} in PBS to 1, 1.5, 2.0 and -0.5, -1, -1.5, -2.0 V and in ACN/0.1 M $[Bu_4N]BF_4$ to 0.5, 1, 1.5, 2.0 and -0.5, -1, -1.5, -2.0 V. In each case, the initial potential (E_i) was 0 V.

For experiments involving potential scans treatments in PBS, the electrode was washed with MQ water after each scan in PBS or FCA solution. For experiments involving potential scan treatments in ACN/0.1 M $[Bu_4N]BF_4$, the electrode was washed with ACN and then MQ water after each scan in ACN/0.1 M $[Bu_4N]BF_4$, and with MQ water followed by ACN after each scan in FCA solution.

The maximum time between each scan was six minutes. This time period is important in the soaking experiments which are discussed later. Separate samples were prepared for each scanning direction. Hence, four different experiments were carried out with each layer.

Table 4.8. lists the potentials to which the layers can be scanned without apparent changes, i.e. the layers were stable to applied potentials within these ranges. A further 0.5 V increment outside the ranges given, led to changes in the probe scan. PPF samples, modified with TDA or DAD with various electrolysis times, were also stable when scanned within the ranges listed Table 4.8. The underlying GC was stable to -1.5 V in PBS and -2 V in ACN/0.1 M $[Bu_4N]BF_4$ (Chapter 3). Thus, the negative potential affected the layers and not the underlying surface. Some surface degradation could have occurred at positive potentials, as previously discussed. These results are discussed at the end of this section, along with the results of soaking and sonicating experiments.

Table 4.8. Potential ranges within which TDA and DAD layers are stable.

Amine layer	Medium	Potential range / V
TDA	PBS	-1.0 to 2.0
	ACN/0.1 M $[Bu_4N]BF_4$	-1.0 to 1.5
DAD	PBS	-0.5 to 2.0
	ACN/0.1 M $[Bu_4N]BF_4$	0 to 2.0

To establish that the apparent changes in the modifier layers after potential scans outside the ranges listed in Table 4.8. were due only to the effect of potential, the same procedures including all the washing steps were carried out, without applying a potential during the 'scanning' steps. Instead of each of the 'scanning' steps, the GC rods modified with TDA and DAD were soaked in either PBS or ACN/0.1 M $[Bu_4N]BF_4$ for six minutes (six minutes was the maximum time between each scan). Hence, four separate experiments were carried out.

FCA CV scans showed that simply soaking in PBS has no detectable effects on the TDA and DAD layers and soaking in ACN/0.1 M $[Bu_4N]BF_4$ has no effect on the DAD layer. However, when TDA was soaked in ACN/0.1 M $[Bu_4N]BF_4$, the FCA response was observed after the first soaking step. After the second step, the response was similar to an as-prepared GC rod. Therefore, apart from when TDA was scanned in ACN/0.1 M $[Bu_4N]BF_4$, the potential ranges (Table 4.8.) within which the TDA and DAD layers were found to be stable, reflect the effect of potential on the layers.

In order to determine which step in the ACN/0.1 M $[Bu_4N]BF_4$ soaking procedure caused the changes in the TDA layer, the effect of each step on the TDA layers was examined. The steps were: (a) soaking in ACN/0.1 M $[Bu_4N]BF_4$; (b) repeated scanning in FCA solution; and (c) the repeated washing steps. TDA layers (5 mM, electrolysis time 10

minutes) were subjected to experiments as outlined in Table 4.9. Peak current ratios of (i_{pa} after treatment)/(i_{pa} as-prepared GC rod) of FCA probe were average values from at least two different samples.

Table 4.9. Effects on TDA layers by each of the steps in the ACN/0.1 M $[Bu_4N]BF_4$ soaking procedure. Each experiment was performed on a freshly prepared layer.

Experiment	Peak current ratio [a,b]
None	0
Soaked in ACN/0.1 M $[Bu_4N]BF_4$ for 30 minutes	0.29
Scanned 3x in FCA solution	0
Soaked in FCA solution for 30 minutes	0
Immersed in ACN/0.1 M $[Bu_4N]BF_4$ every minute for 10 minutes	0.39

[a] Peak current ratio was (i_{pa} after treatment)/(i_{pa} as-prepared GC rod) of FCA probe.
[b] Uncertainty on peak current ratios is ± 0.05.

From the peak current ratios in Table 4.9, it appears that it is the exposure to ACN/0.1 M $[Bu_4N]BF_4$ that affects the TDA layer. To further investigate the changes in the layer after ACN/0.1 M $[Bu_4N]BF_4$ treatment, TDA-modified PPF was analysed by AFM depth profiling before and after a soaking protocol. A soaking protocol involving fewer steps than the scanning procedures (refer above) was used. The protocol to which the TDA layer (5 mM, electrolysis time 10 minutes) was subjected to was as follows:

Wash with ACN => Soak in ACN/0.1 M $[Bu_4N]BF_4$ for 10 minutes => *Wash with ACN* => *Wash with MQ water* => Scan 10 x in FCA solution => *Wash with MQ water* => *Wash with ACN* => Soak in ACN/0.1 M $[Bu_4N]BF_4$ for 10 minutes => *Wash with ACN* => *Wash with MQ water* => Scan 10 x in FCA solution

Treating a TDA layer on a GC rod to this protocol gave a peak current ratio of (i_{pa} after protocol)/(i_{pa} as-prepared GC rod) of 0.55 ± 0.10, and for a TDA layer on a PPF surface, the maximum peak current ratio of 0.55.

For AFM depth profiling experiments, two scratches were made at each of the three TDA layers and the scratch was imaged near the top and bottom of each of the six scratches before and after the soaking protocol. The changes in thicknesses of the TDA layers on PPF, treated with the soaking protocol, are shown in Table 4.10. Overall, there is a significant variation in the magnitude of changes in layer thickness after the protocol, however, in nearly all cases, the layer thickness increases or remains unchanged, within experimental uncertainty. Most importantly, there is no evidence of significant loss of the layer. All twelve scans of the six scratches captured after the protocol showed that the scratches were filled with debris as illustrated in AFM images of scratches in Figure 4.9. The debris is probably clumps of TDA modifiers that desorbed during the protocol and deposited in the scratch or debris generated from making the scratch. The thickness results are discussed further at the end of this section.

Table 4.10. Thickness changes of TDA layers subjected to the soaking protocol. Thicknesses were measured of the same area of the same scratch before and after the protocol.

Sample	Scratch	Area of scratch	Before protocol	After protocol	Thickness change
TDA 1	1	Bottom	4.7 ± 0.3	5.5 ± 0.3	+0.8
		Top	5.6 ± 0.3	6.3 ± 0.3	+0.7
	2	Bottom	4.4 ± 0.3	5.8 ± 0.3	+1.4
		Top	4.9 ± 0.3	5.6 ± 0.3	+0.7
Average for sample			**4.9 ± 0.5**	**5.8 ± 0.3**	
TDA 2	1	Bottom	4.6 ± 0.3	4.9 ± 0.3	+0.3
		Top	5.0 ± 0.3	4.7 ± 0.3	-0.3
	2	Bottom	4.8 ± 0.3	4.9 ± 0.3	+0.1
		Top	5.1 ± 0.3	5.6 ± 0.3	+0.5
Average for sample			**4.9 ± 0.4**	**5.0 ± 0.3**	
TDA 3	1	Bottom	4.5 ± 0.3	4.0 ± 0.3	-0.5
		Top	4.4 ± 0.3	4.9 ± 0.3	+0.5
	2	Bottom	4.2 ± 0.3	4.2 ± 0.3	0
		Top	4.2 ± 0.3	4.5 ± 0.3	+0.3
Average for sample			**4.3 ± 0.5**	**4.4 ± 0.3**	

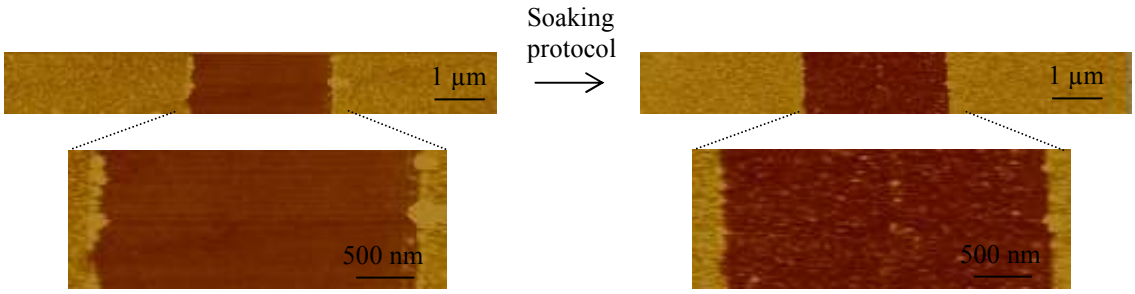

Figure 4.9. AFM images of the bottom area of scratch 2 of sample TDA 1 before and after the soaking protocol, showing debris in the scratch.

Sonication of TDA and DAD layers in various solvents also provided some insights into the stability and composition of the layers. Modifiers were attached to GC rods with an electrolysis time of 5 minutes. The (i_{pa} after modification)/(i_{pa} as-prepared GC rod) for FCA CV scans for both layers were approximately 0.06. Modified GC rods were sonicated in 0.1

M HNO_3, 0.1 M NaOH, MQ water or ACN for 10 minutes and the (i_{pa} after sonication)/(i_{pa} as-prepared GC rod) was estimated. For the aqueous solvents, the rod was rinsed with MQ water after sonication, prior to scanning in FCA solution and for ACN, the electrode was washed with ACN before sonication and ACN then MQ water after sonication, before scanning in FCA solution. At least two freshly prepared amine layers were sonicated in each solvent.

The peak current ratios are detailed in Table 4.11. (Individual measurements are given in Appendix 4.). A CV scan of the FCA probe at a TDA-modified GC rod after sonication in ACN is shown in Figure 4.10. The order of apparent stability of the TDA layers in the solvents (from most to least stable) is NaOH > MQ water > ACN > HNO_3 and for DAD it is ACN > MQ water > NaOH > HNO_3.

Comparing the two different layers in the same solvent, TDA appears to be less affected in HNO_3 and NaOH compared to DAD. In MQ water and ACN, TDA seems to be more affected than DAD. Some of the contribution to the change in current ratio for TDA in ACN is possibly due to the washing steps before and after sonication, as similarly observed with the soaking experiments. No change to the DAD layer was observed in ACN which is consistent with the results from soaking experiments.

The peak current ratio for the TDA layer in ACN in Table 4.11. is similar to when a TDA layer, modified with an electrolysis time of 10 minutes, was soaked in ACN/0.1 M $[Bu_4N]BF_4$ for 30 minutes (Table 4.9.). However, the value of 0.28 ± 0.05 is significantly smaller compared to when the TDA layer, modified with an electrolysis time of 10 minutes, was treated with the 'scanning' procedure in ACN/0.1 M $[Bu_4N]BF_4$ with soaking (refer

above). This suggested that with the 'scanning' procedure in ACN/0.1 M $[Bu_4N]BF_4$ with soaking, that the washing steps in ACN had a significant impact on the TDA layer. This is supported by the peak current ratio after the TDA was immersed in ACN/0.1 M $[Bu_4N]BF_4$ every minute for 10 minutes (Table 4.9.).

Table 4.11. Effect of sonication on TDA and DAD layers. Sonication was for 10 minutes in the respective solvents.

Solvent	TDA	DAD
	Peak current ratio [a]	
None	0.06 ± 0.05	0.06 ± 0.05
0.1 M HNO_3	0.51 ± 0.11	0.73 ± 0.02
0.1 M NaOH	0.12 ± 0.07	0.17 ± 0.06
MQ water	0.21 ± 0.05	0.09 ± 0
ACN	0.28 ± 0.05	0.06 ± 0.05

[a] Peak current ratio was (i_{pa} after sonication)/(i_{pa} as-prepared GC rod) of FCA probe.

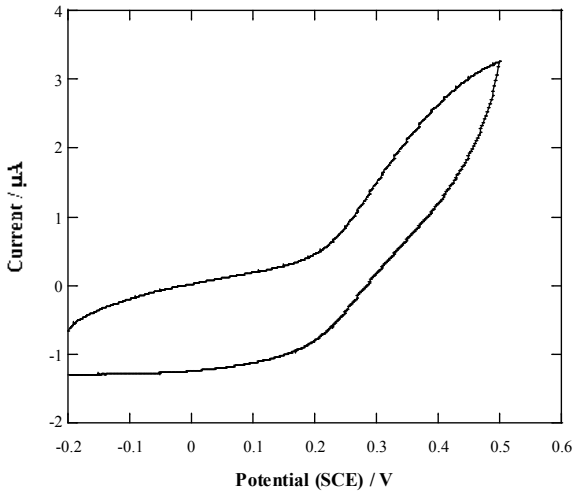

Figure 4.10. FCA CV scans after a TDA layer (5 mM, electrolysis time 5 minutes) was sonicated in ACN for 10 minutes. Scan rate = 100 mVs^{-1}.

Changes to the layers were also monitored over 60 minutes sonication. TDA and DAD layers were sonicated in 0.1 M HNO_3 and TDA layers were sonicated in MQ water.

For HNO_3, the electrode was rinsed with MQ water before and after scanning in the FCA solutions and for MQ water washing was only carried out after scanning. Ice was placed in the sonicator to maintain the temperature of the water in the sonicator at room temperature. From Figure 4.11, when both TDA and DAD layers were sonicated in 0.1 M HNO_3, the peak current ratios of the FCA solution for the DAD layers increases at a faster rate compared to the TDA layers, over the period from 0.5 to 20 minutes. At 60 minutes sonication, both TDA and DAD layers have similar peak current ratios. From Figure 4.12, sonication of the TDA layers in HNO_3 and MQ water caused the peak current ratios of the FCA solution to increase over the 60 minutes. The rate of increase in ratios is faster when sonication was performed in HNO_3 compared to MQ water.

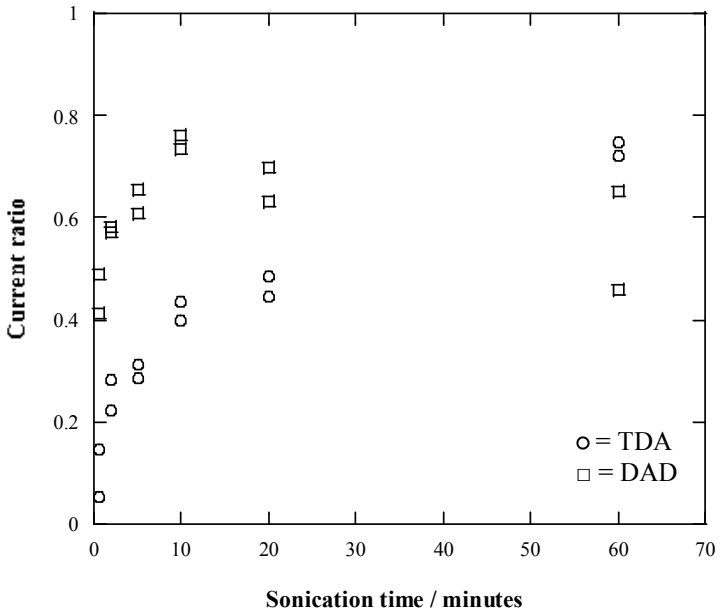

Figure 4.11. Sonication of TDA and DAD layers in 0.1 M HNO_3 over a period of 60 minutes. Current ratio (i_{pa} after sonication)/(i_{pa} as-prepared GC rod) was of the peak or measured at 0.35 V of the FCA response.

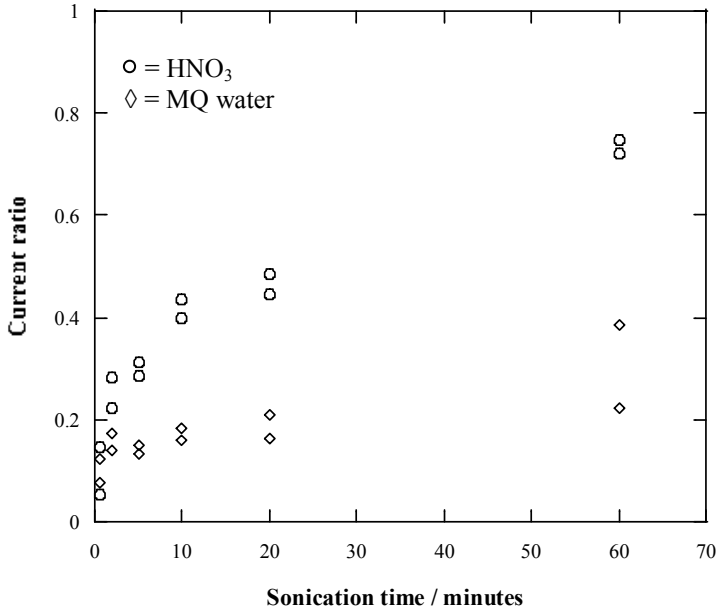

Figure 4.12. Sonication of TDA in 0.1 M HNO_3 and MQ water over a period of 60 minutes. Current ratio (i_{pa} after sonication)/(i_{pa} as-prepared GC rod) was of the peak or measured at 0.35 V of the FCA response.

To summarise the results of the investigations into the effects of potential scans, soaking and sonicating in different media on TDA and DAD layers, a lists of the findings are given as follows:

(i) With increasing modification times, the current ratios of the probe scans recorded after modification decreases and the thicknesses of the layers increases. This suggests that the layers grow laterally and then vertically.

(ii) Using the given modifier concentrations and E_f values, the thickness of layers are larger than the calculated length of TDA and DAD modifiers when the

electrolysis time is > 5 minutes for TDA and > 2 minutes for DAD. Layer thickness increases with electrolysis time, up to 5 – 6 nm.

(iii) From the scanning experiments, the potential ranges within with the TDA and DAD layers are stable in PBS are: -1.0 to 2.0 V for TDA and -0.5 to 2.0 V for DAD and in ACN/0.1 M $[Bu_4N]BF_4$ are: 0 to 2.0 V for DAD.

(iv) From the soaking experiments, exposure of the TDA layer in ACN/0.1 M $[Bu_4N]BF_4$, by soaking and washing, affected the layer. AFM depth profiling experiments performed before and after the soaking protocol showed that overall the thickness of the TDA layer increases or remains the same and that most importantly there is no evidence for significant loss of the layer. Debris was present in scratch after protocol which is possibly clumps of physisorbed modifiers desorbed from the layer.

(v) From the sonication experiments, both TDA and DAD layers are most affected when sonication is carried out in 0.1 M HNO_3. After 60 minutes sonication in 0.1 M HNO_3, both TDA and DAD layers have similar peak current ratios.

(vi) Changes in the probe response after the treatments do not follow changes in layer thickness.

In order to attempt to explain the return of the probe response from scanning, soaking and sonicating these layers, tentative scenarios of changes within the layers are proposed in Figure 4.13. The key point is that the layers can become more ‘open’ to FCA while still remaining attached to the surface as concluded by layer thickness measurements.

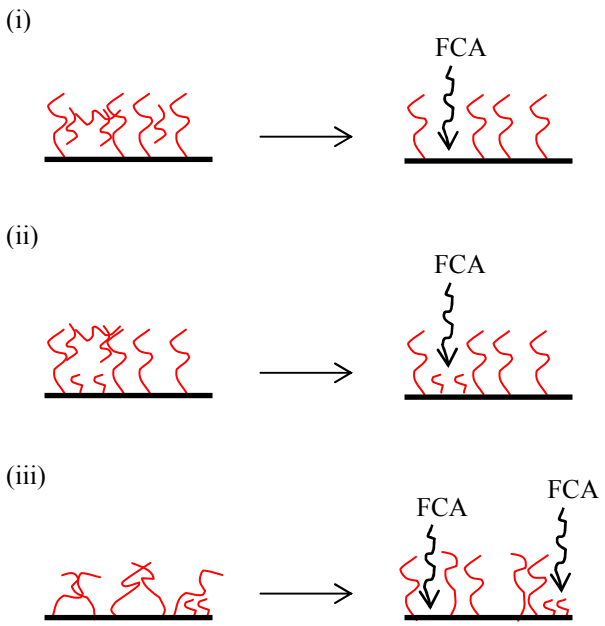

Figure 4.13. Illustrations depicting the possible changes within layer leading to the return of the FCA probe response. (i) Layer where holes are formed due to desorption of physisorbed modifiers. (ii) Layer where thin patches are formed due to desorption of physisorbed modifiers. (iii) Reorganisation of the layer where holes and thin patches are formed.

As proposed in illustration (i) of Figure 4.13, TDA modifiers are physisorbed within the attached layer, most probably via hydrophobic "micelle-like" interactions, and are desorbed during the soaking protocol. The holes are large enough or closely spaced to avoid pinhole (microelectrode) behaviour of the probe but smaller than the lateral detection limit of the AFM (which is 10 nm using the given AFM set-up). (All the CV scans obtained after treatment when changes were observed had the appearance of linear diffusion of the probe to the electrode rather than radial diffusion.) Illustration (ii) proposes the situation where the multilayer formation is inhomogeneous across the layer. During soaking patches

are created that are thin enough to permit the FCA probe response. The thickness of the layer in the patches would have to be smaller than or similar to that using an electrolysis time of 1 minute as the FCA response is not observed at longer electrolysis times. Again, the size of the patches must be smaller than the lateral resolution of the AFM. The third scenario (illustration (iii)) portrays the covalently attached layers as disorganised and during soaking these layers are reorganised and reoriented so that holes or thin patches form allowing FCA probe response. Also, physisorbed modifiers may also desorb as a result of reorganisation and reorientation contributing to the formation of holes and thin patches. A combination of the three scenarios where the desorption of physisorbed modifiers and the reorganisation and reorientation of the layer could possibly be occurring giving rise to holes and thin patches that allow for the FCA response.

From scanning experiments, TDA layers in PBS and DAD layers in PBS and ACN/0.1 M $[Bu_4N]BF_4$, the layers are affected when potentials are scanned in the negative direction but less so at positive potentials (Table 4.8.). This is an interesting result and the underlying reasons are unclear.

For the soaking experiments that mimicked the scanning ones i.e. instead of applying a potential during a scanning step, the layers are soaked for six minutes, the observations appear to depend on the solubility of the modifier in the scanning media. TDA is significantly more soluble than DAD in ACN/0.1 M $[Bu_4N]BF_4$ and both amines are insoluble in PBS. Thus, changes in the FCA probe response are only observed after the TDA layer is exposed to ACN/0.1 M $[Bu_4N]BF_4$.

Solubility and electrostatic repulsions are probable explanations for the outcome of the sonication experiments. The solubility of TDA and DAD modifiers is increased at low pH as the amines are protonated.[28] Hence, the physisorbed modifiers are most easily desorbed when sonication is carried out in HNO_3. Electrostatic repulsions between the protonated amines would also cause the layer to be more 'open'. The changes are more prominent for the DAD layer possibly because there are twice the number of amines that can be protonated and cause desorption and reorganisation. As previously mentioned, the solubility of TDA in ACN/0.1 M $[Bu_4N]BF_4$ is greater than for DAD modifiers which can also account for these sonication results.

When TDA and DAD layers were sonicated in HNO_3 over a period of 60 minutes, the peak current ratio is larger than for the DAD layer than the TDA layer for the majority of the 60 minutes. Several explanations are possible: (i) there is more physisorbed material within the DAD layer compared to the TDA layer; (ii) the DAD modifiers are more soluble in HNO_3 compared to TDA due to twice the number of protonated amines; (iii) there are twice the amount of positive charge for repulsions between protonated DAD modifiers and (iv) the chemically attached DAD modifiers have twice the amount of positive charge within the layer leading to a more 'loosely packed' structure.

Over the 60 minute period during which TDA layers is sonicated in HNO_3 or MQ water there is a continual rise in peak current ratio. This suggests there is a steady constant removal of material, which is greater in HNO_3 compared to MQ water, as predicted by solubility. This suggests that longer sonication times is required to remove all the physisorbed monomers within the TDA layer.

Previous work with carbon surfaces modified via the oxidation of aryl acetates has also shown that the layer was indeed present even though changes in the probe response is observed after negative potential scans. When 1-naphthylmethylcarboxylate and 4-methoxybenzylcarboxylate modifier layers were attached to GC and PPF surfaces, the apparent rate of electron transfer of the $Fe(CN)_6^{3-}/Fe(CN)_6^{4-}$ probe is slow. When negative potentials are applied to the layers, the probe response becomes consistent with faster electron transfer kinetics and the thickness of the layer decreases. However, when positive potentials are applied to the same layer, the probe response remains kinetically fast and the change in thickness of the layer is reversed.[29] A similar study was also carried out with *p*-NB layers on GC and PPF surfaces formed by the reduction of its corresponding aryl diazonium salt. AFM depth profiling experiments shows that the layer was present even though changes in the $Fe(CN)_6^{3-}/Fe(CN)_6^{4-}$ probe response is observed after negative potentials are applied.[30] Reasons for probe changes that are given in these studies are (i) the desorption of physisorbed modifiers, (ii) the expulsion of ions from within the layer which allows for the diffusion of probe molecules into the layer and (iii) the conductivity of the layers was altered by the potential scans.[29,30]

The proposed explanation for changes within the layer (Figure 4.13.) is also supported by x-ray photoelectron spectroscopy (XPS) data from separate experiments where ethylene diamine layers attached to GC plates were soaked in phosphate buffer (PB) which caused the probe redox response to return. The C : N ratios, N_{1s} binding energies and relative signal sizes were very similar for as-modified layers and those exposed to PB

buffer. This suggests that only small changes in the layers are occurring. These experiments were carried out by Amy Cruickshank, Department of Chemistry, University of Canterbury.

Surface concentration of amines in TDA and DAD layers

The surface concentrations of the amines in TDA and DAD layers were estimated by coupling with FCA. Using this approach to estimate amine surface concentrations depends on the yield of the amide bond formation between surface amines and FCA. The surface concentrations of the electroactive coupled Fc group of FCA and hence the amines were estimated from the electrochemistry of the coupled layers. For both the oxidation and reduction peaks of Fc, the peak areas were estimated by fitting curves (using best fit baselines) and integration. The surface concentration was calculated from the average of the four peak area values and the error included all the values for the separate samples.

Coupling of FCA was either carried out in (i) aqueous PB with coupling agent 1-ethyl-3-(3'-dimethylaminopropyl)carbodiimide hydrochloride (EDCI) and activating agent *N*-hydroxysuccinimide (NHS) or (ii) in an organic media dichloromethane (DCM) with coupling agent 1,3-dicyclohexylcarbodiimide (DCC) and base diisopropylethylamine (DIPEA). These procedures are widely used for formation of amide bonds between amino groups and carboxylic functional groups.[5-9] The mechanism for amide bond formation via coupling a carboxylic acid to an amine is detailed in Appendix 0. Coupling of FCA to the secondary amines within TDA and DAD layers is possible, however, is expected to occur at a reduced rate compared to the primary amines within the DAD layers. The redox response of the coupled Fc group was recorded in either an aqueous solution of 0.1 M $NaClO_4$ or

PBS with a scan rate of 100 mVs^{-1}. The potential ranges used for observing coupled Fc was within the range for which these layers are stable (refer Table 4.8.).

Experiments involving analysis of the coupled layer by CV in aqueous $NaClO_4$ solution

The TDA and DAD layers (5 mM, electrolysis time 1 minute) were modified with a short electrolysis time with the intention of grafting a monolayer (Figure 4.7. and Table 4.7.). DCM, a hydrophobic solvent, was selected for the coupling reaction to promote the extended conformation of the hydrophobic TDA and DAD layers. Short electrolysis times and solvent selection was intended to promote reaction between the amines within the layer and FCA. The solution used for CV of the coupled layer was aqueous 0.1 M $NaClO_4$ as poorly hydrated (hydrophobic) anions such as ClO_4^- form ion pairs with the Fc^+ groups, resulting in symmetrical and more distinct CV scans for the coupled Fc redox response.[13,15]

Similar 'blank' experiments were carried out without the coupling agents EDCI or DCC to account for electrostatically attached FCA. In PB (pH 7.4), the carboxylic acid of FCA is partly deprotonated (pK_a FCA (Fe^{2+}) = 6.44)[26] and the amines are expected to be protonated (protonation constant 9 – 10), giving rise to electrostatic interactions. Eight 'blank' experiments were prepared – 2x TDA in FCA/NHS/PB, 2x DAD in FCA/NHS/PB, 2x TDA in FCA/DIPEA/DCM, 2x DAD in FCA/DIPEA/DCM. The replicate CV scans for the same modifier and solution, PB or DCM, were averaged and the surface concentration was calculated. This value was subtracted from the corresponding samples where the coupling agents were present.

Table 4.12. outlines the eight different samples prepared and the electrochemical data extracted from CV scans shown in Figure 4.14. The labels used for each sample are also listed in Table 4.12.

Table 4.12. TDA and DAD layers treated in FCA solution.

Medium	Modifier layer	Coupling solution	Sample label	E_{pa} / V	E^0 / V	ΔE_p / V
Aqueous PB	TDA	FCA/EDCI/NHS	TDAFcAq	0.33, 0.47, 0.65	-	-
	TDA	FCA/NHS	TDAFCAAq	0.29	-	-
	DAD	FCA/EDCI/NHS	DADFcAq	0.29, 0.71	-	-
	DAD	FCA/NHS	DADFCAAq	0.27, 0.54	-	-
Organic DCM	TDA	FCA/DCC/DIPEA	TDAFcOrg	0.50	0.37	0.26
	TDA	FCA/DIPEA	TDAFCAOrg	-	-	-
	DAD	FCA/DCC/DIPEA	DADFcOrg	0.59	0.49	0.20
	DAD	FCA/DIPEA	DADFCAOrg	-	-	-

'-' = not observed or unable to be calculated.

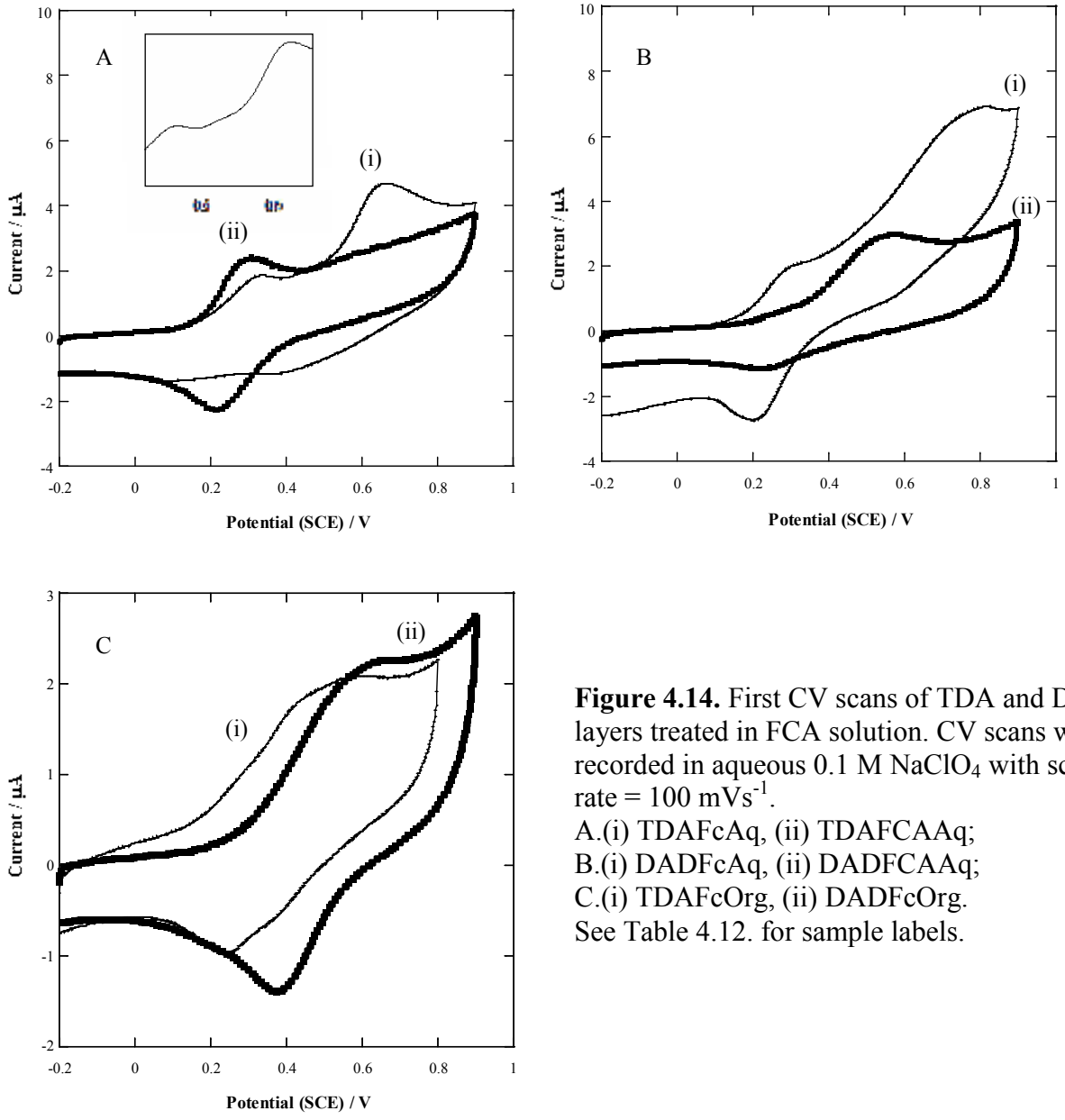

Figure 4.14. First CV scans of TDA and DAD layers treated in FCA solution. CV scans were recorded in aqueous 0.1 M $NaClO_4$ with scan rate = 100 mVs^{-1}.
A.(i) TDAFcAq, (ii) TDAFCAAq;
B.(i) DADFcAq, (ii) DADFCAAq;
C.(i) TDAFcOrg, (ii) DADFcOrg.
See Table 4.12. for sample labels.

(a) Coupling in aqueous medium: TDAFcAq, TDAFCAAq and DADFcAq, DADFCAAq

CV scans for TDAFcAq show multiple oxidation peaks and TDAFCAAq (absence of EDCI) has one oxidation peak (Figure 4.14.A.). From Figure 4.14.B, CV scans of both DADFcAq and DADFCAAq (absence of EDCI) have two oxidation peaks. In addition to the complex CV scans from coupling in aqueous media, the CV scans have poor chemical reversibility. Hence, it is difficult to assign the peaks with certainty. The CV scans for TDAFCAAq and DADFCAAq show that there is a significant contribution from electrostatically attached FCA groups and the response from electrostatically attached species is also observed in CV scans of samples where coupling is carried out with the coupling agents (Figure 4.14.A.(i). and Figure 4.14.B.(i).). It is assumed that additional peaks seen in the presence of EDCI are due to covalent attached Fc groups but the irreversibility of the response makes further analysis of little value. These experiments demonstrate that it is important to carry out 'blank' experiments to differentiate between covalently coupled and electrostatically attached species. One method to avoid electrostatic interactions is to perform the coupling reaction in an organic solution (refer later). Note: it was subsequently pointed out that coupling may not have occurred because the electron withdrawing power of the cyclopentadienyl rings results in the ferrocene succinimide ester being very prone to hydrolysis.[31]

From a different point of view, electrostatic accumulation of FCA at the TDA and DAD layers may give useful information about the surface concentration of the amines. The surface concentration of amines in the TDA layer (sample TDAFCAAq, Figure

4.14.A.(ii).) is estimated to be 1.1 x 10^{-10} mol.cm^{-2} and in the DAD layer (sample DADFCAAq, Figure 4.14.B.(ii).) it is estimated as 1.2 x 10^{-10} mol.cm^{-2}.

(b) Coupling in organic medium: TDAFcOrg, TDAFCAOrg and DADFcOrg, DADFCAOrg

In order to avoid electrostatic attachment of FCA to the amine layers, coupling of FCA was carried out in DCM. For these experiments, analysis of the CV scans is significantly more straightforward. In the absence of the coupling agents, 'blank' samples TDAFCAOrg and DADFCAOrg shows no redox response indicating there is a negligible amount of electrostatically attached FCA.

Figure 4.14.C.(i). shows CV scans of TDAFcOrg and Figure 4.14.C.(ii). of DADFcOrg in aqueous $NaClO_4$ solution. The oxidation peak for TDAFcOrg occurs at a less positive potential than DADFcOrg. A possible explanation for this observation uses the "ion-gated mediated electron transfer" effect. From FCA probe scans at the modified layers (Table 4.6.) and AFM depth profiling (Figure 4.7. and Table 4.7.), TDA layers are deduced to be a less compact and thinner layer than DAD layers. Hence, TDA layers allow penetration of the anion to the Fc group more freely in comparison to the DAD layers. The $E_{1/2}$ for the attached Fc groups in both samples are significantly more positive than for FCA in solution ($E_{1/2}$ = 0.26 V vs. saturated calomel electrode (SCE)) suggesting that the Fc^+ ions are destabilised buried in the alkane, non-polar environment[10] or bound Fc groups are more difficult to oxidise.[32]

For TDAFcOrg, both the oxidation and reduction peaks of the coupled Fc show double peaks and the CV scan is asymmetric with $i_{pa}/i_{pc} \approx 1.8$, ($i_{pc}$ is the cathodic/reduction peak current). These observations suggest that there is partial aggregation of the Fc redox centres into domains with different local or electrochemical microenvironments. Another possibility is that there are interactions between neighbouring electroactive groups during oxidation.[12,13] In the latter case, the splitting of the peaks arise due to repulsive interactions between neighbouring Fc groups. In SAM-based surfaces, a Fc^+ centre is found to increase the oxidation potential of the neighbouring Fc group and even weakly affect the next nearest Fc, via electron hopping between groups.[14] Peaks for DADFcOrg are very broad, with peak width at half height of up to 300 mV. This indicates electron transfer is sluggish or that Fc groups are found in a range of different local and electrochemical microenvironments.[33] Peak separations between oxidation and reduction peaks (ΔE_p) approximate to 200 mV and 260 mV for TDAFcOrg and DADFcOrg, respectively, also indicating slow electron transfer. (ΔE_p for FCA in solution is approximately 80 mV.) Slow electron transfer can be accounted for by the "ion-gated mediated electron transfer" effect.[11]

The coupled Fc surface concentration is $(0.6 \pm 0.3) \times 10^{-10}$ mol.cm^{-2} for TDA layers and $(1.1 \pm 0.1) \times 10^{-10}$ mol.cm^{-2} for the DAD layers. Although the yield of amide bond formation of FCA to surface-bound amine functionalities is not known, it can be assumed that the yields are similar at both TDA and DAD layers. Hence, the surface concentration of coupled Fc and thus of amine groups is approximately twice for the DAD layer compared to the TDA layer. DAD layers have approximately twice the amine surface

concentration of TDA layers as DAD is a diamine and TDA is a monoamine. This suggests that the surface concentration of modifiers TDA and DAD in both layers is similar. The calculated maximum surface concentration for Fc monolayer is 4.5 x 10^{-10} mol.cm^{-2} assuming hexagonal close packing with Fc spheres of diameter 0.66 nm.[10] Hence, the packing of Fc centres is not the limiting factor in determining surface concentrations.

Other observations concerning these samples are that repeated scanning results in a drop in current for all samples apart from the 'blank' samples in the organic solution. The decrease in current is most significant in the first to third scans; from the fourth to tenth, only small changes were observed. An explanation to account for the current drop is that covalently coupled Fc groups are cleaving off during scanning. Control experiments analysed the effect of repeated scanning in aqueous 0.1 M $NaClO_4$ on the TDA and DAD layers. FCA probe scans showed no change after repeat 20 scans over the same potential range. Control experiments were also carried out where TDA and DAD layers were scanned within the same potential range in aqueous 0.1 M $NaClO_4$ or PBS. No peaks were present. A longer coupling time of 96 hours gave a similar surface concentration as for the 24 hour coupling period.

Experiments involving analysis of the coupled layer by CV in PBS solution

Various samples were prepared using different electrolysis times, coupling compounds (O-(7-azobenzotriazol-1-yl)-1,1,3,3-tetramethyluronium hexfluorophosphate (HATU)/DIPEA, EDCI/NHS) and coupling solvents (PB, dimethylformamide (DMF), 1:1

DMF:DCM) with the aim of optimising the coupling of FCA groups. All samples were analysed by CV scans in PBS solutions.

However, despite using different electrolysis times, coupling compounds and coupling solvents to increase the redox response of couple Fc, it became apparent that PBS was not a suitable electrolyte solution and that the electrolyte solution was crucial for the detection of the redox response. These conclusions were further investigated by changing the electrolyte solution from aqueous 0.1 M $NaClO_4$ to PBS. Figure 4.15. shows (i) the 10^{th} scan for DADFcOrg overlaid on (ii) CV scan when solution was changed to PBS. The redox response is barely detectable in PBS. A possible explanation for the poor response is that the anions present in PBS – PO_4^{3-} and Cl^-, are highly hydrated and so are less likely to form ion pairs with the Fc^+ groups[13,15] or that covalently coupled Fc groups are cleaving off during the scan.

The sample was then scanned 20 times in PBS followed by a scan in aqueous $NaClO_4$ to confirm that repeated scanning in PBS caused covalently coupled Fc to be cleaved from the layer. The redox response decreases significantly as depicted in Figure 4.16. Figure 4.16.(i). is the 10^{th} scan for DADFcOrg in aqueous $NaClO_4$ and Figure 4.16.(ii). is the CV scan in aqueous $NaClO_4$ after 20 scans in PBS. The current for the 20 scans in PBS decreased with scan number also indicating loss of Fc groups. Similar experiments were carried out at TDAFcAq and DADFcAq with similar results.

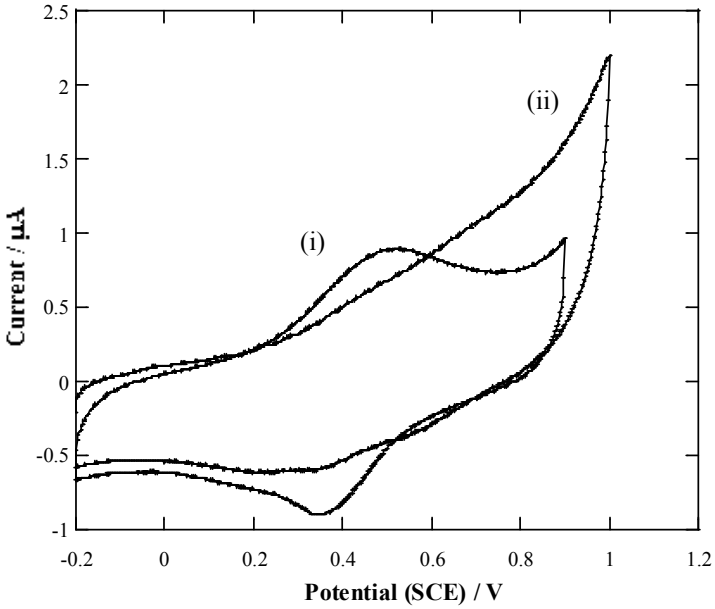

Figure 4.15. CV scans illustrating the influence of electrolyte solution on detecting the Fc response. (i) 10th scan for DADFcOrg in aqueous 0.1 M $NaClO_4$ and (ii) 1st scan in PBS using surface in (i) after electrolyte solution was changed to PBS. Scan rate = 100 mVs^{-1}.

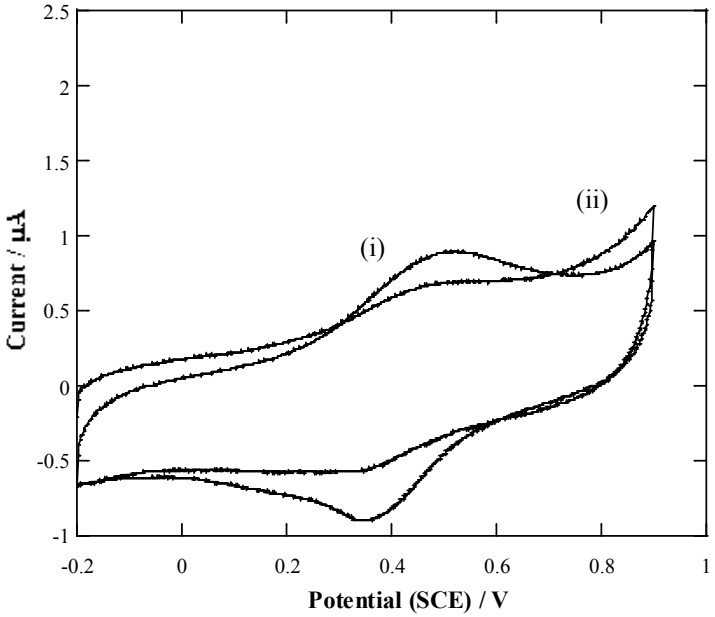

Figure 4.16. CV scans illustrating the effect of repeated scanning in PBS on attached Fc groups. (i) 10th scans for DADFcOrg in aqueous 0.1 M $NaClO_4$ and (ii) 1st scan in aqueous 0.1 M $NaClO_4$ after surface in (i) was subjected to 20 scans in PBS. Scan rate = 100 mVs^{-1}.

4.3.5. HA and TGD

A series of experiments were carried out to compare the layers formed by the oxidation of HA and TGD. HA is a monoamine and is relatively hydrophobic whereas TGD is a diamine and is relatively hydrophilic. Similar explanations for TDA (monoamine) and DAD (diamine) modifiers can be used here to explain the behaviour of HA and TGD.

Attachment and analysis by AFM depth profiling

Amine oxidation

From CV scans in Figure 4.2, the initial scan for HA gives a chemically irreversible broad peak at $E_{pa} \approx 1.1$ V which is assigned to a one-electron amine oxidation. Similar electrochemical behaviour is observed for TGD with regards to the shape of the peak, the current for amine oxidation and the current decrease in the final CV scan after an electrolysis time of 10 minutes. However, the oxidation of TGD occurs at 100 mV more positive at approximately 1.0 V. This observation was also seen with TDA and DAD and similar comments are relevant for HA and TGD.

Another observation when comparing monoamine (HA) and diamine (TGD) oxidation CV scans is that the peak currents are different. However, the peak current for the diamine (TGD) is not twice that for the monoamine (HA) as expected if the electrochemical equivalent amines of TGD, 11 atoms apart, are non-interacting. Thus, in order to observe the oxidation of the other amine of TGD, the potential was scanned out to 2 V. A peak was present at 1.85 V. This suggests that the two amines of TGD, 11 atoms apart, are interacting and the oxidation of one shifts the oxidation of the other to a more positive potential. This

is analogous to the electrochemical behaviour of DAD. The standard modification process used E_f of 1.2 V, thus presumably only one amine of the TGD formed a C-N bond at surface. The attachment of one amine of the diamine modifier to the surface is consistent with other reports.[23,24]

Probe scans after modification and analysis by AFM depth profiling

FCA probe scans were used to investigate the blocking properties of the layer. Table 4.13. gives the data extracted from the FCA probe CV scans and the thicknesses, as measured by AFM depth profiling, for the HA and TGD layers formed using specific modification conditions (modifier concentration, electrolysis time or number of scans). The E_{pa} and peak current ratios from FCA probe scans were averaged values from at least three samples. Figure 4.17. shows typical FCA probe CV scans at the two layers.

From data in Table 4.13, using a higher concentration of HA modifier increases the blocking behaviour of the layer when the electrolysis time is 10 minutes. Using a modifier concentration of 200 mM, the FCA CV scan after modification shows no peaks which is consistent with the presence of a compact, blocking and insulating surface layer of 'limiting' thickness that inhibits electron transfer between the solution probe and the carbon surface.

As the electrolysis time or number of scans is increased for the attachment of TGD layers, the response of the probe although subtle suggests a more blocking layer is attached (Table 4.13.). Drastic changes are not observed presumably because there are electrostatic interactions between the protonated amines of TGD and the anionic FCA probe, as

previously discussed for the DAD layers. The probe response caused by the electrostatic interactions between the probe and layer is less pronounced in longer diamines such as DAD and PGD (refer later). This is probably because the electrostatically attached FCA groups are further away from the carbon electrode with the long chain modifiers and the electron transfer is slowed causing the redox response to decrease. Additionally, the DAD and PGD layers are less hydrophilic compared to TGD layer (refer water contact angles), thus less water is trapped within those layers. This would result in more 'tightly packed' layers, helping to also reduce the probe responses.

Table 4.13. E_{pa} and peak current ratios of FCA CV scans obtained at HA and TGD-modified carbon surfaces and the thicknesses of these layers on PPF. Electrochemical data are obtained from different samples to layer thickness data. The minimum number of monolayers was calculated using the calculated length of HA as 1.0 nm and TGD as 1.5 nm, assuming perpendicular attachment to surface.

Carbon surface	**[amine] / mM**	**Electrolysis time or no. of scans**	**E_{pa} of probe after modification [a] / V**	**Peak current ratio [b,c]**	**Thickness / nm (no. of samples)**	**Min. no of monolayers**
GC or PPF	none	none	0.30	none	none	none
			HA			
PPF	5	10 minutes	0.46	0.55	3.0 ± 0.3	3
PPF	10	10 minutes	Not measured		2.9 ± 0.3	3
GC plate	5	10 minutes	0.44	0.63	Not measured	
GC plate	200	10 minutes	No peak	0	Not measured	
			TGD			
PPF	5	1 scan	0.33	1.00	1.1 ± 0.4 (2)	1
PPF	5	3 scans	0.33	1.00	Not measured	
PPF	5	2 minutes	0.33	0.97	3.4 ± 0.7 (2)	2
PPF	5	10 minutes	0.35	0.77	3.0 ± 0.8 (3)	2
GC plate	200	10 minutes	0.37	0.80	Not measured	
PPF	5	20 scans	FCA response not recorded		2.5 ± 0.4 (2)	2

[a] Uncertainty on E_{pa} is ± 0.02 V.
[b] Peak current ratio was (i_{pa} after modification)/(i_{pa} as-prepared carbon surface) of FCA probe.
[c] Uncertainty on peak current ratios is ± 0.05.

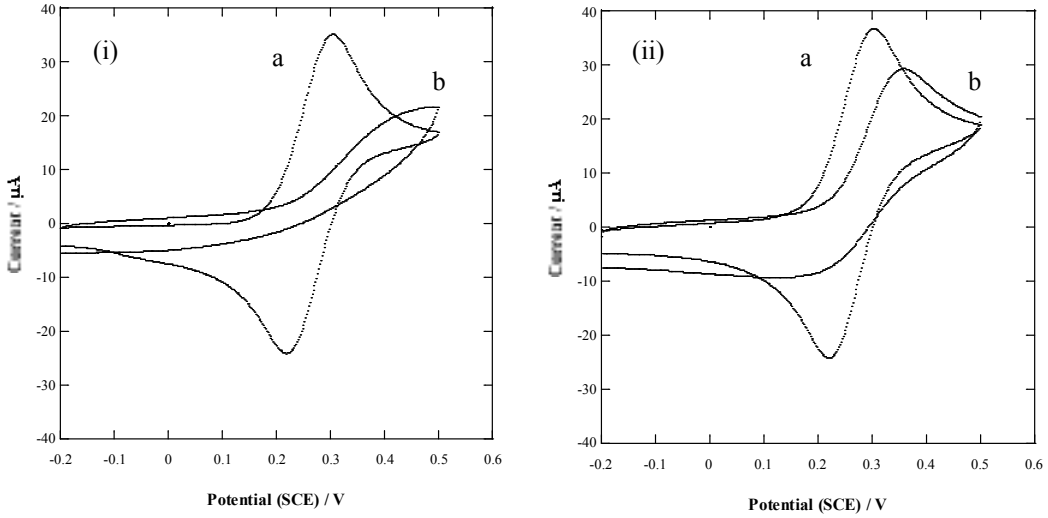

Figure 4.17. FCA CV scans before (a) and after (b) modification of PPF surfaces with (i) HA and (ii) TGD layers. Both layers were attached using 5 mM modifier solutions and an electrolysis time of 10 minutes. Scan rate = 100 mVs^{-1}.

The FCA CV scans at the TGD layers exhibit very low reduction peak currents. This is attributed to the positive charge on the Fc^{+} centre of FCA (from its oxidation) compensating the negative charge on the carboxylic acid functionality giving FCA a net zero charge. The net zero charge causes the electrostatically accumulated probe to dissociate from the layer giving lower current for reduction than oxidation (Figure 4.17.).

Considering the thicknesses of the TGD layers going from 1 scan to a 2 minutes electrolysis, the thickness of the layer increases and the response of the probe indicates that a more blocking layer is present. When increasing the electrolysis time from 2 to 10 minutes, the thickness is similar for both electrolysis times; however, the probe response indicates a more blocking layer for the 10 minute electrolysis. These observations suggests that the layer growth is initially vertical where modifiers attach to surface-bound modifiers

followed by lateral growth where modifiers attaches to unmodified areas and the surface density of the modifiers increases.

From Table 4.13, the thickness of the HA layer (5 mM, electrolysis time 10 minutes) is 3.0 ± 0.3 nm corresponding to three HA molecules (assuming they were attached perpendicular to the surface). This thickness is not increased when the modifier concentration is doubled. As for TDA, multilayer formation with the monoamine HA is interesting and assumed to be a result of radical generation during amine oxidation. Multilayers of the diamine TGD are formed when the electrolysis time is 2 minutes and longer. The mechanism for multilayer formation of TGD is assumed to be the same as for DAD.

Coupling of FCA to TGD layers

FCA was coupled to the amines of the TGD layers (5 mM, electrolysis time 10 minutes) on PPF surfaces with the intention of estimating the surface concentration of amines in the TGD layer as carried out for TDA and DAD layers.

After coupling, the redox response of the attached Fc group was recorded in PBS between -0.2 and 0.6 V with a scan rate of 100 mVs^{-1}. Control experiments showed that when a TGD layer was scanned in PBS between -0.2 and 0.6 V no peaks were observed.

Figure 4.18. shows the first CV scan of FCA coupled to TGD. From the CV scan, it appears the coupling of FCA to the TGD layer is successful and that the electrochemistry of coupled Fc can be observed in PBS. However, when the experiment was repeated without the EDCI and NHS, similar sized peaks (within 10%) were present at identical potentials.

This suggests that the response observed in Figure 4.18. can be attributed to electrostatically attached FCA.

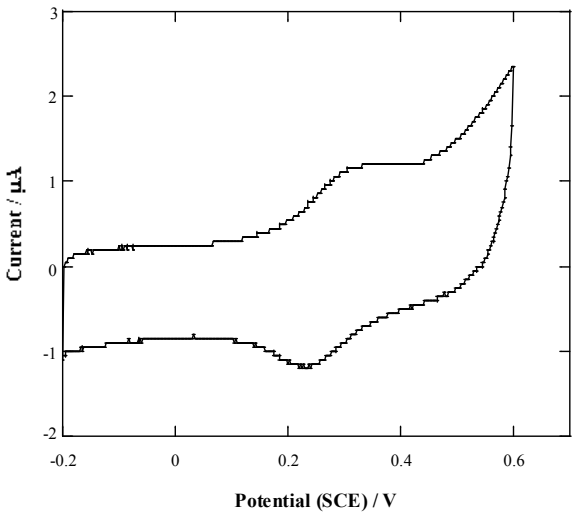

Figure 4.18. First CV scan of a TGD layer treated in a FCA coupling solution. CV scan was recorded in PBS with scan rate = 100 mVs^{-1}.

TGD layers used in work described in other chapters

The TGD layers are used in work described in the other chapters for the adsorption of protein (Chapter 6), adhesion of NPs (Chapter 7) and molecular patterning (Chapter 8 and 9a).

As discussed in Chapter 8, in order to investigate the effect of second modification on already attached TGD layers, layers were subjected to various potentials and also to modification with another modifier. In summary, the TGD layers (5 mM, electrolysis time 10 minutes) are unchanged when the potential was scanned to 1.3 V in ACN/0.1 M $[Bu_4N]BF_4$, however, changes in the peak current ratio of (i_{pa} after scan)/(i_{pa} as-prepared

GC rod) is observed when the electrolysis time for modification was 2 minutes. Negative potential scans in ACN/0.1 M $[Bu_4N]BF_4$ affect the TGD layers.

As part of experiments detailed in Chapter 9a, NBC was coupled to TGD layers (5 mM, electrolysis time 2 minutes) during a 2 hour coupling period in which TGD-modified PPF surfaces were immersed into 0.1 NBC in DMSO. Coupling also occurred with a shorter coupling time of 10 minutes with a 0.5 M NBC in DMSO solution. Evidence for the coupling is provided by water contact angle measurements (refer above), assembly of citrate-capped gold NPs and the reduction of the *p*-nitrophenyl group in 0.25 M H_2SO_4 (Chapter 7). The stability of the TGD layers to immersion in DMSO for 2 hours was verified using water contact angle measurements (refer above) and the assembly of citrate-capped gold NPs. These observations are the same for an as-modified TGD layer.

4.3.6. PGD

PGD is a polymeric diamine and a significantly larger molecule than the other amine modifiers.

Attachment

Amine oxidation and probe scans after modification

For PGD, the conditions for its attachment including E_f, electrolysis time, concentration and rate of mass transport were varied and their effect on the resulting layer was monitored using CV scans of FCA.

The determination of E_{pa} for PGD was not straightforward as three oxidation peaks at 0.4, 1 and 1.5 V were present. To determine which oxidation process leads to attachment, the potential was held at 0.1 V increments between 0.6 – 1 V for 10 minutes ([PGD] = 50 mM). The FCA CV scan showed little change. The peak at 0.4 V was thus attributed to an impurity that does not attach to the surface. When E_f was > 1 V, the FCA CV scans after modification indicated that a blocking layer of PGD was attached to the surface. Hence, the second peak was assumed to be the amine oxidation leading to attachment, and E_f = 1.3 V was used for modification.

The relationship between blocking behaviour of the layer and electrolysis time was monitored by the decrease in FCA peak current ratio of (i_{pa} after modification)/(i_{pa} as-prepared GC rod), as detailed in Table 4.14. After an electrolysis time of 8 minutes using [PGD] = 50 mM, the peak current ratio was close to 0. As for the DAD layers, pinholes or electrostatically attached FCA are possibly present in the PGD layer modified with electrolysis times of 5, 8 and 10 minutes, giving rise to the small current ratios. Figure 4.19. shows FCA CV scans before and after modification with electrolysis time of 10 minutes.

PGD is a longer diamine compared to DAD, thus the diminishment of the current ratio with modification time was expected to be faster for PGD compared to DAD (Table 4.6.). However, with PGD the current ratio is only significantly reduced when the electrolysis time is longer than 2 minutes whereas with DAD the current ratio is very low after 1 modification scan. A possible explanation for this is that the PGD layer is more hydrophilic compared to the DAD layer (refer water contact angles) and the higher number

of water molecules trapped in the PGD layer makes it more 'loosely packed' allowing for the FCA probe response.

Table 4.14. Current ratios of FCA CV scans obtained at PGD-modified GC rods prepared using different modification times.

Electrolysis time	Current ratio [a] at peak [b] or at 0.35 V
2 minutes	0.47 [b]
5 minutes	0.16
8 minutes	0.06
10 minutes	0.06

[a] Uncertainty on current ratios of (i_{pa} after modification)/(i_{pa} as-prepared GC rod) is ± 0.05.

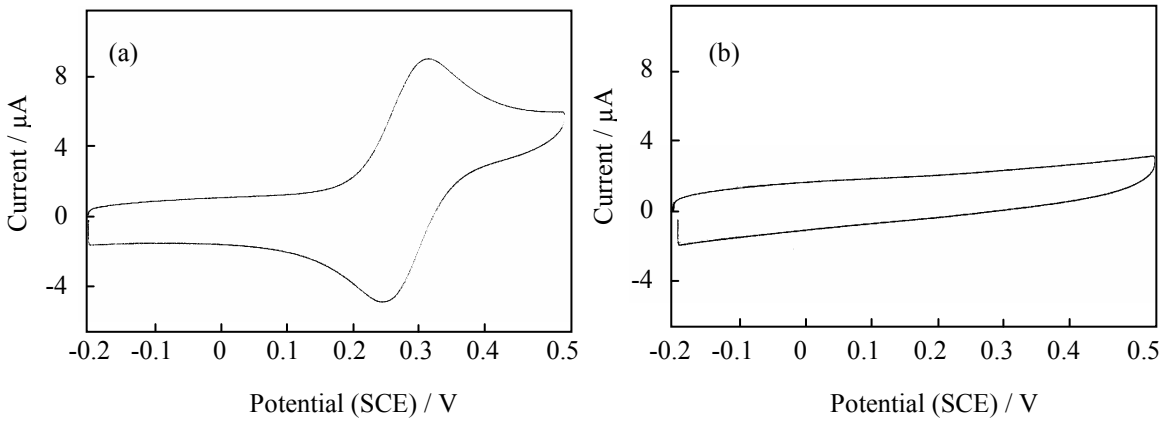

Figure 4.19. FCA CV scans before (a) and after (b) modification of a GC rod with PGD. Layers were attached using a 50 mM modifier solution and an electrolysis time of 10 minutes. Scan rate = 100 mVs^{-1}.

Formation of modified surfaces is controlled by mass transport of the modifier and/or electron transfer to the modifier. To briefly investigate these processes, modification of PGD was carried out in unstirred and stirred solutions, and with different modifier concentrations. PGD is a relatively large molecule and so is expected to have a low

diffusion coefficient compared to the other amine modifiers. The low diffusion coefficient should make the diffusion control time domain longer and easier to detect than with the smaller amines.

Two PGD concentrations, 50 and 100 mM, and the electrolysis times of 2, 5 and 10 minutes for each concentration were utilised for modification in unstirred solutions. A PGD concentration of 50 mM and electrolysis times of 2, 5 and 10 minutes were used for modification in stirred solutions. The blocking properties of the PGD-modifier layer at GC rods were observed by FCA probe scans.

Figure 4.20. shows the current ratios from the CV scans of FCA at PGD-modified surfaces. The amount of growth of the layer is assumed to be approximately inversely proportional to the current ratio. At the short electrolysis times (up to 2 minutes), the rate of growth of the layer appears to be mass transport controlled because a more blocking layer has formed with the higher modifier concentration and is also increased by solution stirring. After the 5 minutes electrolysis, the differences in current ratios are less marked suggesting that electron transfer control has become important. After 10 minutes electrolysis, the layers are essentially the same indicating that electron transfer has determined the amount of growth of the layer at longer electrolysis times.

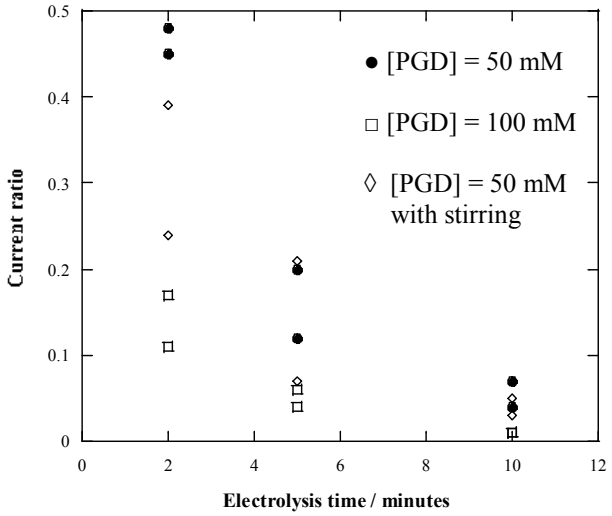

Figure 4.20. Graph showing the current ratios of FCA CV scans obtained at PGD-modified GC rods prepared using different modifier concentrations, electrolysis times and with stirring. Current ratio (i_{pa} after sonication)/(i_{pa} as-prepared GC rod) was of the peak or measured at 0.35 V of the FCA response.

Based on these results, the PGD layers used in work discussed in the following chapters are prepared with E_f = 1.3 V, electrolysis time of 10 minutes, [PGD] = 50 mM and without stirring.

Stability of PGD layers

To investigate the stability of the PGD layers, modified GC rods with PGD attached (50 mM, electrolysis time 10 minutes) was sonicated in MQ water for 10 minutes. The FCA peak current ratio of (i_{pa} after sonication)/(i_{pa} as-prepared GC rod) was 0.3 indicating that some changes within the layer had occurred, however, the bulk of the layer remained.

Analysis by AFM depth profiling

The thickness of the PGD layers (50 mM, electrolysis time 10 minutes) was 5.1 ± 0.3 nm measured using AFM depth profiling. This indicates that the PGD modifiers are in a folded, collapsed configuration as the estimated length of a PGD modifier was > 15 nm.

4.3.7. NPEA

NPEA is an aromatic amine in contrast to the other amines discussed above and it has an electrochemically active *p*-nitrophenyl group. From the reduction of the *p*-nitrophenyl functionality, the surface concentration of the NPEA modifiers in the layer can be estimated.

Neutralisation of amine chloride salt

The NPEA modifier was purchased as the ammonium chloride salt and the amine was prepared by neutralisation of the salt. The ^{1}H NMR spectrum of the NPEA modifier showed a broad signal at δ 1.95 ppm which was assigned to the ^{1}H's on the amine and indicated that neutralisation of the amine chloride salt had occurred, yielding NPEA. This signal was absent in the starting yellow salt. All other signals present in the starting material were present in the NPEA spectrum at very similar chemical shifts.

Attachment

Amine oxidation and probe scans after modification

Figure 4.2. shows the CV scan obtained for oxidation of NPEA. In the initial scan, there are three chemically irreversible peaks at 0.4, 0.9 and 1.2 V. The peak at 1.2 V is assigned to the one-electron oxidation of the amine and the smaller peaks at 0.4 and 0.9 V are attributed to impurities in the NPEA modifier. To investigate this, 5 mM of the ammonium chloride salt was dissolved in ACN/0.1 M $[Bu_4N]BF_4$ and the potential was scanned to 1.3 V at a GC rod. A sharp oxidation peak was observed at 0.8 V. This suggested that the peak at 0.9 V in the amine solution may be due to impurities in the ammonium chloride salt. The peaks at 0.4 and 0.9 V were observed in all samples of NPEA prepared from the same sample of ammonium chloride salt.

When preparing the layers, a CV scan was recorded in the modifier solution after electrolysis. Electrolysis times were 1, 2, 10, 15, 20 and 25 minutes. The current of the final CV scans decreased with increasing electrolysis times. After holding at 1.3 V for 10 minutes or longer, no peak was seen in the final scan and the current was low.

From the FCA CV scans recorded after modification, a decreased FCA response was observed for electrolysis times of 1 and 2 minutes and a blocking layer was achieved after 10 minutes electrolysis.

Electrochemical reduction of NPEA layers

The reduction of the *p*-nitrophenyl group of NPEA to amino derivatives was carried out in either (i) 0.1 M H_2SO_4 or (ii) in ACN/0.1 M $[Bu_4N]BF_4$ followed by 0.1 M H_2SO_4.

For (ii), the electrochemical reduction involved two scans in ACN/0.1 M $[Bu_4N]BF_4$ from -0.5 to -2 V, and two scans in 0.1 M H_2SO_4 from 0.6 to -1 V. The first CV scan for the reduction in ACN is shown in Figure 4.21.(i). and the two scans for reduction in acid are depicted in Figure 4.21.(ii).

Obtaining a well-defined peak for the reduction of *p*-nitrophenyl group attached to PPF surfaces in ACN/0.1 M $[Bu_4N]BF_4$ was challenging. As seen in Figure 4.21.(i), two reduction peaks are present. The second reduction peak is assigned to the one-electron reduction of *p*-nitrophenyl to a nitrophenyl radical anion (Equation 4.1.) and its corresponding oxidation peak appears at -1.5 V. The prepeak observed at -1.4 V is consistently present for all samples even with prolonged degassing with $N_{2(g)}$ to remove O_2. However, when the process was repeated at a GC rod with NPEA attached with an electrolysis time of 10 minutes, the prepeak was not present. The surface concentration calculated for this GC rod sample was $(18.2 \pm 0.5) \times 10^{-10}$ mol.cm^{-2} which was similar to PPF with NPEA attached with same electrolysis time (refer later Figure 4.25. and Table 4.18.). This suggests that the prepeak observed with PPF samples is not due to NPEA modifier. It is possible that with the different cell set-ups it was harder to completely remove traces of O_2 from the PPF surfaces.

As shown in Equation 4.1, the reduction is expected to be reversible. However, the reduction process is hardly reversible which may be due to protonation of the radical anion by residual water.[34]

The second and third scans of the reduction in ACN are not shown as similar peaks were present as for the first scan. However, the current of the peaks of the later scans were smaller, consistent with the poor reversibility of the reduction process.

4.1. $$]\text{-}NH_2CH_2CH_2ArNO_2 \rightleftarrows]\text{-}NH_2CH_2CH_2ArNO_2^{\bullet -}$$

When the NPEA layer was scanned in acid, the expected CV scans for reduction in acid of *p*-nitrophenyl group to amino derivatives in a protic solvent were observed.[27,35] Figure 4.21.(ii). shows the CV scans of a NPEA layer (5 mM, electrolysis time 20 minutes) in acid and the processes (Equation 4.2, 4.3. and 4.4.)[25,27,35] corresponding to the peaks are also shown. As labelled in Figure 4.21.(ii), peak 1 is assigned to the reduction of NO_2 to NH_2 and NHOH, peak 2 corresponds to the oxidation of NHOH formed in peak 1 to NO. In the second scan, peak 3 is attributed to the reduction of NO back to NHOH and peak 2 is assigned to the oxidation of the NHOH to NO. The CV scans were terminated at a potential more positive than the oxidation of NHOH to NO, thus the amino derivatives that are present at the reduced surface should only be NH_2 and NO. However, considering the inequality of peaks 2 (1^{st} scan) and 3 in the CV scans, it appears that the NHOH derivative is more chemically stable than NO and it may be assumed that the NHOH derivative is the more stable species of this redox couple under ambient conditions. Hence, NH_2 and NHOH (and possibly NO) groups should be present at the reduced NPEA layer.

4.2. $]\text{-}NH_2CH_2CH_2ArNO_2 + 2e^- + 2H^+ \longrightarrow]\text{-}NH_2CH_2CH_2ArNO + H_2O$

4.3. $]\text{-}NH_2CH_2CH_2ArNO + 2e^- + 2H^+ \rightleftharpoons]\text{-}NH_2CH_2CH_2ArNHOH$

4.4. $]\text{-}NH_2CH_2CH_2ArNHOH + 2e^- + 2H^+ \longrightarrow]\text{-}NH_2CH_2CH_2ArNH_2 + H_2O$

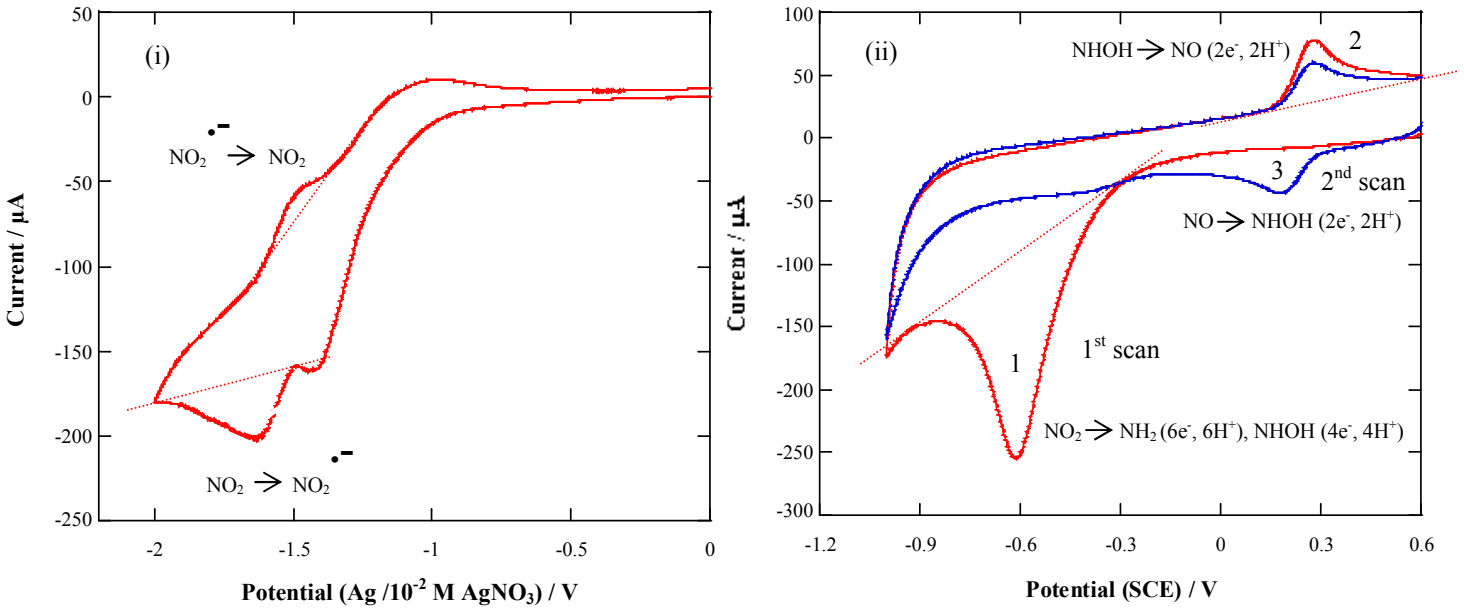

Figure 4.21. CV scans of the reduction of *p*-nitrophenyl groups of the NPEA layers attached to PPF surfaces in (i) ACN/0.1 M $[Bu_4N]BF_4$ and/or (ii) 0.1 M H_2SO_4. The dotted lines represent the linear baselines used in LinkFit for the surface concentration estimations. NPEA layers were modified with a 5 mM modifier solution and an electrolysis time of 20 minutes. Scan rate = 100 mVs^{-1}.

Probe scans at reduced NPEA layers

After the *p*-nitrophenyl group was reduced in either (i) 0.1 M H_2SO_4 or (ii) in ACN/0.1 M $[Bu_4N]BF_4$ followed by 0.1 M H_2SO_4, the FCA CV scans showed responses similar to those at as-prepared PPF. The return of the response is assumed to be due to the generation of surface species and defects during reduction that allows for electrostatic

interactions with FCA giving a response.[25] The surface species generated are positively charged and FCA is negatively charged (deprotonation of the acid), at pH 7.4 in PBS. This is an indication that amino derivatives formed as a result of the reduction processes (Equations 4.2, 4.3. and 4.4.) and led to the return of the probe response that was slowed or inhibited at the as-prepared NPEA layer. Another possible explanation is that during the reduction processes, physisorbed NPEA modifiers desorb or reorganise, creating holes and thin patches that allow the FCA response. This is expected to occur in similar processes as those proposed for the TDA and DAD layers (Figure 4.13.).

Analysis by AFM depth profiling

The significant change in the probe response after the NPEA layer was reduced (refer above) led to investigations using AFM depth profiling before and after the layer was reduced. The NPEA layers, attached with different electrolysis times, were reduced in either (i) 0.1 M H_2SO_4 or (ii) in ACN/0.1 M $[Bu_4N]BF_4$ followed by 0.1 M H_2SO_4.

Figure 4.22. and Table 4.15. give the layer thicknesses for NPEA layers prior to electrochemical reduction in acid. The maximum thickness of the NPEA layer is approximately 8 nm which corresponds to a minimum of ten NPEA monolayers with calculated length of 0.8 nm (NO_2 group rather than NH_2) and assuming the groups are attached perpendicular to the surface. The mechanism for multilayer formation is expected to be similar for the reduction of diazonium salts where the subsequent modifier attaches in the *ortho* position of the already attached modifier.[36,37] With NPEA, the maximum thickness is higher compared to the aliphatic layers (approximately 6 nm) possibly due to

ease of electron transport over greater distances through the electron-rich aryl rings allowing further growth of the layer.

When the thickness of the layer was measured using the same scratch before and after the reduction process in acid, the layer thickness was found to decrease after reduction by 29% on average, with a range between 21 – 41% (Figure 4.22. and Table 4.15. (step 1 to 2)). Other workers have also observed a decrease in layer thicknesses during electrochemical reductions of nitroazobenzene[35] and *p*-NB[30] layers in acid (H_2SO_4). In their work, the shrinkage is partially reversed by treatment in ACN. Hence, the behaviour is attributed to ion-solvent induced shrinking and swelling from the replacements of electrolyte present in the layers. For this behaviour to occur, the layers formed are 'loosely packed' with free volume.[35] Therefore, with the NPEA layers, attempts were made to reverse the shrinking by either: (i) cycling repeatedly (20 scans) from 0 to 0.4 V in ACN/0.1 M $[Bu_4N]BF_4$ and/or (ii) subjecting the layer to the modification conditions without the modifier. The changes in the layer thicknesses after these steps are shown in Figure 4.22. and Table 4.15. (steps 3 and 4). However, both these treatments causes further shrinkage of layer between 11 – 32% and the shrinkage caused by reduction in acid is not reversible. Thus, possible explanations for the decrease in NPEA layer thickness induced by reduction in acid are that electrolyte ions are replaced during acid reduction and this process is not reversible or that there is significant loss of the layer during the reduction in acid. The reasons for the further shrinkage of 11 – 32% after the treatments are also unclear. It is noted that for scratch 1 and 2 for the NPEA layer modified with an electrolysis time of 25 minutes, the amount of shrinkage induced by the reduction in acid and the repeated

scanning in ACN/0.1 M $[Bu_4N]BF_4$ varies between the two scratches. This suggests that the shrinkage is inhomogeneous within a layer.

Figure 4.22. and Table 4.15. Changes in layer thickness with reduction in acid and attempts to reverse the shrinkage caused by reduction in acid.

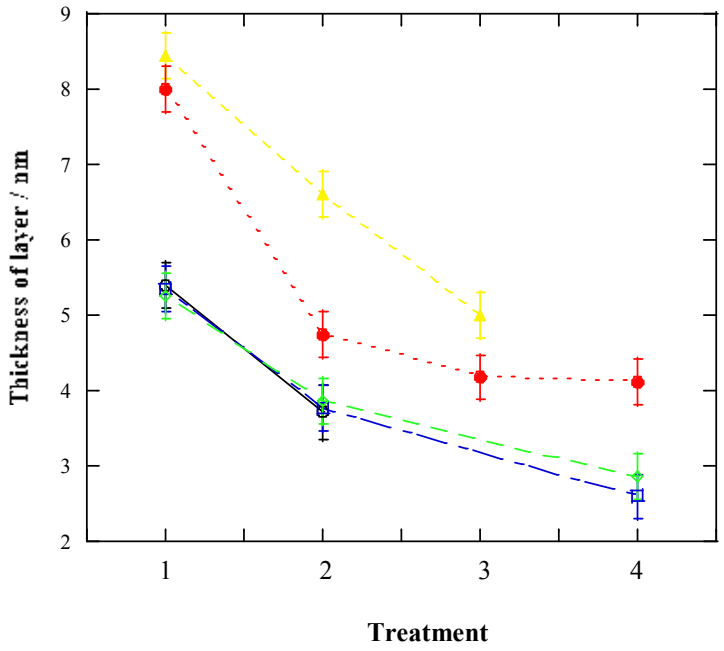

Electrolysis time 15 minutes
○ Scratch 3
Electrolysis time 15 minutes
□ Scratch 1
◊ Scratch 2
Electrolysis time 25 minutes
Δ Scratch 1
● Scratch 2

Treatment

1 = as-modified NPEA layer

2 = NPEA layer reduced in acid

3 = NPEA layer after repeated cycling in ACN/0.1 M $[Bu_4N]BF_4$

4 = NPEA layer after subjected to modification conditions without the modifier

Electrolysis time / minutes	Sample label	Thickness of layer before reduction in acid / nm	Thickness of layer after reduction in acid / nm	% shrinkage	Thicknesses of layers after attempts to reverse shrinkage caused by reduction in acid	
					Repeated cycling [a]	'Blank' modification [b]
15	Scratch 3	5.4 ± 0.3	3.7 ± 0.4	31	-	-
15	Scratch 1	5.3 ± 0.3	3.8 ± 0.3	28	-	2.6 ± 0.3
	Scratch 2	5.3 ± 0.3	3.9 ± 0.3	26	-	2.9 ± 0.3
25	Scratch 1	8.4 ± 0.3	6.6 ± 0.3	21	5.0 ± 0.3	-
	Scratch 2	8.0 ± 0.3	4.7 ± 0.3	41	4.2 ± 0.3	4.1 ± 0.3

[a] Repeat cycling (20 scans) from 0 to 0.4 V in ACN/0.1 M $[Bu_4N]BF_4$.
[b] Modification conditions without the modifier.
- Treatment not done or scratch not analysed.

The thicknesses of the reduced NPEA layers are detailed in Figure 4.23. and Table 4.16. Of the samples in Table 4.16, only the sample modified with an electrolysis time of 1 minute was reduced in both solutions, the others were only reduced in acid. From Figure 4.23. and Table 4.16, the thickness of the reduced NPEA layer increases with electrolysis time. A plateau is reached after an electrolysis time of 20 minutes and the maximum thickness recorded is approximately 6 nm. However, considering the shrinkage as a result of reduction in acid, all the thicknesses in Figure 4.23. and Table 4.16. are approximately 29% lower compared to the as-modified, non-reduced layer. To obtain a monolayer of NPEA, an electrolysis time of 1 minute was applied. Multilayers were formed at longer electrolysis times.

Figure 4.23. and Table 4.16. Plot of thickness of reduced NPEA layers against period of electrolysis. Dotted lines are only a visual guide. The minimum number of monolayers was calculated using the calculated length of reduced NPEA (NH_2 group rather than NO_2) as 0.8 nm, assuming perpendicular attachment to surface.

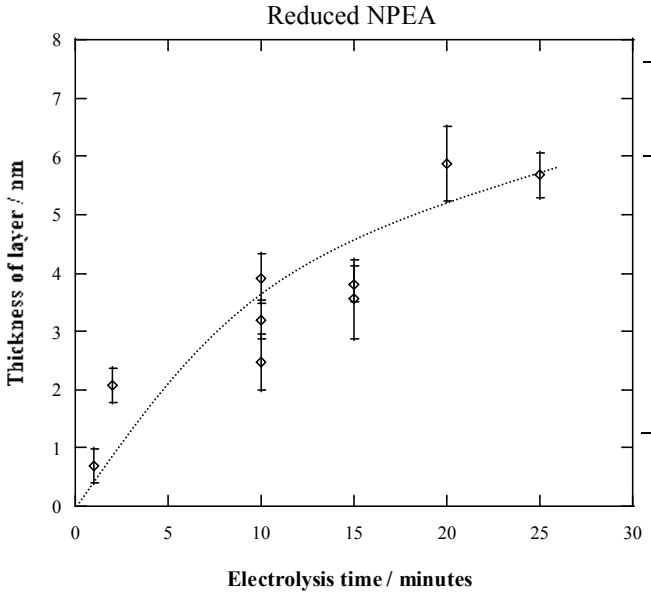

Electrolysis time / minutes	Thickness of layer / nm	Uncertainty / nm [a]	Min. no. of monolayers
1	0.7	0.3	1
2	2.1	0.3	3
10	3.2	0.3	4
10	3.9	0.4	5
10	2.5	0.5	3
15	3.6	0.7	5
15	3.8	0.3	5
20	5.9	0.6	7
25	5.7	0.4	7

[a] Uncertainty includes instrumental inaccuracy and the standard deviation of the measured layer thicknesses.

Surface concentration of NPEA

The surface concentration of NPEA modifiers was estimated from the peak areas of the first reduction CV scans carried out in ACN/0.1 M $[Bu_4N]BF_4$ and 0.1 M H_2SO_4. The NPEA surface concentration was estimated for layers prepared with varied electrolysis times. Peak areas were calculated by curve fitting and the dotted lines are similar to the linear baselines used in LinkFit (Figure 4.21.).

For reduction in ACN, the total peak area of the reduction and oxidation pair was averaged and surface concentration was estimated from the averaged peak area (Figure 4.21.(i).). For reduction in acid, the surface concentration of NPEA was calculated from the peak areas 1 and 2 recorded in the first reduction scan (Figure 4.21.(ii).). The total peak area was divided by 6 (NO_2 to NH_2 (six-electron) or NO_2 to NHOH (four-electron) plus NHOH to NO (two-electron)), and surface concentration was estimated from the averaged peak areas.

Figure 4.24. and Table 4.17. detail surface concentrations estimated from CV scans recorded in acid and layer thicknesses of reduced NPEA layers. The plot of surface concentration vs. layer thickness gives a non-linear relationship and shows that as the layer grows and more NPEA groups are attached to the surface, not all the *p*-nitrophenyl groups are detectable during electrochemical reduction in acid. This suggests that the surface concentration values, especially with thicker layers, may be an underestimation. The shrinkage in layer thickness due to reduction in acid (Figure 4.23. and Table 4.16.) is a probable explanation for this. Other workers investigating *p*-NB layers on GC surfaces

have also reported that only a fraction of *p*-nitrophenyl groups are electrochemically reduced when the reduction is carried out in 1 M HCl + 1 M KCl.[25]

As indicated with a dotted line in Figure 4.24, a layer with thickness corresponding to a monolayer of reduced NPEA has a surface concentration of (0.34 ± 0.5) x 10^{-9} mol.cm^{-2}. The monolayer thickness is assumed to be 0.8 nm, corresponding to NPEA modifiers oriented perpendicular to the surface. This value is approximately 25% of a closed-packed monolayer, considering that the calculated closed-packed surface concentration for *p*-NB on a flat surface is 1.35 x 10^{-9} mol.cm^{-2}.[38] Previous workers have reported a *p*-NB surface concentration at a carbon surface of 21 ± 3% of a closed-packed monolayer,[27] which agrees well with the NPEA surface concentration of 25%. Possible explanations for the low surface concentrations are that the layers are 'loosely packed' or that only a fraction of *p*-nitrophenyl groups are reduced in the first reduction scan.

From Figure 4.25. and Table 4.18, for all the NPEA layers prepared with different electrolysis times, the surface concentration of NPEA groups estimated from reduction in ACN is higher than from reduction in acid. To explain this difference, it is proposed that the NPEA layer has an extended conformation in ACN/0.1 M $[Bu_4N]BF_4$ and thus more or all *p*-nitrophenyl groups are accessible for reduction than in 0.1 M H_2SO_4. During reduction in acid solution, the layer shrinks restricting the number of electroactive *p*-nitrophenyl groups. The data in Figure 4.22. and Table 4.15. showing the decrease in layer thickness after reduction in acid support this observation. Further supporting this explanation is the observation of a linear relationship between NPEA surface concentration estimated from reduction in ACN and electrolysis time (Figure 4.25. and Table 4.18.). In contrast to data

obtained from reduction of the layer in acid, surface concentrations determined from reduction in ACN increased with electrolysis time.

Figure 4.24. and Table 4.17. Plot of NPEA surface concentration estimated from reductions in acid against thickness of reduced NPEA layers. Dotted line is the surface coverage for a layer with monolayer thickness.

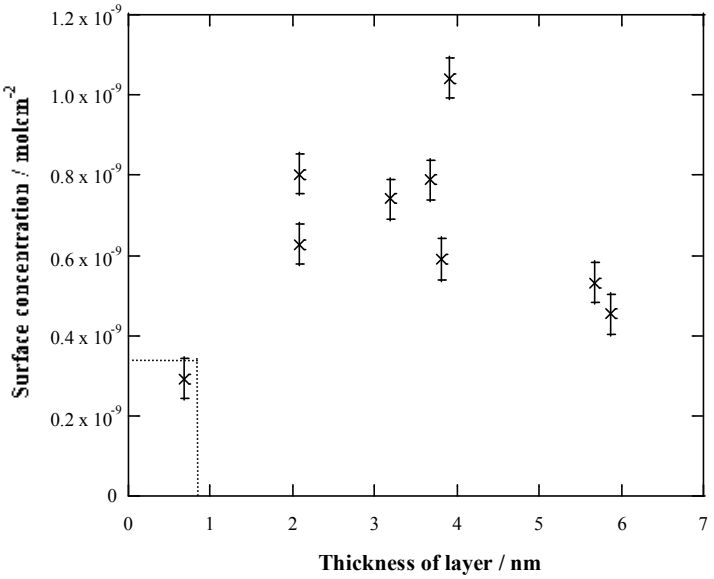

Electrolysis time / minutes	Thickness of layer [a] / nm	Surface concentration estimated from reduction in acid / ± 0.5 x 10^{-9} mol.cm^{-2}
1	0.7	0.29
2	2.1	0.63
2	**2.1**	0.80
10	3.2	0.74
10	3.9	1.04
15	**3.7**	0.79
15	3.8	0.59
20	5.9	0.45
25	5.7	0.53

[a] Bold values are from different samples than the samples used for surface concentration estimations.

Figure 4.25. and Table 4.18. Plot of NPEA surface concentration estimated from reductions in acid and/or ACN against electrolysis time.

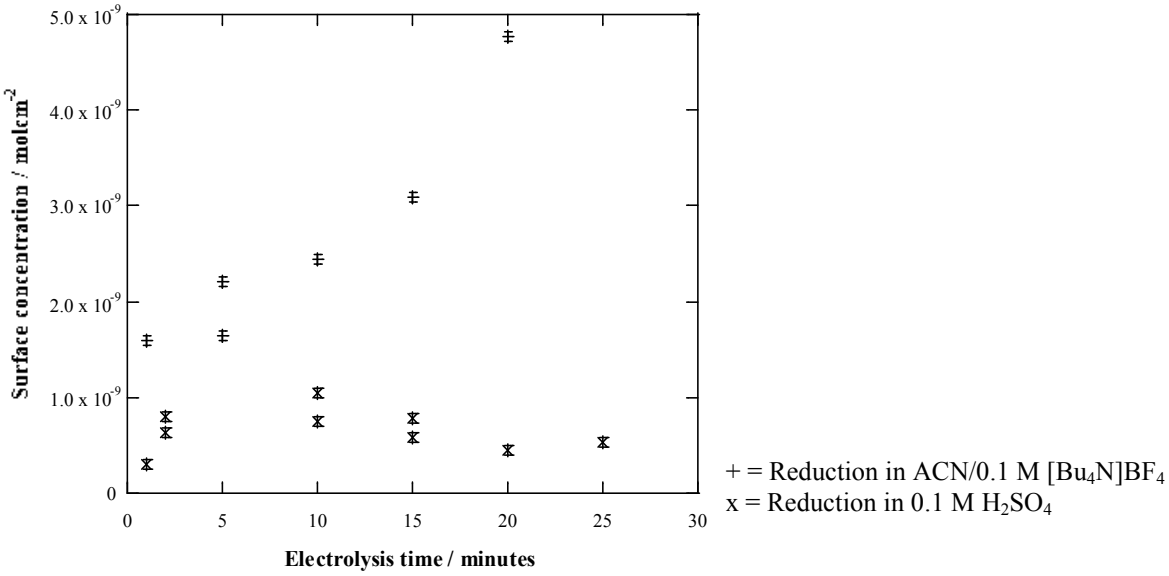

Electrolysis time / minutes	Surface concentration estimated from reduction in ACN / ± 0.5 x 10^{-9} mol.cm^{-2}	Surface concentration estimated from reduction in acid / ± 0.5 x 10^{-9} mol.cm^{-2}
1	1.60	0.29
2	Not measured	0.63
2	Not measured	0.80
5	2.20	Not measured
5	1.64	Not measured
10	Not measured	0.74
10	Not measured	1.04
10	2.44	Not measured
15	3.09	Not measured
15	Not measured	0.79
15	Not measured	0.59
20	Not measured	0.45
20	4.77	Not measured
25	Not measured	0.53

4.4. Conclusions

In this chapter, seven different primary amine modifiers – TDA, DAD, HA, TGD, PGD, NPEA and *p*-NA, were attached to GC and PPF surfaces. Modification of PPF by the oxidation of amines has not been previously investigated. Water contact angle measurements showed that attachment of TDA, HA, DAD layers rendered that carbon surface hydrophobic and it was hydrophilic when PGD and TGD layers were attached. For each of the modifiers, a number of interesting results were obtained.

TDA and DAD:

- The two electrochemical equivalent amines of DAD, 12 carbons apart, were interacting and the oxidation of one shifted the oxidation of the other to a more positive potential. Thus, using the given applied potential, it was assumed that a C-N bond was formed at surface and the other amine was not surface-bound.
- Both the TDA and DAD layers appeared to grow laterally across the surface initially and then vertically where the modifiers attached to already attached modifiers.
- Both TDA (monoamine) and DAD (diamine) showed multilayer growth at prolonged electrolysis (> 5 minutes for TDA and > 2 minutes for DAD).
- To summarise the stability experiments, the changes in the probe after the layers were scanned, soaked and sonicated appeared to be due to desorption of physisorbed modifiers or reorganisation of surface-immoblised modifiers. These processes created holes and thin patches that allowed for the return of the probe

response. There was no evidence for large scale loss of the layer as a result of these treatments, as determined by layer thickness measurements.

- The modifier surface concentration was monitored by coupling FCA to the amines groups within the layer. When coupling was performed in aqueous media, the CV scans were complex with multiple oxidation peaks arising from a mixture of electrostatically and covalently attached ferrocene groups. These experiments demonstrated that it is important to carry out 'blank' experiments in order distinguish between responses from covalently coupled and electrostatically attached species. Performing the coupling reaction in organic media showed no contribution from electrostatically attached FCA groups and assuming the yield of the coupling reaction was similar at both TDA and DAD layers, the surface concentration of modifiers TDA and DAD in both layers was similar. $NaClO_4$ is a suitable electrolyte solution for observing the response of coupled Fc groups and PBS is unsuitable.

HA and TGD:

- Using the given applied potential, only one of the two electrochemically equivalent interacting amines of the TGD modifier attached to the surface.
- The TGD layer grew vertically where the modifiers attached to already attached modifiers and then laterally across the surface.
- Multilayers of HA (monoamine) and TGD (diamine) were formed with prolonged electrolysis.

- Negative potentials affected the TGD layers and coupling of NBC to TGD layers was successful.

PGD:

- At short electrolysis times (up to 2 minutes), the rate of growth of the layer appeared to be mass transport controlled and at longer electrolysis times (after 10 minutes electrolysis) electron transfer determined the amount of growth of the layer.
- Attached PGD modifiers are in a folded, collapsed configuration.

NPEA:

- Obtaining a well-defined reversible reduction CV in ACN/0.1 M $[Bu_4N]BF_4$ was difficult, whereas reduction in 0.1 M H_2SO_4 gave expected CV scans for reduction in acid of *p*-nitrophenyl group to amino derivatives in a protic solvent.
- FCA probe CV scans at the reduced surfaces were similar to the as-prepared carbon surface.
- Reduction in acid caused a vertical shrinkage of the layer of approximately 29%.
- Multilayers of NPEA were formed at prolonged electrolysis (> 1 minute).
- The surface concentrations of *p*-nitrophenyl groups estimated from CV scans for reduction in acid may be an underestimation whereas when reduction was performed in ACN/0.1 M $[Bu_4N]BF_4$, reliable surface concentration estimations were obtained.

- The surface concentration of NPEA estimated from electrochemical reductions in acid for a layer with monolayer thickness was approximately 25% of a closed-packed monolayer.

4.5. References

(1) Herlem, G.; Goux, C.; Fahys, B.; Dominati, F.; Goncalves, A. M.; Mathieu, C.; Sutter, E.; Trokourey, A.; Penneau, J. F. *Journal of Electroanalytical Chemistry* **1997**, *435*, 259-265.

(2) Herlem, G.; Reybier, K.; Trokourey, A.; Fahys, B. *Journal of the Electrochemical Society* **2000**, *147*, 597-601.

(3) Lakard, B.; Herlem, G.; Fahys, B. *Journal of Chemical Physics* **2001**, *115*, 7219-7226.

(4) Lakard, B.; Herlem, G.; Lakard, S.; Fahys, B. *Theochem* **2003**, *638*, 177-187.

(5) Liu, A.; Anzai, J. *Langmuir* **2003**, *19*, 4043-4046.

(6) Li, J.; Ng, H. T.; Cassell, A.; Fan, W.; Chen, H.; Ye, Q.; Koehne, J.; Han, J.; Meyyappan, M. *Nano Letters* **2003**, *3*, 597-602.

(7) Wang, X.; Gershman, Z.; Kharitonov, A. B.; Katz, E.; Willner, I. *Langmuir* **2003**, *19*, 5413-5420.

(8) Seo, K.; Jeon, I. C.; Yoo, D. J. *Langmuir* **2004**, *20*, 4147-4154.

(9) Kim, E.; Kim, K.; Yang, H.; Kim, Y. T.; Kwak, J. *Analytical Chemistry* **2003**, *75*, 5665-5672.

(10) Rowe, G. K.; Creager, S. E. *Langmuir* **1991**, *7*, 2307-2312.

(11) Sumner, J. J.; Creager, S. E. *Journal of Physical Chemistry B* **2001**, *105*, 8739-8745.

(12) Chambers, R. C.; Inman, C. E.; Hutchison, J. E. *Langmuir* **2005**, *21*, 4615-4621.

(13) Kazakeviciene, B.; Valincius, G.; Niaura, G.; Talaikyte, Z.; Kazemekaite, M.; Razumas, V. *Journal of Physical Chemistry B* **2003**, *107*, 6661-6663.

(14) Peter, M.; Lammertink, R. G. H.; Hempenius, M. A.; Vancso, G. J. *Langmuir* **2005**, *21*, 5115-5123.

(15) Valincius, G.; Niaura, G.; Kazakeviciene, B.; Talaikyte, Z.; Kazemekaite, M.; Butkus, E.; Razumas, V. *Langmuir* **2004**, *20*, 6631-6638.

(16) Solak, A. O.; Eichorst, L. R.; Clark, W. J.; McCreery, R. L. *Analytical Chemistry* **2003**, *75*, 296-305.

(17) Adenier, A.; Chehimi, M. M.; Gallardo, I.; Pinson, J.; Vila, N. *Langmuir* **2004**, *20*, 8243-8253.

(18) Vogler, E. A. *Advances in colloid and interface science* **1998**, *74*, 69-117.

(19) Jakubowicz, A.; Jia, H.; Wallace, R. M.; Gnade, B. E. *Langmuir* **2005**, *21*, 950-955.

(20) Faucheux, N.; Schweiss, R.; Lutzow, K.; Werner, C.; Groth, T. *Biomaterials* **2004**, *25*, 2721-2730.

(21) Chirakul, P.; Perez-Luna, V. H.; Owen, H.; Lopez, G. P.; Hampton, P. D. *Langmuir* **2002**, *18*, 4324-4330.

(22) McCarley, T. D.; Lufaso, M. W.; Curtin, L. S.; McCarley, R. L. *Journal of Physical Chemistry B* **1998**, *102*, 10078-10086.

(23) Liu, J.; Dong, S. *Electrochemistry Communications* **2000**, *2*, 707-712.

(24) Deinhammer, R. S.; Ho, M.; Anderegg, J. W.; Porter, M. D. *Langmuir* **1994**, *10*, 1306-1313.

(25) Ortiz, B.; Saby, C.; Champagne, G. Y.; Belanger, D. *Journal of Electroanalytical Chemistry* **1998**, *455*, 75-81.

(26) Benito, A.; Martinez-Manez, R.; Soto, J.; Tendero, M. J. L. *Journal of the Chemical Society, Faraday Transactions* **1997**, *93*, 2175-2180.

(27) Brooksby, P. A.; Downard, A. J. *Langmuir* **2004**, *20*, 5038-5045.

(28) Database: *SciFinder Scholar 2005*.

(29) Brooksby, P. A.; Downard, A. J.; Yu, S. S. C. *Langmuir* **2005**, *21*, 11304-11311.

(30) Yu, S. S. C.; Downard, A. J. *e-Journal of Surface Science and Nanotechnology* **2005**, *3*, 294-298.

(31) Gooding, J., Personal communication, **2006**.

(32) Moutet, J.-C.; Saint-Aman, E.; Ungureanu, M.; Visan, T. *Journal of Electroanalytical Chemistry* **1996**, *410*, 79-85.

(33) Anne, A.; Bouchardon, A.; Moiroux, J. *Journal of the American Chemical Society* **2003**, *125*, 1112-1113.

(34) Barbier, B.; Pinson, J.; Desarmot, G.; Sanchez, M. *Journal of the Electrochemical Society* **1990**, *137*, 1757-1764.

(35) Brooksby, P. A.; Downard, A. J. *Journal of Physical Chemistry B* **2005**, *109*, 8791-8798.

(36) Bahr, J. L.; Yang, J.; Kosynkin, D. V.; Bronikowski, M. J.; Smalley, R. E.; Tour, J. M. *Journal of the American Chemical Society* **2001**, *123*, 6536-6542.

(37) Kariuki, J. K.; McDermott, M. T. *Langmuir* **2001**, *17*, 5947-5951.

(38) Pinson, J.; Podvorica, F. *Chemical Society Reviews* **2005**, *34*, 429-439.

5.1. Introduction

The electrochemical reduction of aryl diazonium cations on conducting and semiconducting surfaces such as cobalt, copper, nickel, zinc, platinum, gold and silicon to yield covalently attached aryl layers has been studied.[1,2] The modification of carbon surfaces, glassy carbon (GC)[3-8] and pyrolysed photoresist film (PPF)[9-12], by this method is also well-known. The aryl layers formed on the carbon materials are stable at high temperatures, in a range of aggressive solvents and to a relatively wide potential range,[5,7,8] and hence are widely used.

The mechanism of the electrochemically-assisted reduction of the aryl diazonium cation at a carbon surface is detailed in Figure 5.1.[2,4,6,11-15] The reduction involves the generation of radical species that form C-C covalent bonds with the carbon surface. An alternative mechanism has also been suggested where azo (-N=N-)/hydrazine (-NH-NH-) derivatives are generated by the reaction of the diazonium cation with the surface phenol or naphthol groups as shown in Figure 5.2.[16,17]

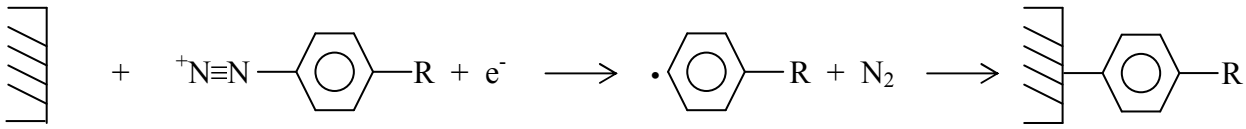

Figure 5.1. The electrochemical reduction of *para* substituted aryl diazonium cation at a carbon surface generating radical species that covalently bind to the surface.

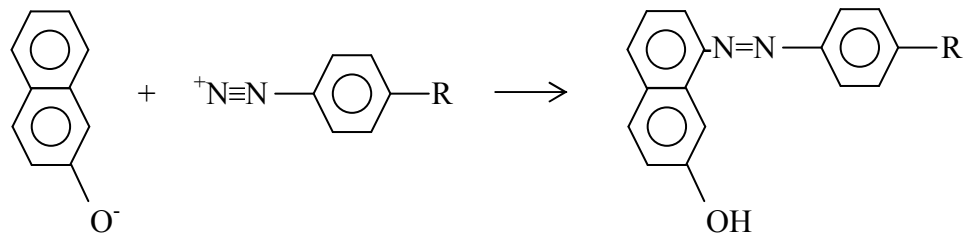

Figure 5.2. Reaction of an aryl diazonium cation with phenol or naphthol groups at a carbon surface.

Both mono- and multilayers have been formed on carbon surfaces from the reduction of aryl diazonium cations. Monolayers were formed by a single reduction scan (from 0.2 to -0.4 V vs. saturated calomel electrode (SCE) using 1 mM of various diazonium salts in acetonitrile (ACN)) which was confirmed by atomic force microscope (AFM) depth profiling.[9] On the other hand, layers up to 100 nm of *para* nitro phenyl (NPh) were obtained by 20 reduction scans (from 0.3 to -2.9 V vs. SCE).[18] The proposed mechanism for multilayer formation involves initially only a few radicals attaching to the surface followed by subsequent radicals attaching to the already attached initial layer, and so on (Figure 5.3.).[3,19] This reaction is described as aromatic homolytic substitution.[2,19] With this reaction, the rates of the reaction at different positions of the aromatic ring are not very different and the electron donating or withdrawing properties of the *para* substituent does not play a major role.[2] Thus, it is possible that the radical attaches to *ortho* or *meta* positions relative to the substituent or even to the derivative of the already attached modifier. However, *ortho* substitution is most likely based on steric reasons.[2,3,13] This would result in layers that have a branched, 'loosely packed' structure and have low surface concentrations per layer.[11,12] It is also possible that some of the aryl rings lose their

aromaticity forming cyclohexadienel rings. As detailed in Figure 5.4, this can occur via a hydrogen atom transfer from the solvent to the radical or a disproportionation reaction between two spatially close cyclohexadienyl radicals resulting in one cyclohexadiene and the other an aromatic ring.[19]

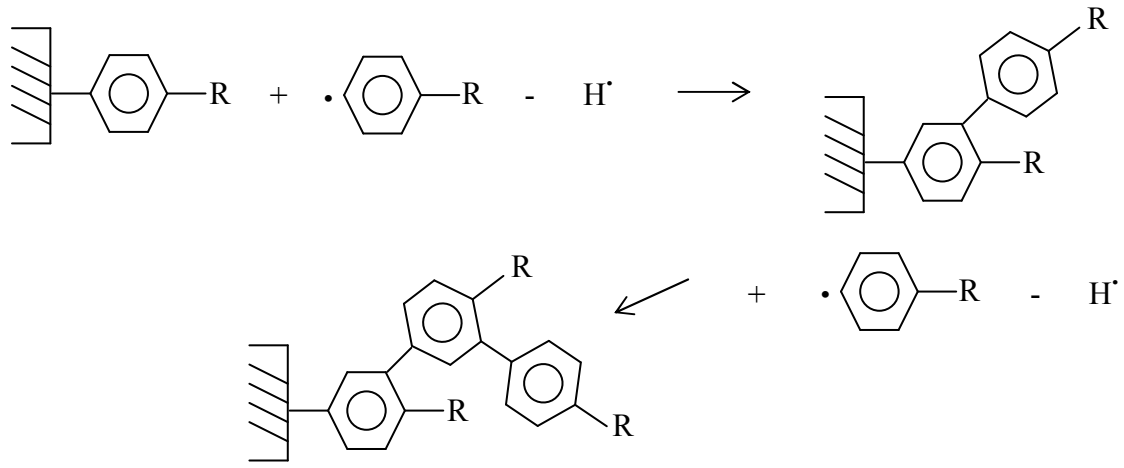

Figure 5.3. Mechanism for multilayer formation by the attachment of radical species to *ortho* positions of already attached modifiers to yield a branched structure.

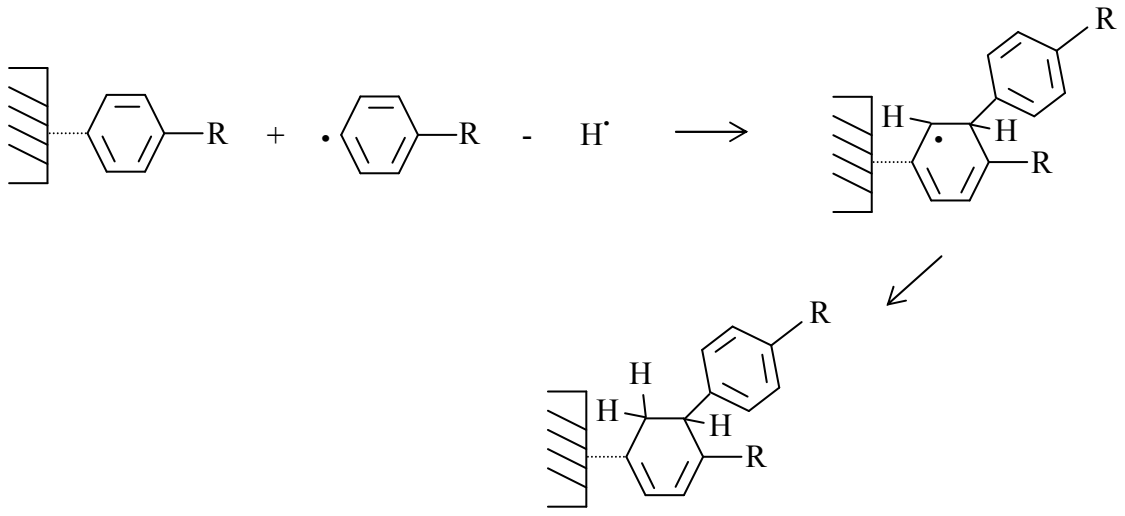

Figure 5.4. Mechanism for multilayer formation where some of the aryl modifiers lose their aromaticity.

Other possible mechanisms for multilayer formation include adsorption (π-π stacking) of reaction products generated from the radicals[2,5] and azo attachments by the reaction of the diazonium cation with already attached species (refer Figure 5.2.)[5,17].

The surface concentration of the modifier and thickness of the aryl layer have been shown to be dependent on a number of factors. These include the aryl derivative, the modifier concentration, the applied reduction potential, the modification (electrolysis) time and the type of carbon surface.[7,8,11]

For *para* substituents, $-(CH_2)_nR$ (n = 0 – 12), the value of n and the polarity of R appear to influence the surface concentration of modifiers when aryl diazonium cations are reduced at hydrogen-terminated silicon surfaces.[20] The surface concentration decreases as n increases which is attributed to surface screening by the substituents. The longer tails are more effective at screening of the surface where the tilted alkyl tail sterically hinders or reduces grafting at sites directly below it.[20] When the R group is polar, the surface concentration is higher in comparison to when R is hydrophobic. It is envisaged that hydrophobic substituents had some contact with the hydrophobic surface and reorientation is necessary for reduction of the aryl diazonium cation to occur. With polar head groups, there is no such contact and reorientation is not required prior to attachment.[20]

The dependence of modifier surface concentration on solution concentration of the aryl diazonium salt, the applied reduction potential and the modification (electrolysis) time has been studied using NPh on different carbon surfaces. The surface concentration is estimated by integration of the voltammetric signals arising from the electrochemical reduction of the *p*-nitrophenyl groups.

The NPh surface concentration on GC increases with higher modifier concentration (0.2, 1 and 5 mM in ACN) and with electrolysis time up to 10 minutes using an overpotential of 0.8 V. At all electrolysis times, a higher surface concentration is obtained using a higher modifier concentration. The 'limiting' surface concentration is 3 – 4 x 10^{-9} mol.cm^{-2}.[7] These values are higher than that calculated for a closed-packed monolayer (1.35 x 10^{-9} mol.cm^{-2})^2 which suggests that more than a monolayer is present.

In another study, experiments were carried out in ACN solutions with a modifier concentration of *ca.* 0.7 mM on PPF surfaces.[11] Surface concentrations are shown to increase with more negative modification potentials. Surface concentrations are 0.6 x 10^{-9}, 1.2 x 10^{-9} and 1.9 x 10^{-9} mol.cm^{-2} using potentials 0.25, 0.5 and 0.75 V more negative than the reduction peak, respectively.[11] The surface concentration also increases with longer electrolysis times up to 10 minutes, using an overpotential of 0.15 V.[11] When the surface concentration is compared with layer thickness, a linear relationship is formed. Using 10 minutes electrolysis, a surface concentration of 1.2 x 10^{-9} mol.cm^{-2} is estimated and the thickness of the layer represents 4 monolayers.[2,11] Hence, the surface concentration for each 'monolayer' is much lower than a close-packed monolayer indicating that these layers are 'loosely packed' perhaps due to branching during multilayer formation (refer above). This study demonstrates that it is important to consider surface concentration values together with thicknesses of layers.

Characterisation of the aryl layers has been carried out using a number of electrochemical (cyclic voltammetry (CV)), spectroscopic (Raman, x-ray photoelectron spectroscopy (XPS)) and microscopy (AFM, STM) techniques.[2,4-12,14,21] AFM depth

profiling is used to determine the thickness of the layers.[9,11,12] AFM depth profiling is carried out by scratching a small area of the layer and measuring the depth of the scratch using non-contact AFM. This technique is used in this work and is described in Chapter 2. When there are electroactive derivatives present in the layer, the electrochemical response of the derivative can be observed, as previously mentioned. A commonly used derivative is the *p*-nitrophenyl functionality.[2,4,7] The one-electron reversible reduction of the attached *p*-nitrophenyl groups is observable in ACN[2,4,7,8,14] and its irreversible reduction to amino species can be carried out in a variety of protic solutions such as H_2SO_4[11,12] and ethanol/water[7,14,22].

In this work, reduction of aryl diazonium cations is used to modify carbon surfaces. This method is used in addition to modification by oxidation of amines in order to achieve a wider range of surface properties. Tailoring surface properties by attaching aryl layers (*para* methyl phenyl (MP), *para* hexyl phenyl (HP) and *para* polyethylene glycol phenyl (PEG)) is useful for the investigations into adsorption of protein (Chapter 6) and the assembly of nanoparticles (NPs) (Chapter 7) onto carbon surfaces. A broad range of surface layers is also useful for molecular patterning (Chapter 9). The different chemical properties of the layers are expected to permit the visualisation of the patterns. Aryl modifiers *para* methyl benzene diazonium tetrafluoroborate (*p*-MB), *para* methylene carboxylic acid benzene diazonium tetrafluoroborate (*p*-MCA) and *para* nitro benzene diazonium tetrafluoroborate (*p*-NB) are used for patterning in Chapter 9. Also, layers (*para* methylene carboxylic acid phenyl (MCA) and NPh) prepared by the reduction of aryl diazonium cations are suitable for subsequent coupling reactions. In the case of NPh, electrochemical

reduction of the *p*-nitrophenyl group to generate amino functionalities, that can undergo coupling reactions, is carried out.

Therefore, the aim of this work is three-fold. The first is to attach various aryl layers in order to expand the surface properties and secondly, to form layers that can be used for subsequent coupling reactions. The third aim is to characterise the resulting layers generated by the electrochemical reduction of the *p*-nitrophenyl group of NPh when reduction is carried out in three different solutions – 0.25 M H_2SO_4, ethanol/water (1:9 by volume) + 0.1 M KCl or 0.02 M benzoic acid/ACN/0.1 M $[Bu_4N]BF_4$ (tetrabutyl ammonium fluoroborate), using electrochemistry and XPS.

5.2. General experimental methods

5.2.1. Preparation of GC plates or rods

The aryl layers discussed in this chapter were attached to GC plates or rods prepared in three different ways. The preparation methods were different from that in Chapter 3 when the modified plates are used for the adsorption of protein (Chapter 6) or when the surfaces are used for the attachment of *p*-NB (later section).

Experiments involving adsorption of protein: GC plates were polished with a 1 μm alumina/water slurry on a Leco polishing cloth in a figure 8 motion and rinsed in distilled water. Plates were then sonicated in MilliQ (MQ) water for 10 minutes and in IPA (isopropyl alcohol)/ACN (1:1) and activated carbon slurry (50:50 by volume) for another 10 minutes.[23] The plates were then rinsed in ACN, followed by MQ water and dried with $N_{2(g)}$ before electrochemistry was carried out.

Experiments involving the attachment of *p*-NB: The GC plates or rods were polished on a 1 μm alumina/water slurry in a figure 8 motion and then washed with distilled water. Surfaces were sonicated in MQ water then ACN for about 1 minute each and then dried with $N_{2(g)}$ before electrochemistry was carried out.

5.2.2. Synthesis of aryl diazonium salts

para polyethylene glycol benzene diazonium tetrafluoroborate (*p*-PEG) was synthesised by Dr. Alan Happer, Department of Chemistry, University of Canterbury following a reported procedure.[13] The other aryl diazonium tetrafluoroborate salts were synthesised using a method from the literature in which the starting *p*-aniline is converted to an aryl diazonium with sodium nitrite and fluoroboric acid.[6] In the general procedure, 5 mmol of *p*-aniline starting material was added to 2 mL of 40% fluoroboric acid prediluted with 2 mL of MQ water. The mixture was stirred to aid dissolution and was cooled in an ice bath. A solution of 5 mmol (0.3462 g) of sodium nitrite dissolved in 0.7 mL of MQ water was then added dropwise to the stirred mixture while maintaining the temperature near 0 °C. The precipitate formed was cooled to below 0 °C in a salt/ice bath and collected in an ice cooled plastic filter funnel. 1 – 2 mL of ice cooled 5% fluoroboric acid, methanol and then ether was used to wash the product. The salt was dried under vacuum suction in the dark and then stored under vacuum at room temperature in the dark. Metal spatulas were not used in any part of the procedure and extra caution was exercised as diazonium salts can be explosive.

^{1}H nuclear magnetic resonance (NMR) for *p*-MB was as follows (d^6 acetone, 500 MHz) δ 2.67 ppm (s, 3H, C**H$_3$**-Ar-$N_2^+BF_4^-$), 7.80 ppm, (d, 2H, CH_3-Ar**H**-$N_2^+BF_4^-$), 8.40 ppm (d, 2H, CH_3-Ar**H**-$N_2^+BF_4^-$).

^{1}H NMR for *para* hexyl benzene diazonium tetrafluoroborate (*p*-HB) was as follows (d^6 acetone, 500 MHz) δ 0.99 ppm (m, 3H, C**H$_3$**$(CH_2)_5$-Ar-$N_2^+BF_4^-$), 1.45, 1.77, 2.17, 2.83 ppm (all m, 10H, CH_3(C**H$_2$**)$_5$-Ar-$N_2^+BF_4^-$), 7.60 ppm (m, 4H, $CH_3(CH_2)_5$-Ar**H**-$N_2^+BF_4^-$).

^{1}H NMR for *p*-MCA was as follows (d^6 acetone, 500 MHz) δ 2.17 ppm (m, 2H, HOOCC**H$_2$**-Ar-$N_2^+BF_4^-$), 4.18 ppm (s, 1H, **H**OOCCH_2-Ar-$N_2^+BF_4^-$), 8.13 ppm (d, 2H, HOOCCH_2-Ar**H**-$N_2^+BF_4^-$), 8.89 ppm (d, 2H, HOOCCH_2-Ar**H**-$N_2^+BF_4^-$).

^{1}H NMR for *p*-NB was as follows (d^6 acetone, 500 MHz) δ 8.98 ppm (d, 2H, NO_2-Ar**H**-$N_2^+BF_4^-$), 9.30 ppm (d, 2H, NO_2-Ar**H**-$N_2^+BF_4^-$).

5.2.3. Electrochemistry

CV scans of the ferrocene monocarboxylic acid (FCA) probe were recorded before and after each modification to provide qualitative information on the degree of modification.

For attachment of aryl modifiers, the standard final/applied potential (E_f) of -1.12 V was used for all the modifiers apart from *p*-MCA (either -1.12 or -1.0 V) and *p*-NB. These potentials were more negative than the aryl diazonium cation reduction peak, recorded at a scan rate of 100 mVs^{-1} (overpotentials were between -140 and -570 mV). For *p*-NB, the initial scan was to -0.4 V, the potential was held at -0.35 for a given electrolysis time and a final scan to -0.4 V followed. All potentials for *p*-NB were vs. Ag wire.

The most commonly used electrolysis time was 10 minutes. It was anticipated that holding at E_f for 10 minutes would yield a compact aryl layer of 'limiting' thickness. The most common concentration of modifier solutions was usually 5 mM with the exception of 0.8 mM for some *p*-PEG solutions and 0.6 mM for solutions of *p*-NB. The scan rate for modification scans were 100 mVs^{-1} except for *p*-NB for which the scan rate was 200 mVs^{-1}. After modification with *p*-NB, the surface was sonicated for approximately 3 seconds in ACN followed by MQ water before electrochemical reduction of the attached NPh layer. Table 5.1. lists the aryl-modified samples prepared.

Table 5.1. Aryl-modified surfaces prepared using various electrochemical conditions.

Aryl layer	Carbon surface	[Aryl diazonium salt] / mM	E_f / V	Electrolysis time or no. of scans
MP	PPF	5	-1.12	1 scan [a]
	PPF	5	-1.12	10 minutes
	GC plate	5	-1.12	10 minutes
HP	GC plate	5	-1.12	10 minutes
PEG	PPF	0.8	-1.12	10 minutes
	GC plate	5	-1.12	10 minutes
MCA	PPF	5	-1.0 or -1.12	1 minute
	PPF	5	-1.0 or -1.12	10 minutes
NPh	PPF	0.6	-0.4 or -0.35 [c]	2 minutes
	GC plate [b] or rod	0.6	-0.4 or -0.35 [c]	10 minutes

[a] Samples prepared as part of work in Chapter 9a – Approach (iii): "Fill-in" approach using PDMS microchannels.
[b] GC plate was modified using cell set-up (i) where the electrode geometric area is 0.24 cm^2.
[c] Reference electrode was Ag wire.

5.3. Results and discussion

The five aryl diazonium cations attached to carbon surfaces are listed in Table 5.2.

Table 5.2. Aryl diazonium cations modifiers attached to carbon surfaces.

Aryl diazonium cation [a] Ar = aryl ring	**Surface attachment of aryl modifier**] = surface	**Aryl layer**	**Abbreviation**
$^{+}N_2ArCH_3$	**]**-$ArCH_3$	*para* methyl phenyl	MP
$^{+}N_2Ar(CH_2)_6CH_3$	**]**-$Ar(CH_2)_5CH_3$	*para* hexyl phenyl	HP
$^{+}N_2Ar(OCH_2CH_2)_3OCH_3$	**]**-$Ar(OCH_2CH_2)_3OCH_3$	*para* polyethylene glycol phenyl	PEG
$^{+}N_2ArCH_2COOH$	**]**-$ArCH_2COOH$	*para* methylene carboxylic acid phenyl	MCA
$^{+}N_2ArNO_2$	**]**-$ArNO_2$	*para* nitro phenyl	NPh

[a] These are tetrafluoroborate salts where the anion is BF_4^-.

5.3.1. Synthesis of aryl diazonium salts

The synthesis of the aryl diazonium salts was generally straightforward. It was important to add the sodium nitrite solution slowly. When addition was carried out too quickly, no product was formed and brown nitrogen dioxide gas was released. Thus, the reaction was performed carefully in the fumehood with the screen lowered. It was also important to limit the volume of each washing solution to 1 – 2 mL to avoid dissolution of some diazonium salt products. Table 5.3. lists the colours of the aryl diazonium salts.

Table 5.3. Colours of the aryl diazonium salts.

Aryl diazonium salt	**Colour**
p-MB	White
p-HB	Brown
p-PEG	Not recorded
p-MCA	Yellow/orange
p-NB	Yellow

The ^1H NMR spectra of the aryl diazonium salts were compared with those of the starting *p*-aniline derivatives. The broad signal assigned to the ^1H of the amine of the *p*-

aniline was not present in corresponding diazonium salt. Also, a downfield shift of the signals arising from the ^{1}H's of the aryl ring was observed in the spectra of the salts. This indicated that formation of the aryl diazonium tetrafluoroborate salt was successful and that dimerisation or polymerisation had not occurred.

ACN solutions of *p*-MCA appeared to be very light sensitive and went from a yellow/orange to red/brown colour after a few minutes of light exposure. This was presumably due to dimerisation or polymerisation. Thus, the solution was exposed to light as little as possible and fresh solutions were prepared for each modification.

5.3.2. Electrochemistry and attachment

Aryl diazonium cation reduction

The initial and final modification scans for the reduction of *p*-MB diazonium cation at a PPF surface is shown in Figure 5.5. and is typical of all the diazonium salts used. The reductions of the five aryl diazonium cation modifiers are irreversible, as expected for a modification process. Consistent with other reports, it is assumed that the generated radical forms a covalent attachment via a C-C bond to the carbon surface. Final scans were obtained after electrolysis at the potential E_f for a given time.

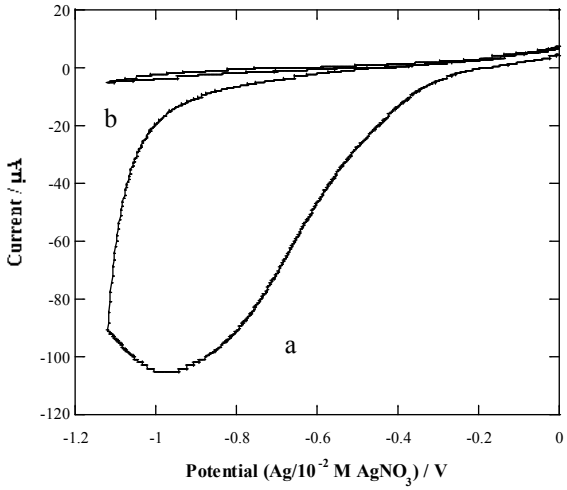

Figure 5.5. Initial (a) and final (b) CV scans for the reduction of the *p*-MB diazonium cations at a PPF surface. [*p*-MB diazonium salt] = 5 mM in ACN/0.1 M $[Bu_4N]BF_4$ and scan rate = 100 mVs^{-1}. Electrolysis time was for 10 minutes.

Table 5.4. lists E_f, potential of cathodic/reduction peak (E_{pc}) and the overpotentials ($E_f - E_{pc}$) for all modifiers. Some modifiers exhibit broad reduction peaks possibly because the initially attached modifiers blocks the surface and slows further reduction as the CV scan proceeded. Broad peaks may also be because the reduction processes of these cations are inherently slow.

Considering the E_{pc} values in Table 5.4. for the irreversible reduction of the aryl diazonium cations performed at identical scan rates, the reduction peaks of *p*-HB, *p*-PEG and *p*-MCA diazonium cations occur at similar potentials and E_{pc} for *p*-MB is more negative. For *p*-NB, the CV scan was recorded using the higher scan rate of 200 mVs^{-1}; this is expected to shift E_{pc} to a more negative value than would be obtained at 100 mVs^{-1}. If it is assumed that the peak potentials indicate relative ease of reduction, the order of aryl

diazonium cations from most relative ease of reduction to most difficult (less negative E_f to most negative E_f) to reduce is *p*-NB > *p*-HB ≈ *p*-PEG ≈ *p*-MCA > *p*-MB.

Table 5.4. Electrochemical conditions and properties for aryl modifiers attached onto carbon surfaces.

Aryl modifier	Carbon surface	[Aryl diazonium salt] / mM	E_f / V	E_{pc} / V	Scan rate	Over-potential / mV	i_{pc} / µA	Current density / µA.cm^{-2}
p-MB	PPF	5	-1.12	-0.98	100	-140	-105	-438
	GC plate	5	-1.12	-0.92	100	-200	-390	-609
p-HB	GC plate	5	-1.12	-0.55	100	-570	-125	-195
p-PEG	PPF	0.8	-1.12	~ -0.6 [b]	100	~ -520 [b]	-18	-75
p-MCA	PPF	5	-1.0 or -1.12	~ -0.7 [b]	100	~ -300 [b] or ~ -420 [b]	-33	-138
p-NB	PPF	0.6	-0.4 [c] or -0.35 [d]	~ -0.2 [b]	200	~ -200 [b] or ~ -150 [b]	-47	-196
	GC plate [a]	0.6	-0.4 [c] or -0.35 [d]	~ -0.2 [b]	200	~ -200 [b] or ~ -150 [b]	-80	-333

[a] GC plate was modified using cell set-up (i) where the electrode geometric area is 0.24 cm^2.
[b] Value estimated from broad reduction peaks.
[c] Initial and final scan to that potential was vs. Ag wire.
[d] Electrolysis at that potential was vs. Ag wire.

Based on the relevant Hammett parameters (σ_p),[24] the electron withdrawing *para* derivatives are expected to be most easily reduced and reduction would occur at a less negative E_{pc}. The most electron withdrawing to least electron withdrawing groups (highest to lowest σ_p values) are nitro > carboxylic acid > oxygen containing alkyl ≈ alkyl.[24] The E_{pc} results followed the expected trend with the exception of the *p*-HB diazonium cation which reduces at a significantly less negative potential than the *p*-MB modifier. It is unclear why the reduction peak potential of *p*-HB appears at such a high potential. The methylene group in the *p*-MCA modifier may have decreased the effect of the electron withdrawing carboxylic acid.

From the equation $i_p = (2.69 \times 10^5) n^{3/2} A D_o^{1/2} C_o^* v^{1/2}$ (refer Chapter 1), cathodic/reduction peak current (i_{pc}) can be dependent on electrode geometric areas, modifier concentrations, scan rates and diffusion coefficients. Thus considering the current densities of the modifiers attached using identical concentrations and scan rates, modifiers with a smaller *para* substituent are expected to have an increased diffusion rates and hence larger current densities. However, this trend is not observed. It is possible that during the modification scans the initially attached modifiers blocks the surface and prevents further reduction or subsequent modifiers attach to already immobilised modifiers, giving rise to varied current densities.

Probe scans after modification procedure

The FCA probe CV scan recorded after the attachment of the aryl layer provided some indication of the blocking properties of the layer. Comparing the FCA probe scans after modification of GC plates with 5 mM solutions and an electrolysis time of 10 minutes, the FCA probe scans after modification with H and PEG showed decreased currents and the potential of anodic/oxidation peak (E_{pa}) of FCA was more positive compared to at the as-prepared surface. However, the probe scan at the MP layer was completely featureless on the current scale used to record the CV scan at the unmodified electrode.

As discussed in the Introduction, studies of the modification of silicon surfaces show that longer *para* substituents result in layers with lower modifier surface concentrations.[20] This appears to be the case here also, considering that the blocking properties of modifiers with longer *para* substituents, *p*-HB and *p*-PEG, are less than *p*-MB

with the methyl substituent. With the HP and PEG layers, the probe molecules were able to diffuse into the layer allowing for electron transfer with the carbon surfaces. This suggests that modification with *p*-HB and *p*-PEG gives layers that had lower surface concentrations and are more 'loosely packed' than MP layers. A similar trend was observed when PPF surfaces were modified with *p*-MB and *p*-PEG. Related work that supports these results has demonstrated that multilayers prepared by diazonium cation attachment have low surface concentrations per layer[11,12] and nitroazobenzene layers, are found to have greater than 50% free volume.[12]

It is interesting that less blocking layers are formed with *p*-HB and *p*-PEG, even though larger overpotentials were used for the modifications compared to *p*-MB (Table 5.4.). As outlined in the Introduction, more negative overpotentials have been reported to result in increased modifier surface concentrations.[11] Evidently, the steric influence of the *para* derivative outweighs this effect.

Control experiments were carried out to investigate the effect of the potential applied during reduction of aryl diazonium cations, on the carbon surfaces. The electrochemical procedure where E_f was -1.12 V (the most negative used for aryl diazonium cation reductions) and electrolysis time was 10 minutes was applied without the aryl diazonium salt present. The FCA probe scans before and after the process were identical and there was no peak present in the initial scan to -1.12 V. This indicates that the modification procedures used for the attachment of the aryl layers does not affect the carbon surface.

5.3.3. Water contact angle measurements

The sessile contact angle of water on the various aryl layers attached to carbon surfaces provided an indication of the wettability of the layer. Figure 5.6. is a digital photograph of a 1 µL water droplet dispensed onto a MP-modified PPF surface (5 mM, electrolysis time 10 minutes) from which the water contact angle was measured (as shown). Images of water droplets on other aryl modified surfaces were also captured and the water contact angles are listed in Table 5.5.

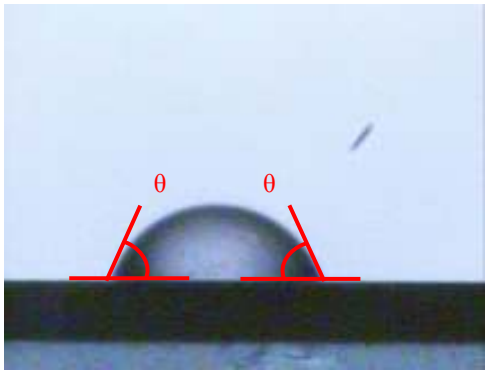

Figure 5.6. Image of 1 µL water droplet on the MP layer (5 mM, electrolysis time 10 minutes) attached to a PPF surface. Water contact angles were measured (as shown), giving a value of 65 ± 4° for this layer.

Table 5.5. Water contact angle of aryl layers attached onto carbon surfaces. These layers were attached with electrolysis times of 10 minutes (unless otherwise stated).

Aryl layer	Carbon surface	[Aryl diazonium salt] / mM and electrolysis time	Water contact angle / °
MP	PPF	5	65 ± 4
	GC plate	5	63 ± 3
HP	GC plate	5	72 ± 3
MCA	PPF	5	67 ± 2
NPh	PPF	0.6, 2 minutes	64 ± 4
	GC plate	0.6	56 ± 2
As-prepared	PPF		72 ± 3
As-prepared	GC plate		71 ± 4

The water contact angles on the aryl layers are similar but appear to be somewhat modulated by the hydrophobicity of the *para* substituent of the modifier. Comparing the layers attached with identical modifier concentrations and electrolysis times, the order of wettability of the layers is hexyl > acetic acid > methyl. This order is not expected as the hydrophobicity of the methyl substituent is expected to be higher than the polar acetic acid. Literature values of water contact angle for an octadecanethiol self-assembled monolayer (SAM) on gold is 105 – 110° [25] and a carboxylic acid terminated layer (3-(pyrrol-1-yl)propanoic acid) assembled on gold is reported as 49° [26]. Hence, it is possible that poor modifier layers are attached using the very light sensitive *p*-MCA modifier, resulting in the water contact angle being influenced by the underlying carbon surface.

The MP layers attached to the GC and PPF surfaces gives essentially the same contact angles indicating that similar layers form on both surfaces. This is somewhat expected as the angles on the as-prepared surfaces are very similar. The contact angle of the NPh layer depends on the electrolysis time. It is assumed that 2 minutes electrolysis gives a thinner layer with a lower modifier surface concentration than 10 minutes electrolysis. The higher contact angle for the thinner layer may be due to the influence of the underlying carbon surface. When the electrolysis time was 10 minutes, the MP, HP and PEG -modified surfaces are considered hydrophobic as the water contact angle is larger than 65°.[27]

5.3.4. Analysis by AFM depth profiling

AFM depth profiling was used to measure the thickness of the MP and PEG layers attached to PPF surfaces using given modification conditions – concentration, electrolysis

time or number of scans and applied potential. The AFM depth profiling technique is described in Chapter 2. Figure 5.7. shows a scratch made in the MP layer from which thickness data were measured. Thickness data are listed in Table 5.6.

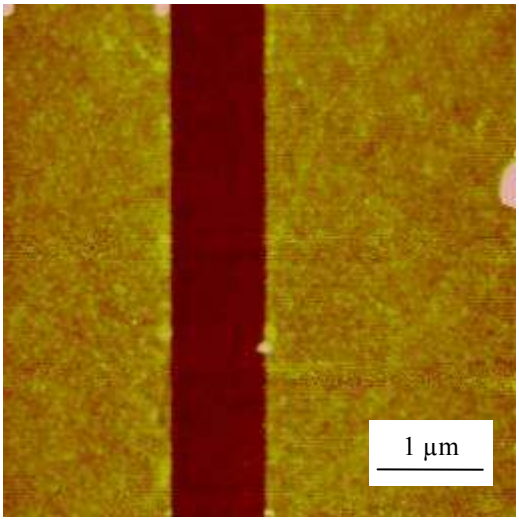

Figure 5.7. AFM image of a scratch made into a MP layer (5 mM, electrolysis time 10 minutes) from which the thickness of the layer was estimated.

Figure 5.6. Thicknesses of aryl layers attached to PPF measured by AFM depth profiling. The minimum number of monolayers was calculated using the calculated length of the modifier.

Aryl layer	[Aryl diazonium salt] / mM and modification conditions	Thickness / nm	Calculated length of modifier / nm	Min. no of monolayers
MP	5, 1 scan	1.6 ± 0.3 [a]	0.6	2
	5, electrolysis time 10 minutes	3.0 ± 0.3		5
PEG	0.8, electrolysis time 10 minutes	3.7 ± 0.3	1.6	2

[a] Samples prepared as part of work in Chapter 9a – Approach (iii): "Fill-in" approach using PDMS microchannels.

For the MP layer, the thickness is larger for an electrolysis time of 10 minutes compared to 1 scan. However, even with a single scan, multilayers of MP are attached. The PEG layer thickness is 3.7 ± 0.3 nm for a layer attached with a 0.8 mM solution and an electrolysis time of 10 minutes. This also corresponds to attachment of more than a monolayer of modifiers. Although the overpotential was significantly more negative for *p*-PEG compared to *p*-MB, the thickness of PEG only correspond to two layers rather than five layers achieved for MP. It is likely that both the lower concentration of *p*-PEG used and the longer *para* substituent of *p*-PEG decreases multilayer formation by hindering attachment of subsequent modifiers to the aryl ring of already attached modifiers and that the influence of overpotential is not as significant as other factors when comparing these two modifiers.

5.3.5. Further experiments on aryl layers

MP

A brief examination of the electrochemical stability of the MP layer (5 mM, electrolysis time 10 minutes) showed that the layer was unchanged after the potential was held at 1.3 V for 10 minutes in ACN/0.1 M $[Bu_4N]BF_4$. This was monitored by FCA CV scans which showed no change before and after application of the potential, indicating that the MP layer is stable at that potential.

MCA

MCA layers were attached to PPF surfaces and used for subsequent coupling reactions. The reaction was amide bond formation between the carboxylic acid groups of the attached MCA layer and amines of tetraethylene glycol diamine (TGD) and was carried out as part of experiments in Chapter 9a. Subsequent attachment of TGD allowed for the assembly of citrate-capped gold NPs onto the surface (Chapter 7). A MCA layer (5 mM, electrolysis time 1 minute, E_f -1.0 V) was immersed overnight in a phosphate buffer (PB) solution with TGD (4 mM), the coupling agent 1-ethyl-3-(3'-dimethylaminopropyl)carbodiimide hydrochloride (EDCI, 40 mM) and the activating agent *N*-hydroxysuccinimide (NHS, 8 mM). The coupling reaction was successful as evidenced by the assembly of citrate-capped gold NPs onto the MCA-TGD layer after an overnight exposure. NPs did not assemble on an identically prepared MCA layer, as discussed in Chapter 7.

NPh

The electrochemical reduction of the *p*-nitrophenyl groups of the NPh layers to yield amino derivatives was investigated because the resulting amino derivatives are useful for subsequent coupling reactions and reduction of these layers are carried out in patterning experiments (Chapter 9a). Reductions were carried out in three different solutions – 0.25 M H_2SO_4, ethanol/water (1:9 by volume) + 0.1 M KCl and 0.02 M benzoic acid/ACN/0.1 M $[Bu_4N]BF_4$.

The NPh modifier surface concentration is commonly estimated from electrochemical reduction CV scans of the *p*-nitrophenyl groups, as outlined in the Introduction. However, the surface concentrations of identically prepared layers obtained from electrochemical reductions in different solutions has not been investigated. In this work, the surface concentration, which indicates the efficiency of reduction, in acid compared to ethanol/water was examined.

Subsequent coupling reactions of nitrobenzoyl chloride (NBC) to NPh layers reduced in acid and ethanol/water were also performed to determine if the reduction products are able to form amide bonds with the acid chloride of NBC. The amount of nitrobenzoyl (NB) coupled was determined by observing the reduction of *p*-nitrophenyl of NB.

Electrochemical reduction in acid and ethanol/water

Identically prepared NPh layers (0.6 mM, electrolysis time 10 minutes) attached to GC surfaces were electrochemically reduced in acid and ethanol/water. The standard reduction process was carried out either in 0.25 M H_2SO_4, 2 scans between 0.7 and -1.0 V or ethanol/water (1:9 by volume) + 0.1 M KCl, 2 scans between 0.5 and -1.4 V. All scans were obtained with a scan rate of 100 mVs^{-1}. Surface concentrations of NPh, NH_2 and coupled NB were estimated electrochemically using NPh layers attached to GC rods, whereas XPS data were obtained from reduced NPh layers on GC plates. Figure 5.8.(i). and Figure 5.8.(ii). show the reduction CV scan in acid and ethanol/water, respectively.

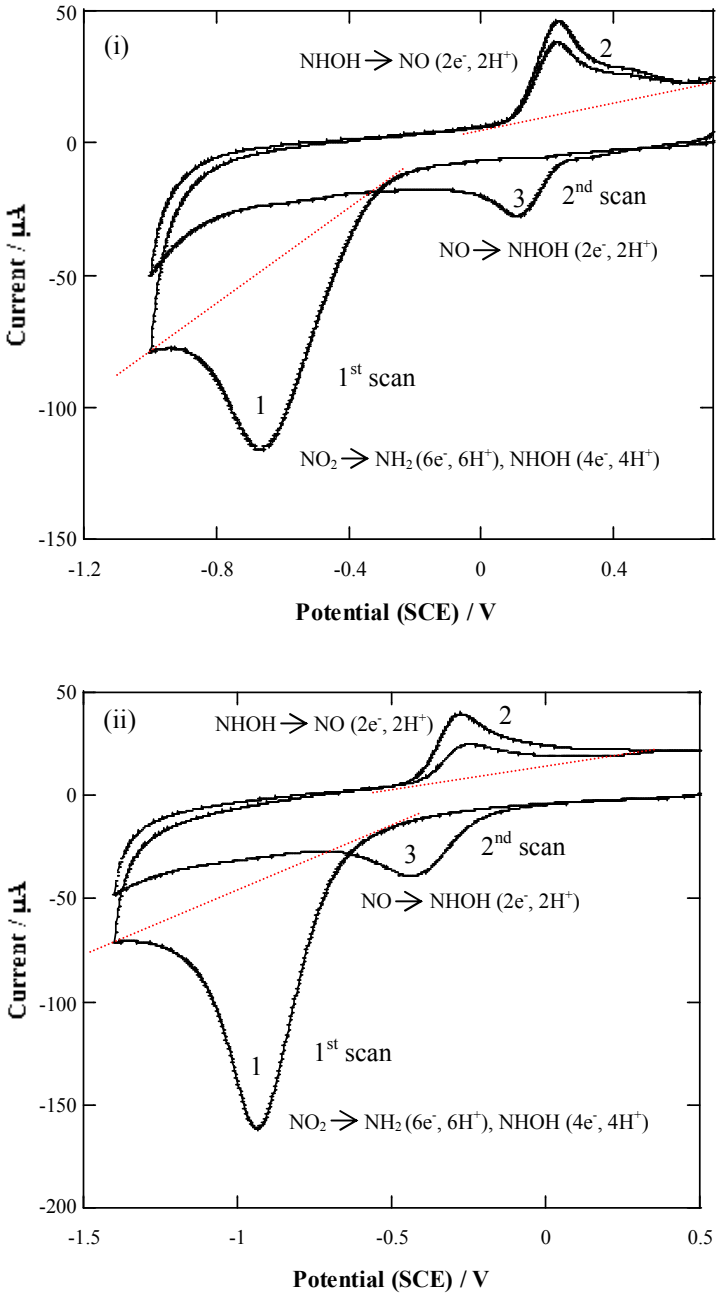

Figure 5.8. CV scans of the reduction of *p*-nitrophenyl groups of NPh layers attached to GC rods in (i) 0.25 M H_2SO_4 and (ii) ethanol/water (1:9 by volume) + 0.1 M KCl. Two reduction CV scans were used for each sample and scan rate for all CV scans = 200 mVs^{-1}.

Reduction CV scans in acid and ethanol/water are as expected for the irreversible reduction of *p*-nitrophenyl groups in a protic solution.[11,12,16] The assignments of each peaks to steps listed in Equations 5.1, 5.2. and 5.3. are shown in Figure 5.8.

5.1. $$]\text{-ArNO}_2 + 2e^- + 2H^+ \longrightarrow]\text{-ArNO} + H_2O$$

5.2. $$]\text{-ArNO} + 2e^- + 2H^+ \rightleftharpoons]\text{-ArNHOH}$$

5.3. $$]\text{-ArNHOH} + 2e^- + 2H^+ \longrightarrow]\text{-ArNH}_2 + H_2O$$

Peak 1 of the first scan is assigned to the reduction of NO_2 to NH_2 and NHOH, peak 2 of the first scan corresponds to the oxidation of NHOH formed in peak 1 to NO. In the second scan, peak 3 is attributed to the reduction of NO back to NHOH and peak 2 is assigned to the oxidation of the NHOH to NO. It is noted that a shoulder is present on peak 2 for the reduction CV scans carried out in acid (Figure 5.8.(i).). The shoulder possibly arises from *p*-nitrophenyl groups in another environment. According to the assignments in the CV scan and considering the reduction scans ended after the oxidation of NHOH to NO, amino derivatives that are expected to be present are NH_2 and NO. However, considering the inequality of peaks 2 (first scan) and 3 in the CV scans, it appears that the NHOH derivative is more chemically stable than NO and it may be assumed that the NHOH derivative is the more stable species of this redox couple under ambient conditions. Hence, NH_2 and NHOH (and possibly NO) groups should be present at the reduced NPh layer.

When reduction was carried out in acid, the peak potentials are at more positive potentials compared to reduction in ethanol/water. This is expected due to the difference in

proton concentration, where reduction is easier in acid due to the higher proton concentration.

From the first reduction CV scan, surface concentration measurements were estimated using linear baselines (shown as dotted lines in Figure 5.8.). The surface concentration of the NPh was calculated from the peak areas 1 plus 2 of the first scan shown in Figure 5.8.(i). and Figure 5.8.(ii). for reductions in acid and ethanol/water, respectively. The total peak area (peak 1 + peak 2) was divided by 6 due to the six-electron process – six electrons are involved in the reduction of NO_2 to NH_2 or of NO_2 to NHOH (four-electron) plus NHOH to NO (two-electron). Table 5.7. lists the NPh surface concentration estimated from the first CV scans. These values rely heavily on the baselines used to determine the peak areas and hence must be viewed as subjected to high levels of uncertainty.

Table 5.7. Electrochemical data for NPh layers after reduction in H_2SO_4 and ethanol/water solutions and also after coupling of NBC.

Reduction process of NPh (solution, no. of scans)	**Surface concentration of NPh / ± 0.5 x 10^{-9} mol.cm^{-2}** [a]	**Surface concentration of NH_2 / ± 1.0 x 10^{-9} mol.cm^{-2}** [a]	**Reduction process of coupled NB** [b] **to NPh, 2 scans**	**Surface concentration of coupled NB / ± 0.5 x 10^{-9} mol.cm^{-2}** [a]
H_2SO_4, 2 scans	3.7	0.4	H_2SO_4	2.0
	3.5	0.5		1.9
H_2SO_4, 100 scans	3.6	0.4	H_2SO_4	1.6
Ethanol/water,	6.2	1.5	Ethanol/water	2.2
2 scans	5.6	1.5		2.2

[a] Surface concentrations were estimated from the first CV scans and all three surface concentrations (NPh, NH_2 and coupled NB) were from the same sample.
[b] Coupled NB was derived from coupling NBC.

From the reductions in acid of the *p*-nitrophenyl groups of the NPh layer, the observed surface concentration of NPh is (3.5 – 3.7 ± 0.5) x 10^{-9} mol.cm^{-2}. This is lower than the observed surface concentration estimated from reductions in ethanol/water which is (5.6 – 6.2 ± 0.5) x 10^{-9} mol.cm^{-2}. A possible reason for the higher number of *p*-nitrophenyl functionalities converted in ethanol/water compared to acid is proposed to be because the NPh multilayer resembles an extended conformation in ethanol/water and thus all or more *p*-nitrophenyl groups are available for reduction. It is also possible that the NPh layer shrinks during reduction in acid which may restrict the number of electroactive *p*-nitrophenyl groups available for reduction. This shrinking effect of layers during reduction in acid is also observed for 4-nitrophenylethylamine (NPEA) layers (Chapter 4). Both these surface concentrations are significantly larger than the calculated surface concentration for a closed-packed monolayer for NPh on a flat surface which is 1.35 x 10^{-9} mol.cm^{-2},[2] which indicates multilayers of NPh are attached during modification.

To calculate the surface concentration of NH_2 groups as a result of the reduction of NPh in acid and ethanol/water, the following equation was used:

$$\text{5.4.} \qquad \frac{\text{peak area 1} - (2 \times \text{peak area 2 (first scan)})}{6}$$

where peak area 1 is for the reduction of NO_2 to NH_2 (six-electron) and NO_2 to NHOH (four-electron) and peak area 2 is the oxidation of NHOH to NO (two-electron). The peak area was divided by 6 as reduction of NO_2 to NH_2 is a six-electron process and the surface

concentration was estimated. Table 5.7. lists the NH_2 surface concentration estimated from the first CV scans.

The surface concentration of NH_2 groups calculated from CV scans in acid is (0.4 – 0.5 ± 1.0) x 10^{-9} mol.cm^{-2} and from CV scans in ethanol/water is (1.5 ± 1.0) x 10^{-9} mol.cm^{-2}. Comparing the surface concentration of NPh and of the NH_2 groups, these values suggest that approximately 13% of the NPh layer is converted to NH_2 groups when reduction is in acid and it is approximately 25% when reduction is in ethanol/water.

NBC was coupled to NPh layers reduced in acid and ethanol/water and the amount of coupled NB was determined by observing the reduction of the *p*-nitrophenyl groups of NB. Coupling was performed in order to determine if the reduction products are able to form amide bonds with the acid chloride of NBC and to assess their amounts.

Figure 5.9.(i). and 5.9.(ii). are the reduction CV scans of the *p*-nitrophenyl groups of coupled NB in acid and ethanol/water, respectively. Scans were carried out in the same solution as reduction of NPh layers and Figure 5.9.(i). and Figure 5.9.(ii). are the same samples as Figure 5.8.(i). and Figure 5.8.(ii), respectively. Comparing Figure 5.8.(i). and Figure 5.9.(i). and Figure 5.8.(ii). and Figure 5.9.(ii), the appearance of a peak at a similar potential to peak 1 is an indication that coupling of NBC has occurred. Compared to the reduction of the NPh layer, the reduction of the coupled NB is slightly less well-defined in comparison. This is presumably due to the *p*-nitrophenyl groups of coupled NB being further away from the electrode and requiring electron transfer over a greater distance or in different environments.

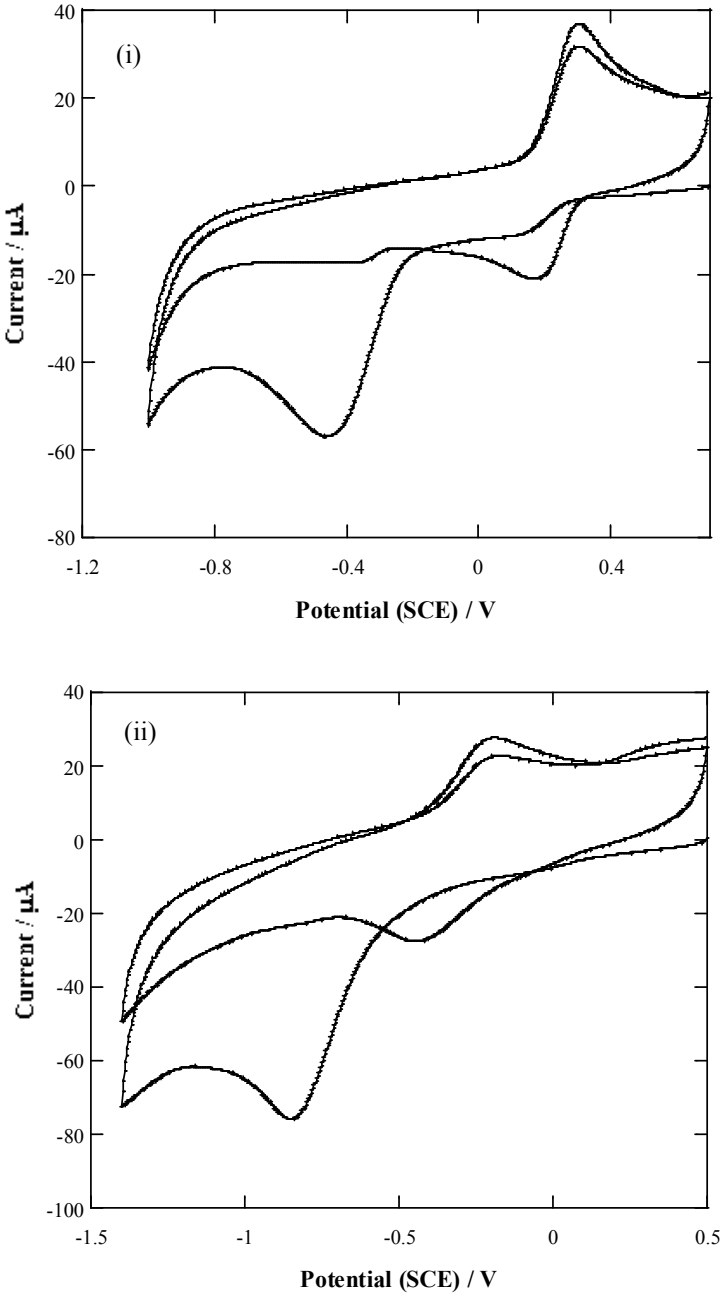

Figure 5.9. CV scans of the reduction of *p*-nitrophenyl groups of NB, coupled to already attached reduced NPh layers on GC rods. Scans were carried out in the same solution as reduction of NPh layers – (i) 0.25 M H_2SO_4 and (ii) ethanol/water (1:9 by volume) + 0.1 M KCl. Figure 5.9.(i). and Figure 5.9.(ii). are the same samples as Figure 5.8.(i). and Figure 5.8.(ii), respectively. Two reduction CV scans were used for each sample and scan rate for all CV scans = 200 mVs^{-1}.

The surface concentration of coupled NB was estimated in the same manner as the surface concentration of NPh. Table 5.7. lists the surface concentrations of coupled NB to NPh layers reduced in acid (2 scans), acid (100 scans) and ethanol/water (2 scans). The longer reduction process of 100 scans was used to investigate whether a higher surface concentration of amino species could be generated for subsequent coupling.

It was anticipated that the surface concentration of the coupled NB groups would be identical to the surface concentration of NH_2 groups if all the NH_2 groups coupled to NBC. However, for both reduction solutions, the surface concentrations of the coupled NB are higher than the surface concentration of the NH_2 groups available for coupling. The ratio of (surface concentration of coupled NB/surface concentration of NH_2 groups after reduction) is 4 for layers initially reduced in acid (2 scans), whereas it is 1.5 for layers initially reduced in ethanol/water (2 scans). The ratio is also 4 when 100 reduction scans in acid was used. This suggests there is no advantage for the prolonged reduction in terms of generating a higher number of amino groups for coupling as there appears to be a 'limited' surface concentration of NBC that can be coupled to the reduced NPh layer (refer later). Considering these data, it is assumed that NBC not only coupled with NH_2 groups but also to NHOH. Other workers have also noted that the NHOH group formed during the incomplete reduction is able to undergo amide bond formation with a carboxylic acid group.[22]

Comparing the surface concentration of NPh (which gives some indication of the efficiency of the reduction), the observed surface concentration in acid is smaller than that in ethanol/water. However, the surface concentrations of coupled NB to the reduced

surfaces in both solutions are similar. This suggested that there is a 'limited' number of NBC species that could be coupled to the reduced layers, possibly only a monolayer on a 'rough' reduced NPh layer. (Calculated surface concentration for a closed-packed monolayer for NPh on a flat surface is 1.35×10^{-9} mol.cm^{-2}.[2])

Electrochemical reduction in ACN

The CV scans for the reduction of *p*-nitrophenyl of NPh (0.6 mM, electrolysis time 2 minutes) on a PPF surface in 0.02 M benzoic acid/ACN/0.1 M $[Bu_4N]BF_4$ are shown in Figure 5.10. Reduction in this solution was carried out as part of experiments in Chapter 9a. The average surface concentration of *p*-nitrophenyl functionalities, calculated from the first reduction scans of different samples, is $(1.5 \pm 0.5) \times 10^{-9}$ mol.cm^{-2}. The water contact angle of the reduced surface decreased from 64 ± 4° of NPh (refer Table 5.5.) to 46 ± 4° and 45 ± 3° after 2 and 10 reduction scans, respectively. This is another indication that reduction had occurred as amino functionalities are more hydrophilic than *p*-nitro groups.

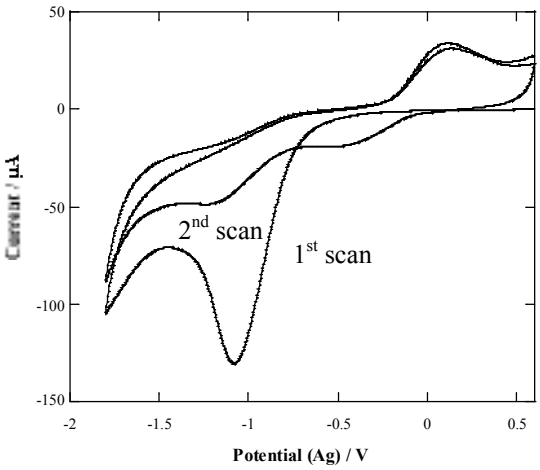

Figure 5.10. Reduction of *p*-nitrophenyl groups of the NPh layer (0.6 mM, electrolysis time 2 minutes) on PPF, in 0.02 M benzoic acid/ACN/0.1 M $[Bu_4N]BF_4$. Two reduction CV scans were carried out and scan rate = 200 mVs^{-1}.

XPS

As outlined in the literature, XPS is a common technique used for analysis of as-prepared and electrochemically reduced NPh layers attached to carbon.[4,5,7,16,19] Figure 5.11. is a representative XPS spectrum of an as-prepared NPh layer.[16] From the spectrum, there are distinctive peaks at 400 and 406 eV, however, there is also a small shoulder/peak at 402 eV. The peak at 406 eV is widely assigned to NO_2 and the peak at 400 eV is variously assigned to azo (-N=N-) groups[5,16,17] (refer above) and NH_2 groups reduced under the XPS beam[19]. The small peak at 402 eV is usually not discussed.

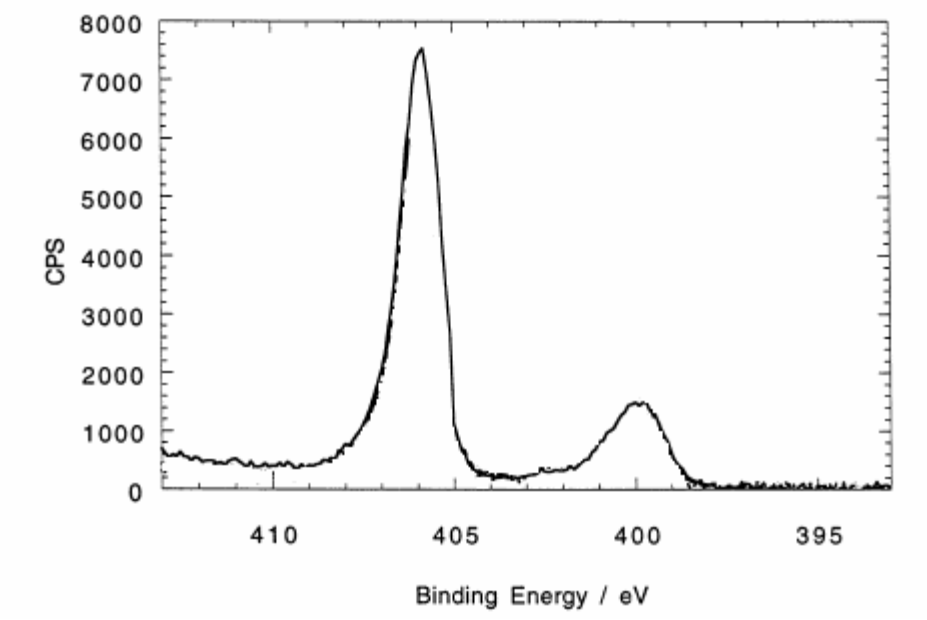

Figure 5.11. A representative XPS spectrum of an as-prepared NPh layer attached to a GC electrode, showing the N_{1s} region from reference 16.

XPS spectra at reduced NPh layers are reported to have peaks at 400 and 406 eV. At the reduced surface, the relative size of the 400:406 peaks is larger in comparison to at the as-prepared layer.[5,16] The peak at 400 eV is assigned to various reduced forms of the *p*-nitrophenyl group – NH_2, NHOH or azoxy ($N{=}N^{+}{-}O^{-}$).[16]

In this work, highly resolved XPS data was obtained of NPh layers electrochemically reduced in acid (H_2SO_4) and ethanol/water in order to firstly, identify all the peaks present in the N_{1s} region, secondly, to attempt to assign the observed N_{1s} peaks and thirdly, to determine whether the reduction products vary with the reduction solution.

Figure 5.12.(i). is a wide scan of the NPh layer reduced in acid and Figure 5.12.(ii). shows the N_{1s} region at high resolution. Table 5.8. lists the samples analysed by XPS and the raw experimental data obtained for the samples. Unless otherwise stated, the conditions

used for reduction here are identical to those used for obtaining the electrochemical data (refer above).

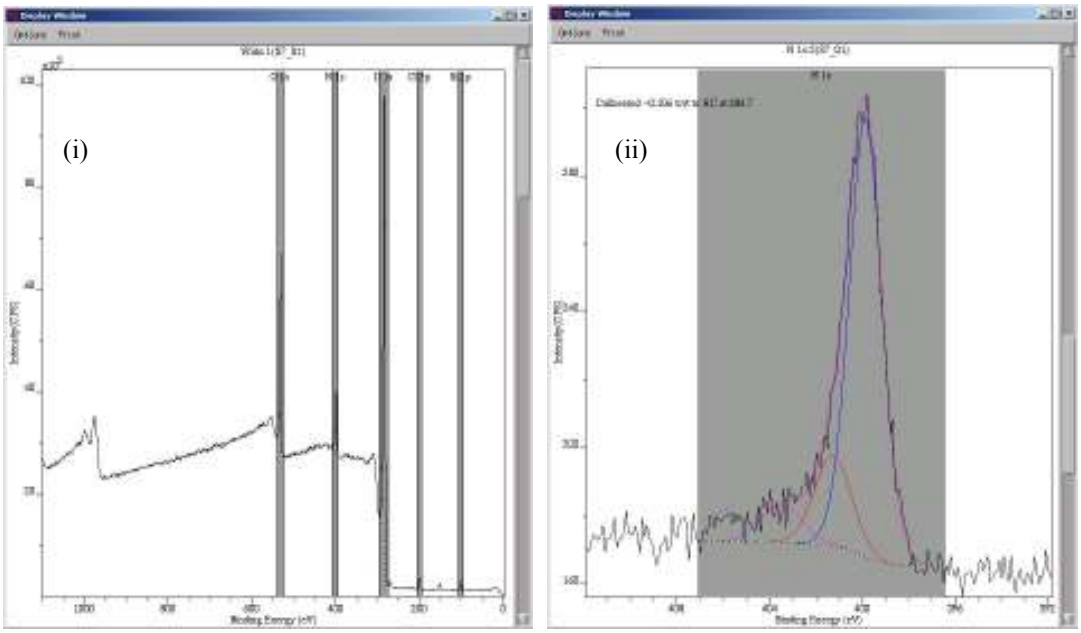

Figure 5.12. XPS spectra of the NPh layer attached to a GC plate reduced in acid. (i) is a wide scan and (ii) is the magnified N_{1s} region.

Table 5.8. Raw experimental XPS data for NPh layers on GC plates after reduction in H_2SO_4 and ethanol/water solutions.

Reduction process of NPh (solution, no. of scans)	**N : C ratio**	**N_{1s} binding energies**	**% at the N_{1s} binding energies**
H_2SO_4, 2 scans	0.08	399.9	71.40
		401.3	16.70
		403.5	7.70
		405.9	4.20
Ethanol/water, 2 scans	0.08	400.0	64.54
		402.0	16.84
		404.1	5.05
		406.1	13.57
	0.06	399.9	57.25
		401.9	27.20
		404.2	6.29
		406.1	9.26
Ethanol/water, potential -0.6 to -1.4 V, 2 scans	0.06	400.0	64.05
		401.9	18.73
		404.2	5.93
		406.1	11.29
Ethanol/water, 1 scan, potential maintained at -1.4 V for 1 hour, then another scan	0.08	400.0	74.10
		402.3	12.40
		404.0	5.80
		406.1	7.70

From the wide scans of the reduced NPh layers, it was calculated that the N : C ratios for all the reduced NPh layers are between 0.06 and 0.08 (Table 5.8.). This indicates that a significant amount of the carbon is sampled from the carbon surface and that all the NPh layers prepared with identical modification conditions are similar. The low ratios may also be a consequence of contamination of samples.

As shown in Figure 5.12.(ii), the spectrum is curve fitted giving four peaks at different binding energies. For all the samples, there are four peaks at different binding energies which are given in Table 5.8. Considering the error in the curve fitting process, the four peak positions for all samples are labelled, for convenience, as 400, 402, 404 and 406 eV (Table 5.9.). These values are used to refer to the order in which the peaks are observed rather than their exact positions, i.e. 400 is the first peak fitted, 402 is the second and so on. Because all the samples are fitted with four peaks, it is very likely that each peak corresponds to the same reduced species in all the samples.

Table 5.9. XPS data for NPh layers on GC plates after reduction in H_2SO_4 and ethanol/water solutions.

Reduction process of NPh (solution, no. of scans)	**Reduction products**			
	% at the N_{1s} binding energies			
	400 eV	**402 eV**	**404 eV**	**406 eV**
H_2SO_4, 2 scans	71.40	16.70	7.70	4.20
Ethanol/water, 2 scans	64.54	16.84	5.05	13.57
	57.25	27.20	6.29	9.26
Ethanol/water, potential -0.6 to -1.4 V, 2 scans	64.05	18.73	5.93	11.29
Ethanol/water, 1 scan, potential maintained at -1.4 V for 1 hour, then another scan	74.10	12.40	5.80	7.70

Table 5.9. shows the percentages of the reduction products corresponding to each binding energy. The percentages for all the samples are relatively similar indicating that the

amounts of each reduction product obtained in acid and ethanol/water are similar. When the reduction potential was between -0.6 and -1.4 V, i.e. with the intention of generating only NH_2 and NHOH (Figure 5.8.), the amounts of each reduction product are similar to when the normal reduction potential range was used. Additionally, the prolonged reduction process of 1 reduction scan followed by maintaining the potential for 1 hour and then another reduction scan also gives similar amounts of the different reduction species compared to 2 scans.

In order to explain these observations, four different nitrogen species are tentatively assigned to the four peaks. The four mostly likely species to be present are NO_2, NH_2, NHOH (and possibly NO) and azo. Considering the experimental data and assignments present in the literature, there are two possible assignment schemes. For both schemes, the peak at 406 eV is assigned to unreacted NO_2 groups with the most certainty and the peak at 404 eV is assigned to NHOH groups. The NHOH group is presumably the most chemically unstable out of the four species and thus is expected to be present in low amounts in the reduced NPh layers.

In the first assignment scheme, the peak at 400 eV is assigned to azo groups. In the literature, a peak at 400 eV is present in the as-prepared layer and is assigned to either azo groups[5,16,17] or NH_2 groups reduced under the XPS beam[19] (refer above). The latter assignment was considered in this work and discounted as the area of the peak at 400 eV did not change over 81 scans of the XPS beam at the same location on the layer. Hence, the peak at 400 eV of the reduced NPh layer is due to the azo groups that were already present in the as-prepared layer. The peak at 402 eV is then assigned to NH_2 species. These

assignments agree with electrochemical data described earlier in this chapter where using 2 reduction scans, approximately 13% of the NPh layer is converted to NH_2 groups when reduction is in acid and it is approximately 25% when reduction is in ethanol/water. Additionally, the ratio of the amounts of species corresponding to XPS peak at 402 eV (NH_2) : 404 eV (NHOH) is on average 3:1 which is consistent with electrochemical data where (peak area 1 – peak area 2 (first scan)) : peak 2 (first scan) (Figure 5.8.) is also approximately 3:1. However, an issue with this scheme is that in the XPS spectrum of the as-prepared NPh layer (Figure 5.11.) the peak at 400 eV is only approximately 20% of the peak at 406 eV (NO_2) and in the experimental data (Table 5.9.), the peak at 400 eV is approximately 66% of all the nitrogen species present. It is not expected that the amount of azo groups increases when the NPh layer is reduced. This remains an unsolved difficulty with this assignment scheme.

In the second assignment scheme, the peak at 400 eV is assigned to the NH_2 groups of the reduced NPh layers because it corresponds to the highest amount of all the reduction products (Table 5.9.). The peak at 402 eV is then assigned to azo groups. One of the issues with this scheme is that a peak at 400 eV is present at the as-prepared layer (Figure 5.11.) and NH_2 is a reduction product. The other problem is that the relative amounts do not agree with the surface concentrations of NH_2 groups obtained from the electrochemical data (refer above). As previously mentioned, the surface concentrations rely heavily on the baselines used to determine the peak areas and hence are subject to high levels of uncertainty.

In summary, the assignments of the peaks are as follows: 400 eV could be azo (and hydrazine derivatives) or NH_2, 402 eV is then assigned as NH_2 or azo, 404 eV is NHOH (and possibly NO) and 406 eV is NO_2. Although there is some uncertainty with assigning reduction products to the four peaks, the highly resolved XPS data has shown that there are more than the two typically reported peaks (400 and 406 eV) present at the reduced NPh surfaces. Future work is intended to be carried out to enable a more certain assignments of the XPS peaks. One important sample to analyse is the as-prepared NPh layer using this particular XPS instrument, in order to determine if the peaks at 400 and 402 eV are present prior to reduction. Another important sample for XPS analysis is a nitroazobenzene layer to be analysed before and after reduction. Prior to reduction it consists of azo and NO_2 functionalities and after reduction it should have hydrazine derivatives, NHOH and NH_2 groups. By process of elimination, these further experiments should allow more definite assignments.

5.4. Conclusions

In this chapter, five aryl layers – MP, HP, PEG, MCA and NPh, were attached to carbon surfaces by the electrochemical reduction of aryl diazonium cations. The synthesis and electrochemical attachment of aryl diazonium cations and characterisation of the aryl layers were discussed.

From the CV scans for the electrochemical attachment of the diazonium cations, it appeared that with the majority of the modifiers E_{pc}, which indicates the ease of reduction,

followed the Hammett parameter. Modifiers with *para* substituents that are electron withdrawing such as *p*-NB has a less negative E_{pc} as they are easier to reduce.

As discussed in the Introduction, the surface concentration and thickness of layer were dependent on the aryl derivative, the modifier concentration, the applied reduction potential, the modification (electrolysis) time and the type of carbon surface. In this work, probe scans at the layers showed that 'loosely packed' layers were present when long substituents were present.

Water contact angle indicated that the majority of these layers are hydrophobic and the wettability of the layers are somewhat modulated by the hydrophobicity of the *para* substituent of the modifier. Layers modified with different electrolysis times gave different water contact angles. AFM depth profiling showed multilayer formation for MP and PEG layers, even when the modification procedure was one cyclic scan.

Subsequent coupling reactions of TGD to MCA and NBC to electrochemically reduced NPh layers via amide bond formations were carried out. The *p*-nitrophenyl groups of the NPh layers were reduced to amino functionalities via irreversible reductions in protic solutions of acid, ethanol/water and ACN. For layers reduced in acid and ethanol/water, the surface concentration of NPh as estimated from reduction scans was higher in ethanol/water compared to acid. NBC was successfully coupled to NPh layers reduced in acid and ethanol/water, via amide bond formations with the NH_2 and NHOH functionalities. Also, experiments suggested that only a 'limited' number of NBC species were coupled to the reduced layers.

Four peaks were observed in XPS spectra collected at the reduced NPh layers. The different peaks were tentatively assigned as 400 eV could be azo (and hydrazine derivatives) or NH_2, 402 eV is then assigned as NH_2 or azo, 404 eV is NHOH (and possibly NO) and 406 eV is NO_2. Future work is intended to be carried out to enable a more certain assignments of peaks.

5.5. References

(1) Bernard, M.-C.; Chausse, A.; Cabet-Deliry, E.; Chehimi, M. M.; Pinson, J.; Podvorica, F.; Vautrin-Ul, C. *Chemistry of Materials* **2003**, *15*, 3450-3462.

(2) Pinson, J.; Podvorica, F. *Chemical Society Reviews* **2005**, *34*, 429-439.

(3) Kariuki, J. K.; McDermott, M. T. *Langmuir* **2001**, *17*, 5947-5951.

(4) Liu, Y.-C.; McCreery, R. L. *Journal of the American Chemical Society* **1995**, *117*, 11254-11259.

(5) D'Amours, M.; Belanger, D. *Journal of Physical Chemistry B* **2003**, *107*, 4811-4817.

(6) Downard, A. J.; Prince, M. J. *Langmuir* **2001**, *17*, 5581-5586.

(7) Allongue, P.; Delamar, M.; Desbat, B.; Fagebaume, O.; Hitmi, R.; Pinson, J.; Saveant, J.-M. *Journal of the American Chemical Society* **1997**, *119*, 201-207.

(8) Delamar, M.; Hitmi, R.; Pinson, J.; Saveant, J. M. *Journal of the American Chemical Society* **1992**, *114*, 5883-5884.

(9) Anariba, F.; DuVall, S. H.; McCreery, R. L. *Analytical Chemistry* **2003**, *75*, 3837-3844.

(10) Anariba, F.; Viswanathan, U.; Bocian, D. F.; McCreery, R. L. *Analytical Chemistry* **2006**, *78*, 3104-3112.

(11) Brooksby, P. A.; Downard, A. J. *Langmuir* **2004**, *20*, 5038-5045.

(12) Brooksby, P. A.; Downard, A. J. *Journal of Physical Chemistry B* **2005**, *109*, 8791-8798.

(13) Bahr, J. L.; Yang, J.; Kosynkin, D. V.; Bronikowski, M. J.; Smalley, R. E.; Tour, J. M. *Journal of the American Chemical Society* **2001**, *123*, 6536-6542.

(14) Wang, J.; Firestone, M. A.; Auciello, O.; Carlisle, J. A. *Langmuir* **2004**, *20*, 11450-11456.

(15) Ruffien, A.; Dequaire, M.; Brossier, P. *Chemical Communications* **2003**, 912-913.

(16) Ortiz, B.; Saby, C.; Champagne, G. Y.; Belanger, D. *Journal of Electroanalytical Chemistry* **1998**, *455*, 75-81.

(17) Saby, C.; Ortiz, B.; Champagne, G. Y.; Belanger, D. *Langmuir* **1997**, *13*, 6805-6813.

(18) Bureau, C.; Levy, E.; Viel, P. *PCT International Applications* **2003**, WO 03018212.

(19) Combellas, C.; Kanoufi, F.; Pinson, J.; Podvorica, F. I. *Langmuir* **2005**, *21*, 280-286.

(20) Allongue, P.; de Villeneuve, C. H.; Pinson, J. *Electrochimica Acta* **2000**, *45*, 3241-3248.

(21) Liu, Y.-C.; McCreery, R. L. *Analytical Chemistry* **1997**, *69*, 2091-2097.

(22) Bath, B. D.; Martin, H. B.; Wightman, R. M.; Anderson, M. R. *Langmuir* **2001**, *17*, 7032-7039.

(23) Solak, A. O.; Eichorst, L. R.; Clark, W. J.; McCreery, R. L. *Analytical Chemistry* **2003**, *75*, 296-305.

(24) Exner, O.; Chapman, N. B. E.; Shorter, J. E. *Correlation Analysis in Chemistry*; Plenum Press, **1978**.

(25) Jakubowicz, A.; Jia, H.; Wallace, R. M.; Gnade, B. E. *Langmuir* **2005**, *21*, 950-955.

(26) Roux, S.; Duwez, A.-S.; Demoustier-Champagne, S. *Langmuir* **2003**, *19*, 306-313.

(27) Vogler, E. A. *Advances in Colloid and Interface Science* **1998**, *74*, 69-117.

6.1. Introduction

The ability to control non-specific adhesion of protein to surfaces is important to prevent fouling of biomaterials and surface-based sensor devices.[1,2] Non-specific adhesion involves physical adsorption which results from attractive forces such as ionic, hydrophobic and/or van der Waals and is entropically driven.[3] Biofouling begins with protein adhesion which triggers the formation of a biofilm containing cells, bacteria and other micro-organisms.[1,4] On the other hand, protein adhesion may be the desired interaction. For example, positioning of proteins at specific sites on the surface allows for the fabrication of biological diagnostic devices.[5]

A large amount of research has been directed at fabrication of chemically well-defined surfaces that either promote or reduce protein adsorption. Many properties of the modifier are shown to contribute to the protein-surface interaction. These include the hydrophobicity, charge and the head group of the modifier when it is attached to the substrate. The effect of the underlying substrate is considered minimal when the modifier layer is attached. Whitesides and co-workers identified four characteristics of head groups of self-assembled monolayers (SAMs) attached to gold surfaces that resist the adsorption of protein: these terminal functional groups are hydrophilic; include hydrogen-bond acceptors; do not include hydrogen-bond donors and their overall charge is neutral.[6] The pH of the protein solution influences the charge on the surface and the protein. At a pH higher than the isoelectric point of the protein, the protein is overall negatively charged and will bind via electrostatic interactions to a positively charged surface.[7] However, protein has also been shown to bind to negatively charged surfaces at a pH where the protein is overall

negatively charged.[8] This was accounted for by the groups of the protein such as lysine (R group = NH_2) that can have electrostatic interactions with the negatively charged surface. Other studies of bovine serum albumin (BSA) adsorbing to SAMs on gold surfaces reveal that non-specific adsorption is reduced in the following order: ethylene glycol > OH > NH_3^+ > COO^- > hydrophobic.[8] However, other studies have shown that hydrophobic interactions do not play a significant role,[1,9] in comparison to steric effects, for example.[1,6] The amount of water associated with the modified surface has commonly been found to be important in influencing its resistance to protein adsorption.[6] The presence of functional groups that are able to have strong interactions with water causes the surface to be protein repellent.[6,10] In summary, current research shows that the mechanism for protein adsorption is not well-defined and that a combination of components affects protein adsorption onto a given surface.[6,11]

The common modifiers coated onto surfaces to render them non-fouling and protein-resistant are poly(ethylene glycol) modifiers and their derivatives.[1,2,6] Resistance to protein adsorption is observed when these modifiers are attached to various substrates including silicon,[4,12] polystyrene,[11] and diamond[12]. With these polymers, molecular conformation, surface concentration and molecular weight influence the protein-surface interaction.[4,10,11,13] As a rule, protein repulsion increases with the extended polymer conformation and with a higher surface concentration of a longer polymer. The amount of hydration via hydrogen bonds on and within the modifier layer is also believed to be important, where the more water molecules present in the close-packed modifier layer, the more resistant the surface is.[10,14] Although it is commonly used, poly(ethylene glycol)

decomposes in the presence of oxygen and transition metal ions and is not protein repulsive at temperatures above 35 °C.[10]

The aims of this work are two-fold. The first goal is to determine the protein adsorption properties of amine and aryl layers covalently attached to glassy carbon (GC) surfaces. The second objective is to investigate the ability of fluorescence microscopy, in conjunction with a fluorescently labelled protein, to provide semi-quantitative estimates of protein adsorption on modified GC surfaces. Other methods that have been used to examine the adsorption of protein at surfaces are contact angle measurements,[9,11] ellipsometry,[4,6] surface plasmon resonance,[2,6,10,11,15] x-ray photoelectron spectroscopy (XPS),[2,9,12] atomic force microscopy (AFM)[1,11,13] and electrochemical techniques including voltammetry,[16-18] capacitance measurements[19] and impedance spectroscopy[16,19,20]. A limitation of these methods is that they provide spatially unresolved information about protein adsorption. Fluorescence microscopy is able to yield spatially resolved details that is important for examining patterned surfaces, for example.

6.2. Experimental methods

6.2.1. Preparation of GC plates

Preparation of GC plates was as detailed in Chapter 4 and 5.

6.2.2. Electrochemistry

Electrochemical settings for surface modifications used in this chapter were adopted from Chapter 4 for amines and Chapter 5 for aryl diazonium salts. A circular area in the centre of each GC plate was modified, using the cell set-up as described in Chapter 2.

6.2.3. Fluorescent tagged protein – BSA-FITC

BSA labelled with the fluorophore, fluorescein isothiocyanate (BSA-FITC) was purchased as fluorescent orange crystals from Sigma (stored at ~ -4 °C) and used as a 1 mg mL^{-1} phosphate buffer (PB) solution (pH 7.4).

Protein treatment

Modified GC plates were incubated in BSA-FITC solution for 1 hour at room temperature in the dark to avoid possible photobleaching of the FITC tag. The BSA-FITC solution was agitated on the orbital shaker only for the first 30 minutes of the treatment. The samples were then removed from the protein solution and washed with PB in two steps. The surface was immersed in PB and the beaker agitated by swirling for 30 seconds. The surface was then placed into another PB solution and the beaker agitated on the orbital shaker for 5 minutes. Samples were stored in fresh PB solution in the dark for up to 4 hours before analysis.

Visualisation of protein

Modified GC plates treated with BSA-FITC were visualised using fluorescence microscopy. The excitation filter of the Hg arc lamp was set between 470 – 500 nm to transmit blue light. The lamp was warmed up for 1 hour prior to analysis. Samples were analysed wet by positioning the plate face down on a small volume of PB dispensed onto the cover slip. The samples were analysed with the lowest objective (10 x) to capture the largest area (500 x 500 μm) for fluorescence intensity analysis. All images were taken with a standard camera exposure time of 6 seconds. Four images were typically captured at the boundary of the modified/BSA-FITC : GC/BSA-FITC regions, as shown in Figure 6.1. The modified/BSA-FITC : GC/BSA-FITC boundary was formed by the gasket used to define the working electrode area during modification. Adsorption of protein at the modified surface was compared with that at an as-prepared GC surface. The total time that the sample was exposed to the blue light was 15 minutes.

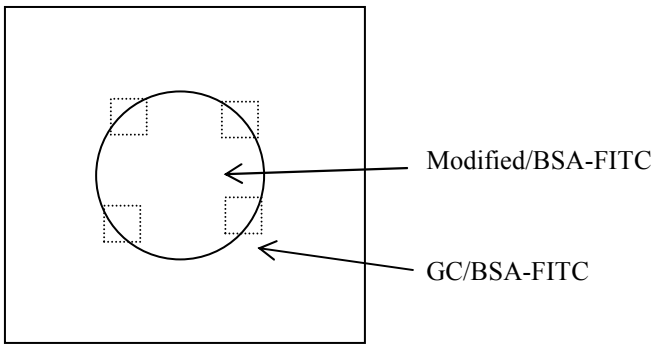

Figure 6.1. A schematic of a sample modified and treated with BSA-FITC. Dotted lines are the images taken at the modified/BSA-FITC : GC/BSA-FITC boundary.

Quantification of the fluorescence of protein

The fluorescence intensity was quantified for the images taken at the modified/BSA-FITC : GC/BSA-FITC boundary, using Image Pro Plus software. One area of interest (AOI) was drawn in each of the regions on either side of the boundary and the FITC fluorescence intensity within the AOI was quantified. Each AOI covered the majority of each region. The fluorescence intensity ratio for that image was calculated by dividing the fluorescence measured in the AOI positioned in the modified region by that measured in the as-prepared GC region. The average of the intensity ratios from the four images was the ratio for that sample and the error is expressed as the standard deviation of the ratios. The AOI was not positioned near the boundary as the boundary was found to be atypically fluorescent. Raw fluorescence intensity measurements are listed in Appendix 6. The ratios and standard deviations for all samples of a particular modifier were averaged to give a mean fluorescence intensity ratio and an uncertainty for that modifier.

Removal of protein

Protein removal from surfaces was carried out by sonicating samples for 5 minutes in each of the three solutions (in the order listed): 5% Tween 20 detergent; hot tap water and cold tap water.

6.3. Results and discussion

Modifiers were selected for protein adsorption studies on the basis of previous studies regarding molecular characteristics that control protein adhesion (refer Introduction).

The six modifier layers selected included three layers that were grafted by oxidation of primary amines: tetraethylene glycol diamine (TGD), *n*-hexylamine (HA) and polyethylene glycol diamine (PGD) and three layers that were grafted by the reduction of corresponding aryl diazonium salts: *para* methyl phenyl (MP), *para* hexyl phenyl (HP) and *para* polyethylene glycol phenyl (PEG). For each modifier, the influence of the layer on protein adhesion could be only tentatively predicted due to the large number of possible contributing factors. It is expected that TGD, PGD and PEG would decrease protein adhesion and HA, MP and HP would increase protein adhesion. Table 6.1. lists the samples prepared. All the modifier layers were attached to the GC plates using an electrolysis time of 10 minutes. The thicknesses (when attached onto pyrolysed photoresist film (PPF) surfaces) and water contact angle measurements of these layers attached using identical modification conditions are detailed in Chapters 4 and 5 and listed in Table 6.1. Considering the calculated lengths of these modifiers, the thicknesses correspond to between 1 and 5 molecular layers. The water contact angles are relevant here as these measurements indicate the wettability of the modifier layers attached to GC surfaces and thus help to predict protein behaviour at the layers. Between two and nine samples were prepared using each modifier (Table 6.1.).

After preparation of the modified surfaces, the samples were incubated in BSA-FITC solution for 1 hour in the dark. BSA is a globular serum protein (Mr = ~66,000 Daltons) and its isoelectric point is 4.6 and therefore has with a net negative charge at pH 7.4.[8,21] BSA is a 'benchmark' protein commonly used in adsorption studies due to its ease of handling and low cost. The fluorescent tag, FITC, has a maximum absorbance at λ =

490 nm (blue light) and emits at λ = 515 nm (green light). After 1 hour, the samples were removed and analysed using fluorescence microscopy.

In initial experiments, the ability of fluorescence microscopy and Image Pro Plus to provide useful information about protein adsorption was investigated. It was quickly established that it is not meaningful to compare the fluorescence intensity from an image captured entirely in the modified region with another captured entirely in the as-prepared GC region because absolute fluorescence intensities varied from image to image taken in the same region. This is possibly due to variations in intensity of excitation light from the Hg lamp and/or the method the software uses to quantify the fluorescence in an image. Therefore, in order to obtain semi-quantitative information about protein adsorption from the fluorescence images, images have to be captured at the boundary to allow direct comparison of the fluorescence from the two regions in the one image.

Another aspect that was considered was the 'warm-up' time of the Hg lamp. The fluorescence intensity ratio for a TGD-modified protein treated GC plate was analysed every minute for 100 minutes. The ratios were found to vary during the first 60 minutes and then were constant. Thus, the lamp was left on for 1 hour prior to analysis of samples. This result also demonstrates that the protein-treated samples are resistant to photobleaching over a period of 100 minutes. The variation of camera exposure time also seemed to affect the fluorescence ratios. Hence, a standard exposure time of 6 seconds was used. Further, the stability of the protein-treated samples was examined. The surfaces are stable to storage in buffer for at least 4 hours and to 6 minutes sonication in PB. The intensity ratios were unchanged after these treatments.

Typical fluorescence microscope images obtained for surfaces modified with PGD and MP are shown in Figure 6.2. For clarity, the contrast and brightness of each image has been adjusted individually. The mean intensity ratios and the associated uncertainty of the modified/BSA-FITC : GC/BSA-FITC boundary for all the samples with the same modifier are listed Table 6.1.

Fluorescence intensity ratios of greater than 1 are obtained for surfaces modified with TGD, MP, HP and PEG, indicating that these modifiers promote greater adsorption of protein than does as-prepared (polished) GC. In contrast, modification with HA and PGD leads to a decrease in measured fluorescence intensity indicating that BSA-FITC adsorption is lower at these modified surfaces compared with as-prepared GC. In all samples, protein adsorbs at both the modified area and as-prepared GC, i.e. no modifier completely prevents protein adsorption under these conditions. Modification with PGD using solution concentrations of 50 and 20 mM gives the same intensity ratio suggesting that the layers formed with these two concentrations are similar.

Table 6.1. Properties of the samples used in protein adsorption experiments and fluorescence intensity ratios calculated at the modified/BSA-FITC : GC/BSA-FITC boundary for the samples. All samples were modified with an electrolysis time of 10 minutes.

Modifier	**Modifier structure** Ar = aryl ring	**Modifier concentration / mM**	**Thickness of layer / nm**	**Minimum no. of monolayers**	**Water contact angle / °**	**Surface wettability?** [a]	**Fluorescence intensity ratios (no. of samples)**
TGD	]-$NHCH_2CH_2(OCH_2CH_2)_3NH_2$	200	Not measured		45 ± 3	Hydrophilic	2.1 ± 0.4 : 1 (9)
HA	]-$NH(CH_2)_5CH_3$	5	3.0 ± 0.3	3	77 ± 2	Hydrophobic	0.7 ± 0.1 : 1 (7)
PGD	]-$NHCH(CH_3)CH_2$-$(OCH(CH_3)CH_2)_a$-$(OCH_2CH_2)_b$-$(OCH(CH_3)CH_2)_cNH_2$ a + c = 2.5, b = 40.5; a, b and c being average values	50	5.1 ± 0.3	1	Not measured	Hydrophilic [b]	0.7 ± 0.1 : 1 (2)
		20	Not measured		59 ± 3		0.7 ± 0.1 : 1 (3)
MP	]-$ArCH_3$	5	3.0 ± 0.3	5	63 ± 3	Hydrophobic	1.5 ± 0.2 : 1 (8)
HP	]-$Ar(CH_2)_5CH_3$	5	Not measured		72 ± 3	Hydrophobic	1.3 ± 0.1 : 1 (4)
PEG	]-$Ar(OCH_2CH_2)_3OCH_3$	5	Not measured		Not measured	Hydrophilic [b]	2.2 ± 0.5 : 1 (2)

[a] When the water contact angle is above 65°, the layer is considered hydrophobic.[22]
[b] Surface wettability as predicted based on the modifier structure.

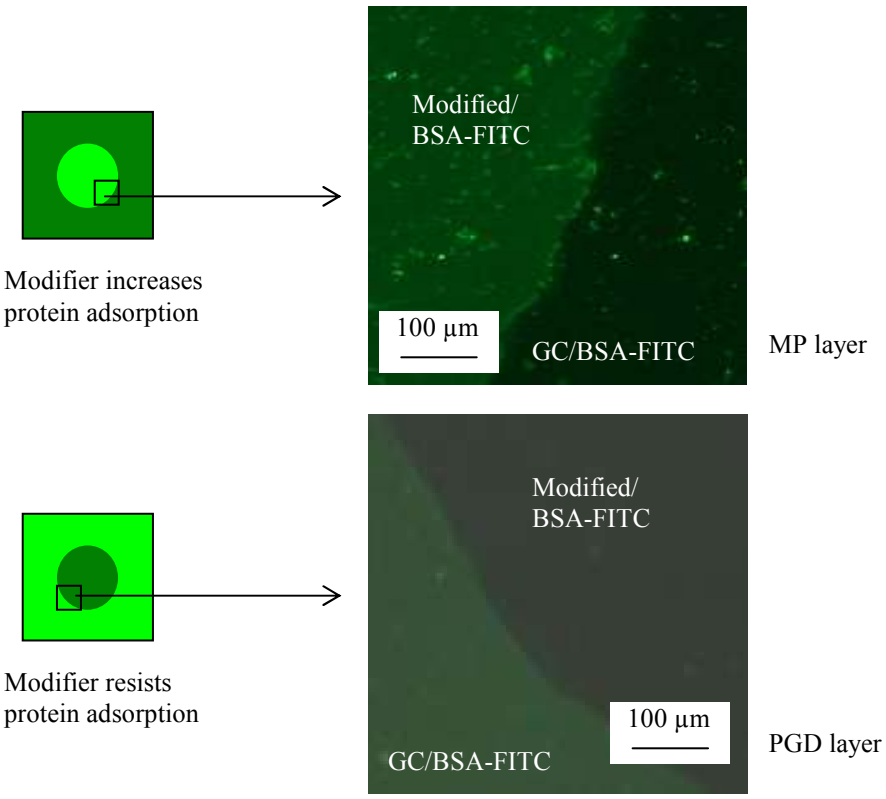

Figure 6.2. Fluorescence microscope images captured at a MP/BSA-FITC : GC/BSA-FITC boundary where MP promotes BSA-FITC adsorption and at PGD modified/BSA-FITC : GC/BSA-FITC boundary where PGD disfavours BSA-FITC adsorption.

A series of control surfaces were also prepared to examine whether the potentials applied during modification alters the GC surfaces and hence influences protein adsorption. The potentials used for the modification with amines or aryl diazonium cations were applied to the as-prepared GC plates in the absence of the amine modifier or aryl diazonium cation. All these control surfaces gave a fluorescence intensity ratio of 1:1, i.e. no difference between the electrochemically-treated area and as-prepared GC. Another control experiment was the examination of modified surfaces which had not been exposed to BSA-

FITC. None of the modifiers are fluorescent. These experiments confirm that the modifier layers are indeed modulating protein adsorption on GC.

To attempt to account for the observed effects of modifier layers on protein adhesion, the properties of each of the modifiers are considered. TGD is hydrophilic, has an ethylene glycol chain and consists of protonated amines at pH 7.4 which are hydrogen-bond donors. HA is hydrophobic and consists of protonated amines at pH 7.4 which are hydrogen-bond donors. PGD has similar properties as TGD; however, it is a longer modifier that is expected to favour the extended conformation in the aqueous protein solution. MP and HP modifiers are both hydrophobic and neutral. The PEG modifier is hydrophilic (as predicted from the structure of the *para* substituent), has a hydrophilic ethylene glycol chain and a hydrophobic aryl group and is neutral. From previous studies as detailed in the Introduction, modifiers that are hydrophobic and have protonated amines which are hydrogen-bond donors have shown to increase protein adsorption, whereas modifiers that are hydrophilic, neutral, long and with ethylene glycol chains have shown to decrease it. Considering the properties of the modifiers, it is clear that predicting whether protein adsorption would be increased or resisted at a modifier layer is not straightforward. Most of the selected modifiers have competing properties influencing protein adsorption. However, a few comments can be made.

For the PGD, MP and HP modifiers, the low surface wettability of the layer appears to be a governing factor in controlling protein adhesion. The decreased adhesion on PGD-modified surfaces may also be due to its length and extended conformation. However, for the other three modifiers – TGD, HA and PEG, other factors apart from the surface

wettability appear to be influential. It is suggested that regarding TGD layers, the electrostatic interactions between the protein and surface is more prominent compared to hydrophilic interactions. The positive charge on the amines on the hydrophilic TGD allows for electrostatic associations with the overall negatively charged BSA. The ratio of amine groups to ethylene glycol groups is much greater for TGD than for PGD, possibly accounting for increased BSA-FITC adsorption at TGD-modified GC and decreased adsorption at PGD-modified GC. With the HA layers, the decreased protein adhesion is difficult to explain. It is possible that the protonation of the buried amines within the layer compromises the low surface wettability (hydrophobicity) and hence protein adhesion capabilities of the HA layer. Although the amines are protonated, they are buried within the layer and hence their electrostatic effect on the protein is shielded to some extent. With the TGD layer, the intrinsic hydrophilic nature is unlikely to be enhanced by the protonation of the amine groups. Thus, charge effects are more likely to be dominant for TGD rather than HA.

All modified surfaces prepared from reduction of aryl diazonium cations promote adsorption of BSA-FITC at GC. Related work demonstrates that multilayers prepared by this method have low surface concentrations per layer[23,24] and for nitroazobenzene, the layers have greater than 50% free volume.[24] Based on these findings, PEG layers are expected to be 'loosely packed' and thus to exhibit compromised protein resistance. The outstanding protein resistant properties reported for PGD SAMs on gold surfaces appear to rely on close-packing of the PGD chains which traps water within the layer;[14] this mechanism is presumably not operative here. Additionally, the open, loose structure of the

multilayers may result in access of protein to hydrophobic aryl groups within the modifying layer, promoting protein adsorption.

Considering the fluorescence intensity data, none of the modified GC surfaces are very good at either promoting or reducing protein adsorption as compared to other studies for example with SAMs on gold surfaces with well-tailored head groups.[2,10] Possible reasons for this are that the underlying GC surface has a strong effect on the protein behaviour, the majority of modifiers have properties and groups with competing effects on protein adsorption and the modifier layers on GC surfaces are very different from SAMs on gold, for example, they are more 'loosely packed'. The properties and groups that have been shown to control protein adhesion are for SAMs on gold (refer Introduction) and may not be applicable to modifier layers on GC surfaces.

The data in Table 6.1. also allow comment on the utility of fluorescence microscopy for examining protein adhesion. For all modifiers, every calculated intensity ratio for a particular modifier has the same relationship to the as-prepared GC surface, i.e. all ratios are either greater than or less than 1. For some modifiers, there is a large range of intensity ratios. Subtle sample-to-sample differences in the layer preparation appear to be the most likely factor to account for these variations. Fluorescence microscopy provides both a qualitative and semi-quantitative measure of protein adhesion.

6.4. Conclusions

Selected modifiers – TGD, HA, PGD, MP, HP and PEG were attached to GC plates and treated with fluorescently labelled protein, BSA-FITC. Fluorescence images were taken

at the boundary of the modified layer and the as-prepared GC. The fluorescence intensities from each side of the boundary were compared to give fluorescence intensity ratios. For each modifier, the properties of the modifier were considered and the protein behaviour at the layer was attempted to be predicted based on previous studies of SAMs assembled on gold surfaces. However, predictions were not straightforward. Results showed that TGD, MP, HP and PEG layers promoted protein adsorption relative to as-prepared GC, whereas HA and PGD disfavoured protein adsorption. For the PGD, MP and HP modifiers, the low surface wettability (hydrophobicity) of the layer appeared to be a governing factor in controlling protein adhesion. For the other modifiers – TGD, HA and PEG, possible explanations for the unexpected behaviour were tentatively assigned to the competing roles between charge/charge density and hydrophobic interactions. The results gave insight into some of the factors controlling protein adsorption at these surface layers and identified modifiers which increased or decreased adsorption of BSA-FITC at GC surfaces.

Comparing these modified GC surfaces to other studies, these surfaces are not very good at either increasing or decreasing protein adsorption. In order to improve the ability of modified GC surfaces to control protein behaviour, future work would involve more careful tailoring of the modifiers so that all the properties and groups present in the layer would either promote or reduce protein adhesion. Longer modifiers would also be of interest in order to attempt to minimise the influence of the underlying GC. However, results described in this work are still of interest, especially for assembling protein on patterned surfaces. Assembly of fluorescently labelled protein would enable the visualisation of

modifiers that promote protein adsorption against a surrounding area of modifiers that resist protein adsorption.

The fluorescence microscopy method of monitoring protein adsorption was simple to use and, even without image capture and analysis, gave an immediate indication of whether a modifier increases or decreases BSA-FITC adsorption relative to as-prepared GC.

6.5. References

(1) Wang, M. S.; Palmer, L. B.; Schwartz, J. D.; Razatos, A. *Langmuir* **2004**, *20*, 7753-7759.

(2) Chen, S.; Liu, L.; Jiang, S. *Langmuir* **2006**, *22*, 2418-2421.

(3) Blawas, A. S.; Reichert, W. M. *Biomaterials* **1998**, *19*, 595-609.

(4) Norde, W.; Gage, D. *Langmuir* **2004**, *20*, 4162-4167.

(5) Kumar, N.; Hahm, J. *Langmuir* **2005**, *21*, 6652-6655.

(6) Ostuni, E.; Chapman, R. G.; Holmlin, R. E.; Takayama, S.; Whitesides, G. M. *Langmuir* **2001**, *17*, 5605-5620.

(7) Lund, M.; Kesson, T.; Joensson, B. *Langmuir* **2005**, *21*, 8385-8388.

(8) Brewer, S. H.; Glomm, W. R.; Johnson, M. C.; Knag, M. K.; Franzen, S. *Langmuir* **2005**, *21*, 9303-9307.

(9) Sweryda-Krawiec, B.; Devaraj, H.; Jacob, G.; Hickman, J. J. *Langmuir* **2004**, *20*, 2054-2056.

(10) Chen, S.; Zheng, J.; Li, L.; Jiang, S. *Journal of the American Chemical Society* **2005**, *127*, 14473-14478.

(11) Lazos, D.; Franzka, S.; Ulbricht, M. *Langmuir* **2005**, *21*, 8774-8784.

(12) Clare, T. L.; Clare, B. H.; Nichols, B. M.; Abbott, N. L.; Hamers, R. J. *Langmuir* **2005**, *21*, 6344-6355.

(13) Pasche, S.; Textor, M.; Meagher, L.; Spencer, N. D.; Griesser, H. J. *Langmuir* **2005**, *21*, 6508-6520.

(14) Harris, J. M.; Zalipsky, S. *Poly(ethylene glycol): Chemsitry and Biological Applications*; American Chemical Society, **1997**.

(15) Holmlin, R. E.; Chen, X.; Chapman, R. G.; Takayama, S.; Whitesides, G. M. *Langmuir* **2001**, *17*, 2841-2850.

(16) Diniz, F. B.; Ueta, R. R. *Electrochimica Acta* **2004**, *49*, 4281-4286.

(17) Moulton, S. E.; Barisci, J. N.; Bath, A.; Stella, R.; Wallace, G. G. *Journal of Colloid and Interface Science* **2003**, *261*, 312-319.

(18) Downard, A. J.; Bin Mohamed, A. *Electroanalysis* **1999**, *11*, 418-423.

(19) Moulton, S. E.; Barisci, J. N.; Bath, A.; Stella, R.; Wallace, G. G. *Electrochimica Acta* **2004**, *49*, 4223-4230.

(20) Zhang, Y.; Fung, Y.; Yao, S. *Chemical Sensors* **2004**, *20*, 760-761.

(21) Peters, T. In *Advances in Protein Chemistry*; Anfinsen, C. B, Edsall, J. T, Richards, F. M, Eds.; Academic Press, **1985**.

(22) Vogler, E. A. *Advances in Colloid and Interface Science* **1998**, *74*, 69-117.

(23) Brooksby, P. A.; Downard, A. J. *Langmuir* **2004**, *20*, 5038-5045.

(24) Brooksby, P. A.; Downard, A. J. *Journal of Physical Chemistry B* **2005**, *109*, 8791-8798.

7.1. Introduction

Assembly of nanoparticles (NPs) on a modified surface allows for the detection and analysis of the functional groups present at the surface. The properties of the assemblies such as fluorescence and number of NPs can provide information about the modifier layer. From another point of view, the immobilisation of NPs on solid surfaces using molecular layers or tethers generates new materials with interesting properties. For example, gold NPs have unique catalytic,[1] chemical and optical properties and are conducting. These unique properties have been exploited in many spectroscopy,[2] electronic[3-5] and biological[2,6-8] applications. Gold NPs have a high affinity for various functionalities such as thiols, amines and cyanide groups.[9] Hence, by tailoring the modifier layers, the properties of the resulting NP assemblies can be controlled. Modified silicon, glass, metal and plastic surfaces have been used for the assembly of metal NPs using a range of approaches based on electrostatic interactions,[9-16] biomolecular recognition[17-19] and covalent coupling[9,20-23]. However, in comparison to these substrates, carbon has been less commonly used.

There has been one report of attachment of gold NPs to planar carbon surfaces via surface-bound molecular layers. Porter and co-workers assembled 30 nm gold NPs onto mercaptobenzene layers attached to glassy carbon (GC) electrodes by electroreduction of the corresponding diazonium salt.[24] In related examples, the attachment of negatively charged 10 nm gold NPs to nitrogen-doped carbon nanotubes is achieved after chemical oxidation of the nanotubes and electrostatic assembly of a cationic polyelectrolyte,[25] and gold NPs are attached to thiol functionalised carbon nanotube after the direct, solvent-free

thermal functionalisation of thiols to the nanotube.[26]

In the context of this work, the aims for the assembly of NPs onto modified carbon surfaces are three-fold. Firstly, NP assembly provides information about the modifier layer. Layers that assemble NPs are identified and information such as the relative amounts of amine functionalities between layers is deduced from NP surface coverage. Secondly, various methods for modulating the surface coverage of NPs are examined. NP surface coverage is important for the various applications discussed above. Thirdly, assembly of NPs allows the visualisation of molecular patterns. The assembly of NPs onto a modifier layer containing suitable functionalities provides contrast against the surrounding modifier layer that does not assembly NPs.

In this work, aldehyde/sulfate-functionalised polystyrene (PS) NPs are assembled onto modifier layers. The PS NPs are readily available, can be used as purchased and have a fluorescent dye incorporated. PS NPs are usually used for protein tagging because of their hydrophobicity and fluorescent properties. In this work, these NPs are assembled on modifier layers that contain amine groups. The interaction that allows assembly is between either the aldehyde or sulfate groups of the NPs and the amines at the surface. The aldehyde groups of the NPs react with the primary amines to yield imine bonds[27] whereas the sulfate groups have electrostatic interaction with the amines, as shown in Figure 7.1.

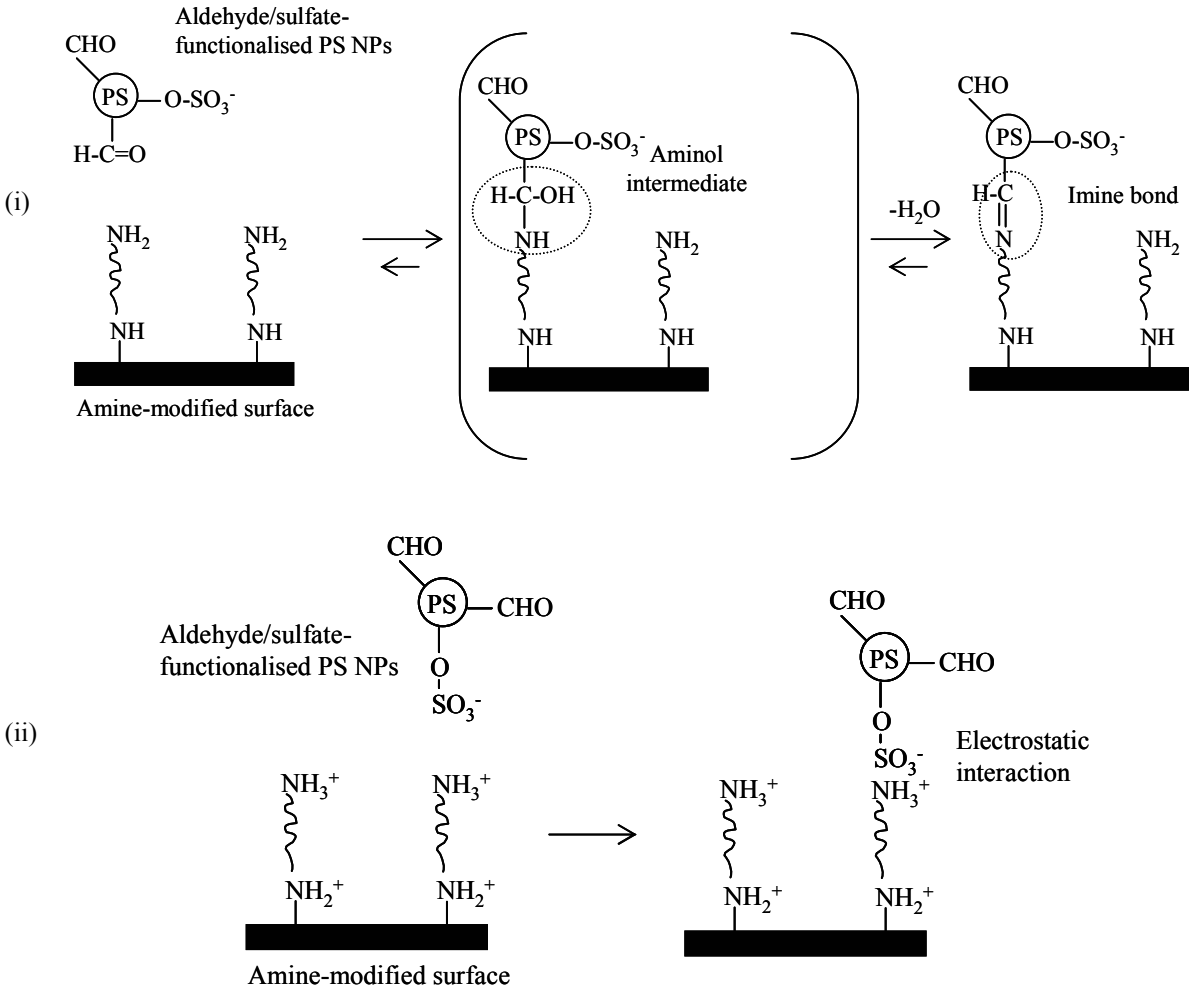

Figure 7.1. Reaction of the amines of the PGD modifier attached to a GC surface with the (i) aldehyde or (ii) sulfate groups on the PS NPs.

Citrate-capped gold NPs are the other type of NPs assembled onto molecular layers in this work. Electrostatic assembly of citrate-capped gold NPs on amine-terminated layers on silicon and gold surfaces is a straightforward method for generating robust NP assemblies.[9,10,12-14,16,28] In this work, NPs assemble onto protonated mono- and diamines layers via electrostatic attractions with the negatively charged citrate groups on the NPs, as

depicted in Figure 7.2. The number and hence surface coverage of the NPs are quantified. Depending on the modifier used and by controlling the electrolysis time for the attachment of the modifier layer, the immersion time in the NP solution and the concentration and pH of the NP solution, the surface coverage of the NP assemblies is controlled. Besides amine layers, these NPs are also adhered to poly(vinyl)alcohol (PVA) as detailed in Chapter 9b.

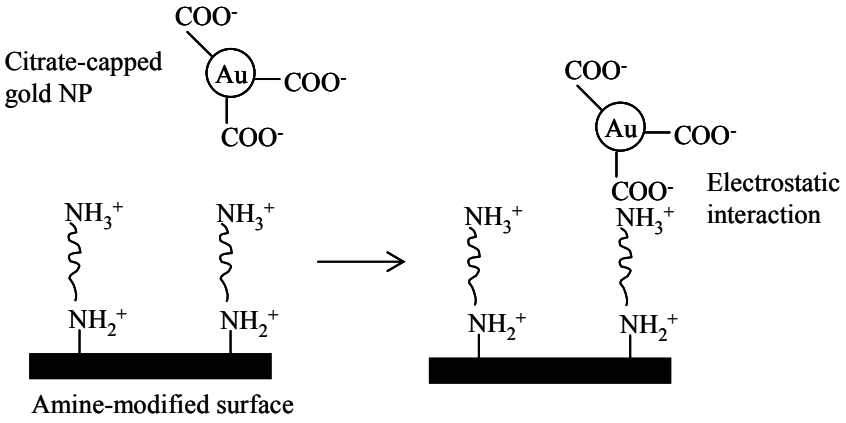

Figure 7.2. Electrostatic interaction between protonated diamines of the modifier layer attached to a PPF surface with the negatively charged citrate groups on the gold NPs.

There are three general methods for the synthesis of gold NPs, namely the citrate[9,29,30], hydroxylamine[31] and sodium borohydride[32] methods. In the first two methods, Au(III) is reduced to Au(0) using citrate or hydroxylamine as the reducing and capping agent. In the third method, sodium borohydride is the reducing agent and reduction is carried out in the presence of alkanethiols which coat the NPs. As reduction occurs and Au(0) atoms are formed, the atoms nucleate to form small clusters. These clusters grow in order to achieve a minimum Gibb's energy and the eventual size is affected by factors

including the concentration of the Au(III) salt, the strength of the reducing agent, temperature, mixing and reaction time among others. For example, the higher the concentration of the Au(III) salt used the larger the NPs and a longer reaction time generally gives a more uniform size and shape distribution due to Ostwald ripening. Ostwald ripening is the growth of larger particles from smaller ones where the larger particles have lower solubility than the smaller ones.[33,34] In this work, NPs are synthesised by the citrate method to obtain citrate-capped gold NPs.

7.2. Experimental methods

7.2.1. General materials and equipment

4-morpholineethanesulfonic acid (MES) buffer of pH 6 was made by dissolving MES and sodium hydroxide in Milli (MQ) water. Concentrations of MES and sodium hydroxide in buffer were 0.027 M and 0.012 M, respectively. Chloroauric acid ($HAuCl_4$, 51% Au(III) by weight, BDH) and sodium tricitrate ($(Na^+COO^-CH_2)_2C(OH)(COO^-Na^+)$, BDH) were used as purchased. The pH meter was calibrated against three standard buffers at pH 4.01 (phthalate), 6.86 (phosphate) and 10.01 (carbonate).

7.2.2. Preparation of GC plates

The preparation of GC plates was as detailed in Chapter 4.

7.2.3. Electrochemistry

Electrochemical settings for modification used in this chapter were adopted from Chapter 4 for amines and Chapter 5 for aryl diazonium salts. A circular area in the centre of each GC plate or pyrolysed photoresist film (PPF) surface was modified, using the cell set-ups as described in Chapter 2.

7.2.4. Aldehyde/sulfate-functionalised PS NPs

The 29 nm yellow-green fluorescent aldehyde/sulfate PS NPs were purchased from Interfacial Dynamics Corporation and used according to manufacturer's instructions.[35] The concentration of PS NPs as purchased is approximately 10^{14} per mL and the NPs have maximum absorbance at λ = 490 nm (blue light) and emit at λ = 515 nm (green light).

Assembly of PS NPs

Prior to assembly, a piece of magic tape (Scotch, 3M) was adhered to a corner of the GC surface. 3 drops of NP solution was diluted in 2 mL of MES buffer and used for assembly. The samples were then completely immersed into the diluted solution of PS NPs for 3 hours. This was carried out at room temperature and in the dark to avoid photobleaching the NPs. After 3 hours, the surface was removed from the NP solution, magic tape removed and the sample was left to air dry. It was then immersed into MQ water and dried under a gentle stream of $N_{2(g)}$.

After this procedure, the GC plates had three different areas: the modified area,

defined by the gasket used during modification of the GC plate, which had been exposed to PS NPs (referred to as 'modified/NPs'); the unmodified area which had been exposed to PS NPs (referred to as 'GC/NPs') and the unmodified area protected by magic tape during assembly of NPs and hence not exposed to PS NPs (referred to as 'GC/no NPs'). These are shown in Figure 7.3.

Visualisation of PS NP assemblies

Samples with PS NP assemblies were visualised using optical and fluorescence microscopy, usually on the same day as assembly. With the fluorescence microscope, the excitation filter of the Hg arc lamp was set between 470 – 500 nm to transmit blue light. The samples were analysed with the lowest objective (10x) to capture the largest area (500 x 500 μm) for fluorescence intensity analysis. All images were taken with a standard exposure time of 6 seconds. Images were collected at the boundary of the modified/NPs : GC/NPs regions (usually 4 images) and the boundary of the GC/NPs : GC/no NPs regions (2 images), as shown in Figure 7.3. An image entirely within the modified/NPs area and entirely within the GC/NPs area was also collected.

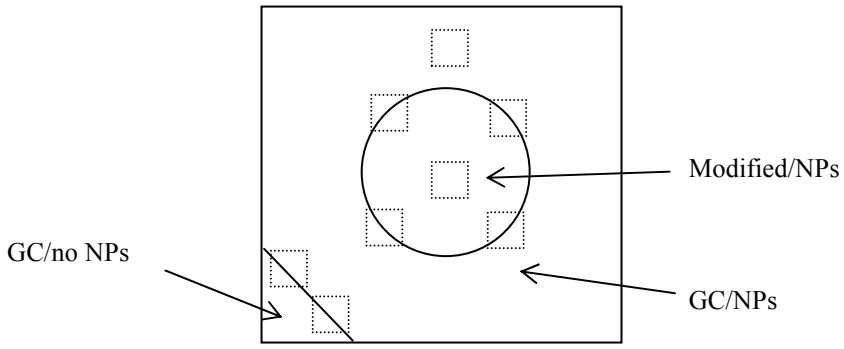

Figure 7.3. GC plate modified with amine-containing modifiers and treated with aldehyde/sulfate-functionalised PS NPs. Dotted line squares show where images were taken.

Quantification of the fluorescence of the PS NP assemblies

The fluorescence intensity was quantified for the images taken at the two boundaries (Figure 7.3.), using Image Pro Plus software. An area of interest (AOI) was defined within each region on both sides of the boundary. The boundary itself was avoided as it was atypically fluorescent. The fluorescence intensity in each AOI was measured. By dividing the two intensity measurements, a fluorescence intensity ratio for the two regions of the image was calculated. Intensity ratios were calculated for all images taken at each of the two boundaries for a sample. The average of the ratios at a boundary was the intensity ratio for the sample and the error was the standard deviation of the ratios, for that boundary. Raw fluorescence intensity measurements are listed in the Appendix 7.

7.2.5. Citrate-capped gold NPs

Synthesis of gold NPs

NPs were prepared by using the previously reported citrate reduction method which gave NPs with diameters ranging from 11 – 15 nm.[9] All glassware was rinsed thoroughly in aqua regia (3:1 HCl:HNO_3) and MQ water before use. The gold salt was extremely hydroscopic and was handled with a plastic or glass spatula rather than a metal one (onto which it reduces upon contact). Solutions were prepared using MQ water. A stirred 500 mL solution of 1 mM chloroauric acid was brought to a "rolling" boil in a 1 L round bottomed flask equipped with a condenser. 50 mL of 38.8 mM sodium citrate solution was then rapidly added resulting in a colour change from pale yellow to burgundy within 60 seconds. The solution was refluxed for 1 hour and then cooled to room temperature without stirring. The gold NP solution was stored in the dark.

Characterisation of gold NPs

NPs were characterised by spectroscopy and microscopy. The size of the NPs was estimated from the ultraviolet-visible (UV-VIS) spectra and from images captured with the transmission electron microscope (TEM). Crystalline structure of the NPs was observed with the high resolution transmission electron microscope (HRTEM).

UV-VIS measurements utilised a UV-VIS 920 spectrometer from GBC. TEM (JEOL 1200EX) images were collected with the help of Manfred Ingerfeld, School of Biological Sciences, University of Canterbury. Samples for TEM were prepared by

deposition of 1 drop of NP solution onto standard formvar-coated copper grids (60960 lines per inch) and drying in air. Images were collected using the microscope operating at 80 eV. The HRTEM instrument was a JEOL 2010 equipped with a LaB_6 filament. HRTEM images were captured by Dr. Richard Tilley at the School of Chemical and Physical Sciences, Victoria University of Wellington. Images were collected with the microscope operating at 200 keV.

Assembly of gold NPs

The standard method for assembly was by immersion of the PPF surface into approximately 2 mL of NP solution. After a 3 hour immersion in the dark at room temperature, the sample was removed from the solution, immersed into MQ water and gently agitated. The surface was dried with a gentle steam of $N_{2(g)}$ and then analysed or stored under vacuum prior to analysis.

Adjustments to the gold NP solutions and assemblies

For experiments that investigated the effect of concentration and pH of NP solution on NP assembly, the concentration was adjusted by dilution with MQ water to 0.01, 0.1 and 0.5 of the original solution concentration. pH was tuned to 7, 8 and 12 by addition of a concentrated NaOH solution.

For experiments that examined the effect of immersion time on NP assembly, all measurements were made using the same modified surface. The samples were immersed

for a set time, removed and analysed under scanning electron microscope (SEM), re-immersed in a fresh NP solution for another set amount of time, removed and analysed and so on.

For stability experiments, NP assemblies of known NP counts were sonicated and scanned in different media. The samples were sonicated in either MQ water, 1 M HCl or 1 M NaOH for 15 seconds and scanned in either phosphate buffered saline (PBS) or ACN (acetonitrile)/0.1 M $[Bu_4N]BF_4$ (tetrabutyl ammonium fluoroborate). The potential range was between 1 and -1.5 V and the reference electrode in ACN/0.1 M $[Bu_4N]BF_4$ was a Ag wire.

Visualisation of gold NP assemblies

The NP assemblies were observed by the eye, optical microscopy and SEM. Topographical images of the NPs were also captured using the atomic force microscope (AFM).

Quantification of the number of NPs in the gold NP assemblies

NPs were counted using Image Pro Plus software. Four AOIs of 100 x 100 nm each were drawn on a 200 kx SEM image and the NPs within it counted using the manual tag option. Two (at least) SEM images were taken for each sample and the average of the eight values was calculated for one sample. The surface coverage of the NPs was expressed as NPs per 10^4 nm^2. When 200 kx images were not taken, the number of NPs in 50 kx or 100

kx images was counted in the same manner using the same AOI and the number of NPs was divided by 4 and 2, respectively. The stated errors accommodate all the eight values. Raw counts are listed in the Appendix 7.

7.3. Results and discussions

7.3.1. Aldehyde/sulfate-functionalised PS NPs

Aldehyde/sulfate-functionalised PS NPs were assembled onto polyethylene glycol diamine (PGD) layers attached to GC plates. PGD layers were modified using 50 mM solutions and an electrolysis time of 10 minutes at final/applied potential (E_f) 1.3 V. Figure 7.4. is an optical microscope image showing the modified/NPs : GC/NPs and GC/NPs : GC/no NPs boundaries. Clearly, the PS NPs assemble on the PGD-modified surface. Figure 7.5.(i). and Figure 7.5.(ii). are images captured using the fluorescence microscope at the modified/NPs : GC/NPs boundary and the GC/NPs : GC/no NPs boundary, respectively. From Figure 7.5.(i), the fluorescence in the modified region is brighter than the GC region. These images confirm that the PS NPs assemble preferentially on the PGD-modified region rather than the as-prepared GC. Figure 7.5.(ii). shows that NPs do assemble on the as-prepared GC. It is not suitable to compare the fluorescence from the image captured solely in the modified region with another captured entirely in the as-prepared GC region because absolute fluorescence intensities varied from image to image. This is possibly due to variations in intensity of excitation light from the Hg lamp and/or the method the software uses to quantify the fluorescence in an image. SEM could not be used for analysis of PS NP

assemblies as the NPs were non-conducting and hence 'flare' under the SEM.

Control experiments were undertaken in which GC plates were treated with the modifying conditions for attaching PGD applied to the surface, however, without the PGD. NPs assembled over the whole surface with no difference between the electrochemically-treated area and the untreated areas. Attempts were made to remove the assembled NPs by washing. The plates were washed by either: (i) dip rinsed in MQ water with agitation (swirling it around using tweezers) followed by sonication in MQ water for 3 minutes or (ii) squirted with MQ water, soaked in 5% Tween 20 solution for 5 minutes and then squirted in MQ water. However, the ratios at the GC/NPs : GC/no NPs boundary did not change considering experimental error. Other control experiments showed that the PGD-modified surface is not fluorescent and the NPs do not assemble on a *para* methyl phenyl (MP) layer (5 mM, electrolysis time 10 minutes) attached to a GC plate, indicating that amine functionalities are indeed required for their assembly.

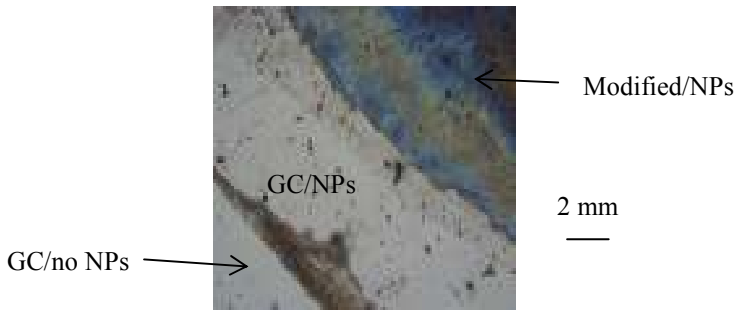

Figure 7.4. An optical microscope image showing the two boundaries – the modified/NPs : GC/NPs boundary and the GC/NPs : GC/no NPs boundary.

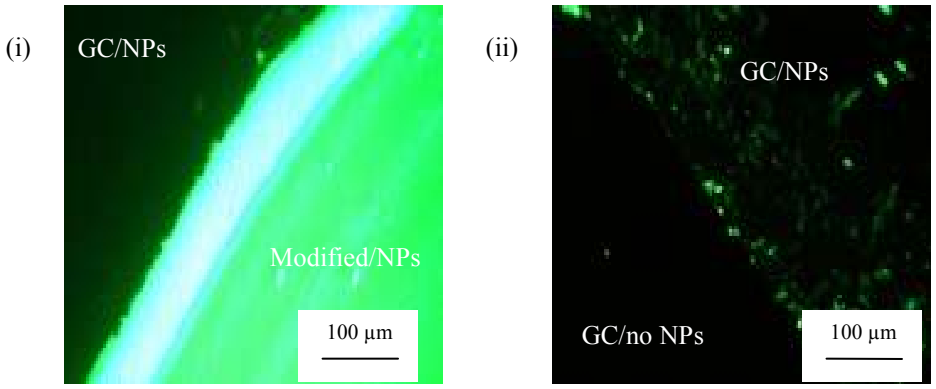

Figure 7.5. Fluorescence microscope images collected of aldehyde/sulfate-functionalised PS NP assemblies at (i) the modified/NPs : GC/NPs boundary and (ii) the GC/NPs : GC/no NPs boundary. Both images were obtained from the same sample.

From the fluorescence images like those shown in Figure 7.5, the average fluorescence intensity ratio was calculated at the two boundaries for each sample and these ratios are listed in Table 7.1.

Table 7.1. Fluorescence intensity ratios calculated for the two boundaries – the modified/NPs : GC/NPs boundary and the GC/NPs : GC/no NPs boundary, for the PGD-modified samples.

Sample no.	Fluorescence intensity ratio	
	modified/NPs : GC/NPs	**GC/NPs : GC/no NPs**
1	5.0 ± 2.7 : 1	4.3 ± 0.4 : 1
2	5.1 ± 0.9 : 1	3.8 ± 0.9 : 1
3	5.5 ± 0.7 : 1	1.8 ± 0.5 : 1
4	6.1 ± 1.2 : 1	3.4 ± 0.8 : 1
5	6.6 ± 1.8 : 1	Not measured
6	7.4 ± 0.5 : 1	5.9 ± 0.7 : 1
7	Not measured	2.4 ± 0.8 : 1

The fluorescence intensity ratio between the modified and as-prepared GC regions

indicates that approximately six times more fluorescent PS NPs assemble on the PGD modifier layer than on the surrounding as-prepared GC surface.

The successful assembly of the PS NPs on PGD layers is accounted for by two possible interactions. The interactions are imine bond formation between the aldehyde groups on the NPs and the amines of PGD or electrostatic interactions between the sulfate groups on the NPs and the amines of PGD. Assembly due to imine bond formation is less probable for a two reasons. Firstly, at pH 6 (pH of NP solution) the majority of the amines of the PGD modifier layer would be protonated (protonation constant of amines 9 – 10) and so is unlikely to react with the aldehyde. The assembly was not carried out at a higher pH so that the amines were deprotonated as imine formation is slow at high pH. These aldehyde/sulfate functionalised PS NPs are commonly used for protein tagging where the aldehyde functionalities react with the amino groups in the protein. For successful covalent coupling to occur, it is critical that the pH of the coupling solution is close to the isoelectric point of the protein i.e. protein is neutral. Secondly, imine bonds are also quite unstable and hydrolysis of these bonds can be carried out with water. However, it is possible that imine bonds form to some extent and the hydrolysis of the bonds is insufficient to cause the NPs to be removed. The size of the NPs (29 nm) is much larger than the PGD modifier. Therefore, it is possible that more than one modifier attaches to one NP and the multiple imine bonds stabilises the NP attachment. The imine bonds are labile and their formation is an equilibrium. When one imine bond breaks, another forms between the aldehyde group on the NP and the amine group on the same or different PGD modifier, allowing NP

assembly.

A more probable explanation for the assembly of PS NPs on the PGD layer is the electrostatic interactions between sulfate groups on the NPs and the amines of the PGD layer. The NPs are functionalised with sulfate groups in order to prevent aggregation of the NPs.[35] The protonation constant of the sulfate group is < 2.[35] Hence, at pH 6 the amines in the PGD layer are protonated (cationic) and the sulfate groups on the NPs are deprotonated (anionic), allowing electrostatic interactions. Assembly may also be attributed to non-specific adsorption. Non-specific adhesion involves physical adsorption which results from attractive forces such as hydrophobic and/or van der Waals and is entropically driven.

These NPs are hydrophobic which makes their attachment onto the hydrophilic PGD layer interesting. The water contact angle of the PGD layer (20 mM, electrolysis time 10 minutes) is 59 ± 3° as detailed in Chapter 4. The driving force for the imine bond formation or electrostatic interaction is able to overcome the hydrophobic interactions so that the hydrophobic NPs assemble on the hydrophilic PGD-modified surface.

The fluorescence intensity ratios at the GC/NPs : GC/no NPs boundary (Table 7.1.) indicates that NP assemble on as-prepared GC. This assembly on as-prepared GC is presumably due to non-specific adsorption. The ratios at this boundary did not change when an additional washing step (3 minutes sonication in MQ water) was carried out in an attempt to remove NPs assembled on the as-prepared GC.

From Figure 7.4. and Figure 7.5. and data in Table 7.1, the PS NPs preferentially assemble at the PGD-modified area although there is a significant amount of assembly on

the as-prepared GC as well. Although the interaction between the aldehyde/sulfate-functionalised NPs and amines of the PGD layer is not clear, their assembly is a useful visualisation method for amines functionalities.

7.3.2. Citrate-capped gold NPs

Characterisation of gold NP solution

Using UV-VIS spectroscopy, the absorption maximum and peak width at half maximum of a gold NP solution enables an estimate of average NP size. The spectrum of the as-prepared solution of colloidal NPs shows an absorption maximum at λ_{max} = 520 nm and peak width at half maximum of 116 nm (Figure 7.6.). Due to the asymmetry of the peak, peak width at half maximum is calculated by the difference between λ_{max} and λ at half maximum to the right of λ_{max} multiplied by two. The absorption maximum corresponds to a NP diameter of approximately 11 nm.[9,31]

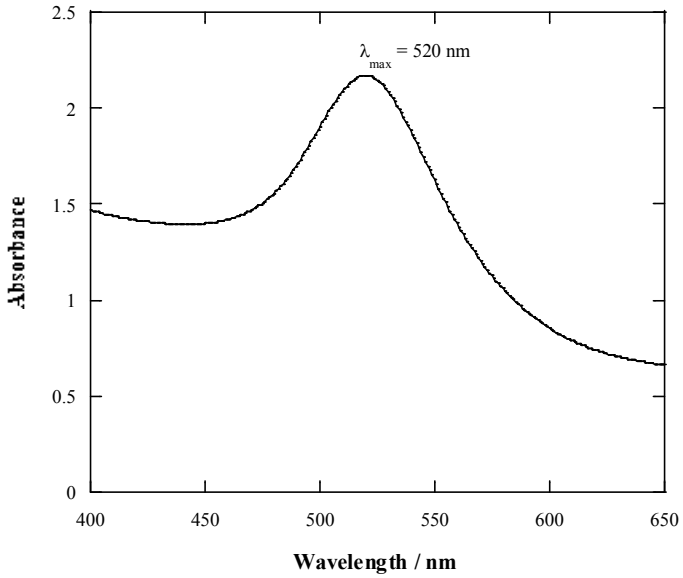

Figure 7.6. UV-VIS spectrum of approximately 11 nm citrate-capped gold NPs.

TEM and HRTEM provided more detailed characterisation of the NPs. Figure 7.7. is a typical TEM image captured at 150 kx. From TEM images, the measured NP diameter ranges from 10 – 16 nm for a sample of 40 NPs, with an average NP size of 11 nm. The NP diameter distribution is depicted in Figure 7.8. and is typical of the size distributions obtained when preparing NPs using the citrate reduction method.[36] The size and shape uniformity of the NPs are influenced by the reflux time used during synthesis. When a reflux time shorter than 1 hour was used, NPs had decreased size and shape uniformity. An average NP diameter of 13 nm is usually reported for the preparation method used here.[9]

The measurement of diameters is an oversimplification as no colloidal gold NP is purely spherical.[31] The HRTEM images in Figure 7.9. illustrates this point more clearly. The diameter measurements taken from the TEM images are the longer of the two axes of

the ellipsoid. The variation in size of NPs is due to the competing rates of new NP formation by nucleation via Au (III) reduction against Au (III) reduction on surfaces of existing NPs. The latter occurs significantly faster; however, continued nucleation gives smaller NPs.[31]

In the HRTEM images, NPs with stacking faults are seen (indicated by arrows in Figure 7.9.). These faults are a result of the coalescence of two NPs with different crystalline structures. The point and plane defects at the stacking faults are from considerable stress due to reorganization of the atoms into a uniform crystalline structure.[37] Coalescence of NPs is driven by a surface energy reduction as the surface area of the resulting NP is lower than the sum of the surface areas of the two original ones. The coalescence process starts with contact and initial fusion, followed by orientation alignment of the crystalline planes at the interface between the coalescing NPs.

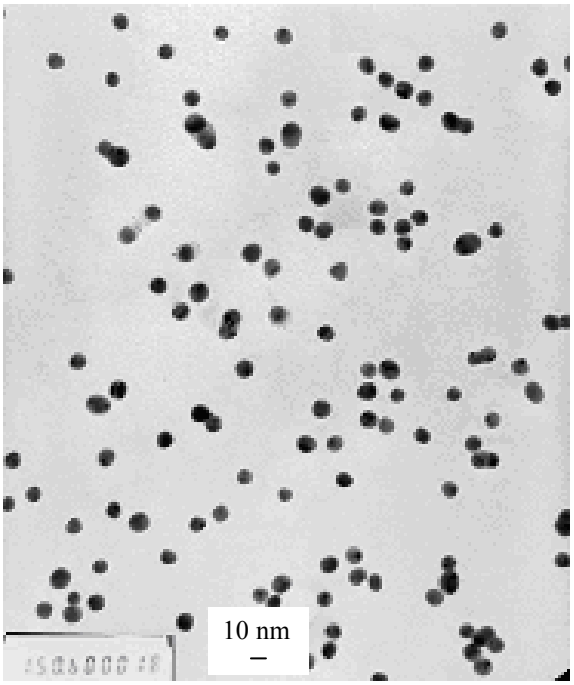

Figure 7.7. A TEM image of citrate-capped gold NPs.

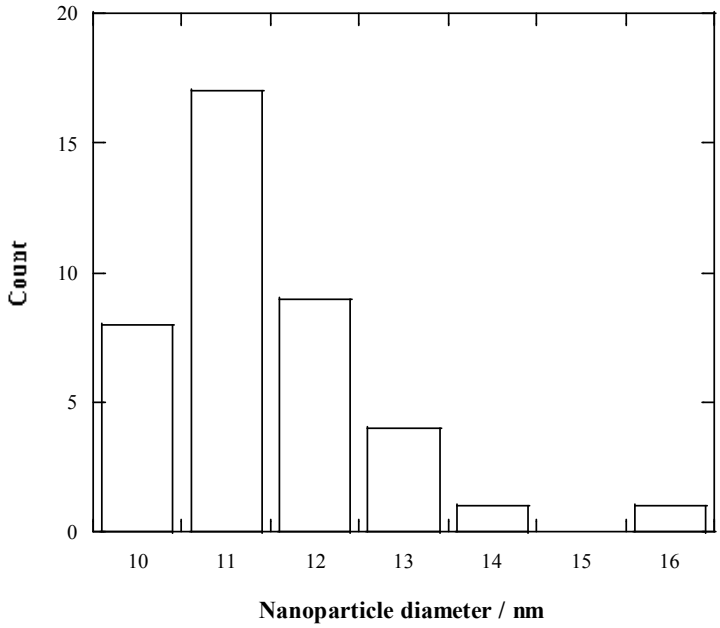

Figure 7.8. Graph showing the NP diameter distribution for a sample size of 40, measured from TEM images.

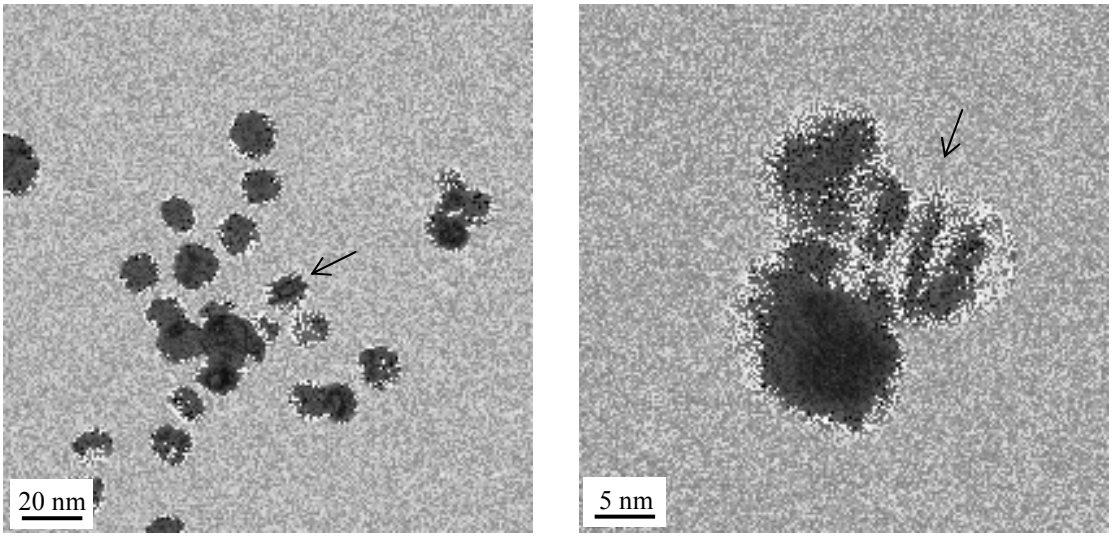

Figure 7.9. HRTEM images of citrate-capped gold NPs. Arrows indicate stacking faults.

The pH of the colloid solution is measured to be 4.2. The NP concentration assuming all gold was reduced to form NPs of 11 nm diameter is 1.3 x 10^{16} NPs L^{-1}. This is calculated using Equations 7.1.

7.1. Mass of Au used = m_{Au} = 0.0985 g

Density of Au = d_{Au} = 19.3 g cm^{-3}

$$\text{Volume of Au} = \frac{m_{Au}}{d_{Au}} = 5.10 \times 10^{-3}\ \text{cm}^3$$

Volume of a Au NP = 6.97 x 10^{-19} cm^3

$$\text{Number of NPs} = \frac{\text{Volume of Au}}{\text{Volume of Au NPs}} = 7.32 \times 10^{15}$$

Volume of NP solution = 0.55 L,

$$\text{NP concentration} = \frac{\text{Number of NPs}}{\text{Volume of NP solution}} = 1.3 \times 10^{16}\ \text{NP L}^{-1}$$

Analysis of gold NP assemblies

Gold NPs assembled on various modifier layers

Citrate-capped gold NPs were assembled on various amine layers attached to PPF surfaces. The monoamine layers included *n*-hexylamine (HA) and *para* nitro aniline (*p*-NA) and the diamine layers were tetraethylene glycol diamine (TGD) and PGD. For all amines, attachment and growth of the layer resulted in a layer containing amines and for diamines, terminal amines were also assumed to be present. Four control surfaces that had no amine functionalities were also prepared: MP and *para* polyethylene glycol phenyl (PEG) layers and two PPF surfaces treated with the modification procedures used (E_f = 1.2 or 1.3 V), but in the absence of modifier. The modifier layers apart from *p*-NA were attached with an electrolysis time of 10 minutes, which gave compact layers of 'limiting' thicknesses (at the chosen potential). Figure 7.10. shows the SEM images of the six different modifier layers and Table 7.2. lists the surface coverage of NPs / 10^4 nm^2 for the various modifier layers and control PPF surfaces. The NP surface coverage values relate to a monolayer of NPs. The NPs assemblies are made up of a monolayer of NPs as determined by AFM depth profiling.

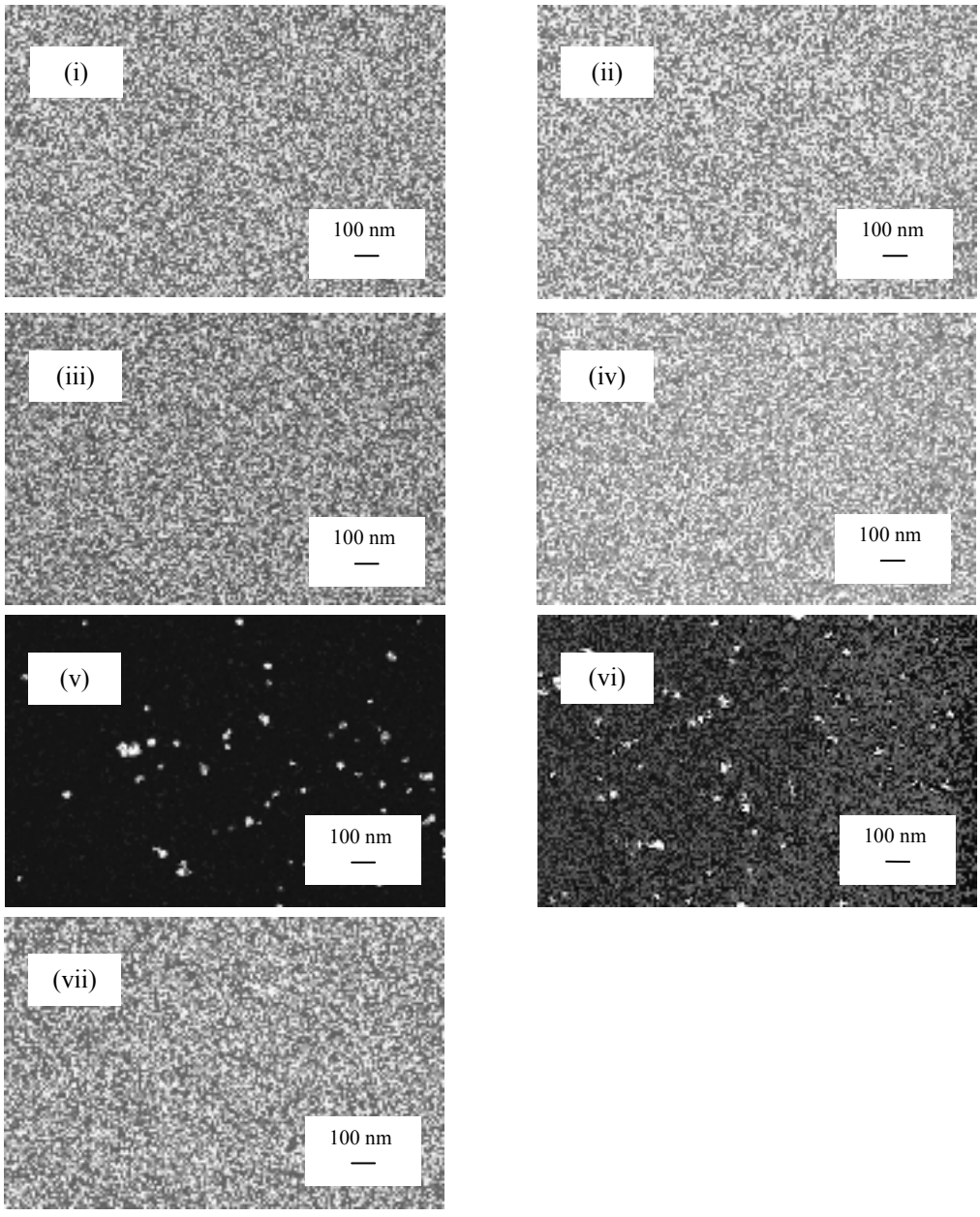

Figure 7.10. SEM images of citrate-capped NP assemblies on various modifier layers: (i) TGD (5 mM, electrolysis time 10 minutes); (ii) *p*-NA (5 mM, modification 1 scan); (iii) HA (5 mM, electrolysis time 10 minutes); (iv) PGD (50 mM, electrolysis time 10 minutes); (v) MP (5 mM, electrolysis time 10 minutes); (vi) PEG (5 mM, electrolysis time 10 minutes); (vii) TGD (5 mM, electrolysis time 2 minutes). Images were captured after an immersion time of 3 hours. NPs solution was used as-prepared.

Table 7.2. Number of citrate-capped gold NPs assembled / 10^4 nm^2 on modifier layers or control PPF surfaces, after immersion time of 3 hours. NPs solution was used as-prepared.

Sample (modifier concentration, electrolysis time)	**Number of NPs assembled / 10^4 nm^2**	**Thickness / nm** Calculated length of TGD = 1.5 nm HA = 1.0 nm PGD > 15 nm (data extracted from Chapter 4)	**Peak current ratio** [a, b] (data extracted from Chapter 4)
TGD (5 mM, 10 minutes)	25 ± 3, 33 ± 5, 38 ± 4 [c], 38 ± 4 [c]	2.5 ± 0.1, 2.8 ± 0.4, 3.4 ± 0.2 [d]	0.77
p-NA (5 mM, 1 scan)	11 ± 2 [d], 11 ± 1 [d]	-	-
HA (5 mM,10 minutes)	11 ± 1, 12 ± 2, 13 ± 2	3.0 ± 0.3	-
PGD (50 mM, 10 minutes)	8 ± 2	5.1 ± 0.3	-
MP (5 mM, 1 scan)	0 ± 0 [e]	-	-
MP (5 mM, 10 minutes)	0 ± 1, 3 ± 2, 1 ± 1	-	-
PEG (5 mM, 10 minutes)	2 ± 1, 2 ± 2	-	-
Control for TGD or *p*-NA (10 minutes at 1.2 V)	0 ± 1, 1 ± 1	-	-
Control for HA or PGD (10 minutes at 1.3 V)	0 ± 1, 0 ± 1, 0 ± 2	-	-
TGD (5 mM, 1 scan)	10 ± 2, 11 ± 2, 12 ± 3 [e*]	1.0 ± 0.2 [e*], 1.2 ± 0.1 [e]	1.00
TGD (5 mM, 20 scans)	25 ± 3 [d*], 26 ± 2 [d#]	2.6 ± 0.2 [d*], 2.4 ± 0.2 [d#]	-
TGD (5 mM, 2 minutes)	10 ± 3, 10 ± 2, 9 ± 2 [f], 9 ± 5 [f], 9 ± 3 [g]	3.7 ± 0.4, 3.0 ± 0.3 [d]	0.97

TGD (5 mM, 20 seconds)	3 ± 2 [h]	-	-
TGD (5 mM, 150 seconds)	10 ± 1 [h]	-	-
TGD (5 mM, 400 seconds)	14 ± 2 [h]	-	-

[a] Peak current ratio was (i_{pa} after modification)/(i_{pa} as-prepared PPF) of FCA probe.
[b] Uncertainty on peak current ratios is ± 0.05.
[c] Samples from immersion time experiment (refer Table 7.4.).
[d] Samples prepared as part of work in Chapter 9a – Approach (i): "Fill-in" approach using PDMS with perforations.
[e] Samples prepared as part of work in Chapter 9a – Approach (iii): "Fill-in" approach using PDMS microchannels.
[f] Samples described in 'NP assembly used in other chapters' section (refer later).
[g] Samples prepared as part of work in Chapter 9a – Approach (iv): "Build-up" approach using PDMS microchannels.
[h] Samples prepared by a potential step to E_f for time as stated; i.e. without the initial or final modification scans as in standard procedure.
[#] and [#] or [*] and [*] means identical samples.
- Not relevant for comparison of TGD layers attached with different electrolysis times.

Besides analysis with the SEM, NPs assembled onto layers is observed by the eye and using optical microscopy. From the digital photographs in Figure 7.11. and optical microscope images in Figure 7.12, the NP assembly on the TGD layer is gold in colour and on the HA layer a green/gold assembly is observed. Relating the colours of the NP assemblies to the NP counts listed in Table 7.2, assemblies with high NP surface coverages appear gold and assemblies with lower coverages are green/gold. The four control surfaces are colourless.

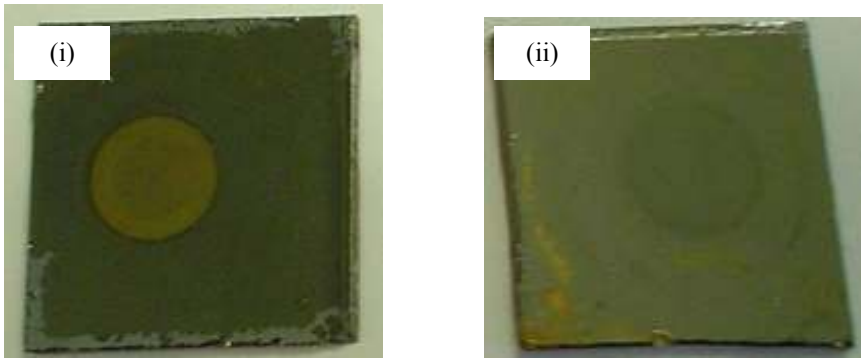

Figure 7.11. Digital photographs of NP assemblies on (i) TGD and (ii) HA layers grafted onto PPF surfaces. Layers were attached using 5 mM modifier solutions and electrolysis times of 10 minutes. Images were captured after an immersion time of 3 hours. NPs solution was used as-prepared.

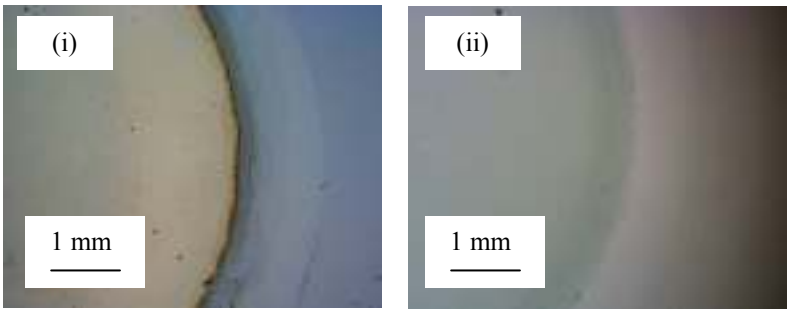

Figure 7.12. Optical microscope images captured at the modified : as-prepared boundary of NP assemblies on (i) TGD and (ii) HA. Layers were attached using 5 mM modifier solutions and electrolysis times of 10 minutes. Images were captured after an immersion time of 3 hours. NPs solution was used as-prepared.

From the SEM images in Figure 7.10. and the NP counts for the various surfaces in Table 7.2, several comments can be made. It appears that the assembly of the citrate-capped gold NPs is controlled by the type of modifier used and also the modification conditions. More NPs assemble on amine-containing modifiers compared to layers without amines, significantly more NPs assemble on the diamine TGD layer compared to the monoamine

HA layer and in varied amounts on the other amine modifiers, *p*-NA and PGD. There is also a difference in NP count when TGD is attached with varying modification conditions.

Very few or no NPs assemble on the four control surfaces (MP, PEG and two surfaces where electrochemical conditions were applied without modifier). Amine groups are not present at these surfaces and so this indicates that NP assembly depends on electrostatic interactions between protonated amines of the layer and the negatively charged citrate groups capping the NPs (at the pH of the NP solution).

For the TGD-modified surface (Figure 7.10.(i).), an extremely dense coating of NPs assemble. Due to the high density of NPs, there is an appearance of aggregation. The NP assembly on HA layers (Figure 7.10.(iii).) attached to carbon surfaces has an appearance typical of those reported for amine-terminated silane layers on silicon substrates.[13,14,28] Surface coverage of NPs on the TGD layer is 25 – 38 NPs / 10^4 nm^2 compared to 11 – 13 NPs / 10^4 nm^2 for the HA layer when both modifiers are attached with identical modifier solution concentrations and electrolysis times. There are approximately three times more NPs assembled on the TGD layer compared to the HA layer.

Several possible factors can be considered to account for larger NP surface coverage on the TGD layer compared to the HA layer. These factors assume that the resulting layer after modification for both TGD and HA are similar. This assumption could be made as the two modifiers are of roughly similar calculated length and both are aliphatic amines. The assumption considers that the conformations of the resulting layers are similar. AFM depth profiling of the layers showed that multilayers are present for both modifiers using the

modification conditions (Chapter 4). As also detailed in Table 7.2, both layers are of similar thicknesses considering experimental error but the greater calculated length of the TGD molecule results in the calculated minimum number of layers of modifiers for TGD (two) being less than that for HA (three).

The first possible factor that contributes to the higher NP surface coverage on the TGD layer compared to the HA layer is the number of cationic sites (protonated amines) present in each layer. When the modified surfaces are immersed into the NP solution (pH 4.2), the amines (protonation constant of amines 9 – 10) are protonated causing electrostatic interactions with the negatively charged citrate groups on the NPs hence resulting in assembly. In Chapter 4, mechanisms for multilayer formation for TGD and HA were suggested. Considering the proposed mechanisms and the minimum number of monolayers estimated from the layer thicknesses (refer above), there is expected to be three cationic sites in both the TGD and HA layers. This disagreement indicates that the layers are disorganised and not well-defined.

Secondly, it is considered that for both the TGD and HA layers there are amines within the layer, however, for TGD, terminal amines are also present. The position of the cationic sites could have played a role and having terminal amines gives an increased NP surface coverage.

The third factor that could be governing the NP assembly is the nature of the surface each amine modifier layer presents to the solution. For the TGD layer, the cationic sites are incorporated in a hydrophilic environment whereas for HA, the layer environment is made

up of hydrophobic hydrocarbons. Approach of the hydrophilic, negatively charged citrate-capped NPs to the hydrophobic HA surface may be restricted by the interfacial water to a larger extent than in the case of the TGD layer. The TGD modifier is more hydrophilic due to the oxygen groups in the chain and this is reflected in the water contact angle measurements detailed in Chapter 4. Water contact angle is 46 ± 3° for the TGD layer compared to 77 ± 2° for the HA layer. Similar effects are well-documented in the case of small molecules undergoing electron transfer at alkanethiol monolayers terminated with hydrophobic and hydrophilic head groups.[38-41]

Considering the position and environment the amines are in within the TGD layer, closer approach of the NPs to the TGD layer, and thus to the cationic sites, may result in part in the apparent greater charge compensation experienced by the NPs assembling at TGD compared with HA layers. This charge screening may be responsible for the higher NP surface coverage observed on the TGD layers compared to the HA layers. In summary, the number, position and environment of the cationic sites are considered to influence NP assembly.

NPs also assemble on other amine-containing layers, *p*-NA and PGD. The NP surface coverage on both monoamine layers of HA and *p*-NA are similar suggesting that there are similar number of amine groups present within both monoamine layers. From the depth profile experiments carried out in Chapter 9a, there is a minimum of three *p*-NA monolayers for the average layer thickness measured which is the same number of HA monolayers present, even though the modification conditions are 1 cyclic scan (*p*-NA)

compared to 10 minutes electrolysis (HA). Although PGD is a diamine, the NP surface coverage on the PGD layer is approximately four times lower than the TGD layer. From the thickness data in Table 7.2. and also in Chapter 4, the thickness of the TGD layer (5mM, electrolysis time 10 minutes) corresponds to three monolayers whereas for PGD, there was possibly only a monolayer of modifier. The higher number of cationic sites in the TGD layer causes the increased assembly compared to the PGD layer. PGD is a significantly larger modifier compared to TGD. The calculated length is 1.5 nm for TGD whereas PGD is > 15 nm long and has side chains. Hence, a PGD modifier would occupy a greater area on the surface compared to a TGD modifier. If the modifiers are of a retracted, 'balled-up' conformation, the surface concentration of modifiers and hence of amines, would be lower for PGD than TGD.

From comparing TGD and HA layers, the number, position and environment of the cationic sites were considered to impact on NP assembly. Therefore, another simple approach to controlling NP assembly, besides using different modifiers, is to tailor only the number of cationic sites by using different modification conditions for the attachment of TGD.

Three sets of modification experiments for TGD were carried out. In the first set of experiments, samples were prepared using 1 scan and 20 scans to E_f. In the second set of experiments, samples were prepared using the standard procedure and 2 and 10 minutes electrolysis. In the third set of experiments, samples were prepared using 20, 150 and 400 seconds electrolysis (without the initial and final modification scans to E_f before and after

electrolysis). NP counts are given in Table 7.2. Comparing 1 scan vs. 20 scans and 2 minutes vs. 10 minutes, the milder of the two modification processes leads to a lower NP surface coverage. Increasing the electrolysis time from 20 to 150 to 400 seconds increases the surface coverage of NPs. Although the NP surface coverage from the three modification sets have little relationship between them, within the sets it is clear that tuning the modification conditions allows the tailoring of NP assembly.

Considering the NP surface coverage together with the layer thickness and/or CV peak current ratio of the ferrocene monocarboxylic acid (FCA) probe (Table 7.2.), information about the structure of the layers can be obtained. For modifications of 1 scan vs. 20 scans, the increased NP assembly is accounted for by the greater number of cationic sites that are present in a thicker layer. This indicates that growth of the layer is occurring with increasing number of modification scans. For the 2 minutes vs. 10 minutes electrolysis, the longer electrolysis results in an increase in NP count while the layer thickness is similar for both electrolysis conditions and the peak current ratio of probe decreases. This suggests that when using electrolysis for modification of TGD, the layer grows vertically and then laterally attaching to unmodified areas (also discussed in Chapter 4). This is consistent with the layer thickness not increasing, but the peak current ratio decreasing indicating a greater modifier surface concentration and NP surface coverage increasing indicating more cationic sites are present.

The NP assemblies are strongly attached to both TGD and HA modified surfaces. As shown in Table 7.3, the NP assemblies on TGD layers were subjected to stability

treatments and the NP surface coverage re-analysed. The NP count on TGD layers remains unchanged after 15 seconds of sonication in MQ water and 1 M HCl. The NP surface coverage on the HA layer remains as 13 ± 2 NPs / 10^4 nm^2 after the surface was sonicated for 15 seconds in MQ water. When the TGD sample was sonicated in 1 M NaOH, aggregation of NP is observed at the surface. Aggregation indicates that screening of the NP surface charge allows NPs to approach each other sufficiently closely so that van der Waals forces dominate. In this case, aggregation is due to a double effect of firstly, the negative charge on the citrate groups being compensated by the Na^+ ions; and secondly, the pH of 1 M NaOH being above the protonation constant of the amines within the TGD layer, hence the amines groups are neutral. (Aggregation also occurs in NP solution which is adjusted to pH > 12 by the addition of concentrated NaOH solution). These assemblies on TGD layers are also stable when scanned between 1 and -1.5 V in PBS and ACN/0.1 M $[Bu_4N]BF_4$. Samples were stored for a year in air at room temperature and were re-analysed. The NP count remains the same after a year.

Table 7.3. Effects of sonication and potential scan treatments on NP assemblies on TGD layers.

Treatment	Number of NPs assembled prior to treatment / 10^4 nm^2	Number of NPs assembled after treatment / 10^4 nm^2
Sonicate for 15 seconds in:		
MQ water	25 ± 3	22 ± 1
1 M HCl	14 ± 2	13 ± 2
1 M NaOH	10 ± 1	Aggregation
Scanning between 1 and -1.5 V in:		
PBS	10 ± 2	10 ± 2
ACN/0.1 M $[Bu_4N]BF_4$ [a]	10 ± 2	11 ± 2

[a] Reference electrode was a Ag wire.

Alterations to gold NP assembly conditions

In addition to using different modifiers and electrolysis conditions to control NP assembly, NP assembly conditions are altered to achieve the desired NP surface coverage. The immersion time in the NP solution and the concentration and pH of the NP solution were varied for TGD layers (5 mM, electrolysis time 10 minutes). The resulting NP surface coverages are listed in Table 7.4. and plotted in Figure 7.13. For the immersion time experiments, only two samples were used. The samples were immersed for a set time, removed and analysed under SEM, re-immersed in a fresh NP solution for another set amount of time, removed and analysed and so on. Freshly prepared TGD-modified surfaces were prepared for all other experiments.

Table 7.4. Number of citrate-capped gold NPs assembled / 10^4 nm^2 on TGD layers (5 mM, electrolysis time 10 minutes), where alterations to the immersion time, concentration and pH of the NPs solution were made.

Assembly conditions			**Number of NPs assembled / 10^4 nm^2**
Immersion time (minutes)	**Concentration (NP L^{-1})**	**pH**	
1	1.3×10^{16}	4.2	1 ± 1, 1 ± 2
22	1.3×10^{16}	4.2	19 ± 3, 20 ± 3
60	1.3×10^{16}	4.2	34 ± 4, 32 ± 4
180	1.3×10^{16}	4.2	38 ± 4, 38 ± 4
1560	1.3×10^{16}	4.2	34 ± 3, 35 ± 3
180	1.3×10^{14}	4.2	0 ± 0
180	1.3×10^{15}	4.2	1 ± 2, 1 ± 2
180	6.5×10^{15}	4.2	22 ± 2
180	1.3×10^{16}	4.2	25 ± 3, 33 ± 5, 38 ± 4 [a], 38 ± 4 [a]
180	1.3×10^{16}	4.2	25 ± 3, 33 ± 5, 38 ± 4 [a], 38 ± 4 [a]
180	1.3×10^{16}	7	28 ± 3, 23 ± 4
180	1.3×10^{16}	8	7 ± 2, 9 ± 2
180	1.3×10^{16}	12	1 ± 1, 1 ± 1

[a] Samples from immersion time experiment.

Figure 7.13. Plots illustrating the effect of (i) immersion time, (ii) concentration and (iii) pH of NP solution on the number of NP assembled. (i),(iii) NP concentration = 1.3 x 10^{16} NP L^{-1}; (ii),(iii) immersion time = 180 minutes; (i),(ii) NP solution pH = 4.2. Insert in (i) is an expanded plot of shorter immersion times. Dotted line in (iii) provides a visual guide.

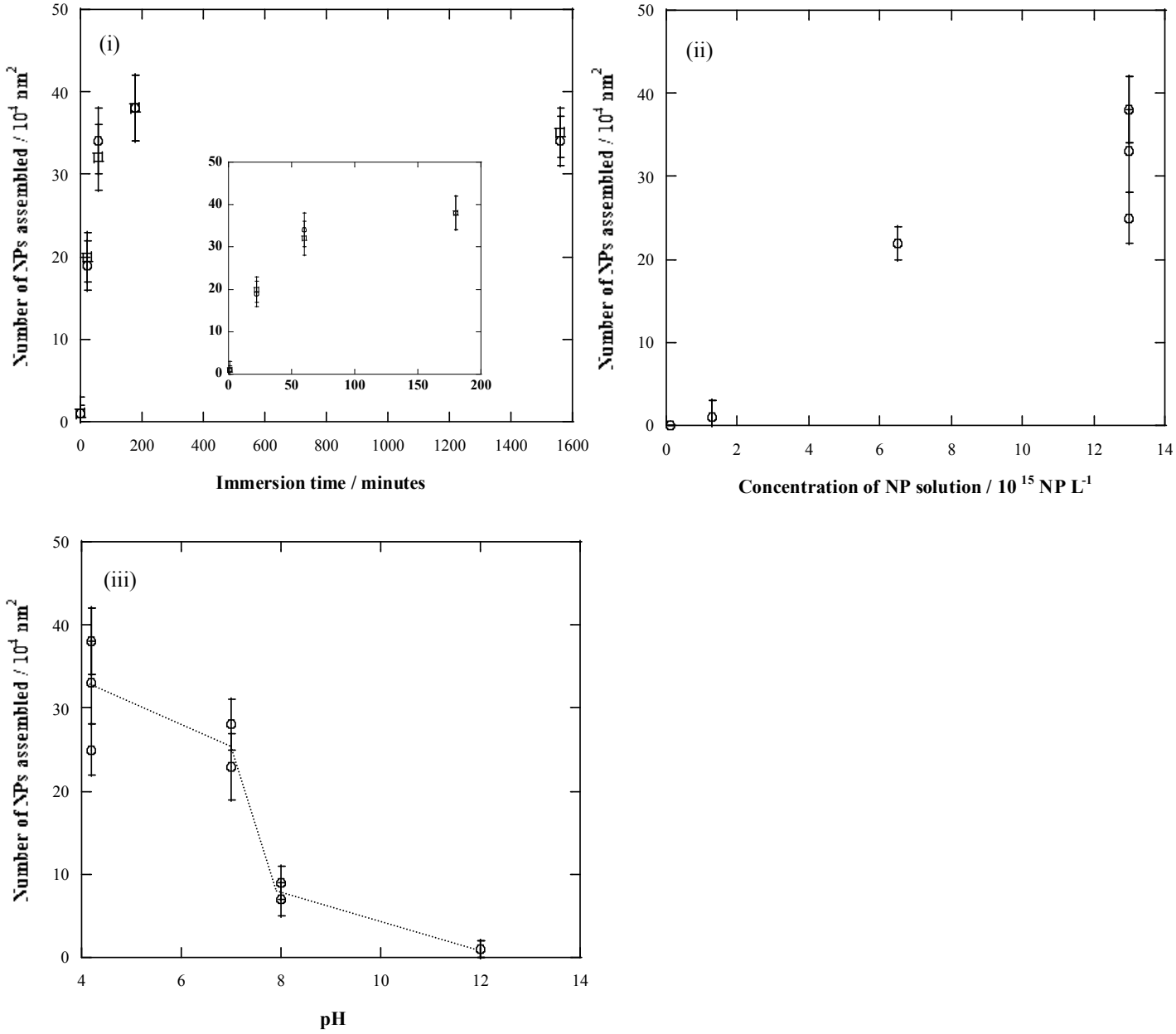

Figure 7.13.(i). is a plot of NP surface coverage against immersion time of the TGD modified surface in the NP solution. Within 60 minutes of immersion, "saturation" surface coverage is reached and maintained up to an immersion time of 26 hours. The "saturation" surface coverage is 32 – 38 NPs / 10^4 nm^2. For 11 nm diameter NPs, the maximum value is calculated as 105 NPs / 10^4 nm^2. Thus, the "saturation" surface coverage is only 36% of the calculated maximum for a closed-packed monolayer. This value is in remarkable agreement with that of Natan and co-workers who report a "saturation" surface coverage of approximately 30% on a glass substrate with immobilised organosilane polymers and NPs with diameter of 15 nm. They studied the kinetic influences of assembly of gold NPs from solution onto the surface. They found that at short immobilisation times, NP surface coverage is proportional to $(time)^{1/2}$, however, at longer immobilisation times (after 60 minutes) interparticle repulsions result in the "saturation" coverage.[23] Similar observations are made in this work where the kinetics of assembly is rather fast, however, it is countered by interparticle repulsions after 60 minutes.

NP surface coverage increases with NP concentration as shown in Figure 7.13.(ii). At concentration half of the original solution, approximately half of the "saturation" surface coverage is observed. This experiment shows that by tuning the NP concentration, the number of NP assembled is controlled (when the immersion time is 180 minutes). However, it is possible that a higher surface coverage may be observed from NP solutions of reduced concentrations if the immersion time is longer than 180 minutes.

TGD layers were immersed into NP solutions after adjusting the pH of the solutions

from 4.2 to 7, 8 and 12. Fresh NP solutions were used for each pH adjustment. Figure 7.13.(iii). is a plot of NP surface coverage against pH of the NP solution. A small decrease in NP surface coverage is observed between the original pH of the NP solution of 4.2 and 7, followed by a significant decrease between pH 7 and 8 and then another small decrease between pH 8 and 12. Further increase of pH above 12 causes aggregation of the NPs and a black solution, presumably due to charge compensation of citrate ions by the Na^+ ion from NaOH. Liu and co-workers also demonstrate the pH dependence of NP surface coverage.[16] The surface coverage of citrate-capped gold NPs on *p*-aminothiophenol-modified gold surfaces depends on the pH of the gold NP solution and closely follows the expected extent of protonation of the aminothiophenol layer.

The NP surface coverage dependence on the pH of the NP solution is explained by the degree of protonation of the amines within the TGD layers. When the pH is sufficiently higher (2 pH units) than the protonation constant, the amines are deprotonated and are no longer able to interact electrostatically with the negatively charged citrate-capped NPs. Therefore from Figure 7.13.(iii), it is possible to estimate the protonation constant of at least one of the amines of the attached TGD to be approximately 7.5. Besides reducing the number of cationic sites for NP assembly, deprotonating the amines influences the environment the sites are in. Deprotonation causes the TGD layer hydrophilicity to be lowered which may also contribute to the decreased NP surface coverage. The pK_a values for citric acid are 3, 4 and 6, hence, over the pH range used, the citrate is predominantly deprotonated.

Gold NP assembly on other modifier layers

In addition to the many modifier layers used in NP assembly experiments described in the previous sections, NP assembly is also examined on other modified PPF surfaces. These surfaces, as listed in Table 7.5, are used as part of experiments in Chapter 9a.

Table 7.5. NP assembly onto modified PPF surfaces as part of experiments in Chapter 9a. NP assembly was for 3 hours unless stated otherwise. NPs solution was used as-prepared.

Sample (modifier concentration, electrolysis time, E_f)	**Treatment prior to NP assembly**	**Number of NPs assembled / 10^4 nm^2**
TGD (5 mM, 2 minutes)	No treatment	9 ± 2
TGD (5 mM, 2 minutes)	Coupling NBC to TGD by immersing TGD layer into 0.1 M NBC in DMSO for 2 hours	8 ± 2
TGD (5 mM, 2 minutes)	Immersed into DMSO for 2 hours	9 ± 5
MCA (5 mM, 1 minute, E_f -1.12 V)	No treatment	0 ± 0 [a]
NPh (0.6 mM, 2 minutes)	No treatment	0 ± 0
NPh (0.6 mM, 2 minutes)	Electrochemical reduction of *p*-nitrophenyl functionalities in the NPh layer to amino groups by *2 scans* in 0.02 M benzoic acid/ACN/0.1 M $[Bu_4N]BF_4$	7 ± 1
NPh (0.6 mM, 2 minutes)	Electrochemical reduction of *p*-nitrophenyl functionalities in the NPh layer to amino groups by *10 scans* in 0.02 M benzoic acid/ACN/0.1 M $[Bu_4N]BF_4$	9 ± 1

[a] Overnight immersion in NP solution.
∗ [and #] Result discussed in text.

It is envisaged that the coupling of nitrobenzoyl chloride (NBC) to an already attached TGD layer could be monitored by the assembly of citrate-capped gold NPs. The

NP count is 9 – 10 NPs / 10^4 nm^2 on the TGD layer (Table 7.2.) and 8 ± 2 NPs / 10^4 nm^2 on the TGD layer exposed to NBC coupling solution (Table 7.5.). The difference is very small possibly because the yield of the coupling reaction is small and the underlying TGD layer consists of protonated amines/amides which are able to assemble NPs. The sample was then scanned in 0.25 M H_2SO_4 with the NPs attached and peaks characteristic for the reduction of *p*-nitrophenyl groups of NBC in acid were observed supporting the coupling of NBC. The TGD layer is unaffected when exposed to DMSO for 2 hours without NBC as also determined by the number of citrate-capped gold NPs assembled (Table 7.5.).

For another coupling reaction of TGD to surface-immobilised *para* methylene carboxylic acid phenyl (MCA), it is important to test that no NPs attach to the as-prepared MCA layer (Table 7.5.).

Assembly of gold NPs is also used to monitor the electrochemical reduction of *p*-nitrophenyl functionalities in the *para* nitro phenyl (NPh) layer to amino groups. The conversion is successful as indicated by NP assembly onto the amines generated from the reduction (Table 7.5.).

7.4. Conclusions

Two types of NPs were assembled onto amine-containing modifiers layers. Aldehyde/sulfate-functionalised PS NPs were preferentially assembled on the PGD-modified layer compared to the as-prepared GC surface. The NP-surface interaction was presumably due to electrostatic interactions between the negatively charged sulfate groups

on the PS NP and the protonated amines of the PGD layer.

Citrate-capped gold NPs were synthesised by the citrate method and were characterised by UV-VIS, TEM and HRTEM. Gold NPs assembled on PPF surfaces modified with amine-containing modifiers. Hence, assembly was due to electrostatic interactions between the negatively charged citrate groups on the gold NPs and the protonated amines of the layer. By using different modifiers of different chemical natures such as a diamine, hydrophilic TGD vs. a monoamine, hydrophobic HA, and tuning the modification conditions, the number of protonated amines of the layer was tailored and hence the NP surface coverage was controlled. Besides controlling the number of amines that were present, using different modifiers also tailored the position and environment the amines were in which also contributed to NP assembly. The immersion time, concentration and pH of gold NP solution was also adjusted which modulated the NP surface coverage. A NP surface coverage below the "saturation" surface coverage of 32 – 38 NPs / 10^4 nm^2 (36% of a closed packed NP monolayer) can be achieved by tuning one or more of these conditions. NP assembly was also carried out on various other surfaces that were prepared as part of experiments in Chapter 9a – molecular patterning.

7.5. References

(1) Cortie, M. B.; van der Lingen, E. *Materials Forum* **2002**, *26*, 1-14.

(2) Nath, N.; Chilkoti, A. *Topics in Fluorescence Spectroscopy* **2005**, *8*, 353-380.

(3) Mulvaney, P. *Nanoscale Materials in Chemistry* **2001**, 121-167.

(4) McConnell, W.; Brousseau, L. C, III; House, A. B.; Lowe, L. B.; Tenent, R. C.; Feldheim, D. L. *Metal Nanoparticles* **2002**, 319-333.

(5) Ogawa, T.; Kobayashi, K.; Masuda, G.; Takase, T.; Shimizu, Y.; Maeda, S. *Transactions of the Materials Research Society of Japan* **2001**, *26*, 733-738.

(6) Glomm, W. R. *Journal of Dispersion Science and Technology* **2005**, *26*, 389-414.

(7) Csaki, A.; Moller, R.; Fritzsche, W. *Expert Review of Molecular Diagnostics* **2002**, *2*, 187-193.

(8) Daniel, M.-C.; Astruc, D. *Chemical Reviews* **2004**, *104*, 293-346.

(9) Grabar, K. C.; Freeman, R. G.; Hommer, M. B.; Natan, M. J. *Analytical Chemistry* **1995**, *67*, 735-743.

(10) Liu, S.; Maoz, R.; Sagiv, J. *Nano Letters* **2004**, *4*, 845-851.

(11) Maya, L.; Stevenson, K. A.; Muralidharan, G.; Thundat, T. G.; Kenik, E. A. *Langmuir* **2002**, *18*, 2392-2397.

(12) Mendes, P. M.; Jacke, S.; Critchley, K.; Plaza, J.; Chen, Y.; Nikitin, K.; Palmer, R. E.; Preece, J. A.; Evans, S. D.; Fitzmaurice, D. *Langmuir* **2004**, *20*, 3766-3768.

(13) Wang, J.; Zhu, T.; Song, J.; Liu, Z. *Thin Solid Films* **1998**, *327-329*, 591-594.

(14) Seitz, O.; Chehimi, M. M.; Cabet-Deliry, E.; Truong, S.; Felidj, N.; Perruchot, C.; Greaves, S. J.; Watts, J. F. *Colloids and Surfaces A* **2003**, *218*,

225-239.

(15) Tien, J.; Terfort, A.; Whitesides, G. M. *Langmuir* **1997**, *13*, 5349-5355.

(16) Zhu, T.; Fu, X.; Mu, T.; Wang, J.; Liu, Z. *Langmuir* **1999**, *15*, 5197-5199.

(17) Demers, L. M.; Park, S.-J.; Taton, T. A.; Li, Z.; Mirkin, C. A. *Angewandte Chemie* **2001**, *40*, 3071-3073.

(18) Demers, L. M.; Ginger, D. S.; Park, S. J.; Li, Z.; Chung, S. W.; Mirkin, C. A. *Science* **2002**, *296*, 1836-1838.

(19) Zhang, H.; Li, Z.; Mirkin, C. A. *Advanced Materials* **2002**, *14*, 1472-1474.

(20) Yamanoi, Y.; Yonezawa, T.; Shirahata, N.; Nishihara, H. *Langmuir* **2004**, *20*, 1054-1056.

(21) Chan, E. W. L.; Yu, L. *Langmuir* **2002**, *18*, 311-313.

(22) Huang, X.; Huang, H.; Wu, N.; Hu, R.; Zhu, T.; Liu, Z. *Surface Science* **2000**, *459*, 183-190.

(23) Grabar, K. C.; Smith, P. C.; Musick, M. D.; Davis, J. A.; Walter, D. G.; Jackson, M. A.; Guthrie, A. P.; Natan, M. J. *Journal of the American Chemical Society* **1996**, *118*, 1148-1153.

(24) Harnisch, J. A.; Pris, A. D.; Porter, M. D. *Journal of the American Chemical Society* **2001**, *123*, 5829-5830.

(25) Jiang, K.; Eitan, A.; Schadler, L. S.; Ajayan, P. M.; Siegel, R. W.; Grobert, N.; Mayne, M.; Reyes-Reyes, M.; Terrones, H.; Terrones, M. *Nano Letters* **2003**, *3*, 275-277.

(26) Zanella, R.; Basiuk, E. V.; Santiago, P.; Basiuk, V. A.; Mireles, E.; Puente-Lee, I.; Saniger, J. M. *Journal of Physical Chemistry B* **2005**, *109*, 16290-16295.

(27) Smith, M. B.; March, J. *March's Advanced Organic Chemistry: Reactions, Mechanisms, and Structure*; Wiley and Sons, **2001**.

(28) Liu, S.; Zhu, T.; Hu, R.; Liu, Z. *Physical Chemistry Chemical Physics* **2002**, *4*, 6059-6062.

(29) Enustun, B. V.; Turkevich, J. *Journal of the American Chemical Society* **1963**, *85*, 3317-3328.

(30) Freeman, R. G.; Hommer, M. B.; Grabar, K. C.; Jackson, M. A.; Natan, M. J. *Journal of Physical Chemistry* **1996**, *100*, 718-724.

(31) Brown, K. R.; Walter, D. G.; Natan, M. J. *Chemistry of Materials* **2000**, *12*, 306-313.

(32) Brust, M.; Walker, M.; Bethell, D.; Schiffrin, D. J.; Whyman, R. *Chemical Communications* **1994**, 801-802.

(33) LaLonde, A. D.; Norton, M. G.; Zhang, D.; Gangadean, D.; Alkhateeb, A.; Padmanabhan, R.; McIlroy, D. N. *Journal of Materials Research* **2005**, *20*, 3021-3027.

(34) Beszeda, I.; Gontier-Moya, E. G.; Imre, A. W. *Applied Physics A* **2005**, *81*, 673-677.

(35) Interfacial Dynamics Corporation; www.idclatex.com, **2003**.

(36) Link, S.; El-Sayed, M. A. *Journal of Physical Chemistry B* **1999**, *103*, 4212-4217.

(37) Jose-Yacaman, M.; Gutierrez-Wing, C.; Miki, M.; Yang, D. Q.; Piyakis, K. N.; Sacher, E. *Journal of Physical Chemistry B* **2005**, *109*, 9703-9711.

(38) Slowinski, K.; Chamberlain, R. V.; Miller, C. J.; Majda, M. *Journal of the American Chemical Society* **1997**, *119*, 11910-11919.

(39) Slowinski, K.; Slowinska, K. U.; Majda, M. *Journal of Physical Chemistry B* **1999**, *103*, 8544-8551.

(40) Becka, A. M.; Miller, C. J. *Journal of Physical Chemistry* **1993**, *97*, 6233-6239.

(41) French, M.; Creager, S. E. *Langmuir* **1998**, *14*, 2129-2133.

8.1. Introduction

As detailed in Chapter 9 (Figure 9.1.), approaches to patterning molecules on carbon surfaces are investigated. In some approaches, poly(dimethyl)siloxane (PDMS) is used as a material used to block part of the surface for patterning. The PDMS blocking material used are either with circular perforations or with microchannels. This chapter details development of experimental methods and preliminary experiments carried out with PDMS.

PDMS is a colourless, elastomeric material and forms reversible, van der Waals interactions when in contact with hydrophobic surfaces as it is itself intrinsically hydrophobic.[1] Figure 8.1. shows its structure. Pyrolysed photoresist film (PPF) is the surface used with PDMS as it is smoother than glassy carbon (GC) and found to form a reversible, watertight and conformal seal with PDMS.

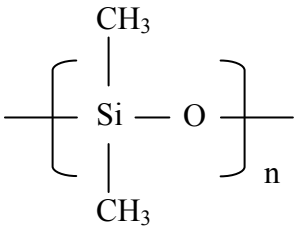

Figure 8.1. Structure of PDMS

8.2. Experimental methods

The methods detailed in this section are the optimised methods derived from the preliminary experiments discussed in the next section.

8.2.1. Preparation of PDMS with perforations

The PDMS used for these experiments was fabricated during the curing/crosslinking preliminary experiments as detailed in the next section. Circular perforations were made through PDMS by forcing either a leather hole punch or a hollow metal rod made from silver steel, straight through the PDMS.

With the silver steel cutter, the PDMS was placed on a soft piece of rubber or another piece of PDMS and cut by slowly rotating the rod through PDMS. The cutting end of the silver steel rod was sharpened on the inside i.e. the cutting edge was the outside the rod. The diameter of the cutting edge of the cutter was taken with electronic callipers under a magnifying glass.

8.2.2. Preparation of silicon master

The silicon master was also used to prepare PDMS patterned with perforations. The design for the mask to pattern the silicon wafer with tall features was created using L-edit and was transferred to chrome plated on glass by Paul Jereback at Stanford University. The silicon wafer initially went through standard photolithography procedures of coating with positive photoresist, exposing through the mask in a mask aligner followed by developing. The silicon wafer with patterned photoresist was then plasma etched using a deep reactive ion etcher which removed approximately 300 μm of the 500 μm silicon wafer. The photoresist helped to slow the etching of the features. The photoresist was then removed using a matrix stripper followed by a wet bench clean in H_2SO_4/H_2O_2. This was carried out at Stanford University with the help of Dr. Charles Schaper and Senyo Dogbe.

8.2.3. Preparation of PDMS microchannels

PDMS microchannels refer to enclosed channels with inlets and outlets. They were utilised by sealing a piece of PDMS with relief/excavated structures (microchannels) onto a PPF surface. Three sides of the microchannels were PDMS and the fourth (bottom) was PPF. As depicted in Figure 8.3, the first step in fabricating PDMS microchannels was to design a mask. The pattern of the mask determines the pattern of the SU-8 photoresist master and hence the pattern of the PDMS microchannels. The second step was to fabricate a SU-8 photoresist master (or template) with features that the PDMS was cured on. Standard photolithography was used in creating the SU-8 photoresist master. SU-8 is a negative photoresist. Standard photolithography typically refers to exposing selected areas of photoresist that is coated onto an entire surface usually a silicon wafer, to ultraviolet (UV) light through a mask. Depending on the type of photoresist, the exposed (positive photoresist) or masked (negative photoresist) areas are removed during developing. The third step was to cure the PDMS on the SU-8 photoresist master. The cured (or hardened) PDMS microchannels were the complementary, inverse pattern of the SU-8 photoresist master.

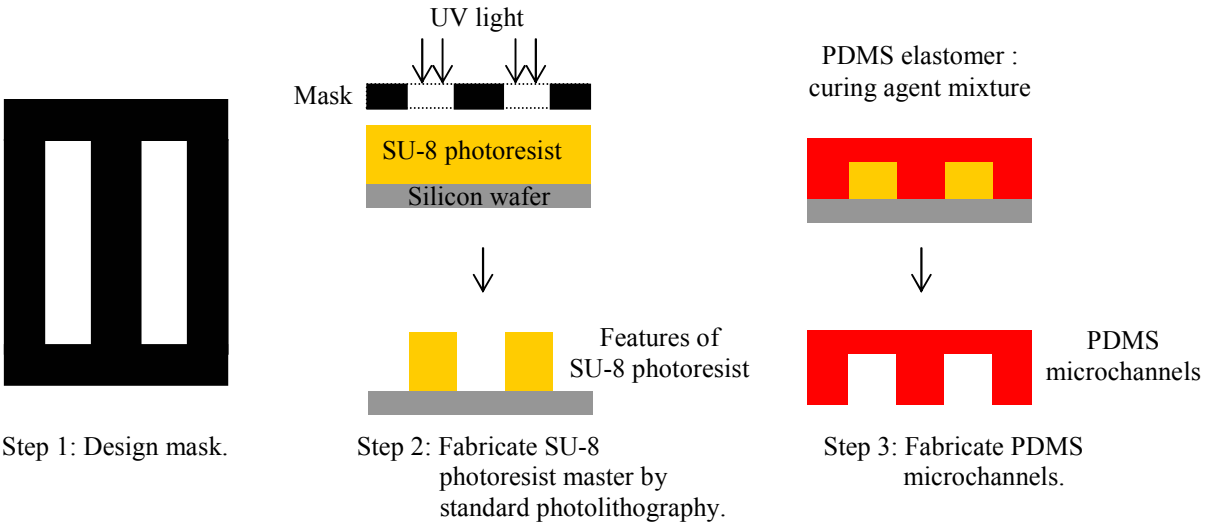

Figure 8.3. Schematic illustrating the three-step procedure for fabricating PDMS microchannels.

Design of masks used in photolithography

Five different masks were designed in order to achieve different patterns of PDMS microchannels as listed below. All apart from the series of *letters* have micro-scale channels.

1. *Y-shaped* pattern with lines **115 µm** wide
2. Series of *letters* – XYZ and UC, with lines **1 mm** wide
3. Two lines in a *plus* sign pattern, each ***100* µm** wide
4. Two lines in a *plus* sign pattern, each ***200* µm** wide
5. Two *parallel lines*, each **20 µm** wide, with a spacing of 380 µm between the lines

The dimensions of the masks in bold were measured from images of the masks captured under the optical microscope. Error on these measurements was ± 2 μm. The patterns are referred to in the text by their italicised label. For the *parallel lines* mask, the spacing between the lines was measured from optical microscope images of the resulting SU-8 photoresist master. The masks were dark field as SU-8 photoresist is a negative photoresist. A dark field mask indicates that the majority of the UV light is blocked out during exposure in the mask aligner when fabricating the SU-8 photoresist master. Thus, the majority of the SU-8 photoresist was masked and was removed when the master was developed.

The *Y-shaped* and *parallel lines* masks were made from transferring the pattern from a replica onto glass, resulting in a chrome plated mask. These two masks were made by Erwin Berthier and Gary Turner at the Department of Electrical Engineering, University of Canterbury. The *plus 100*, *plus 200* and *letters* masks were designed using CorelDRAW 8 and were printed on OHP films at Precision Lithographics on Tuam St, Christchurch. The films were stuck to a glass plate with tape before placing in the mask aligner.

Fabrication of SU-8 photoresist master

SU-8 photoresist was spin coated on 4" *p*-type, prime grade Si (100). The wafers were used as-purchased or cut into 4 pieces before spin coating. The colourless, thick photoresist was poured straight from the 200 mL bottle onto the wafer, due to its viscosity. Spin coating was carried out in two steps: the first was at 1500 rotations per minute (rpm)

for 15 seconds followed by 3000 rpm for 20 seconds. The acceleration in both steps was set so that the spin coater took 5 seconds to reach the set rotation speed. The wafer was placed on a 1 cm thick Al plate and soft baked on a hot plate set at 110 °C for 1 hour. The Al plate slowed down the heat transfer from the hot plate to the wafer so as to achieve a more even heating through the thick photoresist. Even heating prevented cracking of the photoresist. The wafer was then cooled for 10 minutes before it was exposed in the mask aligner.

The wafer was aligned under the mask in the mask aligner and the photoresist exposed to UV light for 20 seconds. The wafer was then post baked on the 110 °C hotplate with the Al plate for 10 minutes. After cooling to room temperature, the SU-8 photoresist was developed in SU-8 developer. Developing was done by placing the whole wafer into a petri dish of developer. During developing, the exposed areas of the negative SU-8 photoresist remained whereas the masked areas were removed by the developer after about 10 minutes. The wafer was then placed into another petri dish with clean developer and washed with isopropyl alcohol (IPA) before drying with $N_{2(g)}$. Hard baking in the 95 °C oven for 5 minutes was the last step.

Fabrication of PDMS microchannels

A ratio of 10:1 by weight of PDMS elastomer : curing agent was mixed thoroughly in a plastic container by stirring for 2 – 3 minutes with a plastic pipette. Other ratios of elastomer : curing agent were also used depending on the rigidity of the PDMS required, i.e. 10:1 being softer than 10:2 and so on. Thorough mixing was crucial to homogeneous curing of the PDMS. The thick, colourless mixture was then degassed in air or more quickly by

careful application of a vacuum, to avoid getting bubbles in the resulting PDMS structure. Care was taken by turning on the vacuum in bursts, so the mixture did not overflow. The mixture was slowly poured onto the SU-8 photoresist master which was positioned on a platform, and allowed to run off the edges. Slow pouring was important to avoid introduction of air bubbles. Bubbles were removed using a pipette. The mixture was then cured in a 95 °C oven for 20 – 30 minutes. The resulting PDMS was very carefully peeled off so as to not remove the SU-8 photoresist features. The PDMS was rinsed with ethanol and dried with $N_{2(g)}$ prior to use and in some cases extraction steps were carried out to remove the uncrosslinked materials prior to use.

8.2.4. Electrochemistry

Electrochemistry in PDMS with circular perforations

The PDMS with the perforation was placed on a PPF surface forming a seal and the perforation defined the electrode geometric area. The cell was positioned on top of the PDMS with the hole in the cell aligned around the perforation in the PDMS. Figure 8.2. illustrates the set-up. The probe or modifier solution was then introduced into the perforation using a Pasteur pipette and the remainder of the solution was then poured into the cell.

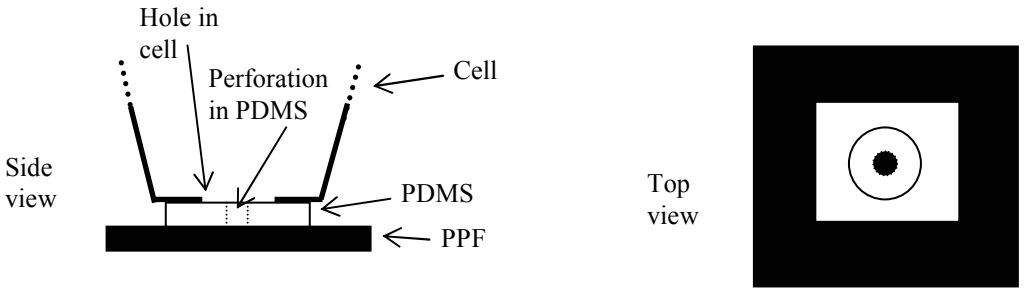

Figure 8.2. Set-up for performing electrochemistry in circular perforations through PDMS.

Electrochemistry in PDMS microchannels

A small piece of the patterned PDMS that could fit within the o-ring of the electrochemical cell was cut out, with a pen knife, from the bulk piece of PDMS microchannels. The piece was typically 8 – 9 mm wide and 4 – 5 mm long which fitted within the viton o-ring with a diameter of 9.4 ± 0.2 mm. The PDMS with the desired pattern formed a conformal seal with PPF upon contact. With the *Y-shaped, plus 100, plus 200, parallel lines* PDMS microchannels, a micro-drop of solution was carefully placed using a micropipette at one of the microchannel entrances. The acetonitrile (ACN) solution flowed through the microchannels by capillary action. The flow was observed by eye. The o-ring was placed around the rectangular piece of PDMS and the cell, with a hole at the bottom, was clamped in place. The PDMS was thinner than the height of the o-ring (1.8 ± 0.2 mm) allowing the cell to be clamped down onto the o-ring without contacting the PDMS. Solution was then introduced around the PDMS using a Pasteur pipette (being careful not to trap air bubbles) and the bulk of the solution was then poured into the cell.

For the *letters* pattern, the letter-shaped microchannels were not open-ended and inlets and outlets were situated above the microchannels. The patterned PDMS was cut around the desired letters from the bulk piece of PDMS microchannels. The inlets and outlets were multiple perforations above the pattern made using hypodermic tubing of 0.8 mm diameter. The modifier solution was very carefully added into pattern using a Pasteur pipette so that a minimal number of air bubbles was present. No o-rings were used and the cell was clamped onto PDMS with the hole at the bottom of the cell aligned over as many perforations through the PDMS as possible. The bulk of the solution was then poured into the cell. Larger PPF surfaces of 20 mm by 30 mm were made to allow for more than one letter on the one surface.

8.3. Results and discussion

Initial experiments were performed to establish the feasibility and conditions for patterning. Considerations of the proposed patterning approaches (Figure 9.1.) suggested that there were a number of aspects that needed to be examined and/or optimised for successful application of these approaches. Requirements are that PDMS must be mechanically stable, must seal to the PPF so that solution does not leak into 'blocked' areas, must maintain its integrity and must be able to be removed from the surface without leaving residues. For both "fill-in" approaches (Figure 9.1.(i). and Figure 9.1.(iii).), the electrochemical attachment of the second modifier must not affect the already attached

molecules. Preliminary tests for the "build-up" approach (Figure 9.1.(iv).) are detailed in the section describing that approach in Chapter 9a.

8.3.1. Curing/crosslinking

Many curing processes were tried in order to achieve a flat piece of not patterned mechanically stable PDMS. The processes varied in the elastomer : curing agent ratio, the curing apparatus and the curing conditions. These curing processes are outlined in Appendix 8. From the results in Appendix 8, mechanically stable PDMS requires that the PDMS elastomer and curing agent are thoroughly mixed, bubbles introduced during mixing are removed prior to curing, a glass ring is not used to contain mixture during curing on a silicon wafer base and that the curing temperature is below 180 °C. The PDMS pieces used for the preliminary tests and the (i): "fill-in" patterning approach using perforated PDMS (Chapter 9), were made using the two procedures in Appendix 8. that resulted in usable PDMS.

The curing/crosslinking process, detailed in Scheme 8.1, is an addition reaction and is also referred to as hydrosilation of the double bonds.[2] The PDMS elastomer component consists of a siloxane oligomer terminated with vinyl groups (**1** in Scheme 8.1.) and a platinum-based catalyst. The curing agent component contains the same siloxane oligomer terminated with vinyl groups (**1** in Scheme 8.1.) as the base and another siloxane oligomer that has at least three silicon hydride bonds (**2** in Scheme 8.1.). When the elastomer and curing agent components are mixed together, the catalyst aids the addition of the silicon hydride bonds of **2** across the double bonds of **1**, forming Si-CH_2-CH_2-Si linkages. An

advantage of this type of addition reaction is that no waste products are generated. Increasing the temperature can accelerate the curing/crosslinking reaction.

The thickness of the usable PDMS was between 1 and 4 mm. A suitable sized piece (smaller than the PPF surface – 14 x 14 mm) of PDMS was cut out from the bulk piece, sonicated in ethanol for at least 3 seconds and dried with $N_{2(g)}$ prior to use.

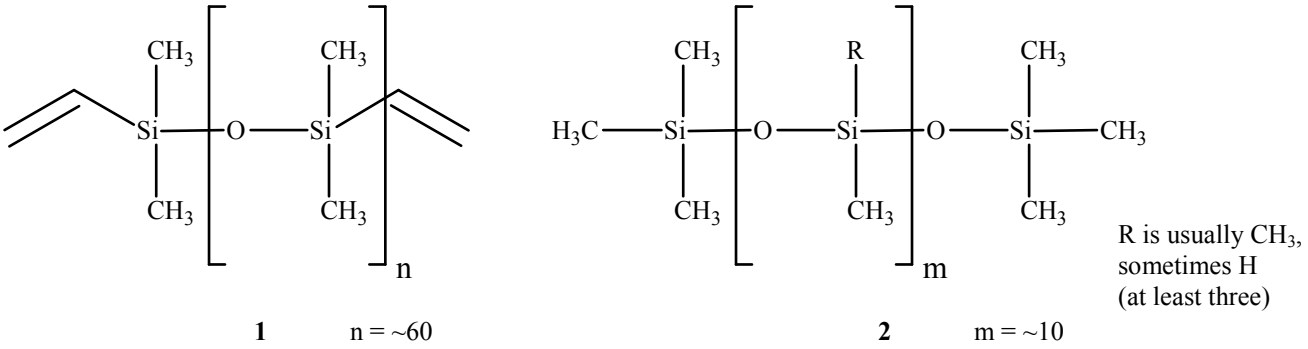

1 n = ~60 **2** m = ~10

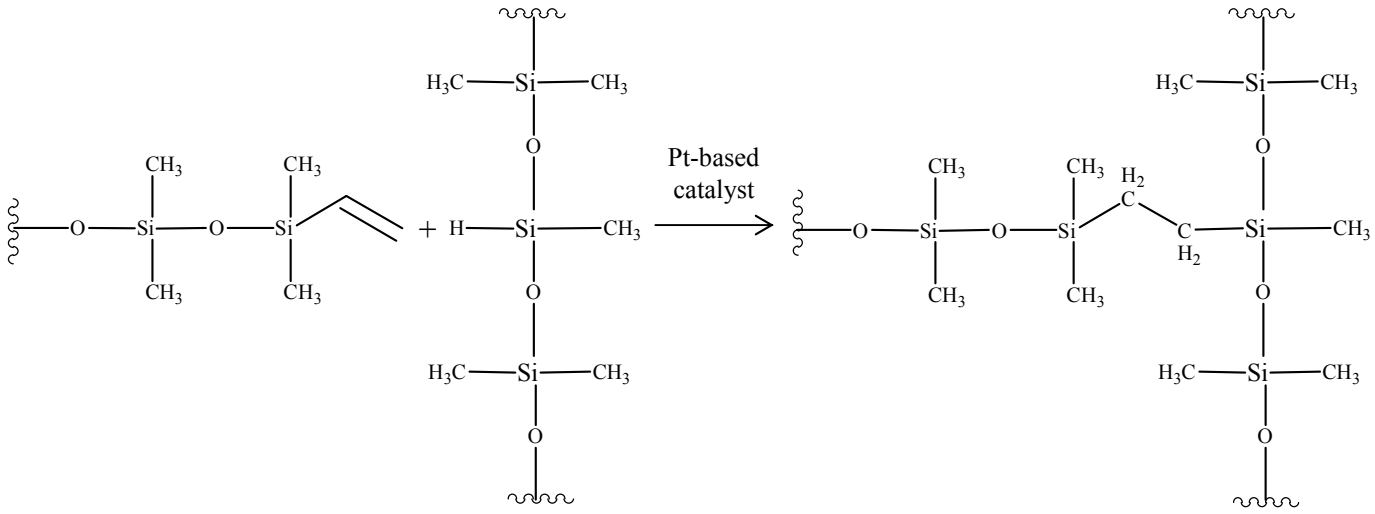

Scheme 8.1.

8.3.2. Seepage and swelling

Tests were performed to ensure that seepage under the PDMS does not occur, i.e. that PDMS forms a conformal seal with the PPF surface and that swelling of the PDMS does not occur with conditions used for electrochemistry, i.e. that the area of electrode remains the same. A perforation (diameter 1.9 mm, area 0.03 cm^2) was cut in PDMS using a hollow metal rod and a ferrocene monocarboxylic acid (FCA) probe scan was recorded at the PPF surface. The probe solution was then replaced with ACN (electrochemical modification solvent) and the cell set-up was left overnight and another probe scan was taken the next day. The currents of the two scans were identical within the typical variations observed between probe scans at identical surfaces, indicating that a seal is maintained between the PDMS and PPF and that the PDMS does not swell or degrade in ACN. PDMS is previously reported only to swell to 1.01:1 (length of PDMS in solvent : length of dry PDMS) in ACN.[3]

The seepage and swelling test was repeated with the ferrocene (Fc) probe in ACN/0.1 M $[Bu_4N]BF_4$ (tetrabutyl ammonium fluoroborate) with the PDMS on PPF left in the probe solution for 12 hours. The perforation dimensions were smaller with diameter of 1.3 mm and area of 0.013 cm^2. Results showed no evidence for leakage or swelling.

The sensitivity of these methods is restricted to only detecting large-scale leakage or swelling, however, small-scale effects which could be significant when using PDMS microchannels could not be detected by this method.

8.3.3. Residues

Another important test is to determine whether PDMS left residues after being in contact with PPF and exposed to ACN. ACN was placed into a perforation made in PDMS and left for one hour, after which the cell was emptied and the PDMS removed. One hour was the maximum time that the PDMS would be in contact with PPF for any modification process. The PDMS did not leave residues that could be detected by eye or atomic force microscope (AFM) depth profiling of the area previously covered by PDMS.

Another residue test was carried out by recording the Fc probe in ACN/0.1 M $[Bu_4N]BF_4$ through a perforation in PDMS at different locations on the one PPF surface. One scan was taken and the PDMS sealed on PPF was left in the probe solution for 12 hours. The PDMS was then moved to another area so that the perforation was positioned over an area previously in contact with PDMS. Another scan was recorded. The peak currents for both scans were within 1% of each other. This suggests that PDMS does not leave a continuous residue layer, however, the probe scans could not detect whether there are small islands of PDMS residues remaining at the surface. In this experiment, the PPF also looked clean by eye and AFM depth profiling experiments showed no residues.

The third residue test is carried out to determine whether PDMS residues (if any) would cause the assembly of citrate-capped gold nanoparticles (NPs). A flat piece of PDMS was sealed onto an as-prepared PPF surface and it was immersed into ACN for an hour. The PDMS was then removed and the PPF surface was immersed into the NP solution for 3 hours. No NPs assembled as analysed under the scanning electron microscope (SEM).

8.3.4. Effect of second modification on already attached modifiers

The effect of the second modification on the already attached modifiers is important in the "fill-in" approaches (Figure 9.1.(i). and Figure 9.1.(iii).). Experiments were carried out to determine whether the conditions used for the second modification step during "fill-in" patterning affects the modifiers already attached to the surface. The effect of applied potential on already attached modifiers was examined by applying potentials scans in ACN/0.1 M $[Bu_4N]BF_4$ to both positive and negative potentials, to tetraethylene glycol diamine (TGD) layers attached to GC rods. Layers were prepared using a range of electrolysis times as listed in Table 8.1. and covered the entire area of the electrode. Fc probe scans were used to monitor the effect of the extended potential scans and changes were expressed as Fc peak current ratio of (anodic/oxidation peak current (i_{pa}) after extended scan)/(i_{pa} as-prepared GC rod). Table 8.1. summarises the experiments and outcomes, where the Fc peak current ratio of (i_{pa} after modification)/(i_{pa} as-prepared GC rod) was 0 except for the 1 scan modification which was 0.8.

Table 8.1. Experiments examining the effect of scanning in ACN/0.1 M $[Bu_4N]BF_4$ on TGD layers, attached with various electrolysis times.

[TGD], electrolysis time or no. of scans	**E_f when scan in ACN /0.1 M $[Bu_4N]BF_4$**	**Peak current ratio** [a, b]
5 mM, 2 minutes	1.3	0.6
5 mM, 10 minutes	1.3	0
5 mM, 1 scan	-1.12	0.9
5 mM, 10 minutes	-1.12	0.2, pinholes

[a] Peak current ratio was (i_{pa} after scan)/(i_{pa} as-prepared GC rod) of Fc probe.
[b] Uncertainty on peak current ratios is ± 0.05.

From the results in Table 8.1, a higher degree of modification, as a result of using prolonged modification conditions, decreases the effect of scanning in either direction. Positive potentials affects the TGD layers when a relatively sparser layer was attached with an electrolysis time of 2 minutes, however, with an electrolysis time of 10 minutes the layer is unchanged when the potential was scanned to 1.3 V. Negative potentials affect the TGD layers. These results are also discussed in Chapter 4.

Another important aspect with dual modification by the "fill-in" approach is to determine if the second modifier attaches to or within the layer of already attached modifier. This is possible as during the electrochemical processes radicals are generated. The effect of the second modification scan on already attached modifiers was investigated by subjecting the TGD layers (5 mM, electrolysis time 10 minutes) to an electrochemical modification of 1 scan in a solution of *para* methyl benzene diazonium tetrafluoroborate (*p*-MB) or *para* nitro aniline (*p*-NA). TGD layers covered the entire area of the electrodes and layers were only scanned once in the solutions of the second modifier as in actual patterning experiments. The second modifier was attached with "milder" electrochemical conditions relative to the first with the intention of achieving two homogeneous areas of each modifier, with no mixing of the layers. For all patterning methods, the ability to visualise the pattern is the most important factor when selecting the modifiers.

Changes in the layer of already attached modifiers was expressed as Fc peak current ratio of (i_{pa} after second modification scan)/(i_{pa} as-prepared GC rod) which was 0.7 ± 0.05 when the second modifier was *para* methyl phenyl (MP) and 0.1 ± 0.05 when it was *p*-NA.

The Fc peak current ratio prior to the scan in the second modifier solution of (i_{pa} after first modification)/(i_{pa} as-prepared GC rod) was 0.

Compared to the data in Table 8.1, the TGD layer becomes less blocking after scanning in the *p*-MB or *p*-NA modifier solution compared to after scanning in the absence of modifier. This is unexpected because if the second modifier attached to the TGD within the layer or to the GC surface between the TGD modifiers, the resulting layer would have been more blocking to the Fc probe.

8.3.5. PDMS with perforations

Circular perforations made by cutters

In the "fill-in" patterning approach using PDMS with circular perforations made by cutters, the first modifier is attached in the perforation. The following step is to remove the PDMS (by peeling it off) and to attach the second modifier where the electrode area is defined by an o-ring that is larger than the first modified area.

The diameter of the perforation in the PDMS which is also the area for the first modifier in the "fill-in" patterning approach was measured in three ways. Firstly, the diameter of the perforation in PDMS was measured under the optical microscope. Secondly, measurements were estimated from electrochemical scans of probe scan before modification and the first modification scan. These scans were each carried out at a GC rod electrode before the identical scan was recorded at the PPF surface through the perforation in PDMS. By comparing the currents observed for the GC rod of a known geometric area, the diameter of the perforation in PDMS was calculated. Thirdly, the diameter of the

modified area was measured using the AFM camera and vision system. These three diameter values were always identical considering error.

Table 8.2. lists the dimensions of the two pieces of perforated PDMS made using the different cutters that was used for molecular patterning experiments as detailed in Chapter 9a. The leather hole punch was used to obtain large perforations in PDMS compared to the hollow silver steel rod. The silver steel rod gave perforations with well-defined edges as it is a tough material and the cutting edge did not blunt when cutting. Additionally to avoid blunting, PDMS was placed on a soft piece of rubber or another piece of PDMS and cut by slowly rotating the rod through PDMS. An optical microscope image of the perforation made in PDMS number 2 with well-defined edges is depicted in Figure 8.4. The silver steel cutter was also sharpened on the inside rather than the outside, which was intended to reduce spreading of the PDMS during cutting and allow better correspondence between the diameter of the cutter and the perforation cut in PDMS. The size of the perforation in the PDMS is not only determined by the diameter of the cutting edge of the cutter but also the thickness of the PDMS. A smaller perforation was made with thicker PDMS (~ 4 mm) for PDMS number 2.

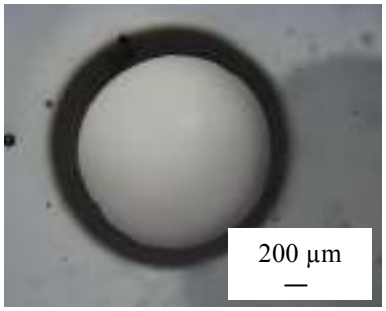

Figure 8.4. Optical image of perforation cut in PDMS using hollow metal rod made from silver steel.

Table 8.2. Two pieces of PDMS with circular perforations made using various cutters.

PDMS no.	Perforation size in PDMS/ area for 1st modification [a]	Diameter of cutting edge of cutter [b]
1	Diameter = 4.0 mm, Area = 0.13 cm^2	Leather hole punch, not measured
2	Diameter = 1.4 mm, Area = 0.015 cm^2	Hollow metal rod made from silver steel, 2.3 mm

[a] Maximum error on diameter measurement of perforation in PDMS was ± 0.05 mm.
[b] Error on measurement of outer diameter of cutter was ± 0.2 mm.

Complex patterns of perforations

Two other ways were tried for fabricating more complex patterns of perforations through PDMS rather than a circular perforation, however, with limited success.

(i) Silicon master

The silicon master with raised features was used as a template for curing PDMS such that there were perforations in the resulting PDMS, as shown in Figure 8.5. The horizontal dimensions of the features of the silicon master ranged from 1 – 5 mm and the heights were 300 μm.

This method was unsuccessful as when the elastomer : curing agent mixture was poured onto the silicon master, the mixture was too viscous and PDMS formed over the features. When the mixture was spin coated onto the silicon master, giving a thinner layer of PDMS, the PDMS formed around and also over some of the features and tore when it was peeled off. This method for creating perforations is similar to the 'dry lift-off' patterning method, where the template is a photoresist pattern on a silicon wafer and the thickness of the cured PDMS is in the micro-scale.[4,5] Another problem with this approach using the silicon master was the resulting PDMS was rough and did not form a good seal with the PPF surface. This was due to roughening of the silicon master during its fabrication using deep reactive ion etching.

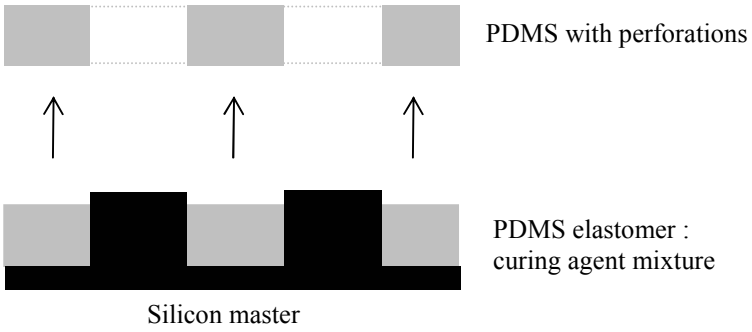

Figure 8.5. Method for making more complex patterns of perforations through PDMS using a silicon master.

(ii) Teflon block

A teflon block with finely machined features was made at the mechanical workshop in the Chemistry Department. Two 2 cm tall, 1 mm wide and 5 mm long raised

strips/features with 1 mm spacing between them were machined on a 2.3 x 2.3 cm teflon block. The strategy was the same as described for the silicon master, but the features were significantly taller to prevent PDMS from curing over the features. The elastomer : curing agent (10:3) mixture was poured onto the teflon block. A glass ring was used to contain the mixture during curing in order to achieve thicker PDMS. The 10:3 ratio and the thicker PDMS were used to avoid tearing the PDMS on removal after curing. Perforations were present; however, the base of PDMS was too rough to form a seal with PPF because of rough base of teflon block, as shown in Figure 8.6. The top of PDMS was not flat from PDMS curing up the sides of the features and thus the top side also did not form seal with PPF.

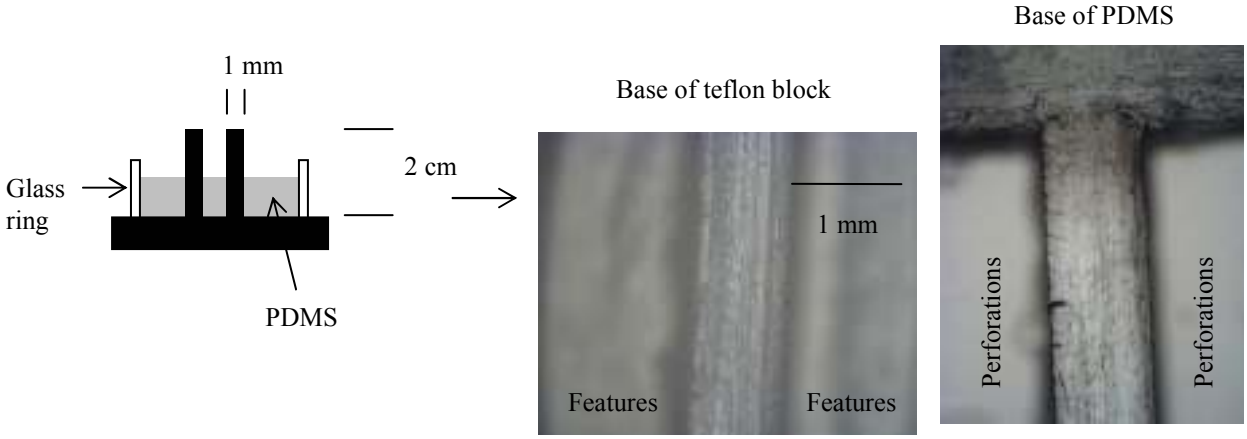

Figure 8.6. Attempted method for making more complex patterns of perforations through PDMS using a teflon block. The base of the PDMS formed was an inverse replica to the micro-scale of the base of the teflon block as shown in the optical microscope images.

In summary, apart from cutting perforations through PDMS using cutters, methods for making patterns of perforations in PDMS were unsuccessful. However, at this point, it was decided that molecular patterning was possible using PDMS microchannels where the

modifier solution was flowed through the channels rather than in the perforations. The thickness of the bulk of the PDMS with microchannels is in the millimetre range and thus is easy to handle.

8.3.6. PDMS microchannels

This section describes the significant amount of method development and refinement undertaken to achieve suitable masks and to fabricate SU-8 photoresist masters of acceptable quality. The curing method to obtain suitable PDMS microchannels was derived from the curing/crosslinking experiments as discussed above.

Design of masks used in photolithography

Under the optical microscope, the masks with the *Y-shaped* and *parallel lines* patterns were of high quality and had acceptable straight edges, however, the *plus 100*, *plus 200* and *letters* masks printed at Precision Lithographics did not have straight edges. Due to the fact that the resolution of the masks is reflected in the master and subsequently the PDMS, these masks were only suitable for preliminary molecular patterning experiments. Table 8.3. lists the width of the different mask designs which were measured from the optical microscope images. Optical microscope images of some of the masks are shown in Table 8.4.

Fabrication of SU-8 photoresist master

The method detailed in the Experimental section was the optimised procedure used for the fabrication of SU-8 photoresist masters and was the outcome of the many attempted procedures that resulted in unsuitable SU-8 photoresist masters as detailed in Appendix 8. SU-8 photoresist masters are deemed of unacceptable quality when the features are not of identical dimensions and straightness of edges as the mask used to fabricate it and more importantly if the features do not adhere to the silicon wafer.

The optimised method was used only to fabricate the *parallel lines* masters. The SU-8 masters with the other four patterns were made in one of the earlier trial experiments. From the results of these trial experiments detailed in Appendix 8, the component of the process and their influence on the quality of the masters are listed below:

(i) *Si (100) wafer*: *p*-type prime grade and 1 μm silicon nitride test grade gave identical results.

(ii) *Period between spin coating and soft bake*: immediate soft bake or a delay of 12 hours gave the same results.

(iii) *Time for soft bake and use of Al plate during soft bake*: a 10 and 30 minute soft bake time, with or without the Al plate gave the same results.

(iv) *Exposure time*: a 3 – 4 minute exposure time allowed for light spreading and so the SU-8 photoresist features were larger than the mask.

(v) *Use of Al plate during post bake*: post bake with or without the Al plate gave similar results.

Using the *parallel lines* mask (width of each line 20 μm) with very straight edges, the soft bake time with Al plate was increased to an hour and the exposure time was adjusted to fabricate 20 μm wide lines (Figure 8.7.). 20 μm wide lines were obtained when the exposure time was 20 seconds. With 15 seconds exposure, the SU-8 photoresist lifted off. The exposure time is critical as too long an exposure time creates larger features than those on the masks due to spreading of the light under the mask by reflection off the silicon wafer and the chrome mask and too short an exposure time causes problems with the poor adhesion of developed SU-8 photoresist to the silicon wafer.

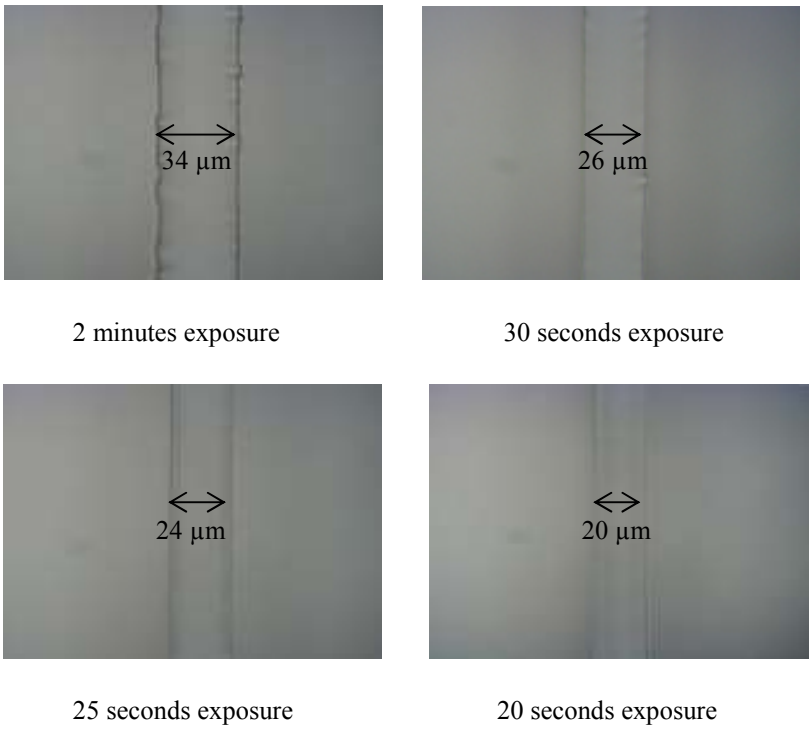

Figure 8.7. Optical microscope images showing the effect of exposure time on the width of the SU-8 photoresist line.

With the two main issues of correspondence between mask and master and the adhesion of the photoresist features resolved, the method as detailed in the Experimental section was used for fabricating *parallel lines* SU-8 photoresist masters of suitable standards. For the other master designs, the defects of some of the resulting SU-8 photoresist masters are seen in the optical microscope images in Table 8.4.

The quality of the masters was examined by the optical microscope and a cross sectional profile was carried out with the profilometer. The widths of the SU-8 photoresist features, listed in Table 8.3, were measured from optical microscope images and some images are shown in Table 8.4. The error on measurements from the optical microscope images was ± 2 μm. The heights of the features were taken from the cross sectional profile and are listed in Table 8.3. Two profiles were recorded with the profilometer and heights from each profile averaged for each master. The error on the height readings was ± 2 μm.

PDMS microchannels

The optimised method for curing PDMS on SU-8 photoresist masters was based on the knowledge gained in curing/crosslinking preliminary experiments discussed above for curing a flat piece of PDMS, and is detailed in the Experimental section. The bulk PDMS had a thickness of 1.6 – 1.7 mm measured by electronic callipers. The widths of the microchannels were measured from optical microscope images, some of which are shown in Table 8.4. and listed for all designs in Table 8.3. As shown in the images in Table 8.4. the defects of the master are transferred to the PDMS microchannels.

From the measurements in Table 8.3, it appears that the PDMS microchannels shrank up to 36% (*parallel lines*) in width when the PDMS was peeled off the master. With the narrower microchannels, it was difficult to obtain accurate optical microscope images. This is because images were taken with the PDMS microchannel facing upwards towards the microscope and focusing on top of the PDMS rather than the bottom of the trench/microchannel was challenging. Therefore, the width of 14 μm is a rough estimate. Shrinkage of only up to 1% is reported to occur when the PDMS is removed from a master and hence it is assumed that the value of 14 μm is a significant underestimation of channel width.[6] The depth of the PDMS microchannels could not be measured using the profilometer due to the elasticity of the PDMS material and thus is assumed to be similar to the height of the SU-8 photoresist master.

Table 8.3. Dimensions of the features of the masks, SU-8 photoresist masters and PDMS microchannels of the various designs. Error on the measurements was ± 2 μm.

	Y-shaped	***Letters***	***Plus 100***	***Plus 200***	***Parallel lines***
Width of mask	115 μm	-	100 μm	200 μm	20 μm
Width of master	184 μm	-	152 μm	256 μm	22 μm [a]
Width of PDMS microchannels	172 μm	-	129 μm	234 μm	14 μm [a]
Height of master	20 μm	60 μm	62 μm	59 μm	49 μm

[a] Spacing between the lines (measured from optical microscope images) was 380 ± 2 μm.

Table 8.4. Optical microscope images of masks, SU-8 photoresist masters and PDMS microchannels.

	Y-shaped	***Plus 200***	***Parallel lines***
Mask	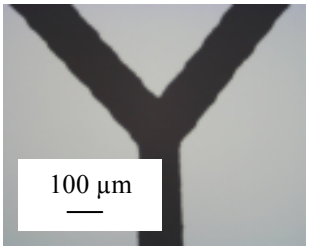	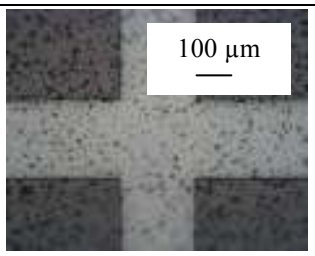	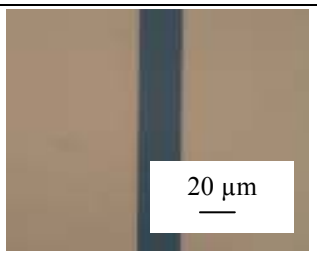
SU-8 photo-resist master	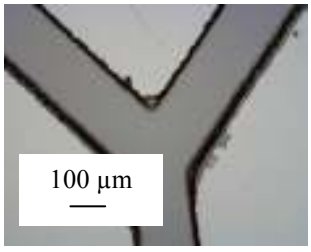	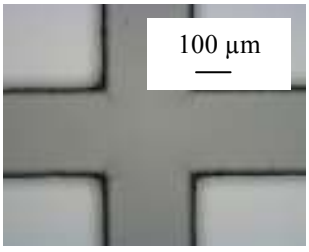	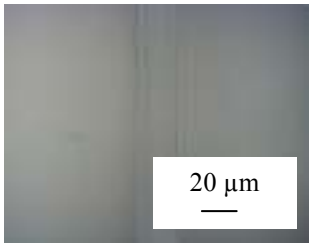
PDMS micro-channels	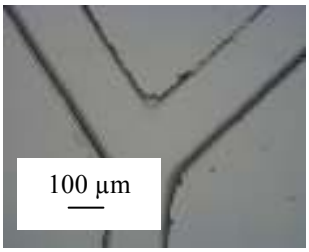	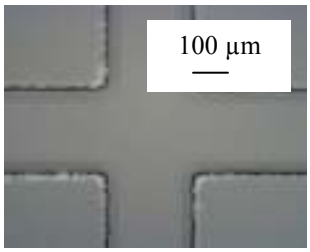	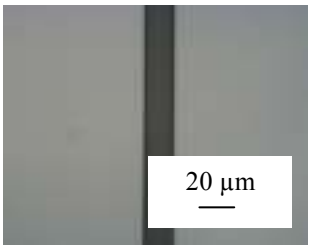

8.4. Conclusions

In this chapter, the preparation of PDMS with perforations and PDMS microchannels that were used for molecular patterning in Chapter 9a was investigated. The methods for curing/crosslinking PDMS; making perforations in PDMS; fabrication of masks, SU-8 photoresist masters and PDMS microchannels and performing electrochemistry in perforations and microchannels were established. Preliminary experiments showed that large-scale seepage of solution under PDMS or swelling of PDMS in ACN did not occur as tested using redox probe species. Residue tests indicated that residues did not remain when PDMS had been in contact with the as-prepared PPF surface. The examination of residues was carried out by eye, AFM depth profiling, redox probe scans and assembly of citrate-capped gold NPs. The effect of potential scans and electrochemical attachment of the second modifier on already attached TGD layers was also examined.

8.5. References

(1) Sia, S. K.; Whitesides, G. M. *Electrophoresis* **2003**, *24*, 3563-3576.

(2) Campbell, D. J.; Beckman, K. J.; Calderon, C. E.; Doolan, P. W.; Ottosen, R. M.; Ellis, A. B.; Lisensky, G. C. *Journal of Chemical Education* **1999**, *76*, 537-541.

(3) Lee, J. N.; Park, C.; Whitesides, G. M. *Analytical Chemistry* **2003**, *75*, 6544-6554.

(4) Jackman, R. J.; Duffy, D. C.; Cherniavskaya, O.; Whitesides, G. M. *Langmuir* **1999**, *15*, 2973-2984.

(5) Duffy, D. C.; Jackman, R. J.; Vaeth, K. M.; Jensen, K. F.; Whitesides, G. M. *Advanced Materials* **1999**, *11*, 546-552.

(6) Xia, Y.; Whitesides, G. M. *Angewandte Chemie* **1998**, *37*, 550-575.

9.1. Introduction

Molecular patterning, in the context of this work, involves creating modified surfaces with spatially defined functionalities, where the two different organic molecules are covalently attached in pre-determined locations on the single planar surface. Although a large amount of research has been carried out on the patterning of gold and silicon surfaces, there are few examples of patterning on carbon surfaces. One example of molecular patterning on carbon surfaces is the selective ultraviolet (UV) irradiation of deposited photobiotin causing site-specific binding and micron-scale protein patterns.[1] Another example of patterning on carbon is carried out by mechanical removal of a selected area (scratch) of surface-bound layers by an atomic force microscope (AFM) tip so that the underlying surface is exposed. The second modifier is subsequently attached in the scratch using electrochemical methods to give nano-scale patterns.[2] In this chapter of work, the aim is to devise approaches to patterning molecules on carbon surfaces and methods to visualise the patterns.

9.1.1. Approaches to molecular patterning

Three main approaches to molecular patterning are undertaken in this work, namely the "fill-in", "build-up" and "selective conversion" strategies. These approaches are outlined in Figure 9.1. The materials used to block part of the surface for patterning are poly(dimethyl)siloxane (PDMS), poly(vinyl)alchol (PVA) or films of Au and NiCr (nichrome). This chapter is organised into different parts according to the blocking material used for patterning – 9a. PDMS, 9b. PVA and 9c. metal films.

(i) "Fill-in" approach where blocking material has perforations:

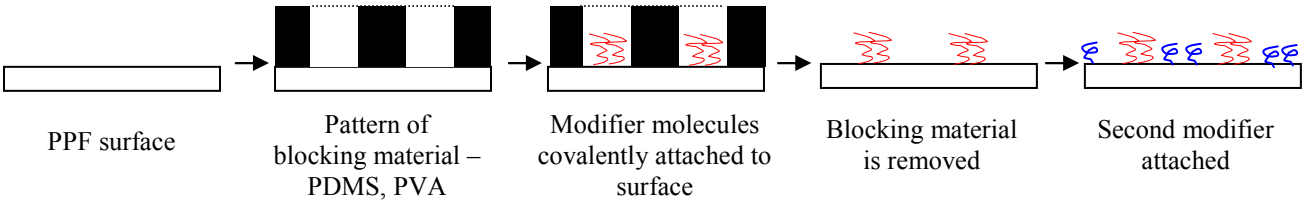

(ii) "Fill-in" approach where blocking materials are islands:

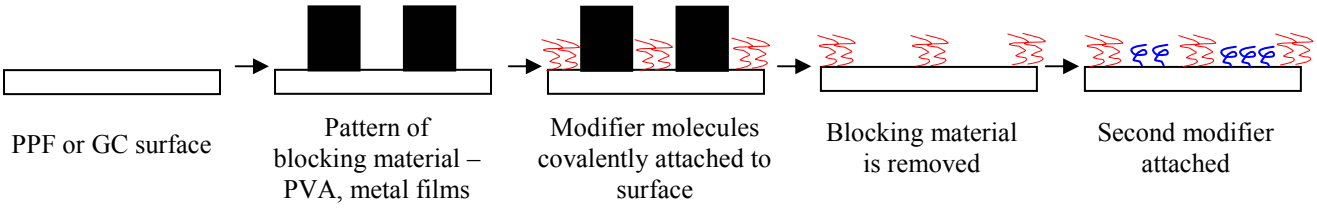

(iii) "Fill-in" approach where blocking material has microchannels:

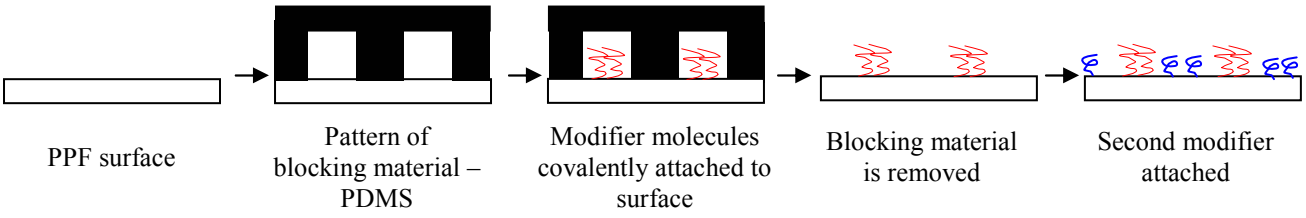

(iv) "Build-up" approach where blocking material has microchannels:

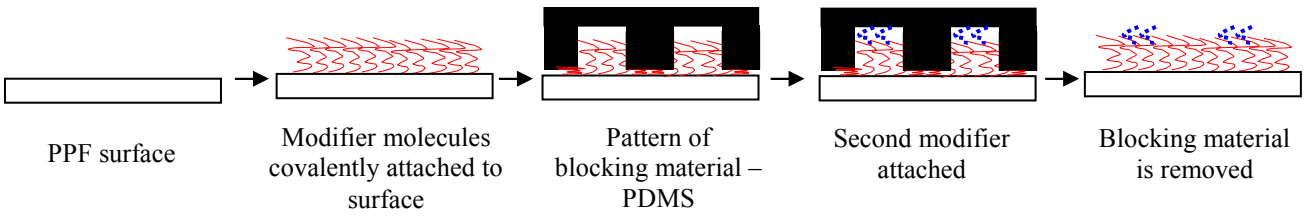

(v) "Selective conversion" approach where blocking material has microchannels:

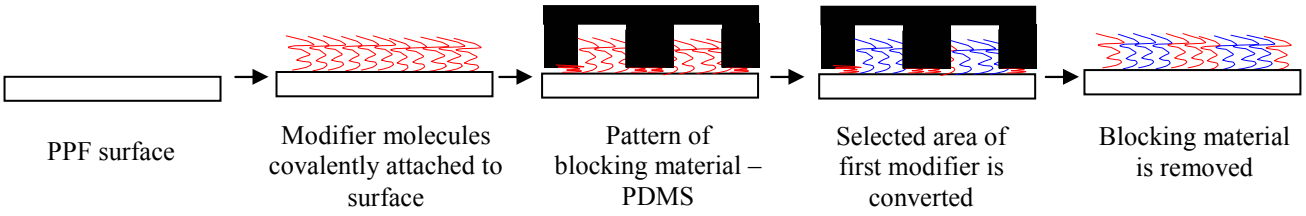

Figure 9.1. The five main approaches to patterning molecules on carbon surfaces used in this work were (i) "fill-in" where the blocking material has perforations, (ii) "fill-in" where the blocking material are islands, (iii) "fill-in" where the blocking material has microchannels, (iv) "build-up" and (v) "selective conversion".

9.1.2. Blocking materials

Of the three blocking materials – PDMS, PVA and metal films, only PDMS has been used for molecular patterning on surfaces. PDMS is widely used for soft lithography, i.e. micro-contact printing (or stamping) and in microfluidics devices (or microchips).[3-5]

Patterning using micro-contact printing is reviewed in Chapter 1. With microfluidics, small volumes of solution are moved through microchannels embedded in the chip. Conventional microfluidic devices have been fabricated in materials such as silicon and glass. However, their production is generally expensive and time consuming and hence the shift to polymeric substrates. Of all the polymers used for fabricating chips, PDMS is the most popular.[5] Generally, the microchannels are embedded in the PDMS by replica molding on an SU-8 photoresist master and then the PDMS is sealed onto the substrate such as glass or silicon. Using PDMS to fabricate microfluidic devices was introduced by Whitesides and co-workers with the aim of using these devices for biological procedures.[6] The focus for the development of PDMS microfluidic devices has not changed

since then,[7,8] and chips for cells,[9] protein,[10,11] and DNA[12] have been fabricated. Various surface treatments of the PDMS microchannels are possible such as silanisation or phospholipids bilayer attachment after oxygen plasma treatment. These treatments are important as most of the biological systems require aqueous solvents and surface alterations can also impart biospecificity into the device and reduce protein adsorption for example.[5]

In this work, PDMS is utilised in less conventional approaches. Of the four approaches where PDMS is used as the blocking material shown in Figure 9.1, approach (i): "fill-in" where blocking material has perforations and (iv) "build-up", have been previously used to pattern surfaces other than carbon. Other workers have used a 'dry lift-off' method,[13,14] which is identical to the "fill-in" approach (i), that involves spin coating the elastomer : curing agent mixture onto a photoresist patterned silicon master so that the polymer is thinner than the photoresist. After curing, the PDMS is peeled off and sealed on a surface where it acts as the blocking material while evaporating or electroplating various materials. The PDMS is then removed giving the patterned surface.

The "build-up" approach can be considered an alternative to consecutive micro-contact printing. Consecutive micro-contact printing involves modification of the surface with molecules consisting of a specific functionality followed by stamping a pattern of another molecule onto the modified surface. On contact, the second molecule reacts with the surface-bound one to yield a covalent bond. Amide bonds are formed by printing amines onto a surface functionalised with carboxylic anhydride moieties[15] and carboxylic acid groups onto an amine terminated surface[16]. Other combinations are a hydroxyl functionalised ligand onto an anhydride derivatised surface to give ester bonds[17] and

printing amines onto an aldehyde terminated surface to yield imines.[18] In the "build-up" approach, the second molecule flows through PDMS microchannels sealed to the modified surface and couples to the already attached first modifier. This approach uses the principles of microfluidics and has been previously used on an anhydride-terminated SAM layer attached to a silicon surface with amines flowing through the microchannels[19] and on an amine-terminated silicon surface with acid chloride functionalised molecules in the microchannels[20].

The properties of PDMS were discussed in Chapter 8. The second blocking material used is PVA. PVA is most commonly used in adhesives. However, PVA has been used in more technical processes as a material for high-resolution pattern formation and materials transfer printing.[21-23] PVA is soluble in water but can be made insoluble by a photochemical process that crosslinks the polymer chains. For this process to occur, a mixture of PVA solution and the crosslinking agent, ammonium dichromate, is coated on the surface. The PVA : crosslinking agent mixture effectively acts like a negative photoresist so that the selected areas exposed to UV light crosslinks and is insoluble in water whereas the masked areas are developed and removed in water. The resulting patterns adhere well to the surfaces used such as glass, indium tin oxide (ITO) and steel.[24-27] In devices used for information displays and light-emitting diodes, patterns of PVA are used as an underlying layer for following depositions and phosphor is deposited in patterns using PVA : crosslinking agent solution as a solvent. The structure of PVA is given in Figure 9.2.

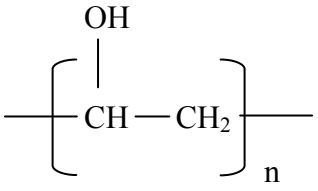

Figure 9.2. Structure of PVA

Metal films are the third blocking material utilised for molecular patterning. Thin metal films of various kinds are commonly deposited onto substrates for the fabrication of integrated circuits and other electronic devices. Frequently deposited metals include nichrome and gold, which are used in this work. The nichrome alloy is deposited by evaporation or sputtering and gold is coated onto a surface by evaporation, sputtering or electroplating.[28]

Removal of nichrome and gold using wet etches is common practice and a variety of commercially available etches for these metals are used. The metal film is typically patterned using photoresist and standard photolithography. The photoresist is coated onto the metal film and selected areas of the photoresist are exposed to UV light through a mask. Depending on the type of photoresist, the exposed (positive photoresist) or masked (negative photoresist) areas are removed during developing. The pattern of photoresist acts as an etch mask i.e. metal is only etched in areas without the protective layer of photoresist.[29]

9.1.3. Visualisation of molecular patterns

Apart from devising various approaches to molecular patterning on carbon surfaces, an equally important aspect of this work is to develop a series of visualisation methods for patterns of modifier layers on carbon surfaces. Previous methods that have been used to visualise molecular patterns on surfaces include condensation figures, using the scanning electron microscope (SEM) and AFM and assembly of nanoparticles (NPs). Properties of the carefully selected molecules are exploited in these visualisation methods.

When a surface is patterned with areas of different molecules that have varied physical properties, especially interfacial free energy, the condensation of water droplets onto the two areas give a different distribution of droplets that allows the pattern to be observed.[30]

When the surface-immobilised molecules are insulating, the primary electrons in the beam of the SEM reflect off the underlying conducting surface and the secondary electrons are scattered by the modifiers. Depending on their composition, the molecules have different scattering capabilities which affect the number of electrons that reach the detector, thus determining the brightness of the SEM image. Increased scattering causes fewer electrons to reach the detector and thus that area of the pattern appears darker. Molecules with different chemical compositions are chosen to provide sufficient contrast to capture the pattern.[31,32]

The AFM provides several ways to analyse molecular patterns. When used in tapping mode, the difference in topography of the pattern boundary is measured.[2] The AFM is also used in the contact mode in ambient conditions. Contact mode AFM is used to

measure four properties: (i) friction or lateral force changes over pattern boundaries; (ii) friction forces when scanning over each modifier at one time; (iii) topography at pattern boundaries and (iv) adhesion forces in air. The friction and adhesion forces depend on the wettability of the surface. When carried out in air, the friction force is expected to be higher when scanning over a hydrophilic modifier than a hydrophobic one due to more water molecules present at the hydrophilic surface.[33] Similarly, the capillary forces are anticipated to be higher at a hydrophilic surface thus increasing the adhesion force. Figure 9.3. depicts the meniscus, which produces the capillary force, between the AFM tip and the surface modified with hydrophilic modifiers.

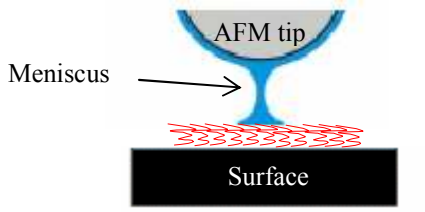

Figure 9.3. Diagram showing a meniscus that forms between the AFM tip and the surface modified with hydrophilic modifiers. The meniscus produces the capillary force and occurs when AFM experiments are carried out in ambient conditions.

NPs have been assembled onto molecular patterns that consist of modifiers with different affinities for the NPs. An example is the assembly of citrate-capped gold NPs on a pattern consisting of amino and nitro groups.[32] This approach to NP assembly allows for NP patterning that is relevant for biosensors, electronics, and optical devices.[32]

9.2. Experimental methods

9.2.1. Materials

The PDMS elastomer (Sylgard 184) and the curing agent were used as purchased from Dow Corning. Nano™ SU-8 50 (diluted by 50% with SU-8 developer ((1-methoxy-2-propyl) acetate)) photoresist and the Nano™ remover PG (SU-8 cleaner) were purchased from Microlithography Chemicals Corporation. SU-8 developer ((1-methoxy-2-propyl) acetate) was from Merck.

PVA was used as purchased as a 7% by weight aqueous solution from Fibrelay, Incorporated. The green PVA solution contained a dye. PVA sticky tape was from Shercon. These PVA materials were supplied by Dr. Charles Schaper from Stanford University. MilliQ (MQ) water used to remove PVA.

Nichrome (NiCr) wire was 80% Ni and 20% Cr by weight.

9.2.2. Instruments

The two spin coaters used for PPF fabrication were also used in this section of work. A Suss MA 6 mask aligner, with a UV light source of 6.9 – 7.1 $mWcm^{-2}$ at λ = 365 nm, was used for photolithography. The oxygen plasma asher was from E.T. Equipments. A Prior Scientific light microscope from was used for quick-and-easy viewing of PDMS on PPF. The vacuum evaporator used for depositing metal films was from Blazers. Shadow masks were made by the Department of Chemistry mechanical workshop at the University of Canterbury.

9.2.3. Electrochemistry

Electrochemical settings used in this chapter were adopted from those discussed in Chapter 4 for amines and Chapter 5 for aryl diazonium salts.

Methods for performing electrochemistry using PDMS with perforations and microchannels were described in Chapter 8. For the "fill-in" patterning approach where the PDMS has perforations or microchannels, after the first modifier was attached, the PDMS was peeled off, the PPF surface rinsed with acetonitrile (ACN), MilliQ (MQ) water, dried with $N_{2(g)}$ and the second modifier attached with the standard conditions. For the second modification, the o-ring used in the electrochemical cell was placed over the majority of the pattern of already attached modifier. For the "selective conversion" approach, the modifier layer was attached with a standard sized o-ring. The PDMS microchannels were positioned in the centre of the modified area. After the electrochemical-assisted conversion of selected areas of the modifier layer, the PDMS was peeled off and the PPF surface rinsed with ACN and then MQ water. The samples was then dried with $N_{2(g)}$ and analysed.

Larger viton o-rings (diameter 9.4 ± 0.2 mm) than those used in the standard cell set-up were used with PVA and metal films. These o-rings were sufficiently large to fit around the PVA and metal film patterns in order for modifiers to attach around or within the patterns of blocking materials.

9.2.4. Molecular patterning using PVA

For the majority of the experiments, PVA solution was applied to the PPF surface by spin coating until PVA was a constant colour and formed a solid sheet. Spin coat speed

and time were used to give the desired PVA sheet thickness as measured by spin coating onto a silicon wafer and scratching with a pin (silicon wafer not scratched) and profiling the scratch using the profilometer. Unless otherwise stated, spin coating was carried out at 1000 rotations per minute (rpm) for 1 minute which resulted in a 1.0 – 1.1 μm thick PVA sheet. The PVA sheet was exposed to $N_{2(g)}$ briefly before use to aid drying of the PVA and increase adhesion to the PPF surface.

The PVA sheet was removed in two ways. Firstly, by dissolving in water and secondly by peeling off the PPF surface. Dissolving in water was carried out most commonly, by either repeatedly squirting with water from a squeeze bottle; holding the sample with tweezers and swirling around in a beaker of water; leaving the surface to soak in water or least commonly, sonicating in water. The PVA sheet was also simply peeled off using tweezers or more conveniently, using PVA sticky tape when the PVA sheet was too thin to handle with tweezers. The sticky tape was stuck onto the PVA sheet and peeled off together with the PVA sheet.

9.2.5. Molecular patterning using metal films

Deposition of metals on carbon surfaces

Metal films, nichrome and gold were deposited onto PPF and glassy carbon (GC) by evaporation under vacuum. Figure 9.4. is an illustration of the vacuum evaporator used. Patterns of the metal films were fabricated by positioning a shadow mask (stencil), over the GC or PPF surface during deposition. The shadow mask and the surface were held in position on the chuck using clips. The chuck was suspended upside down in the

evaporating chamber. With the chuck holder used, typically three shadow mask-surface could be exposed during a single evaporation.

Two different shadow masks were used to give different patterns of metal films. The first gave a three dot pattern and the second gave a two line pattern. For the three dot pattern, the dots were 0.8, 1.4 and 2 mm in diameter. The two lines were each 1 mm wide and 5 mm long with 1.25 mm spacing between the lines (total area 0.1 cm^2). The resulting metal film pattern corresponded to the perforations in the shadow mask.

Equations 9.1. were used to determine the length of wire needed for the desired metal film thickness.[34] 20 – 30% more than the calculated length was used.

9.1. Surface area of the sphere defined by surface-sample distance

$= \frac{4}{3} \pi r^2$, where r = source-sample distance (25 cm)

Volume of layer of metal deposited on surface of sphere (v)

= Surface area of sphere x Thickness of metal layer required = $\frac{4}{3} \pi r^2 \times t$

Length of wire = $v / (\pi d^2 / 4)$

where d = diameter of wire, d_{NiCr} = 0.25 mm, d_{gold} = 0.5 mm.

The length of wire was cut-up into 2 – 3 cm pieces that could fit inside the boat. For the specific quartz crystal in the evaporator, the frequency was increased by 0.4 KHz per 10

nm of metal deposited. Unless stated otherwise, the film thicknesses were 40 nm for nichrome and gold. The metal film thickness was confirmed by the profilometer.

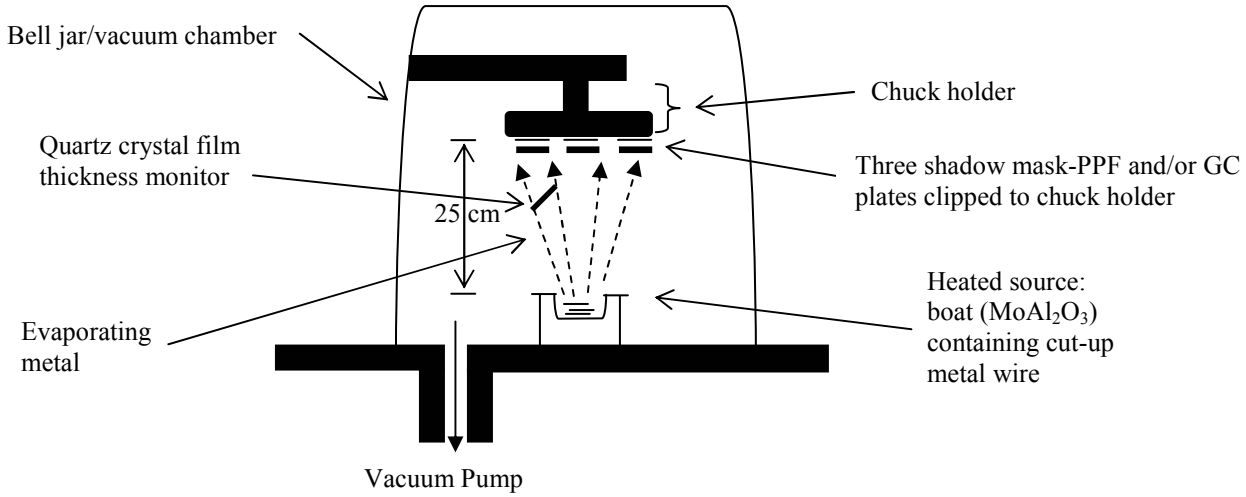

Figure 9.4. Schematic of the vacuum evaporator used for the deposition of metal films onto PPF and GC surfaces.

Removal of metal films from carbon surfaces

The wet etches used for the removal of nichrome and gold thin metal films were adapted from the literature. The wet etch used to remove nichrome was the standard aqueous etch solution of ceric (Ce^{4+}) ammonium sulfate (16.45 g) and concentrated perchloric acid (4.3 mL) in water (100 mL).[29] The carbon surface was immersed into the etch solution until the nichrome had dissolved, as examined by eye. This typically happened after about 40 seconds. The sample was then immersed into MQ water and dried in $N_{2(g)}$ prior to use.

Instead of immersion, nichrome was also removed by pouring the etch solution across the surface five times over a period of 1 minute, after which, the nichrome was not visible by eye.

Gold films deposited on carbon surfaces were etched by immersing into aqueous solutions of either KCN/$K_3Fe(CN)_6$ (200 mM/2 mM),[35] I_2/KI (99 mM/602 mM)[29] or KCN/KOH (1 M/2 M)[35,36]. The surfaces were left in each etch until the film was gone by examination with the eye. This took varying times depending on the etch, the total area and the thickness of gold film pattern deposited. The sample was then rinsed with MQ water and dried in $N_{2(g)}$ prior to use.

9.2.6. Visualisation methods for molecular patterns

Contact mode AFM

Contact mode AFM was performed with a Veeco NanoProbe™ DNP-S20 cantilever with four triangular Si_3N_4 oxidation sharpened tips. The bottom of the cantilever was coated with 15 nm of Cr and the top had 60 nm of Au. DNP-S20 specifications are listed in Table 9.1.

For some experiment, tips were coated with 3-aminopropyltriethoxy silane (APTES) (Aldrich, 99%). The DNP-S20 cantilevers were initially rinsed by immersing in acetone, methanol and isopropyl alcohol (IPA) and dried with $N_{2(g)}$ and then were fully immersed into a neat solution of APTES for 30 minutes in thoroughly cleaned glassware, in air and at room temperature. The silanised tips were then washed by immersing in IPA and then dried with $N_{2(g)}$.

Table 9.1. Specifications of the contact mode AFM cantilever and tip used.

Specifications	**DNP-S20** 			
	A	**B**	**C**	**D**
Force constant, k	0.58 N/m	0.12 N/m	0.32 N/m	0.06 N/m
Cantilever length	100 – 115 μm	180 – 196 μm	100 – 115 μm	180 – 196 μm
Cantilever width	20 – 30 μm	33 – 49 μm	13 – 21 μm	18 – 28 μm
Cantilever thickness	0.4 – 0.7 μm	0.4 – 0.7 μm	0.4 – 0.7 μm	0.4 – 0.7 μm
Resonance frequency	40 – 75 kHz	14 – 26 kHz	40 – 75 kHz	12 – 24 kHz
Tip curvature radius	Normally 10 nm, maximally 40 nm			
Tip Height	2.5 – 3.5 μm			
Full tip cone angle	35°			

For contact mode AFM, the settings on the AFM were as follows: ramp size: 1 μm, scan rate: 1 Hz, samples per line: 512, spring constant: 0.3 N/m, deflection set point: 0 V, deflection limit: 20 V, integral gain: 3 and proportional gain: 3. Friction scans (with an 1:1 aspect ratio) were obtained over boundaries of the molecular pattern with a scan area of 10, 15 or 20 μm and of modifiers with scan area of 500 nm and 10 μm. Topography used a scan area of 15 μm. The Z range (in V) for friction and nm for height was adjusted to improve contrast. For adhesion force curves, the data scale was set at 1 μm and Z-start position was adjusted to find the curve.

The collection of adhesion force curves was performed by recording ten adhesion force curves at four different locations in both the first modifier and second modifier regions, using both the untreated and silane-treated tips, i.e. 160 curves were collected in total. For each of the four different tip-modifier combinations – untreated tip, first modifier; untreated tip, second modifier; silanised tip, first modifier and silanised tip, second

modifier; processing of the force curve files required firstly exporting each file in an ASCII format so that it could be opened as an Excel file. The Excel file had the extending and retracting parts of the curve separated out so that they were side by side rather than overlaid and the deflection unit was converted from nm to V. From the Excel file, the data had to be cut and pasted into another Excel file and saved as a Text file. This was repeated for each case so that there were four Text files each with forty sets of deflection values. A Matlab program (Appendix 9a.), adapted from a program written by Dr. Alexis Pietak from the Department of Mechanical Engineering, University of Canterbury, was used to: read the Text file; extract desired values; convert the deflection back to nm by multiplying with the X sensitivity value; replot the curves to obtain the minimum point of the curves (maximum change in deflection); multiply that value by the force constant of the tip and finally zero the background to get the adhesion force. The average and the standard deviation of the forty adhesion forces were then calculated. The X sensitivity (nm/V) was estimated by manually measuring the lowest point on the printed raw force curve and plot of same curve in Excel and calculating the conversion factor going from nm to V. Four curves, one out of ten from each of four locations, were used to estimate the X sensitivity in each case.

Steam

Samples were held vertically with a small clamp attached a retort stand. Steam was generated by boiling water containing boiling chips and heated on a hotplate. When the sample was moved into the line of the steam, a pattern was observed due to the condensation of water. The pattern was captured by a video camera. Video recordings

rather than still image capture were used as there was a delay between pushing the capture button on the camera and the capturing of the image. The video camera was set up by Michael Pearce from the Department of Chemistry, University of Canterbury. Still photographs were extracted from the video recordings using Windows Movie Maker.

NP assemblies

Citrate-capped gold and aldehyde/sulfate-functionalised PS NPs were assembled in the same way as detailed in Chapter 7. The citrate-capped gold NPs were quantified in the same manner as detailed in Chapter 7 and raw counts are listed in Appendix 9a.

9.3. Results and discussion

9a.1. Patterning using PDMS

Results and discussion of the preliminary experiments carried out with the blocking material PDMS were detailed in Chapter 8. These experiments established its feasibility and conditions for molecular patterning using the three approaches in Figure 9.1.

9a.1.1. Approach (i): "Fill-in" approach using perforated PDMS

The first patterning method to be investigated was approach (i) shown in Figure 9.1. Fabrication of micron-scale perforations in PDMS was very challenging and time consuming and hence initial experiments were carried out with millimetre sized perforations. However, from another perspective, if molecular patterns of millimetre size

are intended, they could be easily prepared with PDMS with circular perforations using "fill-in" patterning.

With this approach, the perforation defined the area for the first modification. The subsequent step was to remove the PDMS from the PPF surface and to electrochemically attach the second modifier with an o-ring of a larger diameter than the first modified area. It was possible to estimate the expected currents for the first modification scan from the diameter of the perforation (Chapter 8) and by carrying out the first modification scan at a GC rod prior to the PPF surface. The observed currents usually corresponded with those recorded at the GC rod; in other cases the sample was prepared again. Table 9a.1. summaries the samples that were successfully prepared with the "fill-in" approach where perforations in PDMS were made by cutters. Two other samples were also prepared where only the first modifier tetraethylene glycol diamine (TGD) was attached in perforations in PDMS. TGD was attached to both surfaces using 5 mM solutions and the electrolysis time was 2 and 10 minutes for the different samples. When the electrolysis time was 2 minutes, a TGD layer thickness of 3.0 ± 0.3 nm was measured using AFM depth profiling and it was 3.4 ± 0.3 nm when the electrolysis time was 10 minutes. These thicknesses are similar to those observed for samples modified with the normal set-up without PDMS, detailed in Chapter 4.

Table 9a.1. The two samples prepared with the "fill-in" approach where the perforation in PDMS were made by cutters.

Sample no.	Perforation size in PDMS or area for 1st modification	1st/2nd modifier
1	Diameter = 4.0 mm, Area = 0.13 cm^2 (made from leather hole punch)	HA/TDA
2	Diameter = 1.4 mm, Area = 0.015 cm^2 (made from silver steel rod)	TGD/*p*-NA

Sample 1

The first modifier used was HA (*n*-hexylamine, 10 mM, electrolysis time 10 minutes) and TDA (*n*-tridecylamine, 5 mM, 2 scans to final/applied potential (E_f)) was the second molecule attached. The thickness of the HA layer was measured to be 2.9 ± 0.3 nm by AFM depth profiling experiments performed after TDA was attached. This thickness is similar to the thickness observed for a sample prepared with the standard set-up without PDMS (Chapter 4). The successful preparation of sample 1 shows that HA/TDA is a suitable combination of molecules and that it is possible to perform electrochemistry in PDMS perforations which give layers that are similar to those prepared using the normal cell set-up.

Sample 2

Electrochemical attachment involved scanning 20 times in TGD (5 mM). After 20 scans, the ferrocene (Fc) probe scan was completely flat. The second modifier was *para* nitro aniline (*p*-NA, 5 mM) attached with 1 scan. The (anodic/oxidation peak current (i_{pa}) after *p*-NA modification)/(i_{pa} before *p*-NA modification) for Fc scans was 0.9. Sample 2 was prepared twice.

From experiments carried out to test the effect of the second modification described in Chapter 8, subjecting a TGD layer to a single scan in *p*-NA modifier solution affected the TGD layer. Thus, to test whether *p*-NA attached to the TGD layer during the second modification, AFM depth profiling experiments were carried out in the TGD layer prior to the second modification and then the same scratch was scanned after modification in *p*-NA. Figure 9a.1. shows the thicknesses measured by AFM depth profiling of the various areas.

Scanning the same scratches that were made before attaching *p*-NA gives a small decrease in apparent thickness. For sample 4a, the topography in the scratches was significantly rougher after the second modification indicating that *p*-NA attached in the 1.25 μm x 10 μm scratch and contributes to the decrease in measured thickness. A new scratch in the TGD layer shows no change in thickness within error. From the thickness of the *p*-NA layer, it is estimated that a monolayer is present. This estimation is considering the calculated length of the *p*-NA modifier is 0.7 nm (Chapter 4) and the modifiers were attached perpendicular to the surface.

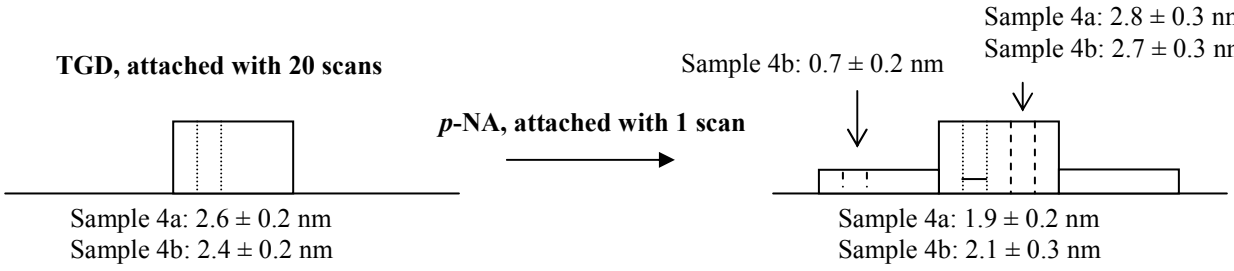

Figure 9a.1. Thicknesses measured by AFM depth profiling of the various layers. The left schematic is of TGD attached in perforation in PDMS and the right is after the PDMS was removed and *p*-NA was attached in the surrounding area. The new dotted lines in the right schematic represents new scratches made in the layers.

Samples 4a and 4b were put into citrate-capped gold NP solutions for 3 hours. TGD is a diamine and *p*-NA a monoamine, thus it was expected that more NPs would assemble on the TGD layer compared to the *p*-NA layer. The circular pattern was visualised under the optical microscope and SEM, giving images shown in Figure 9a.2. The assembly on the TGD and *p*-NA layers appeared gold and green, respectively, to the eye. From the images in Figure 9a.2, the diameter of the circle is 1.4 mm. The density of the NPs is 26 ± 2 / 10^4 nm^2 on TGD layer and 11 ± 2 / 10^4 nm^2 on *p*-NA layer.

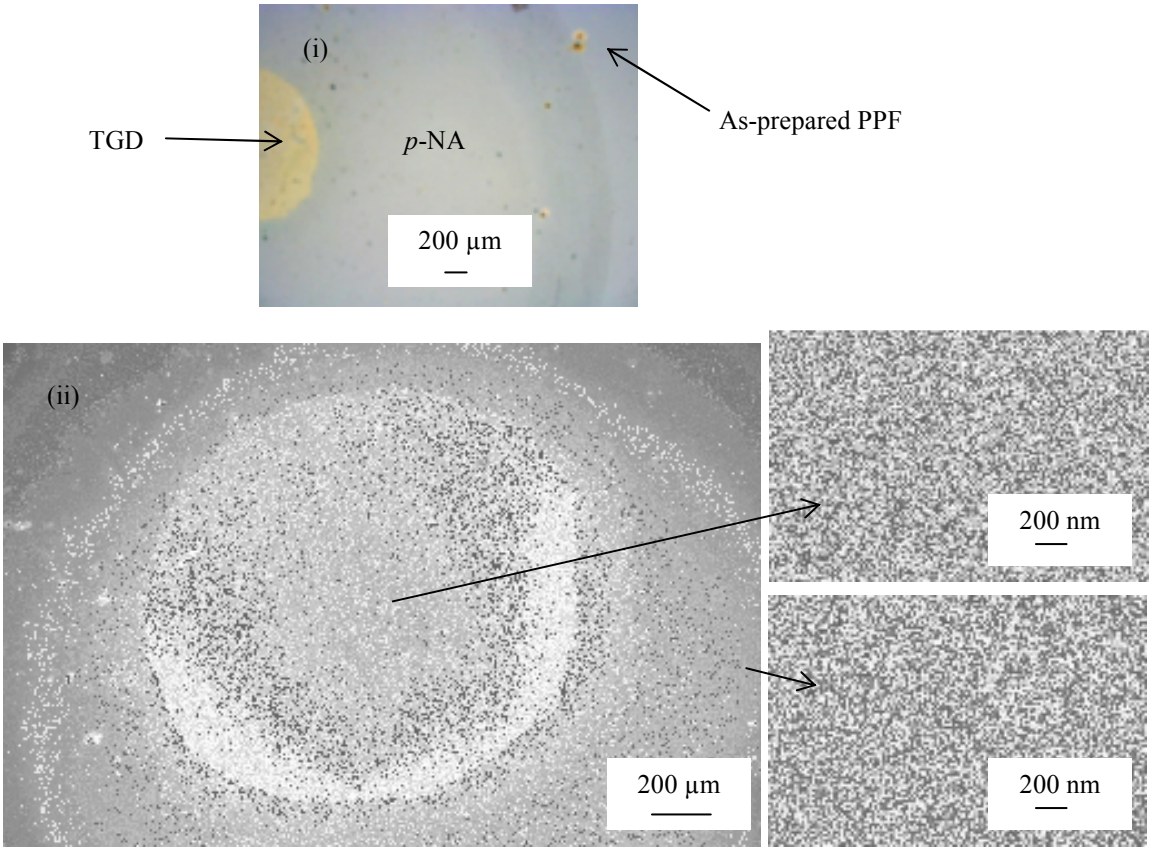

Figure 9a.2. Images of citrate-capped gold NP assemblies on TGD/*p*-NA patterns constructed using perforated PDMS where perforations were made by cutters. (i) optical microscope images and (ii) are images from SEM.

9a.1.2. Approach (iii): "Fill-in" approach using PDMS microchannels

PDMS microchannels allowed for smaller, more precise and complex molecular patterns than those obtained using perforated PDMS.

Electrochemistry in PDMS microchannels

To investigate the resistance contribution that may be present when electrochemical measurements were carried out in the PDMS microchannels, Fc probe scans were recorded at different scan rates in a *Y-shaped* microchannel. At scan rate of 20 mVs^{-1}, peak separation between oxidation and reduction peaks for a reversible process (ΔE_p) was 100 mV and this increased to 240 mV when the scan rate was 500 mVs^{-1}. This indicates that there is significant resistance. To ensure that a reasonable surface concentration of modifier was attached in the microchannels, an increased concentration of modifier of 20 mM, compared to the standard of 5 mM, was used. Scan rate for the initial and final scans was also decreased from the standard 100 mVs^{-1} to 50 mVs^{-1}.

Samples with molecular patterns

Table 9a.2. lists the samples and the modifiers attached. The modifier combination, TGD and *para* methyl phenyl (MP), was chosen to facilitate visualisation of the pattern. Results described in Chapter 8 where the effect of second modification on already attached modifiers was investigated, suggested that MP affected the existing TGD layer. AFM depth profiling experiments were carried out with the *plus 200* sample to investigate this (refer later). For the *parallel lines* pattern, in order to test that the second attachment was

successful, samples were prepared where the order of modifiers attached was reversed so the inverse pattern would be observed. Apart from the samples in Table 9a.2, initial experiments were carried out using the *Y-shaped* and *letters* channels where TGD was attached in the channels.

Table 9a.2. Samples with molecular patterns prepared with the "fill-in" approach using PDMS microchannels.

Pattern	**1st modifier** (scan rate = 50 mVs^{-1})	**2nd modifier** (scan rate = 100 mVs^{-1})
Plus 200	TGD (5 mM, electrolysis time 10 minutes)	MP (5 mM, 1 scan)
Parallel lines	TGD (20 mM, electrolysis time 10 minutes)	MP (5 mM, 1 scan)
	MP (20 mM, electrolysis time 10 minutes)	TGD (5 mM, 1 scan)

Plus 200

PDMS used here is shown in Table 8.3. and Table 8.4. Successive attachment of TGD followed by MP was analysed using AFM depth profiling. Measurements, detailed in Figure 9a.3, show that MP attached to as-prepared PPF around the pattern and did not attach to the TGD layer. The thickness for the TGD layer is consistent with layers prepared with the standard set-up, outlined in Chapter 4.

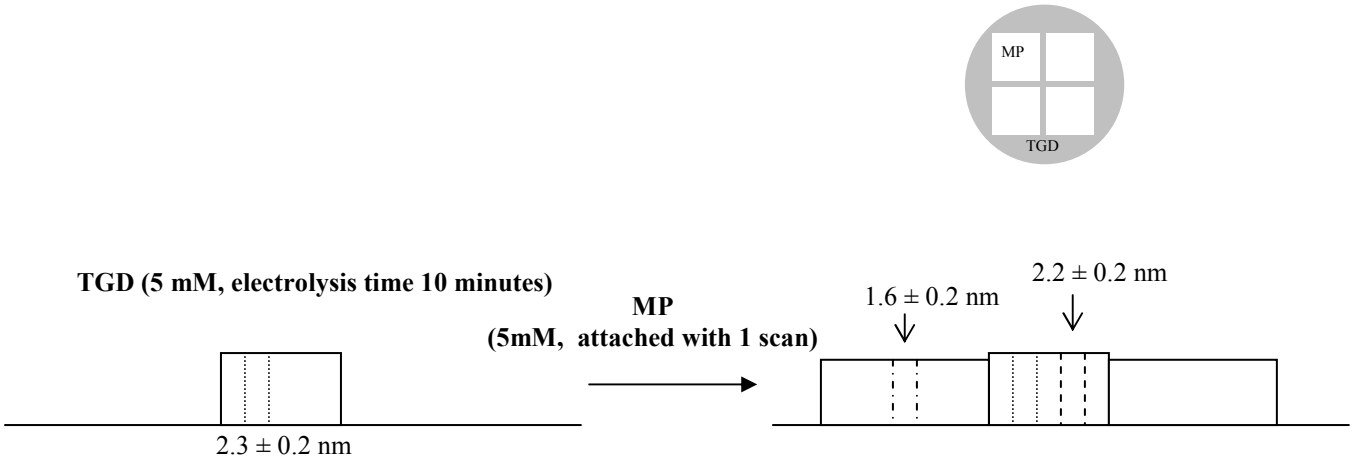

Figure 9a.3. Thicknesses measured by AFM depth profiling of the various layers. The left schematic is of TGD attached in the *plus 200* pattern and the right is after the PDMS was removed and MP was attached in the surrounding area. The new dotted lines in the right schematic represents new scratches made in the layers.

This sample was also analysed by contact mode AFM. Overall, the quality of the AFM images was poor. As anticipated from the water contact angle measurements in Chapter 4 and 5, the adhesion forces, measured using both untreated and APTES treated AFM tips, were higher for TGD compared to MP. However, due to the tediousness of the collection and processing of the data, adhesion forces were not extensively used.

Parallel lines

Patterning experiments using the *parallel lines* microchannels were carried out after refining all the different aspects of the procedure. Two patterns were created by reversing the order of modifiers – TGD/MP and MP/TGD, where the first listed modifier was

attached in the microchannels (the lines) and the second in the surrounding areas around the lines. Three samples of each pattern were prepared using the same procedures.

TGD/MP pattern: The cyclic voltammetry (CV) scans recorded for the attachment of TGD followed by MP are given in Figure 9a.4. The current observed in the initial TGD scan (Figure 9a.4.(i).) was from TGD modification in the microchannels and also the area of PPF not covered by the PDMS. Figure 9a.4.(ii). is the final TGD CV scan after the 10 minute electrolysis and Figure 9a.4.(iii). is the *para* methyl benzene diazonium tetrafluoroborate (*p*-MB) modification scan after the PDMS was removed.

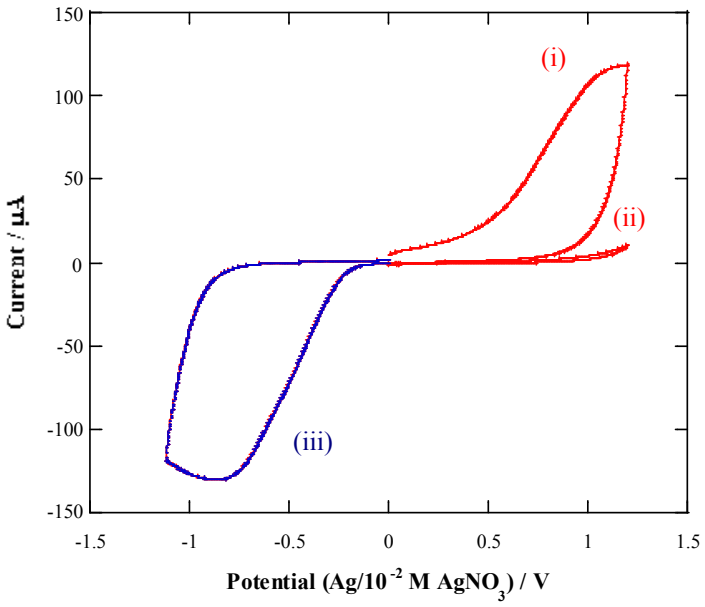

Figure 9a.4. CV scans recorded for the attachment of TGD/MP in the *parallel lines* pattern. (i) initial TGD scan for TGD attachment in the microchannels and the area not covered by the PDMS, (ii) final TGD scan after maintaining the potential at 1.3 V for 10 minutes and (iii) *p*-MB modification scan after PDMS was removed. Scan rate for (i) and (ii) = 50 mVs^{-1} and for (iii) = 100 mVs^{-1}.

The three samples were visualised by methods summarised in Table 9a.3.

Table 9a.3. Visualisation methods used for the three samples of TGD/MP in the *parallel lines* pattern.

TGD/MP	**Visualisation methods**
Sample 1	AFM scan in tapping mode followed by steam video recording
Sample 2	SEM followed by citrate-capped gold NPs assembled (immersion time: 10 minutes) and visualised by optical microscope and then SEM
Sample 3	Optical microscope followed by citrate-capped gold NPs assembled (immersion time: overnight) and visualised by optical microscope and then SEM

The optical microscope images captured are in Figure 9a.5. With the optical microscope, the nanometre thick layer of modifier changes the reflectivity of the surface. The TGD lines were attached with modification conditions using a longer modification time, increased modifier concentration and slowed scan rate, compared to the surrounding MP layer. This resulted in the TGD layer being a thicker layer with possibly higher modifier surface concentration, compared to the MP layer, which alters the reflectivity of the surface to a greater extent and appears darker on the optical microscope images.

Figure 9a.5. Optical microscope images of TGD attached in the *parallel lines* and MP attached in the surrounding area, of sample 3.

Using the AFM, the pattern was seen in the camera and vision system and the right boundary of one of the lines was scanned in tapping mode. The scan is shown in Figure 9a.6. The contrast in the scan between the boundary of the pattern is due to the difference in roughness of the two layers. The difference in the thickness of the TGD and MP layers is too small to be measured.

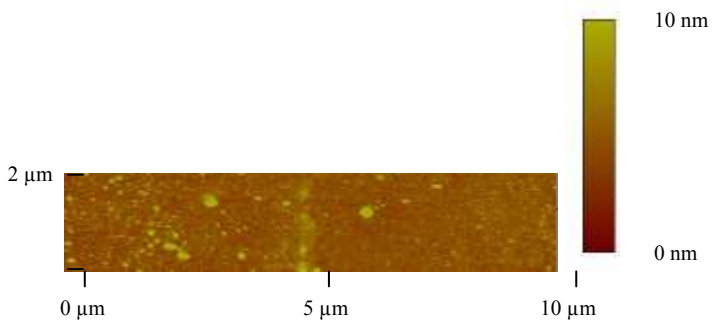

Figure 9a.6. AFM scan in tapping mode of right boundary of the line. The left side of the boundary is the TGD layer attached in the line and the right side is the MP layer, of sample 1.

A still photograph from the steam video recording is shown in Figure 9a.7. When the vertically positioned surface is exposed to steam, water droplets condense onto the cool surface and the differences in wettability of the two modifier layers attached to the surface gives a condensation figure or pattern. The water contact angle is lower for TGD than MP layers (Chapters 4 and 5). The lower angle indicates that the spread of the water drop on the TGD layer is larger than on the MP layer. When the steam condensed onto the TGD/MP patterned surface, the water droplets appear larger on the lines (TGD) than the surrounding area (MP), allowing the pattern to be observed.

Figure 9a.7. Still photograph extracted from steam video recording of TGD attached in the *parallel lines* and MP in the surrounding area, of sample 1.

Under the SEM, the TGD/MP pattern was captured (Figure 9a.8.) with the MP area appearing darker than the TGD lines. This is attributed to the larger amount of scattering of the secondary electrons by the high electron density aromatic rings of MP. The increased scattering causes fewer electrons to reach the detector and thus the MP area is darker. Zooming closer to the surface caused the actual size of the pattern to be distorted and at and above 500 x magnification the detector was saturated and a completely dark image was observed.

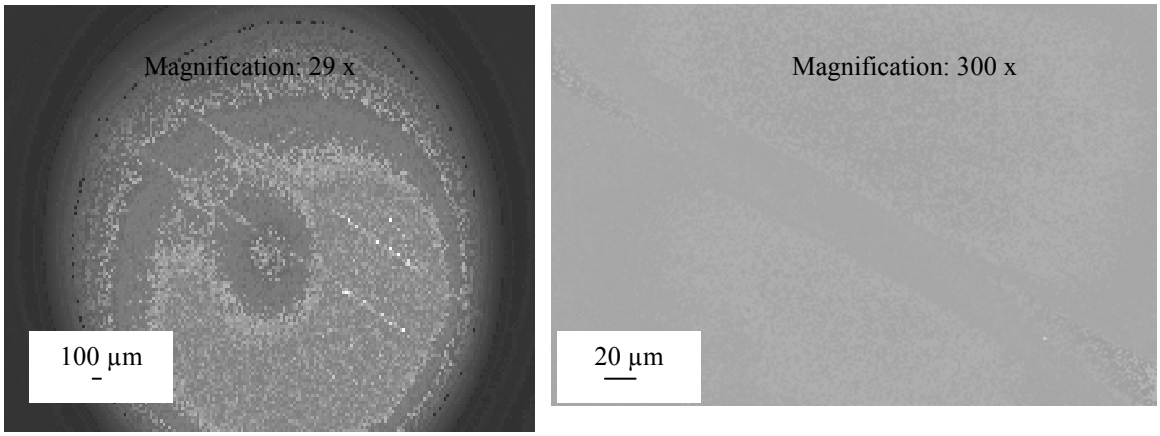

Figure 9a.8. SEM images of TGD attached in the *parallel lines* and MP attached in the surrounding area, of sample 2.

After a 10 minute immersion time in citrate-capped gold NP solution, NPs assembled on TGD and not on MP areas, as expected from results described in Chapter 7. SEM images of the assemblies are shown in Figure 9a.9. The NP count is $3 \pm 2 / 10^4$ nm^2 on the TGD layer and $0 \pm 0 / 10^4$ nm^2 on the MP layer. The line is not wider than 20 μm and the edges are distinct. When an overnight exposure to the NP solution was carried out, the NP count is $20 \pm 3 / 10^4$ nm^2 on TGD and $0 \pm 0 / 10^4$ nm^2 on MP. Lines in the SEM images (Figure 9a.10.) are wider than 20 μm and the edges of the lines are not distinct. This is due to the spill over of the high surface coverage of NPs in the lines ($20 \pm 3 / 10^4$ nm^2) during washing and drying with $N_{2(g)}$ after NP assembly.

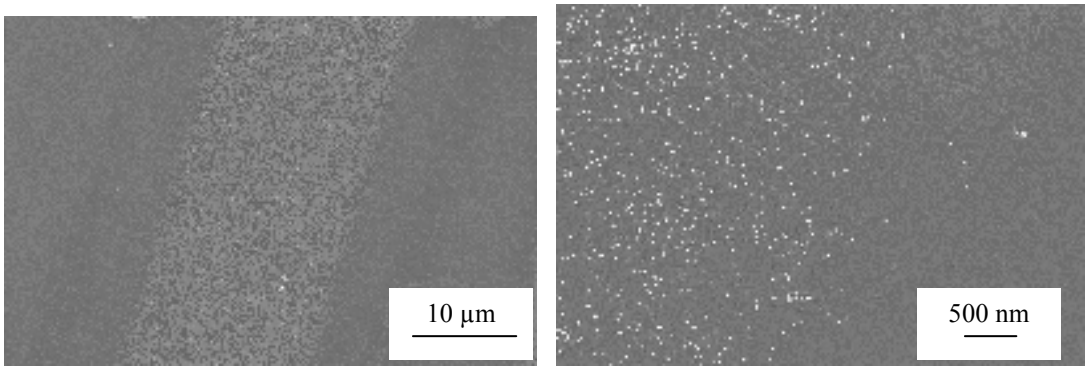

Figure 9a.9. SEM images of citrate-capped gold NP assemblies on TGD attached in the *parallel lines* for sample 2. MP is attached in the surrounding area. An immersion time of 10 minutes was used to assemble NPs.

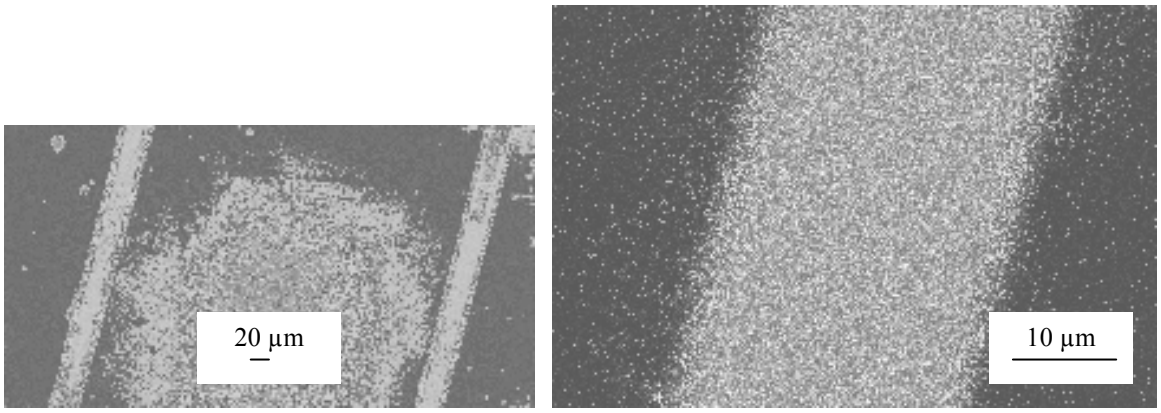

Figure 9a.10. SEM images of citrate-capped gold NP assemblies on TGD attached in the *parallel lines* for sample 3. MP is attached in the surrounding area. An overnight immersion time was used to assemble NPs.

The NP count on the TGD layer after the overnight immersion is lower compared to a TGD layer attached using the standard procedure with a faster scan rate of 100 mVs^{-1}, lower concentration of TGD (5 mM) and an immersion of 3 hours in an identical NP solution (Chapter 7). This is also the case when the immersion time was 10 minutes where the observed NP count is half of that predicted when the standard modification conditions are used. From Chapter 7, it was calculated that the NP count would be 6 NPs / 10^4 nm^2 for an immersion time of 10 minutes.

A possible explanation for the lower NP counts is that the surface concentration of the TGD modifiers in the *parallel lines* was lower than a TGD sample prepared with the standard procedure. This might be expected due to the thin layer of solution in the microchannels, leading to the increased resistance and ohmic (iR, where i is current and R is resistance) drop in the microchannels and hence a lower potential than that applied. Another possibility is that the attachment of MP affected the already attached TGD layer,

causing fewer NPs to assemble. Although the AFM depth profiling experiments from the *plus 200* sample suggested that no MP attached to the surface of the bound TGD layer, it is possible that MP attached to TGD modifiers within the layer and/or to the PPF surface between the TGD modifiers. However, from the experiments that tested the effect of second modification on already attached modifiers (Chapter 8), the TGD layer was less blocking after it was scanned in *p*-MB modifier solution. If the MP attached to TGD modifiers within the layer or to the PPF surface between the TGD modifiers, the resulting layer would have been more blocking to the Fc probe.

MP/TGD pattern: The CV scans for MP attached first in the lines followed by TGD was similar to the TGD/MP samples. As mentioned in Chapter 5, MP layers (5 mM, electrolysis time 10 minutes) are stable after the potential was held at 1.3 V for 10 minutes in ACN/0.1 M $[Bu_4N]BF_4$ (tetrabutyl ammonium fluoroborate). This indicates that the first modifier layer (MP) in the lines would not be affected by potential used for attachment of the second modifier, TGD. The three samples were visualised by methods summarised in Table 9a.4.

Table 9a.4. Visualisation methods used for the three samples of MP/TGD in the *parallel lines* pattern.

MP/**TGD**	**Visualisation methods**
Sample 1	AFM depth profiling followed by optical microscope then citrate-capped gold NPs assembled and visualised by optical microscope and then SEM
Sample 2	AFM depth profiling
Sample 3	AFM depth profiling followed by steam video recording

Optical microscope images are shown in Figure 9a.11. The thicker and possibly denser MP layer in the lines appear darker than the surrounding TGD layer on the optical microscope images due to a higher extent of reflectivity distortion of the surface.

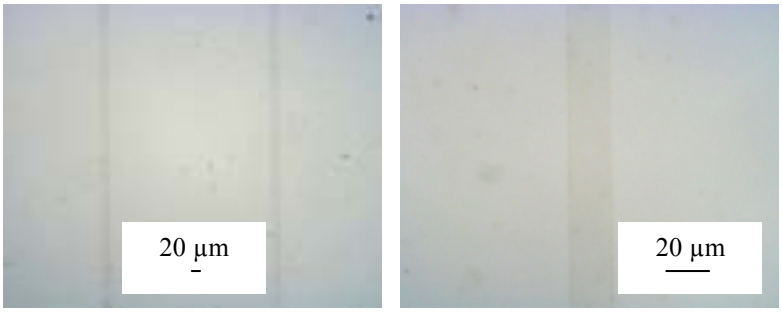

Figure 9a.11. Optical microscope images of MP attached in the *parallel lines* and TGD attached in the surrounding area, of sample 1.

AFM depth profiling results detailed in Figure 9a.12, show that TGD attached to as-prepared PPF around the pattern and did not attach to the surface of the MP layer. The thicknesses are comparable to those for samples prepared under normal modification conditions, as in Chapter 4 and 5.

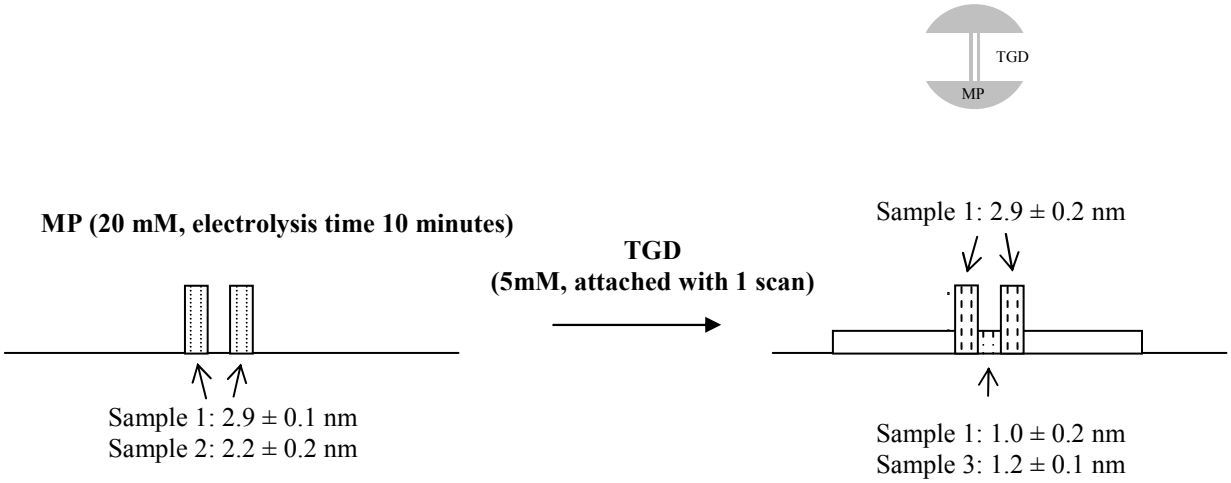

Figure 9a.12. Thicknesses measured by AFM depth profiling of the various layers. The left schematic is of MP attached in the *parallel lines* pattern and the right is after the PDMS was removed and TGD was attached in the surrounding area. The dotted lines in the right schematic represent new scratches made in the layers. AFM depth profiling experiments were carried out for sample 1, 2 and 3.

Still photographs showing a distinctive pattern could not be extracted from the steam video of MP/TGD in the *parallel lines* pattern. With this combination, it was difficult to capture an image of the smaller droplets in the lines with a background of larger droplets. The pattern was visible when the water droplets began to evaporate off the surface after taking the sample out of the steam. Evaporation was faster off the hydrophobic MP layer in the lines compared to the surrounding hydrophilic TGD layer.

After an overnight immersion in citrate-capped gold NP solution, NPs assembled onto the background TGD but not on MP *parallel lines*. Optical microscope images showed poor contrast. SEM images, shown in Figure 9a.13, reveal some spill over of NPs from the TGD layer into the MP lines from washing and drying with $N_{2(g)}$ after NP assembly. The spill over from the NPs in the TGD layer in this sample is significantly less than in the

previous TGD/MP samples presumably because the number of NPs on the TGD layers in this sample (12 ± 3 / 10^4 nm^2) is approximately half that on the TGD layer in the TGD/MP sample. The NPs count on the MP in the *parallel lines* is 1 ± 1 / 10^4 nm^2. The number of NPs on the TGD layer is similar to a TGD layer modified using the standard set-up with identical modification conditions and an immersion of 3 hours in an identical NP solution (Chapter 7). The NP count on the MP lines (1 ± 1 NPs / 10^4 nm^2) is similar to a MP layer attached with the standard procedure with a faster scan rate of 100 mVs^{-1}, lower concentration of *p*-MB (5 mM) and an immersion of 3 hours in an identical NP solution (Chapter 7). This suggests that TGD did not attach within or to the MP layer.

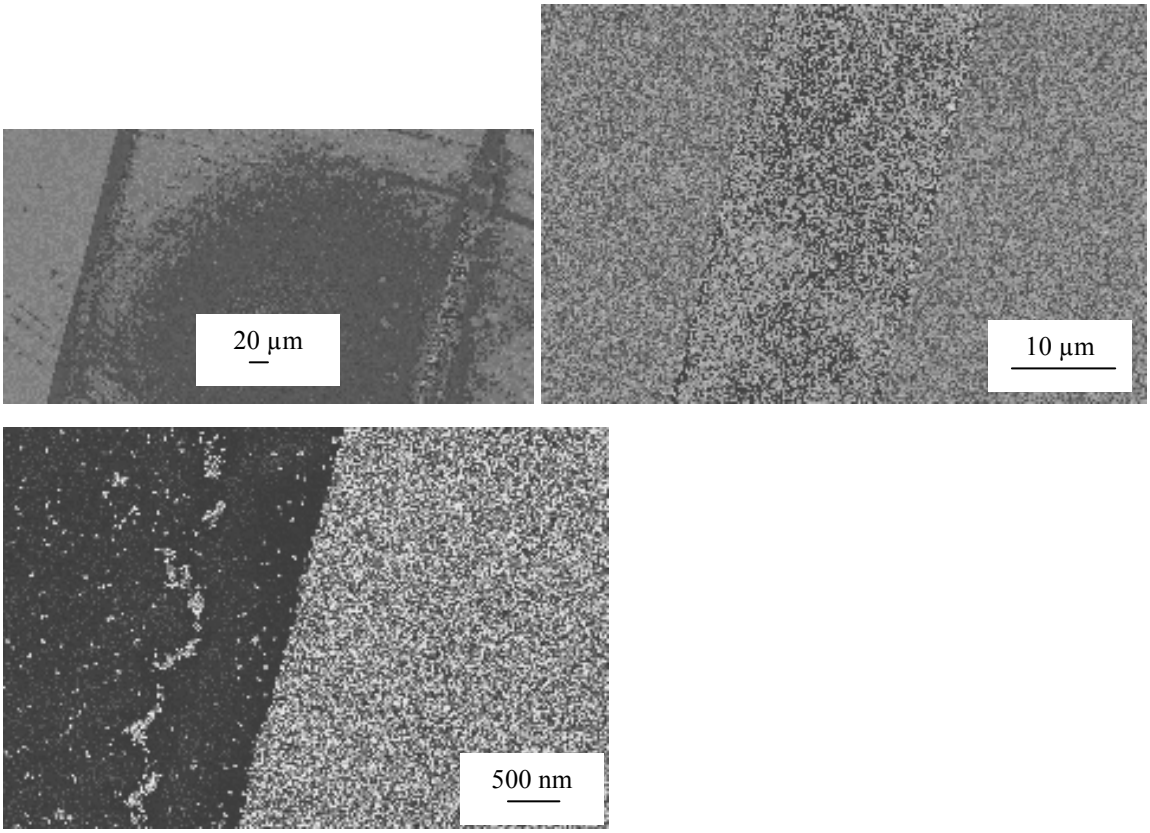

Figure 9a.13. SEM images of citrate-capped gold NP assemblies on TGD attached in the area surrounding the *parallel lines* for sample 1. MP attached in the lines.

9a.1.3. Approach (iv): "Build-up" approach using PDMS microchannels

In this section, patterning using the "build-up" approach as depicted in Figure 9.1.(iv). is discussed. The PDMS microchannels of the *parallel lines* pattern were used in this section and the wider *Y-shaped* microchannel was also used in one experiment. The coupling reaction is amide bond formation between an amine and either a carboxylic acid or acid chloride. The mechanism for amide bond formation via coupling a carboxylic acid to an amine is detailed in the Appendix 0. The coupling agent 1-ethyl-3-(3'-dimethylaminopropyl)carbodiimide hydrochloride (EDCI) and activating agent *N*-hydroxysuccinimide (NHS) were used.

Two main challenges were faced with the "build-up" approach. The first was to ensure that the coupling solution entered the PDMS microchannels when the PDMS was sealed to the PPF surface and the second was to ensure the solution did not degrade the PDMS microchannels over the period of coupling. PDMS degradation was indicated by the PDMS deforming and spontaneously peeling off the PPF, causing the solution to seep under the PDMS. Initial experiments were carried out with various solutions to determine which solutions met the two requirements of filling the microchannels and not degrading the PDMS.

Microchannel filling and PDMS degradation tests

A micro-drop of coupling solution, using a micropipette, was carefully placed at the entrance to the microchannels. The entry of the solution by capillary action was monitored by eye and checked using a light microscope. The factors that determine whether the

PDMS microchannels are filled by capillary action are (i) the surface energy of the PDMS; (ii) the surface energy of the as-prepared or modified PPF and (iii) the polarity of the solvent. The water contact angle of PDMS is > 90° which indicates its hydrophobicity and low surface energy. Hence, the PDMS microchannels are difficult to fill with polar liquids with high surface tensions.[6,37] In these experiments, the three factors were altered by oxygen plasma treatment of the PDMS, modification of the PPF with modifier layers with different wettability or using solvents with different polarity.

The first set of tests utilised as-prepared PPF with PDMS microchannels sealed on. The most logical solvent to use was ACN as it was established in the previous section with the "fill-in" patterning experiments that ACN enters the microchannels and does not degrade the PDMS, even after overnight exposure. However, it proved not to be a suitable solvent for coupling (refer later) and so other solvents were investigated.

Solvents that did not enter the microchannels when sealed to as-prepared PPF were dimethylformamide (DMF), nitromethane and dimethylsulfoxide (DMSO) and solvents that degraded PDMS included tetrahydrofuran (THF) and *N*-methylpyrrolidone (NMP). PDMS microchannels were also treated under oxygen plasma to render the surface hydrophilic. However, after a very short (15 seconds) treatment (1 torr, 400 W), the PDMS would not seal to the PPF surface presumably because it was too hydrophilic.

The second set of tests was the same as the first set but utilised modified PPF surfaces. It was thought that alterations of surface properties after modification may allow entry of coupling solutions into the microchannels, while PDMS would still seal onto the modified PPF surface. The first modifiers used in this approach were TGD and *para*

methylene carboxylic acid (*p*-MCA) and the coupling species were FCA, TGD and nitrobenzoyl chloride (NBC). Four combinations were tried as summarised in Table 9a.5. Solutions included the species that would be used for coupling, i.e. the coupling species, coupling agent, activating agent.

Table 9a.5. Modified samples for which entry of solution into PDMS microchannels was tested.

1st modifier	**Solution**	**PDMS microchannel pattern**	**Enter PDMS microchannel?**
TGD (5 mM, electrolysis time 10 minutes)	FCA/EDCI/NHS/DCM 1 mM/40 mM/8 mM	*Y-shaped*	X
p-MCA (5 mM, electrolysis time 10 minutes, E_f -1 V)	TGD/EDCI/NHS/PB 8 mM/40 mM/8 mM	*Parallel lines*	X
p-MCA (5 mM, electrolysis time 1 minute, E_f -1.12 V)	TGD/EDCI/NHS/DMSO 4 mM/40 mM/8 mM	*Parallel lines*	√
TGD (5 mM, electrolysis time 2 minutes)	NBC/DMSO 0.1 M	*Parallel lines*	√

Dichloromethane (DCM) and phosphate buffer (PB) solutions did not enter the microchannels on the modified PPF surfaces, however, DMSO solutions entered the microchannels when PPF was modified with either *p*-MCA or TGD (but not with as-prepared PPF).

Coupling in PDMS microchannels

To carry out the coupling reaction in the microchannels, the solution was added to the microchannels while the PDMS was sealed to the modified PPF as described earlier and the sample was completely immersed in the coupling solution for a set period. The beaker was sealed with parafilm to reduce evaporation. After coupling, the sample was removed from the beaker and a variety of washing and drying steps were used for the different experiments. Table 9a.6. summarises the coupling experiments.

Table 9a.6. Coupling experiments carried out in *parallel lines* PDMS microchannels.

1st modifier	**Coupling solution**	**Period of coupling**
p-MCA (5 mM, electrolysis time 10 minutes, E_f -1 V)	TGD/EDCI/NHS/ACN 8 mM/40 mM/8 mM	Overnight
p-MCA (5 mM, electrolysis time 1 minute, E_f -1.12 V)	TGD/EDCI/NHS/DMSO 4 mM/40 mM/8 mM or 12 mM/40 mM/16 mM	Overnight
TGD (5mM, electrolysis time 2 minutes)	NBC/DMSO 0.1 M	2 hours
TGD (5mM, electrolysis time 2 minutes)	NBC/DMSO 0.5 M	10 minutes

The first two experiments involved attaching *p*-MCA to the PPF surface followed by attempts to couple to TGD. After a significant number of experiments, it became apparent that *p*-MCA is not a suitable first modifier to be used with PDMS microchannels because PDMS appeared to modify the *p*-MCA layer. The most important experiment that led to this conclusion was carried out by sealing the PDMS microchannels to *p*-MCA layer overnight without any solution. After removing the PDMS, the surface was soaked in citrate-capped gold NPs for 2 hours. A dense layer of NPs assembled on the *p*-MCA. This

was unexpected as results detailed in Chapter 7 showed that NPs do not assemble on a *p*-MCA layer. It is uncertain what caused the NPs to assemble. It is considered that the carboxylic acid groups of *p*-MCA react with uncrosslinked PDMS materials or that UV-induced radicals form in the PDMS and react with the carboxylic acid.[5]

TGD and NBC/DMSO: Instead of having the carboxylic acid, *p*-MCA, at the surface, TGD layers were attached that contained terminal primary amines that were able to couple to the acid chloride, NBC. With an acid chloride, no coupling or activating agent is required and the reaction time for amide bond formation can be significantly shorter than for a carboxylic acid. Having a short period of coupling (2 hours) reduces the possibility of problems arising from the PDMS. To further avoid the possibility that TGD may intereact with PDMS, PDMS was put through a series of extraction steps to remove the uncrosslinked monomers, rinsed with ethanol and dried with $N_{2(g)}$ before use. Extraction steps included swelling the PDMS microchannels in pentane for 2 days, deswelling in toluene for 1 day, ethyl acetate for 1 day and acetone for 1 day, and then drying at 120 °C in an oven for 2 days. These steps were adapted from methods of Whitesides and co-workers.[38] An initial experiment to test whether the extracted PDMS interacts with the TGD layer was to seal a piece of extracted PDMS to half of a TGD layer for 2 hours. The water contact angle and density of NP assembly after a 3 hour immersion was similar in both parts of the TGD layer i.e. area that had contacted the PDMS and the area that had not. Thus, the extracted PDMS appeared not to affect the TGD layer.

Three identical samples were prepared. After the 2 hour coupling, the three samples went through very careful cleaning steps in order to remove the coupling solution from microchannels before peeling off the PDMS. The first step was drying the PPF with PDMS sealed with $N_{2(g)}$, followed by drying under vacuum in a vacuum dessicator until there was no solution left in the microchannels. The sample was then rinsed in clean DMSO and dried with $N_{2(g)}$ and under vacuum again until no solution was left. Samples were analysed under the light microscope to ensure no solution was present after each of the drying steps. Rinsing in clean DMSO and drying was repeated at least twice. It was difficult to completely remove solution from the microchannels and the sample was left under vacuum overnight when required. The PDMS was then removed and the PPF sample was washed in DMSO and then MQ water and dried with $N_{2(g)}$.

Coupling NBC to a TGD-modified surface without PDMS has been previously carried out and analysed as described in Chapters 4 and 7. Coupling NBC to TGD in DMSO was shown to be successful firstly by measuring the water contact angle before (47 ± 2°) and after (56 ± 2°) coupling and secondly by electrochemically reducing the attached *p*-nitrophenyl group in 0.25 M H_2SO_4. Citrate-capped gold NPs assembled on a TGD-nitrobenzoyl (NB) layer (8 ± 2 NPs / 10^4 nm^2) and a TGD layer (9 – 10 NPs / 10^4 nm^2). Additionally, the TGD layer is unaffected when exposed to DMSO for 2 hours without NBC as determined by water contact angle and the number of citrate-capped gold NPs assembled.

The samples were visualised using methods summarised in Table 9a.7.

Table 9a.7. Visualisation methods for TGD coupled to NBC using NBC/DMSO in the *parallel lines* pattern of PDMS microchannels.

TGD/TGD-NB	Visualisation methods
Sample 1	Optical microscope followed by SEM and then steam
Sample 2	Aldehyde/sulfate-functionalised PS NPs assembled and visualised by optical microscope, fluorescence microscope and finally the SEM
Sample 3	Citrate-capped gold NPs assembled and visualised by optical microscope and then SEM

Optical microscope images captured of the TGD/TGD-NB pattern had poor contrast and are not shown. Figure 9a.14. are the SEM images of TGD/TGD-NB in the *parallel lines* pattern. The lines where the NBC coupled to TGD appear darker because of the high electron density of the aryl rings on NBC. This phenomenon has been described earlier. As seen in the images, going to higher magnifications causes the contrast to diminish significantly. A control experiment was carried out without NBC. No lines were present for the control sample when it was visualised with the same brightness and contrast settings on the SEM as for the NBC coupled samples, indicating that NBC had indeed attached to TGD in the coupling reactions.

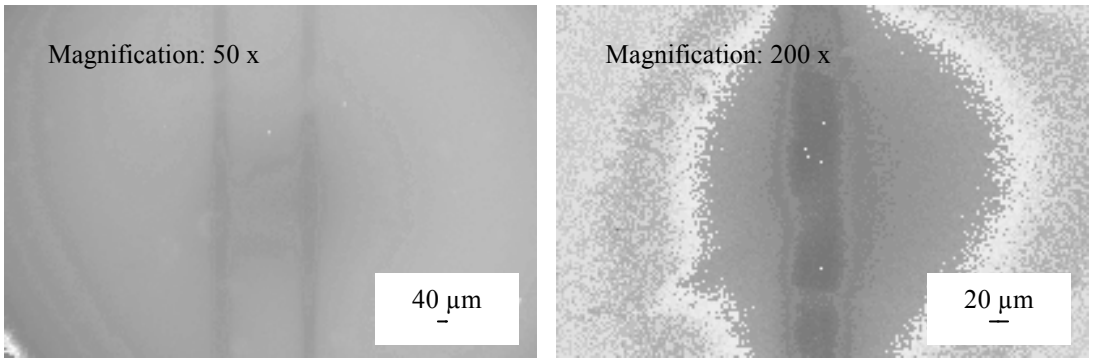

Figure 9a.14. SEM images of NBC coupled to the already attached TGD layer in the *parallel lines* microchannels to give a TGD/TGD-NB pattern, of sample 1.

Figure 9a.15. depict a still photograph from the video recording of steam condensing on the surface. As mentioned above, the water contact angle is smaller for TGD compared to TGD-NB and so the spread of the drop on the TGD layer is greater than for TGD-NB. Thus, for these samples the water droplets are visibly larger on the TGD layer than on the lines (TGD-NB).

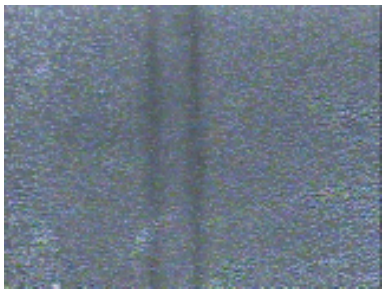

Figure 9a.15. Still photograph extracted from steam video recording of NBC coupled to the already attached TGD layer in the *parallel lines* microchannels to give a TGD/TGD-NB pattern, of sample 1.

Optical microscope and SEM images of aldehyde/sulfate-functionalised PS NPs attached to the TGD/TGD-NB sample after a 3 hour immersion are shown in Figure 9a.16. and Figure 9a.17, respectively. NPs attached on the TGD layer which was consistent with the aldehyde and/or sulfate groups of the PS NPs interacting with the amines of TGD. With the SEM, both the PS NPs (attached to TGD) and the TGD-NB lines are non-conducting. However, the dimensions of the NPs (diameter 29 nm) are significantly larger compared to the thickness of the TGD-NB layer and so has greater scattering ability thus appearing lighter. Under the fluorescence microscope, the lines appeared black and the surrounding area was fluorescent green. Unfortunately, the camera set-up on the fluorescence microscope was not capable of capturing the micron-sized patterns.

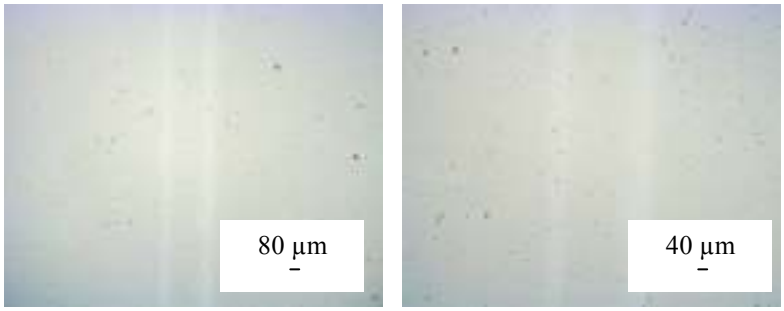

Figure 9a.16. Optical microscope images of aldehyde/sulfate-functionalised PS NP assemblies on the TGD/TGD-NB *parallel lines* pattern, of sample 2. Fewer NPs assembled on TGD-NB in the lines.

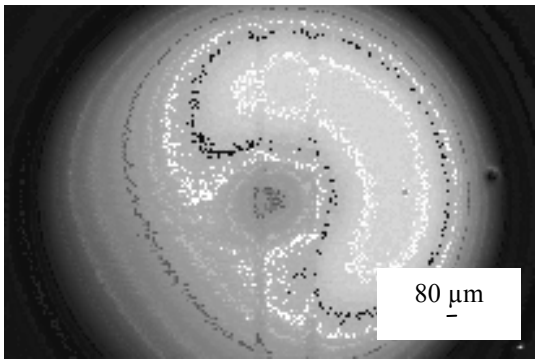

Figure 9a.17. SEM images of aldehyde/sulfate-functionalised PS NP assemblies on the TGD/TGD-NB *parallel lines* pattern, of sample 2. Fewer NPs assembled on TGD-NB in the lines.

Figure 9a.18. and Figure 9a.19. are the optical microscope and SEM images of citrate-capped gold NP assemblies on TGD/TGD-NB after a 3 hour immersion, respectively. The contrast of the NP images was not expected to be significant as NPs would still assemble on the TGD-NB in the lines due to the protonated amines/amides in the underlying TGD layer. The number of NPs on TGD is $9 \pm 3 / 10^4$ nm^2 and on TGD-NB in lines is $1 \pm 1 / 10^4$ nm^2. The NPs count on TGD is similar to the NP count on a TGD layer attached with standard conditions and an electrolysis time of 2 minutes, followed by

soaking in DMSO for 2 hours and immersing in an identical NP solution for 3 hours, as detailed in Chapter 4 and 7. The count on the TGD-NB in the lines is lower than for TGD-NB samples where attachment was carried out without PDMS which is 8 ± 2 NPs / 10^4 nm^2, as mentioned above. This suggested that more NBC attached when coupling was carried out in the PDMS microchannels. The high surface concentration of coupled NB to the TGD layer is able to 'shield' the positive charges from the protonated amines/amides of the TGD layer and also the TGD-NB layer is more hydrophobic compared to the TGD layer. These two properties helped reduce the number of NPs assembled on the TGD-NB lines.

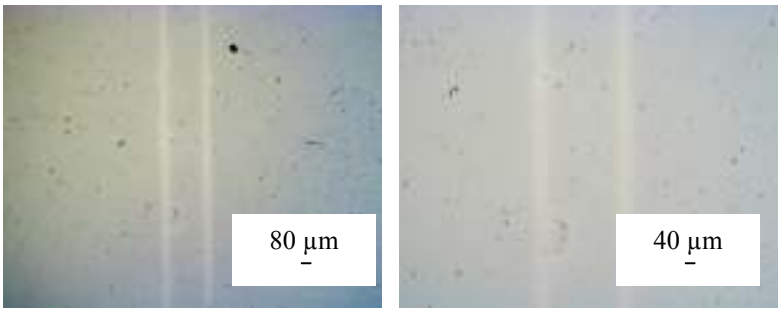

Figure 9a.18. Optical microscope images of citrate-capped gold NP assemblies on the TGD/TGD-NB *parallel lines* pattern, of sample 3. Fewer NPs assembled on TGD-NB in the lines.

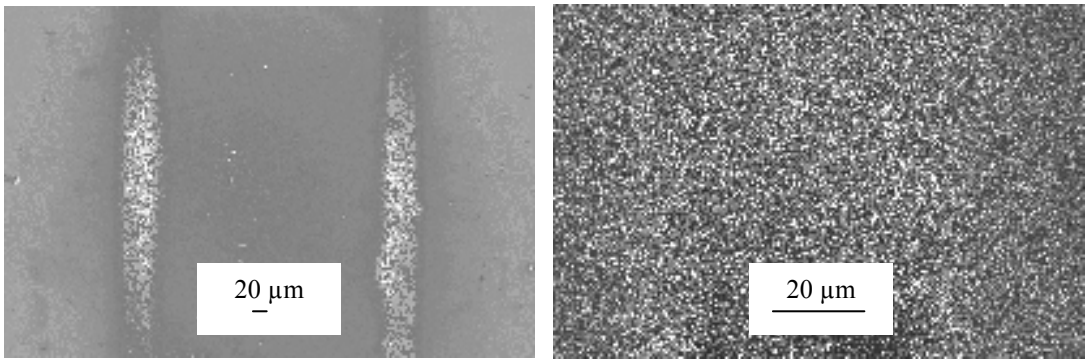

Figure 9a.19. SEM images of citrate-capped gold NP assemblies on the TGD/TGD-NB *parallel lines* pattern, of sample 3. Fewer NPs assembled on TGD-NB in the lines.

From Figure 9a.14. to Figure 9a.19, the TGD-NB lines are approximately twice the width of the PDMS microchannels. This is probably due to leakage of the coupling solution under the PDMS during coupling. The water contact angle on the as-prepared PPF is 72 ± 3°, whereas on a TGD layer (5 mM, electrolysis time 2 minutes) it is 46 ± 3°. Thus, the hydrophobic PDMS may not seal as well to the hydrophilic TGD-modified PPF surface compared to the as-prepared PPF. The seepage experiments performed on as-prepared PPF detailed in the preliminary tests section (Chapter 8) were not capable of detecting seepage on the micron-scale. Other workers have also observed poorer sealing of PDMS to glass modified with an amino-terminated silane as compared to unmodified glass.[20]

Attempts were made to reduce the widths of the lines by using a shorter coupling period of 10 minutes and an increased concentration of 0.5 M NBC (fourth combination in Table 9a.6.). These coupling conditions were tested on a TGD-modified surface (5 mM, electrolysis time 2 minutes) without PDMS and electrochemical reduction of the *p*-nitrophenyl group in 0.25 M H_2SO_4 indicated coupling occurred. Apart from alterations to the coupling conditions, pressure was placed on the PDMS during coupling and different post-coupling cleaning steps were used to avoid leakage. After the coupling period, the sample was immersed into two separate volumes of DMSO and the PDMS was removed while the sample was in the second volume of solvent. However, despite these efforts, the lines were still significantly larger than 20 μm.

The stability of the PDMS microchannels were tested by soaking the PDMS in the coupling solution and observing the widths of the microchannels while in solution, under the optical microscope over 10 minutes. The PDMS appeared to be stable in the coupling

solution even with the increased acid chloride concentration. This supports the previous explanation that it is the poor interaction between the hydrophobic PDMS and the hydrophilic TGD-modified PPF surface that gives rise to wider lines and not PDMS deformation in the coupling solution.

9a.1.4. Approach (v): "Selective conversion" approach using PDMS microchannels

This approach (Figure 9.1.(v).) involved the electrochemical reduction of the already attached *para* nitro benzene (*p*-NB) layer. Only the area of the layer in the PDMS microchannels was reduced. Hence, the resulting pattern was amino functionalities in the lines and *p*-NB in the surrounding area. The reduction of the *p*-nitrophenyl groups of *p*-NB has been carried out in H_2SO_4, ethanol/water and benzoic acid/ACN (Chapter 5). In Chapter 5, the electrochemical reduction of *p*-nitrophenyl functionalities of *p*-NB in 0.02 M benzoic acid/ACN/0.1 M $[Bu_4N]BF_4$ was shown to be successful by the CV scans with peaks assigned to reduction and also the decrease of the water contact angle at the reduced surface. Citrate-capped gold NPs assembled on the reduced surfaces and not on the *p*-NB surface, which is another indication that conversion of the *p*-nitrophenyl to amines had occurred (Chapter 7).

0.02 M benzoic acid/ACN/0.1 M $[Bu_4N]BF_4$ was the selected solution used for the reduction in this section of work as it entered the *parallel lines* microchannels. A series of experiments were carried out, as detailed in Table 9a.8, to determine suitable conditions for this patterning method. For all reduction scans for the *p*-NB layer in the PDMS microchannels, a scan rate of 50 mVs^{-1} was used. The scan rate was slower compared to

that which was used in Chapter 5 (200 mVs^{-1}) for the reduction of a bulk surface i.e. without the microchannels. This adjustment was to counter the effects of resistance associated with carrying out electrochemistry in microchannels. The potential range used at the bulk surface was 0.6 to -1.8 V. PDMS either underwent the extraction process to remove uncrosslinked monomers (same procedure as for PDMS used in the "build-up" approach using TGD and NBC/DMSO) or used as-prepared with the standard washing with ethanol and drying with $N_{2(g)}$. Both types of PDMS appeared to behave similarly in the "selective reduction" experiments.

From Table 9a.8, when the size of the PDMS was smaller than the *p*-NB modified area and the number of reduction scan was ≥ 5 (samples 1 and 2), the PDMS lifted off the surface during the reduction process. When the size of the PDMS was large enough to seal onto the unmodified PPF and the time-scale of the experiment was shorter, PDMS remained sealed to the surface (samples 3 and 4).

Table 9a.8. "Selective conversion" experiments carried out in *parallel lines* PDMS microchannels.

Sample no.	PDMS microchannels	Size of PDMS compared to *p*-NB modified area	Number of reduction scans	Potential range / V [a]
1	Extracted	Smaller than modified area	10	0.6 to -1.8
2	Extracted	Smaller than modified area	5	0.6 to -1.8
3	Unextracted	Larger than modified area	2	0.7 to -1.9
4	Extracted	Larger than modified area	1	0.4 to -1.6

[a] Reference electrode was a Ag wire.

The patterned surface of *p*-NB/amino functionalities were analysed by exposure to steam, the SEM and the assembly of citrate-capped gold NPs. Figure 9a.20. and Figure 9a.21. show the steam image and SEM images, respectively, for sample 4. Similar images were obtained for sample 3. When the steam condensed onto the *p*-NB/amino functionalities patterned surface, the water droplets in the lines are larger compared to those in the surrounding area, which is consistent with the smaller water contact angle on the reduced surfaces (46 ± 4°) compared to the *p*-NB layer (64 ± 4°) as detailed in Chapter 5.

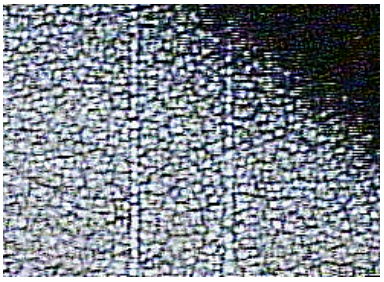

Figure 9a.20. Still photograph extracted from steam video recording of the already attached *p*-NB layer reduced to amino functionalities in the *parallel lines* microchannels to give a *p*-NB/amino groups pattern, of sample 4.

From the SEM images, it is possible to visualise the two separate areas, which only differs by one functional group. From the images, the lines are brighter than the surrounding areas. The lines contain amino groups which scattered the electrons from the SEM to a lesser degree compared to the *p*-nitrophenyl groups in the surrounding area. This was expected due to the lower electron density of the amino groups compared to the *p*-nitrophenyl functionality. These images indicate that the reduction of *p*-NB in the microchannels was successful using the minimum electrochemical conditions of 1 scan and a decreased potential range.

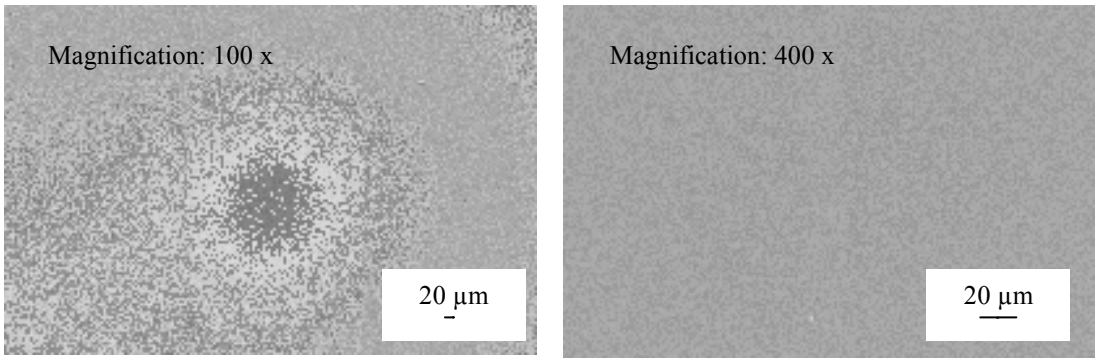

Figure 9a.21. SEM images of the already attached *p*-NB layer reduced to amino functionalities in the *parallel lines* microchannels to give a *p*-NB/amino groups pattern, of sample 4.

After an overnight immersion in a citrate-capped gold NP solution, both samples 3 and 4 were analysed under the SEM. The number of NPs that assembled in the lines (amino groups) was similar compared to the surrounding area (*p*-NB). An explanation for this is that the surface concentration of the amino groups is too low to cause an increased number of NPs to assemble in the *parallel lines*. The low conversion is presumably because of the significant resistance and ohmic drop associated with the thin layer of solution in the microchannels, hence, limiting the surface concentration of amino functionalities.

9b.1. Patterning using PVA

PVA was chosen as the blocking material to be used in the "fill-in" approaches (i) and (ii) to molecular patterning (Figure 9.1.) because it is water soluble and could be made water insoluble when crosslinked via photooxidation. These properties were exploited when perforations were made in PVA for approach (i) and for the removal of PVA in both approaches.

Within approach (i) – "fill-in" approach where the blocking material has perforations, two strategies were envisaged. The first was to dissolve, using water, selected micron-sized areas of a PVA sheet spin coated to the PPF surface. The first modification was to be carried out at PPF in the perforation through the PVA sheet. The next step was to remove the PVA sheet by dissolving in water or simply by peeling off, after which the second modifier was to be attached. The second strategy was to use PVA in a similar procedure to a photoresist. PVA and the chromate crosslinking agents were to be spin coated onto PPF surfaces and UV was irradiated through a mask so that the exposed areas were photooxidised and rendered water insoluble. The masked areas were then to be developed and removed in water and the first modifier was attached in these perforations. The second modification was intended to be performed around the first modifier after the crosslinked PVA sheet was peeled off. The strategy to carrying out approach (ii) – "fill-in" approach where the blocking materials are islands using PVA was to apply 'dots' of PVA onto PPF and to attach the first modifier around the 'dots'. The PVA 'dots' where then to be dissolved and the second modifier attached where the 'dots' had been.

However, after a large number of experiments were carried out, some shortcomings of PVA were realised that prevented its use as a satisfactory blocking material. The key experiments and results are detailed briefly in this part of Chapter 9.

9b.1.1. Preliminary tests

Several tests were performed to establish the suitability of PVA as the blocking material in "fill-in" patterning. The PVA sheet was not soluble in ACN, acetone or ethanol.

Therefore, acetone, ethanol and ACN were used as washing solvents and ACN was also used for electrochemistry. The dye in the commercially available, green PVA solution was not electroactive between 1.5 and -1.5 V. To investigate whether seepage occurred under the PVA sheet, a perforation in a PVA sheet spin coated onto PPF was made by leaving a drop of water to evaporate. A Fc probe scan was recorded at PPF in a perforation through the PVA sheet and left in the cell set-up overnight. A similar scan was recorded the next day and was identical to the previous scan indicating seepage did not occur under the PVA sheet.

Experiments were carried out to examine whether the PVA left residues after it was spin coated onto PPF and then dissolved or peeled off. After removing the PVA sheet, the PPF was examined by eye, by CV using a redox probe, the AFM and/or by assembling citrate-capped gold NPs. For both ways of removing PVA, no residues were detected by eye or CV, however, after immersing in citrate-capped gold NP solution for 1 – 3 hours, NPs assembled. Also, AFM depth profiling experiments and scans showed 1 – 3 nm of residues was present. Washing more vigorously with water at 50 ° C also failed to remove the residues as indicated by NP assembly. The NP assemblies for all the residue tests formed a gold film on PPF which can be seen by eye. The surface-immobilised NPs are also electroactive and a CV scan in 0.1 M $NaClO_4$ gave the typical response for gold surfaces.[39]

Instead of spin coating PVA onto PPF, PVA ‘dots’ (diameter < 2 mm) were left to dry in air for 30 minutes and then in a 60 °C oven for an hour. The ‘dots’ were then removed by squirting with water with the PPF tilted so that the PVA and water ran off only

part of the surface. After a 3 hour immersion in NPs, NPs only assembled on that part of the PPF surface that had contacted PVA i.e. where the dots had been and where PVA and water ran off during washing, indicating residues remained.

Unfortunately, because PVA was unable to be completely removed from the PPF surface and left residues, PVA is an unsuitable blocking material in both strategies within patterning approach (i) and the strategy for approach (ii) (Figure 9.1.).

9c.1. Patterning using metal films

Thin metal films were used as the blocking material in the molecular patterning approach (ii), which is the "fill-in" approach where the blocking materials are islands (Figure 9.1.). The strategy was that a pattern of metal films were to be deposited by evaporation onto the carbon surface and the first modifier was to attach around it. Following that the metals were removed by wet etching (in solution) or by electrochemical oxidation, and the second modifier was to be attached where the metal film had been. Nichrome and gold films were selected because the techniques for their deposition and removal are well-known.

After a large amount of experimentation was carried out, these metal films were deemed as unsuitable blocking materials for "fill-in" patterning. This part of the chapter describes the results of key experiments which led to this conclusion.

9c.1.1. Preliminary tests

The first test was to investigate whether the metal films could be completely removed without affecting the carbon surface. Nichrome films were either removed using a wet etch or by electrochemical oxidative stripping in acid. These films were deposited on a PPF surface in a pattern of three varying size dots. An optical image of the dots is shown in Figure 9c.1.

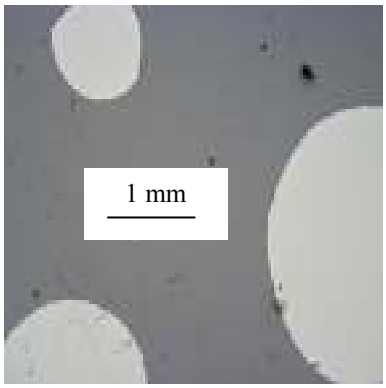

Figure 9c.1. Optical microscope image of nichrome film deposited onto a PPF surface in a three dot pattern using a shadow mask.

After the nichrome was removed by immersing in the wet etch, elemental analysis using the SEM showed no trace of nickel or chromium. However, outlines of the dots were visible by eye. This indicated that during the deposition or removal of nichrome, the PPF surface was affected. To investigate this further, an as-prepared PPF surface was treated with the etch solution (metal films was not present) and a $Ru(NH_3)_6^{3+}$ probe scan was recorded. The probe scan was identical when compared to the scan at the surface before

etching. This suggests that only the areas of the PPF surface that had been in contact with nichrome were altered during the deposition or etching of the metal.

Since the commonly used method of wet etching to remove nichrome film pattern was unsuitable, electrochemical methods were examined. CV scans of a nichrome film in the dot pattern were performed in 0.1 M HNO_3. The first scan showed two peaks, one at 0.9 V and the other at 1.4 V. Considering the standard reduction potentials of these two metals, the peak at 0.9 V was assigned to the oxidation of chromium and the second one to nickel. In the second scan, the peaks were not present indicating that the metals had been oxidised. Electrochemical oxidative stripping of the metal deposited in a two line pattern was then carried out by maintaining the potential at 1.4 V for 5 minutes in 0.1 M HNO_3. After the electrochemical process, the resulting PPF had defects where the nichrome film pattern had been, suggesting that the oxidation of the nichrome damages the PPF surface.

In summary, nichrome is an unsuitable blocking material as it was not possible to remove the nichrome film without affecting the PPF that had been in contact with the metal. The deposition or removal of nichrome affects the PPF surface. Therefore, investigations into using gold films were carried out.

The first wet etch used for the gold films was $KCN/K_3Fe(CN)_6$. There were no outlines or defects left on the surface after the two line pattern of the gold film was removed, as analysed using the SEM. For this pattern, the etching time required was 12 – 13 minutes. Elemental analysis with SEM showed no gold present. To confirm that the underlying PPF was not disrupted by the gold film or its etching, an entire PPF surface was coated with gold and etched. Removal required an immersion time of 20 minutes.

$Ru(NH_3)_6^{3+}$ probe scans were recorded at the as-prepared PPF surface before the gold was deposited, at the gold film and at the PPF surface after the gold was removed. All three CV scans were identical. This suggests that firstly the electrochemical properties of the gold film are similar to the PPF surface and secondly deposition and removal of the gold film using the $KCN/K_3Fe(CN)_6$ etch did not alter the electrochemical properties of the PPF.

The second etch used for the gold film was I_2/KI. Within 30 seconds of immersion of the GC plate with the gold film in the two line pattern, the gold film was removed as observed by eye. After 1 minute, the sample was removed. The FCA probe scans before and after 1 minute in the I_2/KI etch were identical suggesting that the GC plate was not affected by the etch. To confirm that there was no gold present after etching with I_2/KI, a GC plate was covered with a gold film and immersed in etch for 5 minutes. The GC plate was then scanned in 0.1 M HNO_3 from 0 to 1.4 V to test for the characteristic gold electrochemical response.[39] No peaks were present indicating dissolution of the gold film. (CV scan of a gold film gives a reduction peak at 0.84 V.)

$KCN/K_3Fe(CN)_6$, I_2/KI and KCN/KOH were the three gold etches used. The etches for the metal films are oxidising agents and the Equations 9c.1. are the oxidation of gold by the active species in the etches. When gold is exposed to the CN^- ion in the presence of a mild oxidant, such as $Fe(CN)_6^{3-}$ or O_2, the gold is oxidised. The formation of the very stable $Au(CN)^{2-}$ ion drives the reaction. KOH in the KCN/KOH etch maintains the basic pH to prevent formation of toxic and volatile HCN. The I^- ion in the I_2/KI etch increases the solubility of I_2 in water thus increasing the concentration of reactant. The ion also helps to dissolve the AuI product and so drives the etch process forward.

9c.1. $KCN/K_3Fe(CN)_6$ or KCN/KOH etch:

$$4Au + 8CN^- + O_2 + 2H_2O \longrightarrow 4[Au(CN)_2]^- + 4OH^-$$

$$Au + 2CN^- + Fe(CN)_6^{3-} \longrightarrow Fe(CN)_6^{4-} + Au(CN)^{2-}$$

I_2/KI etch: $2Au + I_2 \longrightarrow 2AuI$

9c.1.2. Approach (ii): "Fill-in" approach with islands of gold film

For successful molecular patterning using the "fill-in" approach with islands of gold as the blocking film, the gold film must be able to be removed completely after the first modification. This step was examined using MP as the modifier.

Removal of gold film by wet etching in the $KCN/K_3Fe(CN)_6$, I_2/KI and KCN/KOH

Table 9c.1. lists the experiments carried out to test the requirements for using the $KCN/K_3Fe(CN)_6$ etch with gold films for "fill-in" patterning. The gold films had a thickness of 80 nm. FCA probe scans were used to monitor the modification by MP and the effect of the etching process on the MP layer. The probe scan of an as-prepared PPF surface used in experiment 1 was identical to a continuous gold film modified in experiment 2. The modifier solution concentration of *p*-MB was 5 mM and electrolysis time was 10 minutes. The film was etched using an immersion time of 15 minutes with agitation on the orbital shaker.

Table 9c.1. Current ratios of FCA CV scans of the experiments carried out for "fill-in" approach to patterning using gold films and $KCN/K_3Fe(CN)_6$ etch.

Experiment no.	Initial surface	Current ratio [a] at peak [b] or at 0.35 V	
		(i_{pa} after MP modification)/ (i_{pa} initial surface)	(i_{pa} after etching)/ (i_{pa} initial surface)
1	PPF	0	0.2
2	PPF-gold film entire surface	0.4 [b]	0.6 [b]
3	PPF-gold film in two line pattern	0.1	0.4 [b]

[a] Uncertainty on current ratios is ± 0.05.

From experiment 1, the MP layer was only slightly affected by the etching process, considering that inaccurate replacement of the o-ring for the after etching probe scan could have contributed to the increase in peak current ratio.

The results of experiment 2 indicate firstly that the MP was grafted to the gold film and secondly that etching does not remove all of the gold film with the attached MP modifier. Gold surfaces have been shown previously to be modified by the attachment of aryl diazonium salts[40,41] and also amines[42]. However, the peak current ratio of 0.4 shows that the MP layer attached to the gold film was less blocking compared to the layer at the PPF surface in experiment 1. The MP modified gold film was not completely removed. This indicates that MP acts as an etch mask as has previously been reported for alkanethiols SAMs on gold, sliver, copper, palladium, molybdenum, chromium surfaces[35,43,44] and alkanephosphoic acid on aluminium surfaces.[44,45]

It was considered that etching would be more efficient for a small pattern of gold than for a continuous film. Hence, in experiment 3, the gold film was deposited in a two line pattern and the whole surface modified. The peak current ratio of (i_{pa} after MP

modification)/(i_{pa} initial surface) of 0.1 was between the ratios observed for an as-prepared PPF surface and PPF surface with a gold film deposited over the whole surface. This was expected as the MP modification at gold films was not as blocking as the surrounding PPF surface, therefore allowing the probe response. After etching, the increase of the peak current ratio to 0.4 was consistent with the gold film with MP attached being removed during etching. The gold film in the two line pattern was approximately 40% of the area of the o-ring used in electrochemical cell. The bulk of the gold film was removed during etching as examined by eye. However, inspection of the surface after etching was also carried out using the optical microscope. From the image in Figure 9c.2, it is possible to visualise some areas of the underlying gold film in the two line pattern that remained.

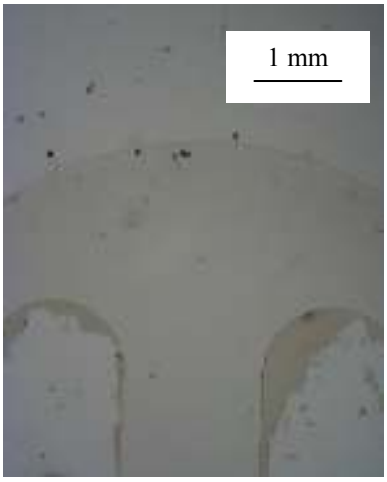

Figure 9c.2. Optical microscope image of MP-modified surface where remains of the gold film deposited in the two line pattern were visible after etching in the $KCN/K_3Fe(CN)_6$ etch.

Increasing the etching time from 15 minutes to 4 hours helped to removed more of the film. However, there were still flakes of gold left at the edges of the two line pattern.

At this point, these observations led to the conclusion that the gold film cannot be completely removed after MP modification, using the $KCN/K_3Fe(CN)_6$ etch. The other two etches, I_2/KI and KCN/KOH, also failed to completely remove the gold film after MP modification.

9.4. Conclusions

Out of the three blocking materials – PDMS, PVA and thin metal films, only PDMS gave molecular patterns using the patterning approaches in this work. The molecular patterns were spatially defined patterns of molecules consisting of different chemical compositions, attached to the one carbon surface.

With the "fill-in" approach, the smallest pattern was the *parallel lines* with a line width of 20 μm and straight edges. *Parallel lines* patterns of TGD/MP and its inverse pattern MP/TGD were successfully created. The electrochemical conditions used for the attachment of the first and second modifiers were very different to avoid the second modifier attaching to the previously modified areas.

Using the "build-up" approach, the most successful combination was where NBC was coupled to selected areas of the already attached TGD layer to present a pattern of TGD/TGD-NB. However, the TGD-NB lines were wider than the width of the microchannels which was presumably due to micron-scale seepage of the coupling solution under the PDMS. An improvement to this approach is to attach a modifier that is less hydrophilic than TGD to aid the sealing of the PDMS to the modified PPF during coupling.

For the "selective conversion" approach, a low yield of amino functionalities was generated for the electrochemical reduction of the *p*-nitrophenyl groups of the already attached *p*-NB layer, in the PDMS microchannels. The low amino surface coverage is presumably because of the significant resistance and ohmic drop associated with the thin layer of solution in the microchannels.

Out of the three approaches, the "fill-in" and "selective conversion" approaches perform electrochemistry in PDMS microchannels, which has not been previously investigated.

Visualisation of the molecular patterns was performed by exposing the surface to steam, using the optical microscope, SEM, AFM, by the assembly of citrate-capped gold NPs and/or aldehyde-sulfate functionalised PS NPs. All these methods exploited the properties of the carefully selected modifiers used in the patterns. Modifier layers with different wettabilites were required to observe condensation figures when the patterned surface was exposed to steam. Optical microscopy depends on the varied thicknesses of the layers, where approximately 1 nm difference was adequate to give sufficient contrast for imaging. Patterns with layers of different thicknesses could also be visualised using the AFM. Molecules with different chemical compositions and thus scattering capabilities were visualised using the SEM. Specific functionalities that are able to assemble the NPs were necessary to be present within the layer if visualisation utilised NP assembly. Out of all these methods, the SEM is the most versatile method and was used to visualise all the molecular patterns prepared using the three different approaches with PDMS microchannels.

PVA was investigated as the blocking material in patterning approaches (i) – "fill-in" approach where the PVA has perforations and (ii) "fill-in" approach where there are islands of PVA. Preliminary experiments showed that when PVA contacted the PPF surface, PVA residues of a few nanometres remained that could not be completely removed. Hence, PVA was an unsuitable blocking material.

Metal films were examined as islands of blocking material in the "fill-in" approach to patterning. Nichrome films could not be deposited or removed without disrupting the carbon surface. Wet etching and electrochemical oxidative stripping was both unsuccessful. For the gold films, the problem was that during the attachment of the first modifier (MP), modifiers attached to the gold films as well as the carbon surface. The modifiers attached to the gold film acted like resists against all three of the common etches used – $KCN/K_3Fe(CN)_6$, I_2/KI and KCN/KOH. The etches were able to remove the bulk gold film, however, its complete removal was not be achieved.

9.5. References

(1) Wilde, L. M.; Farace, G.; Roberts, C. J.; Davies, M. C.; Sanders, G. H. W.; Tendler, S. J. B.; Williams, P. M. *Analyst* **2001**, *126*, 195-198.

(2) Brooksby, P. A.; Downard, A. J. *Langmuir* **2005**, *21*, 1672-1675.

(3) Xia, Y.; Whitesides, G. M. *Angewandte Chemie* **1998**, *37*, 550-575.

(4) Xia, Y.; Whitesides, G. M. *Annual Review of Materials Science* **1998**, *28*, 153-184.

(5) Makamba, H.; Kim, J. H.; Lim, K.; Park, N.; Hahn, J. H. *Electrophoresis* **2003**, *24*, 3607-3619.

(6) Duffy, D. C.; McDonald, J. C.; Schueller, O. J. A.; Whitesides, G. M. *Analytical Chemistry* **1998**, *70*, 4974-4984.

(7) Sia, S. K.; Whitesides, G. M. *Electrophoresis* **2003**, *24*, 3563-3576.

(8) McDonald, J. C.; Whitesides, G. M. *Accounts of Chemical Research* **2002**, *35*, 491-499.

(9) Huang, W.-H.; Cheng, W.; Zhang, Z.; Pang, D.-W.; Wang, Z.-L.; Cheng, J.-K.; Cui, D.-F. *Analytical Chemistry* **2004**, *76*, 483-488.

(10) Zheng, B.; Gerdts, C. J.; Ismagilov, R. F. *Current Opinion in Structural Biology* **2005**, *15*, 548-555.

(11) Romet-Lemonne, G.; VanDuijn, M.; Dogterom, M. *Nano Letters* **2005**, *5*, 2350-2354.

(12) Soper, S, A.; Hashimoto, M.; Situma, C.; Murphy Michael, C.; McCarley Robin, L.; Cheng, Y.-W.; Barany, F. *Methods* **2005**, *37*, 103-113.

(13) Jackman, R. J.; Duffy, D. C.; Cherniavskaya, O.; Whitesides, G. M. *Langmuir* **1999**, *15*, 2973-2984.

(14) Duffy, D. C.; Jackman, R. J.; Vaeth, K. M.; Jensen, K. F.; Whitesides, G. M. *Advanced Materials* **1999**, *11*, 546-552.

(15) Liang, Z.; Li, K.; Wang, Q. *Langmuir* **2003**, *19*, 5555-5558.

(16) Sullivan, T. P.; van Poll, M. L.; Dankers, P. Y. W.; Huck, W. T. S. *Angewandte Chemie* **2004**, *43*, 4190-4193.

(17) Andersson, H.; Jonsson, C.; Moberg, C.; Stemme, G. *Sensors and Actuators, B* **2001**, *B79*, 78-84.

(18) Rozkiewicz, D, I.; Ravoo Bart, J.; Reinhoudt David, N. *Langmuir* **2005**, *21*, 6337-6343.

(19) Perring, M.; Dutta, S.; Arafat, S.; Mitchell, M.; Kenis, P. J. A.; Bowden, N. B. *Langmuir* **2005**, *21*, 10537-10544.

(20) Mela, P.; Onclin, S.; Goedbloed, M. H.; Levi, S.; Garcia-Parajo, M. F.; van Hulst, N. F.; Ravoo, B. J.; Reinhoudt, D. N.; van den Berg, A. *Lab on a Chip* **2005**, *5*, 163-170.

(21) Schaper, C. D. *Proceedings of SPIE-The International Society for Optical Engineering* **2004**, *5374*, 325-336.

(22) Schaper, C. D. *Nano Letters* **2003**, *3*, 1305-1309.

(23) Schaper, C. D. *Langmuir* **2004**, *20*, 227-231.

(24) Yum, J.-H.; Kim, S.-S.; Sung, Y.-E. *Colloids and Surfaces, A* **2004**, *251*, 203-207.

(25) Kang, S. W.; Yoo, J. S.; Lee, J. D. *Journal of Vacuum Science & Technology, B* **1998**, *16*, 2891-2893.

(26) Sasaki, K. Y.; Talbot, J. B. *Advanced Materials* **1999**, *11*, 91-105.

(27) Dunn, A. S. *Photoresists Based on Polyvinyl Alcohol*; John Wiley & Sons, **1992**.

(28) Madou, M. J. *Fundamentals of Microfabrication*; Second ed.; CRC Press, **2002**.

(29) Williams, K. R.; Gupta, K.; Wasilik, M. *Journal of Microelectromechanical Systems* **2003**, *12*, 761-778.

(30) Lopez, G. P.; Biebuyck, H. A.; Frisbie, C. D.; Whitesides, G. M. *Science* **1993**, *260*, 647-649.

(31) Lopez, G. P.; Biebuyck, H. A.; Whitesides, G. M. *Langmuir* **1993**, *9*, 1513-1516.

(32) Mendes, P, M.; Jacke, S.; Critchley, K.; Plaza, J.; Chen, Y.; Nikitin, K.; Palmer Richard, E.; Preece Jon, A.; Evans Stephen, D.; Fitzmaurice, D. *Langmuir***2004**, *20*, 3766-3768.

(33) Noy, A.; Vezenov, D. V.; Lieber, C. M. *Annual Review of Materials Science* **1997**, *27*, 381-421.

(34) Lim, E. F.-H. *Atomic Force Microscope Nanolithography : a thesis submitted in partial fulfilment of the requirements for the degree of Master of Engineering in Electrical and Electronic Engineering at the University of Canterbury, Christchurch, New Zealand*, **2002**.

(35) Kumar, A.; Biebuyck, H. A.; Whitesides, G. M. *Langmuir* **1994**, *10*, 1498-1511.

(36) Weimann, T.; Geyer, W.; Hinze, P.; Stadler, V.; Eck, W.; Golzhauser, A. *Microelectronic Engineering* **2001**, *57-58*, 903-907.

(37) Vogler, E. A. *Advances in Colloid and Interface Science* **1998**, *74*, 69-117.

(38) Lee, J. N.; Park, C.; Whitesides, G. M. *Analytical Chemistry* **2003**, *75*, 6544-6554.

(39) Hamelin, A. *Journal of Electroanalytical Chemistry* **1996**, *407*, 1-11.

(40) Pinson, J.; Podvorica, F. *Chemical Society Reviews* **2005**, *34*, 429-439.

(41) Bernard, M.-C.; Chausse, A.; Cabet-Deliry, E.; Chehimi, M. M.; Pinson, J.; Podvorica, F.; Vautrin-Ul, C. *Chemistry of Materials* **2003**, *15*, 3450-3462.

(42) Adenier, A.; Chehimi, M. M.; Gallardo, I.; Pinson, J.; Vila, N. *Langmuir* **2004**, *20*, 8243-8253.

(43) Burdinski, D.; Brans, H. J. A.; Decre, M. M. J. *Journal of the American Chemical Society* **2005**, *127*, 10786-10787.

(44) Geissler, M.; Wolf, H.; Stutz, R.; Delamarche, E.; Grummt, U.-W.; Michel, B.; Bietsch, A. *Langmuir* **2003**, *19*, 6301-6311.

(45) Goetting, L. B.; Deng, T.; Whitesides, G. M. *Langmuir* **1999**, *15*, 1182-1191.

The work described in this thesis was aimed at controllably changing the properties of carbon surfaces by covalently assembling organic layers. Using the electrochemical oxidation of amines and reduction of aryl diazonium salts, amine and aryl layers were successfully attached to glassy carbon (GC) and pyrolysed photoresist film (PPF) surfaces. By varying the modification conditions such as the electrolysis time, the surface concentrations of modifiers and the thicknesses of the modifier layers were controlled. Prolonged electrolysis times gave layers that had thicknesses larger than a monolayer.

Multilayers had not been previously observed for monoamine modifiers and amine modifiers have not been previously assembled onto PPF surfaces. The attachment of amine modifiers with different chemical compositions allowed for the wettability of the carbon surface to be modulated. Water contact angles for amine-modified carbon surfaces ranged from 45 – 79°. Examination of the stability of the amine layers were carried out by scanning, soaking and sonicating. After these treatments, atomic force microscope (AFM) depth profiling experiments showed that the bulk of the layer was intact at the surface and that changes in the probe only corresponded to the detachment of adsorbed material and/or reorganisation and reorientation within the layer. The amine layers were useful for subsequent covalent coupling of electroactive species such as ferrocene monocarboxylic acid (FCA) and nitrobenzoyl chloride (NBC), via amide bond formations.

Modification of carbon surfaces via the reduction of aryl diazonium salts has been widely studied. The attached aryl layers were only able to slightly alter the wettability of the carbon surface between 56 and 72°, using the modification conditions. These layers were also used for subsequent coupling reactions. It was necessary that the *p*-nitrophenyl

groups of the *para* nitro phenyl (NPh) layer were reduced to yield amino functionalities for coupling. From high resolution x-ray photoelectron spectroscopy (XPS) data, four peaks corresponding to four nitrogen species were present at the electrochemically reduced NPh layers. This is more than the commonly reported two peaks. Further work has to be carried out to enable a more certain assignments of peaks which would involve analysing the as-prepared NPh layer using this particular XPS instrument and a nitroazobenzene layer.

The different layers had varied interactions towards the fluorescently labelled protein, bovine serum albumin-fluorescein isothiocynate (BSA-FITC). However, comparing these modified GC surfaces to other protein adsorption studies, these surfaces are not very good at either promoting or reducing protein adsorption. Future work would involve more careful tailoring of the modifiers to improve the ability of modified GC surfaces to control protein behaviour. For example, to decrease protein adsorption, long, hydrophilic, neutral modifiers consisting of hydrogen-bond acceptors and ethylene glycol groups would be selected. The fluorescence microscopy method of monitoring protein adsorption on modified carbon surfaces was quick and simple to use.

The amine-containing modifiers layers were able to assemble aldehyde/sulfate-functionalised polystyrene (PS) and citrate-capped gold nanoparticles (NPs). By using modifier layers that have different number of amines and wettability, and by tuning the modification conditions, the desired surface concentration of cationic sites and thus density of electrostatically assembled citrate-capped gold NPs was easily modulated. Adjusting the immersion time, concentration and pH of the gold NP solution also allowed control of the NP surface coverage.

Patterns of organic modifiers in pre-determined spatially defined locations on PPF surfaces were successfully created using poly(dimethyl)siloxane (PDMS) as the blocking material and three different approaches. With the "fill-in" and "selective conversion" approaches, electrochemistry was performed in PDMS microchannels which has not been previously investigated. The smallest dimension of the molecular patterns obtained was 20 μm. Significantly smaller patterns have been achieved using PDMS for micro-contact printing of self-assembled monolayers (SAMs) onto gold surfaces. Micro-contact printing of modifiers was not investigated in this work as spontaneous assembly of amine and aryl diazonium salts onto carbon surfaces is not as well established compared to electrochemical attachment. Several visualisation techniques were developed for the molecular patterns which included exposing the surface to steam, using the optical microscope, scanning electron microscope (SEM), AFM and by the assembly of NPs. Out of all these methods, the SEM was the most versatile method which was able to detect areas of patterns only differing in a single functional group.

Appendix 0.

Amide bond formation via coupling a carboxylic acid to an amine[1]

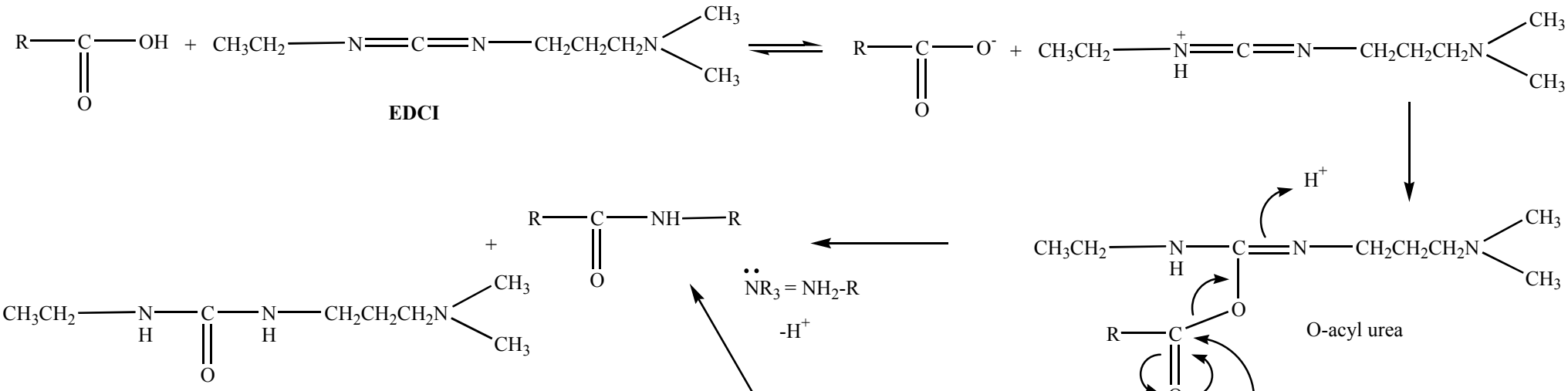

Other coupling agents:

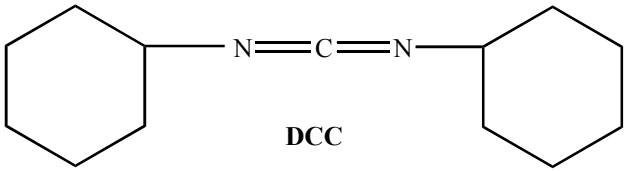

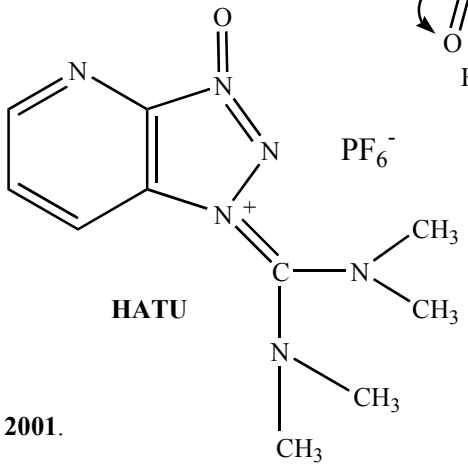

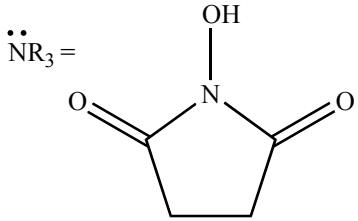

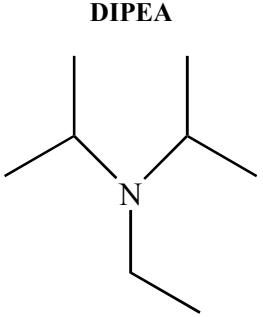

The other coupling agents work similar to EDCI. DCC and HATU are used with a base, DIPEA. It deprotonates the carboxylic acid in the first step and amide in the final step.

[1] Smith, M. B. and March, J. *March's advanced organic chemistry: reactions, mechanisms and structure*, Wiley & Sons, Inc., **2001**.

Appendix 3.

Table 3.1. Procedures the produced poor quality PPF surfaces.

Si(100) wafer type	**Photoresist**	**Photoresist spin coat settings**	**Between coats soft baking in 95 °C oven**	**Photoresist application technique**	**Soft baking prior to pyrolysis**	**Thickness of photoresist measured by profilometer**
n-type	AZ 4620	3000 rpm, 60 s, 1 coat	Not baked	Drop/spin	Overnight in 95 °C oven	5.8 µm
n-type	AZ 4620	3000 rpm, 60 s, 1 coat	Not baked	Drop/spin	3 nights in 95 °C oven	Not measured
n-type	AZ 4620	6000 rpm, 60 s, 2 coats	20 mins, cool 10 mins	Drop/spin	Overnight in 95 °C oven	Not measured
n-type	AZ 4620	6000 rpm, 30 s, 3 coats	20 mins, cool 10 mins	Spin/drop	3-4 hr in 95 °C oven, overnight in 45 °C oven	Not measured
n-type	AZ 4620	6000 rpm, 30 s, 3 coats	20 mins, cool 10 mins	Spin/drop	Overnight in 95 °C oven	Not measured
n-type	S 1813	3000 rpm, 30 s, 4 coats	10 mins, cool 2 mins	Spin/drop	Overnight in 95 °C oven	1.3 µm per coat x 4 coats = 5.2 µm
p-type	S 1813	3000 rpm, 30 s, 4 coats	10 mins, cool 2 mins	Spin/drop	Overnight in 95 °C oven	Not measured
n-type with 1 µm thermal oxide (SiO_2)	S 1813	3000 rpm, 30 s, 4 coats	10 mins, cool 2 mins	Spin/drop	Overnight in 95 °C oven	Not measured
p-type with 1 µm thermal oxide (SiO_2)	S 1813	3000 rpm, 30 s, 4 coats	10 mins, cool 2 mins	Spin/drop	Overnight in 95 °C oven	Not measured

All the above samples were pyrolysed in the 'old' furnace, with temperature increments of 350 °C (45 mins), 550 °C (30 mins), 1100 °C (1 hr) then cool to <100 °C. The multicoats of photoresist were applied in subsequent steps on the same day. At times, pyrolysis took place up to 6 days after photoresist was spun coated. The surfaces were kept in the dark in air during the waiting time.

Below are samples processed in 'new' furnace. Boats were inserted 22 cm into furnace tube unless otherwise stated and only Si(100) *n*-type wafers were used. Photoresist was dropped onto wafer before spinner was started.

Photoresist	Photoresist spin coat settings	Between coats soft baking in 95 °C oven	Soft baking prior to pyrolysis	Pyrolysis details	Distance boat inserted into furnace tube	Thickness of photoresist measured by profilometer
AZ 4620	6000 rpm, 30 s, 3 coats	20 mins, cool 10 mins	3 – 4 hr in 95 °C oven, overnight in 45 °C oven	T increments: 350 °C (45 mins), 550 °C (30 mins), 1080 °C (1 hr) then cool to <100 °C.		Not measured
AZ 4620	6000 rpm, 30 s, 3 coats	20 mins, cool 10 mins	3 – 4 hr in 95 °C oven, overnight in 45 °C oven	T increments: 350 °C (45 mins), 550 °C (30 mins), 1080 °C (1 hr) then cool to <100 °C.	32 cm	Not measured
AZ 4620	6000 rpm, 30 s, 3 coats. Coats were applied over 2 days.	20 mins, cool 10 mins	3 – 4 hr in 95 °C oven, overnight in 45 °C oven	T increments: 350 °C (45 mins), 550 °C (30 mins), 1000 °C (1 hr) then cool to <100 °C.	27 cm	Not measured
AZ 4620	3000 rpm, 30 s, 2 coats	20 mins, cool 10 mins	Overnight in 45 °C oven	T increments: 550 °C (20 mins), 750 °C (20 mins), 1050 °C (1 hr) then cool to <100 °C.		Not measured
AZ 4620	3000 rpm, 30 s, 2 coats	20 mins, cool 10 mins	20 mins in 95 °C oven	T increments: 500 °C (20 mins), 750 °C (20 mins), 1050 °C (1 hr) then cool to <100 °C.		Not measured
AZ 4620	3000 rpm, 30 s, 1 coat	Not baked	20 mins in 95 °C oven	T increments: 550 °C (20 mins), 750 °C (20 mins), 1050 °C (1 hr) then cool to <100 °C.		Not measured

AZ 4620	5500 rpm, 30 s, 2 coats	20 mins, cool 10 mins	Overnight in 45 °C oven	T increments: 500 °C (20 mins), 750 °C (20 mins), 1050 °C (1 hr) then cool to <100 °C.	Not measured
S 1518	3000 rpm, 30 s, 4 coats	20 mins, cool 10 mins	Overnight in 45 °C oven	T increments: 500 °C (20 mins), 750 °C (20 mins), 1050 °C (1 hr) then cool to <100 °C.	Not measured
S 1518	3000 rpm, 30 s, 4 coats	20 mins, cool 10 mins	Overnight in 45 °C oven	T increments: 550 °C (20 mins), 750 °C (20 mins), 1050 °C (1 hr) then cool to <100 °C.	8.5 µm before pyrolysis and PPF 2.2 µm
S 1518	3000 rpm, 30 s, 4 coats	20 mins, cool 10 mins	20 mins in 95 °C oven	T increments: 500 °C (20 mins), 750 °C (20 mins), 1050 °C (1 hr) then cool to <100 °C.	Not measured
S 1518	3000 rpm, 30 s, 4 coats	10 mins, cool 10 mins	20 mins in 95 °C oven	T increments: 500 °C (20 mins), 750 °C (20 mins), 1050 °C (1 hr) then cool to <100 °C.	Not measured
S 1518	3000 rpm, 20 s, 4 coats	10 mins, cool 5 mins	3 hr in 95 °C oven	T increments: 500 °C (20 mins), 750 °C (20 mins), 1050 °C (1 hr) then cool to <100 °C.	Not measured

RMS roughness analysis of as-prepared PPF and GC

PPF samples were from different pyrolysis batches
Tip used was NSC 14/50
Scan rate 1 Hz
z-limit 3 µm

Sample	Image No.	Scan Area		Section Analysis (RMS in nm) Fixed 3 line profiles			Average
			Scan Distance	Line 1 (red)	Line 2 (white)	Line 3 (green, vertical line)	
PPF 1	est13051.000	4 µm x 4 µm	4 µm	0.219	0.215	0.199	**0.21**
	est13051.001	4 µm x 4 µm	4 µm	0.202	0.140	0.162	**0.17**
	est13051.002	4 µm x 4 µm	4 µm	0.210	0.162	0.145	**0.17**
	est13051.003	4 µm x 4 µm	4 µm	0.197	0.220	0.182	**0.20**
	est13051.004	4 µm x 4 µm	4 µm	0.176	0.163	0.195	**0.18**
	est13051.005	4 µm x 4 µm	4 µm	0.220	0.185	0.203	**0.20**
	est13051.006	4 µm x 4 µm	4 µm	0.159	0.190	0.186	**0.18**
	est13051.007	4 µm x 4 µm	4 µm	0.196	0.170	0.209	**0.19**
	est13051.008	4 µm x 4 µm	4 µm	0.189	0.172	0.179	**0.18**
PPF 2	est12111a.000	4 µm x 4 µm	4 µm	0.391	0.407	0.378	**0.39**
	est12111a.001	4 µm x 4 µm	4 µm	0.326	0.317	0.337	**0.33**
						Average for PPF:	**0.22**
GC	GC3aalteredgood	20 µm x 20 µm	4 µm	0.786	0.768	0.922	**0.83**
			5 measurements each 20 µm line	0.640	0.671	0.988	
				0.714	0.709	0.815	
				1.170	0.722	0.873	
				0.828	0.664	1.107	

Water contact angles

Bare PPF

Surface 1					
Drop 1					
Left of drop	74	70	72		
Right of drop	73	71	71		
Drop 2					
Left of drop	73	72	70		
Right of drop	73	71	71		
Surface 2 (different batch cf surface 1)					
Drop 1					
Left of drop	69	69	70		
Right of drop	73	71	70		
Drop 2					
Left of drop	71	73	71		
Right of drop	73	75	73	**72**	**± 3**

Bare GC

Surface 1					
Drop 1					
Left of drop	68	67	69		
Right of drop	67	70	68		
Surface 2					
Drop 1					
Left of drop	73	73	71		
Right of drop	73	72	72		
Drop 2					
Left of drop	72	74	74		
Right of drop	73	74	73	**71**	**± 4**

Appendix 4.

Water contact angles

TDA on PPF (5 mM, electrolysis time 10 minutes)

Surface 1

Drop 1				
Left of drop	76	77	77	
Right of drop	79	76	78	
Drop 2				
Left of drop	79	77	80	
Right of drop	78	78	79	

Surface 2

Drop 1				
Left of drop	79	80	80	
Right of drop	80	81	80	
Drop 2				
Left of drop	80	80	79	
Right of drop	80	80	80	**79 ± 3**

DAD on PPF (5 mM, electrolysis time 10 minutes)

Surface 1

Drop 1				
Left of drop	73	74	73	
Right of drop	73	75	74	
Drop 2				
Left of drop	73	74	74	
Right of drop	73	73	74	

Surface 2

Drop 1				
Left of drop	74	74	74	
Right of drop	73	75	73	
Drop 2				
Left of drop	74	72	72	
Right of drop	75	73	73	**74 ± 2**

TGD on PPF (5 mM, electrolysis time 2 minutes)

Surface 1

Drop 1					
Left of drop	48	46	48		
Right of drop	46	46	47		
Drop 2					
Left of drop	46	48	48		
Right of drop	47	45	48	**47**	**± 2**

After soaking in DMSO for 2 hours

Drop 1					
Left of drop	47	46	48		
Right of drop	48	47	47		
Drop 2					
Left of drop	46	48	48		
Right of drop	47	47	48	**47**	**± 1**

Surface 2

Drop 1					
Left of drop	48	46	47		
Right of drop	47	47	46		
Drop 2					
Left of drop	47	45	46		
Right of drop	47	46	48	**47**	**± 2**

After soaking in 0.1 M NBC/DMSO for 2 hours

Drop 1					
Left of drop	56	55	55		
Right of drop	55	56	57		
Drop 2					
Left of drop	57	57	56		
Right of drop	57	58	58	**56**	**± 2**

Surface 3

Drop 1					
Left of drop	43	46	45		
Right of drop	44	43	45		
Drop 2					
Left of drop	44	44	47		
Right of drop	46	44	44	**45**	**± 2**

TGD on PPF (5 mM, electrolysis time 10 minutes)

Surface 1

Drop 1					
Left of drop	47	47	46		
Right of drop	46	47	45		
Drop 2					
Left of drop	45	47	45		
Right of drop	44	45	44		

Surface 2

Drop 1					
Left of drop	45	48	48		
Right of drop	45	47	45		
Drop 2					
Left of drop	46	47	47		
Right of drop	43	46	46	**46**	**± 3**

TGD on GC plate (200 mM, electrolysis time 10 minutes)

Surface 1

Drop 1				
Left of drop	46	43	46	
Right of drop	47	45	43	
Drop 2				
Left of drop	46	47	44	
Right of drop	44	44	43	

Surface 2

Drop 1				
Left of drop	47	45	47	
Right of drop	46	45	45	
Drop 2				
Left of drop	46	47	47	
Right of drop	46	45	42	**45 ± 3**

HA on GC plate (5 mM, electrolysis time 10 minutes)

Surface 1

Drop 1				
Left of drop	75	77	78	
Right of drop	76	77	79	
Drop 2				
Left of drop	77	78	78	
Right of drop	76	77	78	

Surface 2

Drop 1				
Left of drop	78	76	77	
Right of drop	77	78	78	
Drop 2				
Left of drop	78	78	78	
Right of drop	78	77	77	**77 ± 2**

PGD on GC plate (20 mM, electrolysis time 10 minutes)

Surface 1

Drop 1			
Left of drop	57	58	60
Right of drop	56	59	56
Drop 2			
Left of drop	59	59	58
Right of drop	60	58	58

Surface 2

Drop 1					
Left of drop	60	58	60		
Right of drop	59	59	58		
Drop 2					
Left of drop	61	59	60		
Right of drop	59	60	58	**59**	**± 3**

TDA (5 mM, 1 minute)

Sample no and date prepared, Instrument	Scratch	Scan	File code	Thickness measured by section analysis: Midpoint L	Midpoint R	L of scratch	R of scratch	Thickness measured by localised depth	Av. of scan minus 0.3 nm	Std. Dev. of scan	Var. of scan	Av. of scratch	Std. Dev. of scratch	Var. of scratch	Av. of sample	Std. Dev. or Error of sample
TDA 7305	1	1	est731a.005	1.328		1.356			1.096	0.102	0.010					
Attach FCA						1.389										
DCC/DIPEA/DCM						1.333										
scan in NaClO4						1.574										
Scratch 8:1		2	est731a.006		1.199	1.519			1.089	0.123	0.015					
Scan with scratch tip					1.525	1.343										
Scan 8:1					1.441	1.219										
Tip holder 2					1.417	1.29										
					1.529	1.403						1.092	0.160	0.03		
TDA 21305	1	1	est2131a.013	1.607	1.552	1.646	1.607	1.693	1.276	0.100	0.010					
Attach FCA						1.648	1.330									
DCC/DIPEA/DCM						1.524	1.491									
scan in NaClO4						1.639	1.599									
Scratch 8:1	2	1	est2131a.016	1.152	1.141	1.119	1.177	1.151	0.875	0.045	0.002					
Scan with scratch tip						1.199	1.191									
Scan 8:1						1.186	1.291									
Tip holder 2						1.158	1.163									
		2	est2131a.020	1.091	1.046	1.108	1.123	1.050	0.822	0.056	0.003					
						1.210	1.130									
						1.196	1.136									
						1.182	1.073					0.849	0.072	0.005	1.063	0.124
TDA 3 30305	1	1	est3031a.000	1.515	1.399	1.598	1.767		1.184	0.186	0.035					
Attach FCA						1.152	1.636									
EDCI/NHS/PB						1.526	1.439									
scan in NaClO4						1.579	1.229									

Scratch 8:1		2	est3031a.001	1.710	1.749	1.526	1.667	1.314	0.105	0.011					
Scan with scratch tip						1.621	1.817								
Scan 8:1						1.679	1.656								
Tip holder 2						1.497	1.565				1.249	0.214	0.046		
	2	1	est3031a.002	1.522	1.435	1.612	1.512	1.234	0.065	0.004					
						1.609	1.549								
						1.474	1.631								
						1.522	1.480								
		2	est3031a.003	1.576	1.297	1.546	1.460	1.174	0.116	0.013					
						1.433	1.413								
						1.535	1.552								
						1.636	1.296				1.204	0.133	0.018	1.227	0.252
TDA 5 30305	1	1	est3031a.004	1.508	1.328	1.424	1.460	1.132	0.076	0.006					
Attach FCA						1.427	1.413								
EDCI/NHS/PB						1.443	1.552								
scan in NaClO4						1.467	1.296								
Scratch 8:1		2	est3031a.005	1.500	1.423	1.489	1.327	1.103	0.090	0.008					
Scan with scratch tip						1.456	1.295								
Scan 8:1						1.463	1.270								
Tip holder 2						1.491	1.319				1.118	0.118	0.014		

TDA (5 mM, 2 minutes)

Sample no and date prepared, Instrument	**Scratch**	**Scan**	**File code**	**Thickness measured by section analysis** Midpoint L	Midpoint R	L of scratch	R of scratch	**Thickness measured by localised depth**	**Av. of scan minus 0.3 nm**	**Std. Dev. of scan**	**Var. of scan**	**Av. of scratch**	**Std. Dev. of scratch**	**Var. of scratch**	**Av. of sample**	**Std. Dev. or Error of sample**
TDA 25604		5	1 est1071a.006	1.288	1.260	1.376	1.348	1.299	1.049	0.114	0.013					
						1.398	1.310									
Scratch 8:1						1.155	1.332									
Scan with NSC 14 tip						1.564	1.514									
Scan 1:1																
Tip holder 2			2 est1071a.007	1.271	1.227	1.433	1.283	1.278	1.039	0.104	0.011					
						1.239	1.440									
						1.333	1.246									
						1.508	1.471					1.044	0.154	0.024		
		6	1 est1071a.008	1.254	1.212	1.377	0.983	1.214	0.996	0.173	0.030					
						1.212	1.173									
						1.363	1.589									
						1.550	1.328									
			2 est1071a.009	1.213	1.133	1.194	1.019	1.209	0.898	0.118	0.014					
						1.236	1.091									
						1.053	1.403									
						1.323	1.304					0.947	0.209	0.044	0.996	0.260

TDA (5 mM, 5 minutes)

Sample no and date prepared, Instrument	**Scratch**	**Scan**	**File code**	**Thickness measured by section analysis** Midpoint L	Midpoint R	L of scratch	R of scratch	**Thickness measured by localised depth**	**Av. of scan minus 0.3 nm**	**Std. Dev. of scan**	**Var. of scan**	**Av. of scratch**	**Std. Dev. of scratch**	**Var. of scratch**	**Av. of sample**	**Std. Dev. or Error of sample**
TDA 25604		3	1 est1071a.003	2.899	2.890	2.959	2.899	2.918	2.736	0.306	0.094					
						2.950	2.686									
Scratch 8:1						2.964	3.845									
Scan with scratch tip						3.293	3.094									
Scan 1:1																
Tip holder 2			2 est1071a.004	2.567	2.867	2.558	2.312	2.629	2.360	0.341	0.117					
						2.912	2.141									
						2.777	3.396									
						2.365	2.737					2.548	0.459	0.210		
TDA 1 2205		1	1 1est2205.001	2.465	2.204	2.687	2.62	2.363	2.127	0.175	0.030					
Au NPs	4:1					2..742	2.386									
						2.273	2.21									
Scan with 15/AlBS tip						2.631	2.432									
Scan 8:1																
Tip holder 2			2 1est2205.002	2.726	2.559	2.962	2.615	2.634	2.408	0.107	0.011					
						2.739	2.715									
						2.627	2.777									
						2.696	2.739					2.268	0.205	0.042		
		2	1 1est2205.003	2.142	2.164	2.492	2.246	2.022	1.989	0.158	0.025					
	4:1					2.414	2.515									
						2.363	2.144									
						2.349	2.323									
			2 1est2205.004	3.205	3.221	3.296	2.996	2.891	2.763	0.149	0.022					
						3.185	2.923									
						2.858	3.086									
						2.961	3.074					2.376	0.217	0.047	2.322	0.298

TDA 2 2205		1	1	1est2205.005	3.084	2.884	2.975	3.057	2.901	2.857	0.357	0.127				
Au NPs	4:1						3.185	3.777								
							3.219	2.789								
Scan with 15/AlBS tip							2.975	3.884								
Scan 8:1																
Tip holder 2			2	1est2205.006	2.52	2.446	2.508	2.487	2.505	2.228	0.123	0.015				
							2.588	2.318								
							2.77	2.455								
							2.698	2.51					2.543	0.377	0.142	
		2	1	1est2205.007	2.55	2.698	2.643	2.587	2.517	2.303	0.102	0.010				
	8:1						2.695	2.386								
							2.654	2.716								
							2.517	2.667								
			2	1est2205.008	2.991	2.882	3.091	2.873	2.457	2.598	0.168	0.028				
							2.827	2.885								
							2.972	2.924								
							3.071	2.908					2.451	0.197	0.039	2.497	0.426

TDA (5 mM, 8 minutes)

Sample no and date prepared, Instrument	Scratch	Scan	File code	Thickness measured by section analysis				Thickness measured by localised depth	Av. of scan minus 0.3 nm	Std. Dev. of scan	Var. of scan	Av. of scratch	Std. Dev. of scratch	Var. of scratch	Av. of sample	Std. Dev. or Error of sample
				Midpoint L	Midpoint R	L of scratch	R of scratch									
TDA 25604		4	1 est227041a.016	5.702	4.821	5.639	4.479		4.843	0.559	0.312					
						5.678	4.494									
Scratch 8:1						5.631	4.518									
Scan with scratch tip						5.655	4.814									
Scan 1:1																
Tip holder 2			2 est227041a.017	5.378	5.337	5.385	5.052		4.960	0.191	0.036					
						5.478	5.073									
						5.413	5.087									
						5.427	4.969					4.902	0.590	0.349		
		5	1 est227041a.018	5.455	5.497	5.652	5.431		5.304	0.148	0.022					
						5.796	5.670									
						5.856	5.575									
						5.652	5.454									
			2 est227041a.019	5.623	5.401	5.872	5.643		5.366	0.210	0.044					
						5.623	5.491									
						5.844	5.810									
						5.990	5.360					5.335	0.257	0.066	5.118	0.644

TDA (5 mM, 10 minutes)

Sample no and date prepared, Instrument	Scratch	Scan	File code	Thickness measured by section analysis				Thickness measured by localised depth	Av. of scan minus 0.3 nm	Std. Dev. of scan	Var. of scan	Av. of scratch	Std. Dev. of scratch	Var. of scratch	Av. of sample	Std. Dev. or Error of sample
				Midpoint L	Midpoint R	L of scratch	R of scratch									
TDA 15704		1	1 est207041a.005	4.887	5.022	4.816	4.844	5.131	4.690	0.120	0.014					
						5.215	5.072									
Scratch 8:1						4.994	4.973									
Scan with scratch tip						4.987	4.944									
Scan 1:1																
Tip holder 2			2 est207041a.006	5.205	5.220	4.964	5.106	5.089	4.875	0.121	0.015					
						5.241	5.234									
						5.071	5.156									
						5.432	5.212					4.783	0.170	0.029		
TDA 23704		1	1 est127704.004	5.515	5.129	5.578	5.153	5.223	5.024	0.224	0.050					
						5.278	5.191									
Scratch 8:1						5.790	5.428									
Scan with scratch tip						5.183	5.091									
Scan 1:1																
Tip holder 2			2 est127704.005	4.442	4.281	4.156	4.107	3.941	3.973	0.168	0.028					
						4.248	4.199									
						4.443	4.292									
						4.504	4.395					4.499	0.280	0.078		
		2	1 est127704.006	4.987	4.729	4.798	4.649	4.550	4.492	0.135	0.018					
						4.858	4.868									
						4.788	4.649									
						4.908	4.928									
			2 est277041a.007	4.623	4.511	4.609	4.365	4.309	4.194	0.100	0.010					
						4.511	4.602									
						4.483	4.532									
						4.420	4.469					4.343	0.169	0.028	4.421	0.327

TDA 3 16805	1	1 est188051a.001	3.937	4.064	4.081	4.077	4.042	3.815	0.093	0.009					
Scanning					4.153	4.17									
					4.272	4.073									
Scratch 8:1					4.183	4.208									
Scan with scratch tip															
Scan 8:1		2 est188051a.003	4.594	4.555	4.392	4.536	4.453	4.116	0.116	0.014					
Tip holder 2					4.497	4.256									
					4.295	4.315									
					4.346	4.338					3.965	0.149	0.022		
	2	1 est188051a.005	4.854	4.739	4.483	4.772	4.670	4.444	0.128	0.016					
					4.839	4.779									
					4.971	4.628									
					4.693	4.755								4.205	0.197
TDA 4 16805	1	1 est188051a.009	4.232	4.182	4.17	4.365	4.503	4.042	0.164	0.027					
Scanning					4.585	4.548									
					4.41	4.173									
Scratch 8:1					4.161	4.431									
Scan with scratch tip															
Scan 8:1		2 est188051a.010	4.663	4.713		4.649	4.529	4.230	0.174	0.030					
Tip holder 2						4.55									
						4.38									
						4.223					4.136	0.239	0.057		
	2	1 est188051a.011		4.100		4.111	3.999	3.724	0.070	0.005					
						3.992									
						4.017									
						3.926									
		2 est188051a.012	3.812			3.605	3.514	3.422	0.133	0.018					
						3.861									
						3.767									
						3.774					3.573	0.151	0.023	3.854	0.283
TDA 1 181005	1	1 est18101a.010	4.946	4.873	4.946	4.821	4.753	4.678	0.192	0.037					
Soaking protocol					5.092	4.661									

					5.129	5.048									
Scratch 4:1					5.261	5.224									
Blow with N2															
Scan with 15/AlBS tip		2 est18101a.012	6.235	5.677	5.923	5.567	5.610	5.553	0.298	0.089					
Scan 8:1					6.143	5.489									
Tip holder 2					6.222	5.694									
					6.213	5.611					5.115	0.355	0.126		
	2	1 est18101a.013	4.420	4.915	4.369	4.915	4.485	4.381	0.215	0.046					
					4.487	4.789									
					4.732	4.967									
					4.623	4.789									
		2 est18101a.014	5.341	5.065				4.903	0.195	0.038					
											4.642	0.291	0.084	4.879	0.459
TDA 2 181005	1	1 est18101a.006	4.986	4.887	4.956	4.861	4.826	4.627	0.107	0.011					
Soaking protocol					4.960	4.839									
					5.050	5.046									
Scratch 4:1					5.059	4.732									
Blow with N2															
Scan with 15/AlBS tip		2 est18101a.007	5.372	5.511	4.940	5.555	5.037	4.981	0.214	0.046					
Scan 8:1					5.416	5.430									
Tip holder 2					5.069	5.407									
					5.073	5.283					4.804	0.239	0.057		
	2	1 est18101a.008	5.073	5.222	5.012	5.308	5.003	4.847	0.137	0.019					
					4.948	5.297									
					5.218	5.320									
					5.029	5.184									
		2 est18101a.009	5.638	5.252	5.674	5.140	5.393	5.148	0.247	0.061					
					5.747	5.184									
					5.777	5.288									
					5.630	5.205					4.997	0.282	0.080	4.901	0.370

TDA 3 181005	1	1	est18101a.000	4.806	4.784	4.840	4.903	4.930	4.528	0.075	0.006					
Soaking protocol	4:1					4.947	4.739									
						4.762	4.868									
Scratch 4:1						4.798	4.733									
Blow with N2																
Scan with 15/AlBS tip		2	est18101a.002		4.568	4.755	4.685	5.019	4.399	0.148	0.022					
Tip holder 2	8:1					4.534	4.609									
						4.761	4.747									
						4.775	4.534					4.463	0.166	0.028		
	2	1	est18101a.003	4.839	4.414	4.543	4.267	4.508	4.185	0.297	0.088					
	8:1					4.968	4.039									
						4.759	4.045									
						4.513	4.445									
		2	est18101a.005	4.733	4.394	4.724	4.069	4.895	4.213	0.348	0.121					
	8:1					4.738	4.078									
						5.043	4.074									
						4.582	4.312					4.199	0.458	0.209	4.331	0.487

TDA (5 mM, 12 minutes)

Sample no and date prepared, Instrument	Scratch	Scan	File code	Thickness measured by section analysis Midpoint L	Midpoint R	L of scratch	R of scratch	Thickness measured by localised depth	Av. of scan minus 0.3 nm	Std. Dev. of scan	Var. of scan	Av. of scratch	Std. Dev. of scratch	Var. of scratch	Av. of sample	Std. Dev. or Error of sample
TDA 15704	1	1	est207041a.000	5.983	5.456	6.076	5.456	5.794	5.504	0.290	0.084					
						6.276	5.578									
Scratch 8:1						5.844	5.658									
Scan with scratch tip						6.169	5.549									
Scan 1:1																
Tip holder 2	2	1	est207041a.004	5.062	4.952	5.172	4.878	4.784	4.820	0.199	0.040					
						5.355	5.135									
						5.208	5.208									
						5.098	5.465								5.162	0.352

TDA (5 mM, 20 minutes)

Sample no and date prepared, Instrument	Scratch	Scan	File code	Thickness measured by section analysis				Thickness measured by localised depth	Av. of scan minus 0.3 nm	Std. Dev. of scan	Var. of scan	Av. of scratch	Std. Dev. of scratch	Var. of scratch	Av. of sample	Std. Dev. or Error of sample
				Midpoint L	Midpoint R	L of scratch	R of scratch									
TDA 23704	5	1	est126704.003	5.099	5.089	5.484	5.474	5.110	4.828	0.187	0.035					
						4.958	4.988									
Scratch 8:1						5.059	5.140									
Scan with scratch tip						4.917	5.094									
Scan 1:1																
Tip holder 2		2	est126704.004	5.023	5.344	5.066	5.263	4.901	4.881	0.148	0.022					
						5.197	5.355									
						5.208	5.170									
						5.359	5.108					4.855	0.238	0.057		
	7	1	et48041a.001	5.029	5.207	5.036	4.838	5.174	4.896	0.260	0.068					
						5.470	4.904									
						5.516	5.108									
						5.668	5.207									
		2	et48041a.002	5.174	5.099	5.562	5.624	4.799	4.967	0.257	0.066					
						5.174	5.037									
						5.424	5.212									
						5.587	5.249					4.932	0.366	0.134	4.893	0.436

DAD (5 mM, 1 scan)

Sample no and date prepared, Instrument	**Scratch**	**Scan**	**File code**	**Thickness measured by section analysis** Midpoint L	Midpoint R	L of scratch	R of scratch	**Thickness measured by localised depth**	**Av. of scan minus 0.3 nm**	**Std. Dev. of scan**	**Var. of scan**	**Av. of scratch**	**Std. Dev. of scratch**	**Var. of scratch**	**Av. of sample**	**Std. Dev. or Error of sample**
DAD 21205	1	1	1est222.002	1.248	1.198	1.359	1.52	1.064	0.934	0.134	0.018					
Attach FCA scan						1.205	1.091									
in PBS						1.118	1.161									
						1.279	1.332									
Scratch 8:1																
Scan with scratch tip		2	1est222.003	1.38	1.23	1.633	1.356	1.281	1.072	0.120	0.014					
Scan 8:1						1.515	1.291									
Tip holder 2						1.32	1.434									
						1.398	1.257					1.003	0.180	0.032		
DAD 2305	1	1	est231a.005	1.92	1.812	1.858	1.724	1.819	1.498	0.110	0.012					
Attach FCA						1.878	1.674									
DCC/DIPEA/DCM						1.671	1.612									
scan in NaClO4						1.933	1.877									
Scratch 8:1		2	est231a.006	1.901	1.723	1.877	1.901	1.739	1.559	0.110	0.012					
Scan with scratch tip						1.939	1.955									
Scan 8:1						1.804	1.716									
Tip holder 2						2.07	1.819					1.528	0.156	0.024		

DAD (5 mM, 1 minute)

Sample no and date prepared, Instrument	**Scratch**	**Scan**	**File code**	**Thickness measured by section analysis** Midpoint L	Midpoint R	L of scratch	R of scratch	**Thickness measured by localised depth**	**Av. of scan minus 0.3 nm**	**Std. Dev. of scan**	**Var. of scan**	**Av. of scratch**	**Std. Dev. of scratch**	**Var. of scratch**	**Av. of sample**	**Std. Dev. or Error of sample**
DAD 7305		1	1 est731a.009	1.911		1.824			1.568	0.154	0.024					
Attach FCA						2.026										
DCC/DIPEA/DCM						1.952										
scan in NaClO4						1.625										
Scratch 8:1		2	1 est731a.010	1.953		1.985			1.569	0.098	0.010					
Scan with scratch tip						1.768										
Scan 8:1						1.854										
Tip holder 2						1.783										
			2 est731a.012	2.06		1.997			1.679	0.084	0.007	1.624	0.129	0.017		
						2.056										
						1.891										
						1.892									1.596	0.201
DAD 21305		1	1 1est213.007	1.678	1.633	1.826	1.478	1.557	1.344	0.116	0.014					
Attach FCA						1.837	1.524									
DCC/DIPEA/DCM						1.691	1.543									
scan in NaClO4						1.632	1.68									
Scratch 8:1		2	1 est2131a.009	2.372	1.937	2.322	1.884	2.613	1.886	0.250	0.062					
Scan with scratch tip						2.391	2.005									
Scan 8:1						2.363	2.153									
Tip holder 2						2.176	1.827					1.615	0.276			

DAD (5 mM, 2 minutes)

Sample no and date prepared, Instrument	Scratch	Scan	File code	Thickness measured by section analysis: Midpoint L	Midpoint R	L of scratch	R of scratch	Thickness measured by localised depth	Av. of scan minus 0.3 nm	Std. Dev. of scan	Var. of scan	Av. of scratch	Std. Dev. of scratch	Var. of scratch	Av. of sample	Std. Dev. or Error of sample
DAD 25604	2	2	est03071a.004	1.459	1.310	1.757	1.674	1.488	1.222	0.161	0.026					
		NSC 14				1.745	1.355									
Scratch 8:1						1.575	1.488									
Scan 1:1						1.310	1.583									
Tip holder 2																
		3	est03071a.005	1.361	1.404	1.354	1.177	1.135	1.017	0.096	0.009					
		NSC 14				1.415	1.224									
						1.300	1.379									
						1.375	1.361					1.120	0.187	0.035		
	3	1	est137041a.000	1.569	1.445	1.564	1.599	1.656	1.280	0.104	0.011					
		scratch tip				1.549	1.733									
						1.609	1.480									
						1.743	1.435									
		2	est137041a.001	1.470	1.599	1.801	1.051	1.689	1.174	0.349	0.122					
		scratch tip				1.796	1.722									
						1.079	1.835									
						0.844	1.327									
		3	est137041a.002	1.677	1.561	1.716	1.264	1.575	1.218	0.214	0.046					
		scratch tip				1.405	1.629									
						1.624	1.532									
						1.016	1.702					1.224	0.422	0.178	1.172	0.462
DAD 23704	1	1	est2907041a.010	2.184	2.167	2.349	2.327	2.767	1.932	0.207	0.043					
						2.039	2.127									
Scratch 8:1						2.275	2.011									
Scan with scratch tip						2.167	2.139									
Scan 4:1																
Tip holder 2		2	est2907041a.011	2.306	2.215	2.415	2.296	2.519	1.990	0.161	0.026					
						2.371	2.326									
						2.445	2.146									
						2.219	1.934					1.961	0.262	0.069		

		3	1 est48041a.010	1.417	1.249	1.055	0.959	1.180	1.032	0.226	0.051					
						1.492	1.195									
						1.448	1.379									
						1.569	1.708									
			2 est48041a.011	1.452	1.422	1.472	1.170	1.548	1.231	0.285	0.081					
						1.352	1.149									
						1.830	1.843									
						2.075	1.529									
			3 est48041a.012	1.874	1.803	1.787	2.310	1.273	1.495	0.275	0.076					
						1.890	1.635									
						1.914	1.861									
						1.967	1.436					1.253	0.456	0.208	1.607	0.526
DAD 13205		1	1 est1421a.019	2.458	2.000	2.024	2.267		2.237	0.173	0.030					
Au NPs	8:1					2.458	2.24									
						2.302	2.014									
Scan with scratch tip						2.256	2.355									
Scan 8:1																
Tip holder 2			2 est1421a.020	1.907	1.610	1.579	1.610		1.700	0.145	0.021					
						1.808	1.947									
						1.740	1.576									
						1.687	1.539					1.969	0.226	0.051		

DAD (5 mM, 3 minutes)

Sample no and date prepared, Instrument	Scratch	Scan	File code	Thickness measured by section analysis Midpoint L	Midpoint R	L of scratch	R of scratch	Thickness measured by localised depth	Av. of scan minus 0.3 nm	Std. Dev. of scan	Var. of scan	Av. of scratch	Std. Dev. of scratch	Var. of scratch	Av. of sample	Std. Dev. or Error of sample
DAD 13205	1	1	1est142.004	3.503	2.755	3.284	2.829	3.303	3.115	0.313	0.098					
Au NPs	4:1					3.478	2.833									
						3.169	2.914									
Scan with scratch tip						3.481	2.711									
Scan 8:1																
Tip holder 2		2	1est142.006	3.425	3.706	3.092	3.815	3.557	3.543	0.254	0.064					
						3.444	3.899									
						3.405	3.656									
						3.21	3.759					3.329	0.403	0.162		

DAD (5 mM, 5 minutes)

Sample no and date prepared, Instrument	**Scratch**	**Scan**	**File code**	**Thickness measured by section analysis** Midpoint L	Midpoint R	L of scratch	R of scratch	**Thickness measured by localised depth**	**Av. of scan minus 0.3 nm**	**Std. Dev. of scan**	**Var. of scan**	**Av. of scratch**	**Std. Dev. of scratch**	**Var. of scratch**	**Av. of sample**	**Std. Dev. or Error of sample**
DAD 13205		1	1 1est142.000	4.263	4.308	4.131	4.295	4.240	4.305	0.093	0.009					
Au NPs	4:1					4.265	4.413									
						4.357	4.319									
Scan with scratch tip						4.276	4.486									
Scan 8:1																
Tip holder 2			2 1est142.001	4.010	4.063	3.915	3.762	4.126	4.059	0.160	0.026					
						4.063	4.037									
						4.031	4.421									
						4.154	4.066					4.182	0.185	0.034		
		2	1 1est142.002	3.868	3.88	4.005	3.786	3.767	3.832	0.078	0.006					
	8:1					3.852	3.868									
						3.833	3.711									
						3.762	3.825									
			2 est1421a.003	3.573	3.573	3.735	3.875	3.652	3.649	0.100	0.010					
						3.551	3.595									
						3.617	3.731									
						3.683	3.558					3.741	0.127	0.016	3.961	0.225

DAD (5 mM, 10 minutes)

Sample no and date prepared, Instrument	Scratch	Scan	File code	Thickness measured by section analysis				Thickness measured by localised depth	Av. of scan minus 0.3 nm	Std. Dev. of scan	Var. of scan	Av. of scratch	Std. Dev. of scratch	Var. of scratch	Av. of sample	Std. Dev. or Error of sample
				Midpoint L	Midpoint R	L of scratch	R of scratch									
DAD 15705		1	1 est227041a.000	5.800	5.971	5.708	6.057	5.750	5.630	0.231	0.053					
						5.600	5.902									
Scratch 8:1						6.125	6.422									
Scan with scratch tip						5.828	6.062									
Scan 1:1																
Tip holder 2			2 est227041a.001	5.796	5.554	5.761	5.623	5.456	5.396	0.211	0.044					
						5.865	5.313									
						5.865	5.692									
						6.072	5.658					5.513	0.313	0.098		
DAD 23705		1	1 est14804.001	6.864	6.274	6.953	6.466	6.324	6.267	0.319	0.102					
		4:1				6.784	6.368									
Scratch 8:1						6.864	6.143									
Scan with scratch tip						6.803	6.152									
Tip holder 2																
			2 est48041a.003	6.288	6.028	6.248	6.096	6.348	5.874	0.213	0.045					
		4:1				6.165	6.037									
						6.382	6.038									
						6.523	5.757					6.070	0.383	0.147		
		2	2 est48041a.007	6.67	6.507	6.32	6.435	6.739	6.330	0.208	0.043					
		4:1				6.435	6.646									
						6.906	6.845									
						6.492	6.933									
			3 est48041a.008	6.679	6.435	6.314	6.23	6.761	6.300	0.219	0.048					
		8:1				6.658	6.468									
						6.752	6.839									
						6.912	6.556					6.315	0.302	0.091	6.193	0.488

DAD 4 24805	1	1	est248051a.001	6.061	5.691	6.437	5.567	5.603	5.607	0.344	0.118						
Scanning						6.051	5.966										
						6.373	5.369										
Scratch 8:1						6.147	5.717										
Scan with scratch tip																	
Scan 8:1		2	est248051a.002	5.754	8.567-2.989	6.014	5.568	5.436	5.443	0.207	0.043						
Tip holder 2						6.06	5.717										
						5.717	5.606										
						5.958	5.596					5.525	0.402	0.161			
	2	2	est248051a.004	5.231	7.785-2.989	5.212	4.88	4.688	4.745	0.197	0.039						
						4.889	4.935										
						5.286	4.99										
						5.206	5.129								5.135	0.447	
DAD 5 24805	1	1	est248051a.005	4.578	4.542	4.728	4.507	4.561	4.367	0.137	0.019						
Scanning						4.651	4.92										
						4.564	4.876										
Scratch 8:1						4.679	4.73										
Scan with scratch tip																	
Scan 8:1		2	est248051a.006	5.250	4.749	5.257	4.896	5.088	4.799	0.237	0.056						
Tip holder 2						5.536	4.936										
						5.325	4.837										
						5.181	5.031					4.583	0.273	0.075			
	2	1	est248051a.007	5.221	5.342	5.185	5.314	5.114	4.963	0.162	0.026						
						5.524	5.506										
						5.04	5.214										
						5.354	5.074										
		2	est248051a.010	5.129	4.937	5.121	4.874	5.230	4.770	0.115	0.013						
						5.014	4.979										
						5.171	5.095										
						5.009	5.21					4.866	0.199	0.040	4.725	0.338	

DAD (5 mM, 12 minutes)

Sample no and date prepared, Instrument	Scratch	Scan	File code	Thickness measured by section analysis				Thickness measured by localised depth	Av. of scan minus 0.3 nm	Std. Dev. of scan	Var. of scan	Av. of scratch	Std. Dev. of scratch	Var. of scratch	Av. of sample	Std. Dev. or Error of sample
				Midpoint L	Midpoint R	L of scratch	R of scratch									
DAD 15705	1	2	est227041a.006	6.153	6.243	6.102	6.038	5.689	5.785	0.176	0.031					
						6.192	6.192									
Scratch 8:1						6.153	5.922									
Scan with scratch tip						6.307	5.948									
Scan 1:1																
Tip holder 2	2	1	est227041a.014	6.061	6.353	5.877	6.503	5.246	5.752	0.360	0.130					
						5.687	6.306									
						6.142	6.190									
						6.319	5.891								5.769	0.401

DAD (5 mM, 20 minutes)

Sample no and date prepared, Instrument	Scratch	Scan	File code	Thickness measured by section analysis				Thickness measured by localised depth	Av. of scan minus 0.3 nm	Std. Dev. of scan	Var. of scan	Av. of scratch	Std. Dev. of scratch	Var. of scratch	Av. of sample	Std. Dev. or Error of sample
				Midpoint L	Midpoint R	L of scratch	R of scratch									
DAD 27804		1	1 est278041a.000	5.788	5.384	5.270	5.980	5.549	5.292	0.316	0.100					
		4:1				5.697	5.521									
Scratch 8:1						6.003	5.241									
Scan with scratch tip						5.954	5.123									
Tip holder 2																
			2 est278041a.003	5.761	5.639	5.147	5.481	5.593	5.310	0.268	0.072					
		4:1				5.631	5.765									
						6.182	5.383									
						5.737	5.395					5.301	0.414	0.172		
		2	2 est278041a.007	4.869	4.524	4.754	4.754	4.568	4.451	0.155	0.024					
		4:1				4.984	4.524									
						4.912	4.783									
						4.840	4.754									
		3	1 est278041a.008	4.709	4.889	5.280	5.174	5.017	4.704	0.205	0.042					
		4:1				5.015	4.873									
						4.999	4.803									
						5.388	4.897									
			2 est278041a.009	4.796	4.596	5.369	4.596	4.642	4.677	0.351	0.123					
		4:1				4.958	4.628									
						4.984	5.401									
						5.401	5.377					4.691	0.407	0.165		
		4	1 est278041a.012	6.725	6.646	6.656	6.710	6.848	6.449	0.091	0.008					
		4:1				6.694	6.703									
						6.852	6.803									
						6.916	6.683									

		2 est278041a.013	6.890	6.640	6.820	6.944	6.835	6.637	0.240	0.057					
	4:1				7.386	6.701									
					7.325	7.021									
					7.005	6.737					6.543	0.256	0.066		
	5	1 est278041a.014	5.167	5.013	5.234	5.002	5.207	4.879	0.168	0.028					
	8:1				5.402	5.103									
					5.192	5.004									
					5.538	5.105								5.173	0.675
DAD 26105	1	1 est261051.008	7.878	7.058	7.281	7.747	8.709	7.281	0.571	0.326					
Attach *n* -dodecanoic					7.378	7.462									
acid					7.834	6.718									
					8.228	7.102									
Scratch 4:1															
Scan with scratch tip		2 est261051.010	6.137	5.310	6.333	6.268	6.379	5.738	0.481	0.231					
Scan 8:1					6.621	6.308									
Tip holder 2					5.133	5.960									
					6.351	5.617					6.510	0.747	0.557		

HA (5 mM, 10 minutes)

Sample no and date prepared, Instrument	Scratch	Scan	File code	Thickness measured by section analysis				Thickness measured by localised depth	Av. of scan minus 0.3 nm	Std. Dev. of scan	Var. of scan	Av. of scratch	Std. Dev. of scratch	Var. of scratch	Av. of sample	Std. Dev. or Error of sample
				Midpoint L	Midpoint R	L of scratch	R of scratch									
HA 5504	1	1	est12051.007	3.470	3.359	3.495	3.218	3.229	3.053	0.093	0.009					
						3.336	3.349									
Scratch 8:1						3.343	3.317									
Scan with NSC 14 tip						3.470	3.293									
Scan 1:1																
Tip holder 2		2	est12051.008	3.366	3.253	3.455	3.254	3.159	3.017	0.121	0.015					
						3.375	3.206									
						3.516	3.224									
						3.454	3.225									
		3	est12051.009	3.260	3.185	3.418	3.414	3.073	2.956	0.119	0.014					
						3.249	3.172									
						3.369	3.201									
						3.353	3.117					3.008	0.193	0.037		

TGD (5 mM, 2 minutes)

Sample no and date prepared, Instrument	Scratch	Scan	File code	Thickness measured by section analysis				Thickness measured by localised depth	Av. of scan minus 0.3 nm	Std. Dev. of scan	Var. of scan	Av. of scratch	Std. Dev. of scratch	Var. of scratch	Av. of sample	Std. Dev. or Error of sample
				Midpoint L	Midpoint R	L of scratch	R of scratch									
TGD 23804	1	1	est238041.001	4.010	3.782	3.838	3.191	3.775	3.502	0.224	0.050					
						3.922	3.894									
Scratch 8:1						3.894	3.670									
Scan with scratch tip						3.955	3.896									
Scan 4:1																
Tip holder 2		2	est238041.002	3.935	3.897	3.704	3.796	3.935	3.484	0.115	0.013					
						3.753	3.621									
						3.818	3.602									
						3.731	3.829									
		3	est238041.003	4.060	3.850	3.943	3.876	4.017	3.643	0.173	0.030					
						3.836	3.523									
						4.060	3.975									
						4.078	4.155					3.543	0.305	0.093		
	2	1	est238041.004	4.411	4.285	4.252	4.176	4.388	3.999	0.143	0.021					
						4.256	4.148									
						4.356	4.204									
						4.639	4.176									
		2	est238041.005	3.968	3.772	3.715	3.441	4.130	3.529	0.218	0.048					
						3.884	3.704									
						4.057	3.721									
						4.102	3.620					3.764	0.261	0.068	3.653	0.402

TGD (5 mM, 10 minutes)

Sample no and date prepared, Instrument	Scratch	Scan	File code	Thickness measured by section analysis				Thickness measured by localised depth	Av. of scan minus 0.3 nm	Std. Dev. of scan	Var. of scan	Av. of scratch	Std. Dev. of scratch	Var. of scratch	Av. of sample	Std. Dev. or Error of sample
				Midpoint L	Midpoint R	L of scratch	R of scratch									
TGD 3 29404	1	1	est05051.004	2.826	2.790	2.855	2.841	2.744	2.507	0.092	0.008					
						2.717	2.681									
Scratch 8:1						2.928	2.739									
Scan with NSC 14 tip						2.986	2.775									
Scan 1:1																
Tip holder 2																
TGD	1	1	est248041.005	3.193	2.933	3.150	3.054	3.338	2.719	0.370	0.137					
						2.043	3.199									
Scratch 8:1						3.364	2.996									
Scan with scratch tip						3.191	2.746									
Scan 4:1																
Tip holder 2		2	est248041.006	3.016	3.010	3.516	2.898	3.124	2.835	0.188	0.035					
						3.045	3.437									
						3.207	3.067									
						3.150	3.019					2.777	0.415			

PGD (50 mM, 10 minutes)

Sample no and date prepared, Instrument	Scratch	Scan	File code	Thickness measured by section analysis				Thickness measured by localised depth	Av. of scan minus 0.3 nm	Std. Dev. of scan	Var. of scan	Av. of scratch	Std. Dev. of scratch	Var. of scratch	Av. of sample	Std. Dev. or Error of sample
				Midpoint L	Midpoint R	L of scratch	R of scratch									
PGD 2 19404	1	1	est1904.004	5.345	5.336	5.275	5.120	5.459	5.010	0.093	0.009					
						5.371	5.258									
Scratch 8:1						5.423	5.241									
Scan with NSC 14 tip						5.319	5.267									
Scan 1:1																
Tip holder 2		2	est2004.008	5.390	5.651	5.419	5.779	5.634	5.256	0.184	0.034					
						5.207	5.715									
						5.345	5.622									
						5.631	5.720					5.133	0.207	0.042695		

Sonication

i pa after sonication/*i* pa as-prepared GC rod

			Av.	**Std. Dev.**
TDA	0.1 M HNO3	0.601		
		0.614		
		0.434		
		0.399	0.512	0.11
	0.1 M NaOH	0.192		
		0.049		
		0.124	0.122	0.07
	MQ water	0.250		
		0.248		
		0.159		
		0.182	0.210	0.05
	ACN	0.312		
		0.242	0.277	0.05
DAD	0.1 M HNO3	0.708		
		0.712		
		0.760		
		0.734	0.729	0.02
	0.1 M NaOH	No change		
		0.122		
		0.211	0.167	0.06
	MQ water	No change		
		0.088	0.088	0.00
	ACN	No change		
		No change		

	TDA		**DAD**	
HNO3	0.51, 0.40-0.61	0.51 ± 0.11	0.73, 0.71-0.76	0.73 ± 0.02
NaOH	0.12, 0.05-0.20	0. 12 ± 0.07	0.17, 0.12-0.21	0.17 ± 0.06
MQ water	0.21, 0.16-0.25	0.21 ± 0.05	0.09	0.09 ± 0
ACN	0.28, 0.24-0.31	0.28 ± 0.05	no change	no change

In HNO3

	TDA		DAD	
Time/minutes	**Sample 1**	**Sample 2**	**Sample 1**	**Sample 2**
0.5	0.146	0.052	0.411	0.487
2	0.283	0.222	0.582	0.571
5	0.287	0.314	0.608	0.654
10	0.434	0.399	0.76	0.734
20	0.446	0.485	0.63	0.697
60	0.749	0.722	0.46	0.652

	TDA HNO3		MQ water	
Time/minutes	**Sample 1**	**Sample 2**	**Sample 1**	**Sample 2**
0.5	0.146	0.052	0.077	0.123
2	0.283	0.222	0.172	0.140
5	0.287	0.314	0.132	0.151
10	0.434	0.399	0.159	0.182
20	0.446	0.485	0.163	0.209
60	0.749	0.722	0.385	0.222

Surface coverage of FCA electrostatically attached to TDA and DAD layers without coupling agent EDCI ('blank' experiments)

				0.1	96485	0.24
		FCA -> FCA+ (1e-)	FCA+ -> FCA	/ SR (0.1 Vs-1)	/ F (96485 Cmol-1)	/electrode geometric area PPF (0.24 cm2)
	Linkfit Peak	Oxidation Peak	Reduction Peak	SR = scan rate	F = Faraday's constant	FCA surface coverage (molcm-2)
TDA						
1 minute 30305	Integrated Area	2.1743E-07	3.0468E-07			
Average of 2 'blank' samples	Peak Fit Total Area	2.2235E-07	3.0968E-07			
1st scan out of 10		3rd order	3rd order			
Scans in 0.1 M NaClO4	Total Area	2.1989E-07	3.0718E-07			
	ipa / ipc	7.1583E-01				
	Total Area of the Red. and Ox. / 2	2.6354E-07		2.6354E-06	2.7314E-11	1.1381E-10
DAD						
1 minute 30305	Integrated Area	4.3451E-07	1.2350E-07			
Average of 2 'blank' samples	Peak Fit Total Area	4.3547E-07	9.2113E-08			
1st scan out of 10		2nd order	2nd order			
Scans in 0.1 M NaClO4	Total Area	4.3499E-07	1.0781E-07			
	ipa / ipc	4.035E+00				
	Total Area of the Red. and Ox. / 2	2.7140E-07		2.7140E-06	2.8129E-11	1.1720E-10

Surface coverage of FCA attached to TDA and DAD layers using coupling agent DCC
Surface coverage of actual sample - surface coverage of 'blank' experiments (without DCC) => only COVALENT ATTACHED Fc calculated.

				0.1	96485	0.24	
		FCA -> FCA+ (1e-)	FCA+ -> FCA	/ SR (0.1 Vs-1)	/ F (96485 Cmol-1)	/electrode geometric area PPF (0.24 cm2)	Minus 'blank'
	Linkfit Peak	Oxidation Peak	Reduction Peak	SR = scan rate	F = Faraday's constant	FCA surface coverage (molcm-2)	
TDA							
1 minute 21305	Integrated Area	6.7340E-09	7.8773E-09				
Average of 2 blank samples	Peak Fit Total Area	7.0335E-09	8.0802E-09				
1st scan out of 10		3rd order	3rd order				
Scans in 0.1 M NaClO4	Total Area	6.8838E-09	7.9788E-09				
	ipa / ipc	8.6276E-01					
	Total Area of the Red. and Ox. / 2	7.4313E-09		7.4313E-08	7.7020E-13	3.2092E-12	
1 minute 1 7305	Integrated Area	1.3325E-07	6.43360E-08				
1st scan out of 10	Peak Fit Total Area	1.3488E-07	6.73330E-08				
Scans in 0.1 M NaClO4		3rd order	3rd order				
Not normalised for blanks	Total Area	1.3407E-07	6.5835E-08				
	ipa / ipc	2.0364E+00					
	Total Area of the Red. and Ox. / 2	9.9950E-08		9.9950E-07	1.0359E-11	4.3163E-11	3.9954E-11
1 minute 2 7305	Integrated Area	2.5685E-07	1.71880E-07				
1st scan out of 10	Peak Fit Total Area	2.5827E-07	1.72570E-07				
Scans in 0.1 M NaClO4		2nd order	3rd order				
Not normalised for blanks	Total Area	2.5756E-07	1.7223E-07				
	ipa / ipc	1.4955E+00					
	Total Area of the Red. and Ox. / 2	2.1489E-07		2.1489E-06	2.2272E-11	9.2800E-11	8.9591E-11
						Average	6.4773E-11

DAD

1 minute 21305	Integrated Area		3.3069E-08	2.1723E-08				
Average of 2 blank samples	Peak Fit Total Area		3.3399E-08	2.1537E-08				
1st scan out of 10		2nd order		3rd order				
Scans in 0.1 M NaClO4	Total Area		3.3234E-08	2.1630E-08				
	ipa / ipc		1.536E+00					
	Total Area of the Red. and Ox. / 2		2.7432E-08		2.7432E-07	2.8431E-12	1.1846E-11	
1 minute 21305	Integrated Area		3.0891E-07	2.4162E-07				
1st scan out of 10	Peak Fit Total Area		3.1124E-07	2.4262E-07				
Scans in 0.1 M NaClO4		3rd order		3rd order				
Not normalised for blanks	Total Area		3.1008E-07	2.4212E-07				
	ipa / ipc		1.2807E+00					
	Total Area of the Red. and Ox. / 2		2.7610E-07		2.7610E-06	2.8616E-11	1.1923E-10	1.0739E-10
1 minute 7305	Integrated Area		2.3737E-07	2.6904E-07				
1st scan out of 10	Peak Fit Total Area		2.3963E-07	2.6957E-07				
Scans in 0.1 M NaClO4		3rd order		3rd order				
Not normalised for blanks	Total Area		2.3850E-07	2.6931E-07				
	ipa / ipc		8.8561E-01					
	Total Area of the Red. and Ox. / 2		2.5390E-07		2.5390E-06	2.6315E-11	1.0965E-10	9.7800E-11
1 minute 7305	Integrated Area		3.8140E-07	2.1423E-07				
96 hours of FCA coupling,	Peak Fit Total Area		3.8341E-07	2.1766E-07				
and slow scan rate		3rd order		3rd order				
1st scan out of 10	Total Area		3.8241E-07	2.1595E-07				
Scans in 0.1 M NaClO4	ipa / ipc		1.7708E+00					
Not normalised for blanks								
	Total Area of the Red. and Ox. / 2		2.9918E-07		2.9918E-06	3.1007E-11	1.2920E-10	1.1735E-10
							Average	1.0751E-10
							Std. Dev.	9.7760E-12

NPEA (5 mM, 1 minute)

Sample no and date prepared, Instrument	Scratch	Scan	File code	Thickness measured by section analysis Midpoint L	Midpoint R	L of scratch	R of scratch	Thickness measured by localised depth	Av. of scan minus 0.3 nm	Std. Dev. of scan	Var. of scan	Av. of scratch	Std. Dev. of scratch	Var. of scratch	Av. of sample	Std. Dev. or Error of sample
NPEA 20904	3	1	est289041a.001	1.013	0.928	1.139	0.836	1.000	0.668	0.110	0.012					
ACN reduced						1.069	0.811									
3 scans 20904						1.058	1.046									
Acid reduced 20904						0.918	0.834									
Scratch 8:1		2	est289041a.002	1.004	0.894	0.972	1.001	0.763	0.639	0.101	0.010					
Scan with scratch tip			top part of			1.107	0.969									
Scan 4:1			image			0.833	1.028									
Tip holder 2						0.838	0.916									
			bottom part of	1.080	1.019	1.154	0.987	1.171	0.764	0.098	0.010					
			image			1.247	1.094									
						1.049	0.919									
						0.964	1.017					0.690	0.178	0.032		

NPEA (5 mM, 2 minutes)

Sample no and date prepared, Instrument	Scratch	Scan	File code	Thickness measured by section analysis Midpoint L	Midpoint R	L of scratch	R of scratch	Thickness measured by localised depth	Av. of scan minus 0.3 nm	Std. Dev. of scan	Var. of scan	Av. of scratch	Std. Dev. of scratch	Var. of scratch	Av. of sample	Std. Dev. or Error of sample
NPEA 31804	1	1	1et10904.011	2.270	2.523	2.162	2.381	2.29	2.006	0.095	0.009					
Acid reduced 31804						2.270	2.306									
						2.237	2.325									
Scratch 8:1						2.234	2.372									
Scan with 15/AlBS tip																
Scan 4:1		2	1et10904.012	2.529	2.574	2.303	2.377	2.334	2.142	0.121	0.015					
Tip holder 2						2.307	2.688									
						2.426	2.383									
						2.446	2.499					2.074	0.154	0.024		
	2	1	1et10904.013	2.083	2.292	2.094	2.364	2.655	2.019	0.187	0.035					
						2.183	2.455									
						2.147	2.532									
						2.432	2.277									
		2	1et10904.014	2.263	2.545	2.348	2.518	2.615	2.124	0.135	0.018					
						2.229	2.581									
						2.417	2.457									
						2.261	2.431					2.072	0.230	0.053	2.073	0.277

NPEA (5 mM, 10 minutes)

Sample no and date prepared, Instrument	Scratch	Scan	File code	Thickness measured by section analysis Midpoint L	Midpoint R	L of scratch	R of scratch	Thickness measured by localised depth	Av. of scan minus 0.3 nm	Std. Dev. of scan	Var. of scan	Av. of scratch	Std. Dev. of scratch	Var. of scratch	Av. of sample	Std. Dev. or Error of sample
NPEA 1 31804	1	1	1et10904.007	3.790	3.645	3.931	3.904	3.615	3.542	0.161	0.026					
Acid reduced 31804						3.743	3.659									
						4.105	3.919									
Scratch 8:1						4.008	3.941									
Scan with 15/AlBS tip																
Scan 4:1		2	1et109041a.008	3.803	3.564	3.768	3.591	3.620	3.434	0.144	0.021					
Tip holder 2						3.629	3.599									
						3.939	3.737									
						3.857	3.965					3.488	0.216	0.047		
	2	1	1et109041a.009	3.208	3.164	3.076	3.160	2.823	2.852	0.175	0.031					
						3.544	3.261									
						3.088	3.019									
						3.149	3.182									
		2	1et109041a.010	3.281	3.192	3.436	3.304	2.792	2.948	0.178	0.032					
						3.261	3.454									
						3.255	3.342									
						3.277	3.132					2.900	0.249	0.062	3.194	0.330
NPEA 2 31804	1	1	1et10904.017	4.171	4.422	4.456	4.205	4.401	3.981	0.159	0.025					
Acid reduced 31804						3.997	4.377									
						4.270	4.405									
Scratch 8:1						4.038	4.350									
Scan with 15/AlBS tip																
Scan 4:1		2	1et10904.018	3.966	4.388	4.192	4.260	4.662	3.962	0.182	0.033					
Tip holder 2						4.184	4.229									
						4.076	4.400									
						4.292	4.232					3.972	0.241	0.058		

	2	1 1et10904.019	3.931	4.035	3.908	4.226	4.334	3.778	0.166	0.027					
					3.846	4.113									
					4.090	4.308									
					3.925	4.138									
		2 1et10904.020	3.763	4.351	4.405	4.602	4.417	3.917	0.299	0.089					
					3.892	4.453									
					3.946	4.362									
					3.816	4.381					3.847	0.341	0.117	3.909	0.418
NPEA 8904	1	1 em1909941a.000	2.740	2.952	2.545	3.179	2.318	2.438	0.245	0.060					
Acid reduced 8904		Scratch tip			2.811	2.519									
		2:1			2.779	2.619									
Scratch 8:1					3.003	2.650									
Tip holder 2															
		2 em1909941a.001	3.517	3.014	3.383	2.703	2.714	2.793	0.267	0.071					
		Scratch tip			3.073	3.176									
		2:1			3.402	3.028									
					3.113	2.895					2.615	0.362	0.131		
	2	1 em1909941a.002	2.689	2.782	2.268	3.016	2.295	2.338	0.254	0.064					
		15/AlBS tip			2.619	2.829									
		4:1			2.595	2.806									
					2.291	2.829									
		2 em1909941a.003	2.714	2.367	2.770	2.525	2.409	2.298	0.198	0.039					
		15/AlBS tip			2.856	2.383									
		4:1			2.714	2.354									
					2.859	2.624					2.318	0.322	0.104	2.467	0.485

NPEA (5 mM, 15 minutes)

Sample no and date prepared, Instrument	Scratch	Scan	File code	Thickness measured by section analysis Midpoint L	Midpoint R	L of scratch	R of scratch	Thickness measured by localised depth	Av. of scan minus 0.3 nm	Std. Dev. of scan	Var. of scan	Av. of scratch	Std. Dev. of scratch	Var. of scratch	Av. of sample	Std. Dev. or Error of sample
NPEA 20904	3	1	est240901a.000	3.700	3.734	3.937	3.677	3.493	3.305	0.204	0.042					
Acid reduced 23904						3.315	3.575									
						3.553	3.632									
Scratch 8:1						3.236	3.802									
Scan with 2nd longest																
12/AlBS tip		2	est240901a.001	4.174	4.208	4.289	4.754	4.150	4.050	0.195	0.038					
Scan 4:1						4.368	4.148									
Tip holder 2						4.301	4.557									
						4.539	4.364									
		3	est240901a.002	4.302	4.105	4.122	3.998	3.611	3.786	0.212	0.045					
						3.977	3.977									
						4.050	4.105									
						4.312	4.388					3.714	0.353	0.125		
	5	1	est240901a.003	4.030	4.155	4.147	4.400	3.701	3.566	0.314	0.099					
						3.882	3.579									
						4.022	3.706									
						3.522	3.382									
		2	est240901a.004	3.569	4.058	3.838	3.643	3.335	3.456	0.302	0.091					
						4.132	3.258									
						4.040	3.575									
						3.832	4.040									
		3	est240901a.005	3.816	3.356	3.798	2.934	3.047	3.159	0.369	0.136					
						4.095	3.356									
						3.791	3.307									
						3.418	3.126					3.394	0.571	0.326	3.554	0.671

NPEA 10605	1	1 est116051a.009	3.941	3.964	4.091	3.865	3.976	3.691	0.111	0.012						
Acid reduced 11605					4.178	3.841										
					4.038	4.152										
Scratch 8:1					3.924	3.935										
Scan with scratch tip																
Scan 8:1		2 est116051a.010	4.171	3.969	4.176	4.091	4.186	3.831	0.097	0.009						
Tip holder 2					4.153	4.017										
					4.330	4.140										
					4.161	4.052					3.761	0.147	0.022			
	2	1 est116051a.011	4.322	4.214	4.417	4.150	4.400	3.972	0.106	0.011						
					4.274	4.240										
					4.380	4.102										
					4.322	4.168										
		2 est116051a.012	4.082	3.920	4.044	4.063	3.944	3.760	0.099	0.010						
					4.091	3.958										
					4.138	4.034										
					4.261	4.128					3.866	0.145	0.021	3.814	0.207	

NPEA (5 mM, 20 minutes)

Sample no and date prepared, Instrument	Scratch	Scan	File code	Thickness measured by section analysis Midpoint L	Midpoint R	L of scratch	R of scratch	Thickness measured by localised depth	Av. of scan minus 0.3 nm	Std. Dev. of scan	Var. of scan	Av. of scratch	Std. Dev. of scratch	Var. of scratch	Av. of sample	Std. Dev. or Error of sample
NPEA 31804	1	1	1est10904.003	6.307	6.113	6.268	6.264	6.716	6.043	0.209	0.044					
Acid reduced 31804						6.575	6.198									
						6.299	6.556									
Scratch 8:1						6.027	6.445									
Scan with 15/AlBS tip																
Scan 4:1		2	1est10904.004	6.249	6.405	6.052	6.440	6.757	5.998	0.201	0.040					
Tip holder 2						6.405	6.154									
						6.112	6.290									
						6.118	6.296					6.020	0.290	0.084		
	2	1	1est10904.005	5.982	5.774	6.257	6.420	5.536	5.882	0.445	0.198					
						6.133	5.756									
						6.829	6.268									
						6.996	6.049									
		2	1et10904.006	5.742	5.517	5.813	5.909	5.441	5.548	0.354	0.125					
						5.863	6.661									
						6.282	5.710									
						5.544	5.849					5.715	0.568	0.323	5.868	0.638

NPEA (5 mM, 25 minutes)

Sample no and date prepared, Instrument	Scratch	Scan	File code	Thickness measured by section analysis: Midpoint L	Midpoint R	L of scratch	R of scratch	Thickness measured by localised depth	Av. of scan minus 0.3 nm	Std. Dev. of scan	Var. of scan	Av. of scratch	Std. Dev. of scratch	Var. of scratch	Av. of sample	Std. Dev. or Error of sample
NPEA 2605	1	1	est36051a.000	6.781	7.060	6.638	6.916	6.721	6.568	0.220	0.049					
Acid reduced 3605						6.778	6.956									
						6.821	7.322									
Scratch 8:1						6.531	7.029									
Scan with scratch tip																
Scan 8:1		2	est36051a.001	6.944	6.955	7.086	6.987	6.921	6.649	0.157	0.024					
Tip holder 2						7.153	6.902									
						6.823	6.905									
						7.156	6.604					6.609	0.270	0.073		
	2	1	est36051a.002	5.608	5.201	5.372	5.201	5.305	5.027	0.233	0.054					
						5.420	5.378									
						5.756	4.912									
						5.361	5.084									
		2	est36051a.003	4.793	4.648	4.885	4.897	4.679	4.465	0.135	0.018					
						4.800	4.681									
						4.819	4.458									
						4.878	4.871					4.746	0.269	0.072	5.677	0.381

NPEA (5 mM, 15 minutes)

Sample no and date prepared, Instrument	Scratch	Scan	File code	Thickness measured by section analysis Midpoint L	Midpoint R	L of scratch	R of scratch	Thickness measured by localised depth	Av. of scan minus 0.3 nm	Std. Dev. of scan	Var. of scan	Av. of scratch	Std. Dev. of scratch	Var. of scratch	Av. of sample	Std. Dev. or Error of sample
NPEA 20904	3	2	em220904.001	5.617	5.206	5.765	5.785	5.641	5.399	0.262	0.069					
Not reduced						5.651	5.927									
						5.388	6.082									
Scratch 8:1						6.035	5.592									
Scan with 2nd longest																
12/AlBS tip																
Scan 4:1																
Tip holder 2																
NPEA (5 mM, 25 minutes)																
NPEA 2605	1	1	est26051a.000	8.596	8.511	8.545	8.444	8.602	8.290	0.124	0.015					
Not reduced						8.562	8.596									
						8.849	8.427									
Scratch 8:1						8.764	8.596									
Scan with scratch tip																
Scan 8:1		2	est26051a.001	8.986	8.813	8.758	8.979	8.885	8.602	0.117	0.014					
Tip holder 2						8.711	9.040									
						8.820	8.986									
						8.887	9.061					8.446	0.171	0.029		
	2	1	est26051a.002	8.474	8.614	8.614	8.544	8.780	8.361	0.120	0.014					
						8.544	8.647									
						8.649	8.824									
						8.824	8.754									
		2	est26051a.003	7.794	7.843	7.796	8.008	7.923	7.633	0.116	0.013					
						7.826	7.986									
						8.088	8.075									
						7.851	8.068					7.997	0.167	0.028	8.221	0.239

NPEA (5 mM, 15 minutes)																
NPEA 10605	1	1 est116051a.006	5.684	5.587	5.617	5.703	5.734	5.378	0.089	0.008						
Not reduced					5.729	5.672										
					5.761	5.713										
Scratch 8:1					5.785	5.476										
Scan with scratch tip																
Scan 8:1		2 est116051a.007	5.773	5.377	5.782	5.744	5.610	5.317	0.138	0.019						
Tip holder 2					5.736	5.492										
					5.683	5.467										
					5.604	5.524					5.348	0.164	0.027			
	2	1 est116051a.004	5.316	5.243	5.670	5.308	5.219	5.055	0.152	0.023						
					5.541	5.338										
					5.219	5.424										
					5.450	5.178										
		2 est116051a.005	5.688	5.577	5.541	5.706	5.694	5.448	0.157	0.025						
					5.827	5.761										
					6.030	5.859										
					5.954	5.591					5.252	0.219	0.048	5.300	0.273	

NPEA (5 mM, 25 minutes)

Sample no and date prepared, Instrument	Scratch	Scan	File code	Thickness measured by section analysis Midpoint L	Midpoint R	L of scratch	R of scratch	Thickness measured by localised depth	Av. of scan minus 0.3 nm	Std. Dev. of scan	Var. of scan	Av. of scratch	Std. Dev. of scratch	Var. of scratch	Av. of sample	Std. Dev. or Error of sample
NPEA 2605	1	1	est86051a.000	5.632	5.320	5.656	5.770	5.628	5.219	0.206	0.043					
Acid reduced 3605						5.763	5.275									
Reversing reduction						5.628	5.159									
1. 20 scans in						5.496	5.381									
ACN/0.1 M $[Bu_4N]BF_4$																
0 to 0.4 V 7605		2	est86051a.002	4.879	5.266	5.091	5.228	5.043	4.778	0.147	0.022					
						4.918	5.152									
Scratch 8:1						4.933	5.219									
Scan with scratch tip						4.916	5.216					4.999	0.253	0.064		
Scan 8:1																
Tip holder 2	2	1	est86051a.003	4.374		4.144		4.283	3.975	0.107	0.012					
						4.421										
						4.250										
						4.180										
		2	est86051a.004	4.657	4.666	4.666	4.684	4.573	4.376	0.064	0.004					
						4.633	4.740									
						4.591	4.731									
						4.703	4.792					4.176	0.125	0.016	4.587	0.283
2. then modification	2	1	est116051a.013	4.535	4.454	4.330	4.474	4.639	4.197	0.089	0.008					
conditions without						4.538	4.581									
modifier 11605						4.394	4.555									
						4.443	4.529									
		2	est116051a.015	4.287	4.277	4.305	4.301	4.178	4.037	0.183	0.034					
						4.449	4.848									
						4.283	4.188									
						4.278	4.310					4.117	0.204	0.041		

NPEA (5 mM, 15 minutes)															
NPEA 10605	1	1 est116051a.016	3.007	2.846	3.021	2.929	3.016	2.684	0.086	0.007					
Acid reduced 11605					3.061	2.962									
Reversing reduction					3.076	2.916									
modification					3.115	2.875									
conditions without															
modifier 11605		2 est116051a.017	2.878	2.660	2.918	2.696	2.938	2.508	0.110	0.012					
					2.860	2.660									
Scratch 8:1					2.852	2.791									
Scan with scratch tip					2.932	2.704					2.596	0.140	0.020		
Scan 8:1															
Tip holder 2	2	1 est116051a.018	3.351	3.055	3.188	3.117	3.354	2.920	0.141	0.020					
					3.251	3.066									
					3.382	3.100									
					3.441	3.116									
		2 est116051a.019	3.213	2.979	3.131	3.065	3.219	2.807	0.101	0.010					
					3.213	3.120									
					3.158	2.937									
					2.992	3.156					2.864	0.173	0.030	2.730	0.222

NPEA layers

Reduction in 0.1 M H2SO4, 0.6 V to -1.0 V

					0.1	96485	0.24
		NO2->NH2 (6e-)/NHOH (4e-)		NHOH->NO (2e-)	/ SR (0.1 Vs-1)	/ F (96485 Cmol-1)	/electrode geometric area PPF (0.24 cm2)
	Linkfit curves	Reduction Peak		Oxidation Peak	SR = scan rate	F = Faraday's constant	**NPEA surface coverage (molcm-2)**
1 min (sample 1)		1	1.840E-06	5.846E-07			
		2	1.270E-06	1.140E-07			
		3	2.453E-07				
	Total Area		3.355E-06	6.986E-07			
	Sum of Variance		1.294E-11	7.570E-12			
	Std. Dev.		3.597E-06	2.751E-06			
	Total Area of the Red. and Ox. / 6e-		6.756E-07		6.756E-06	7.002E-11	2.92E-10
2 min (sample 1)		1	5.283E-06	1.02E-06			
		2	8.605E-07	8.05E-07			
		3	5.856E-07				
		4	1.578E-07				
	Total Area		6.887E-06	1.83E-06			
	Sum of Variance		4.186E-11	2.44E-12			
	Std. Dev.		6.470E-06	1.56E-06			
	Total Area of the Red. and Ox. / 6e-		1.452E-06		1.452E-05	1.505E-10	6.27E-10
2 min (sample 2)		1	1.561E-06	2.447E-06			
		2	2.914E-06	3.129E-06			
		3	1.079E-07	8.838E-07			
		4		9.600E-08			
	Total Area		4.583E-06	6.556E-06			
	Sum of Variance		5.192E-11	1.409E-10			
	Std. Dev.		7.206E-06	1.187E-05			
	Total Area of the Red. and Ox. / 6e-		1.857E-06		1.857E-05	1.924E-10	8.02E-10

10 min (sample 1)		1	6.951E-06	5.731E-07			
		2	1.150E-06	1.921E-08			
		3	1.510E-06	8.504E-08			
	Total Area of Peaks		9.611E-06	6.773E-07			
	Sum of Variance		1.351E-10	2.995E-12			
	Std. Dev.		1.162E-05	1.731E-06			
	Total Area of the Red. and Ox. / 6e-		1.715E-06		1.715E-05	1.777E-10	7.41E-10
10 min (sample 3)		1	1.002E-05	8.317E-07			
		2	2.695E-06	2.131E-07			
		3	7.034E-07				
	Total Area of Peaks		1.342E-05	1.045E-06			
	Sum of Variance		9.725E-11	1.494E-12			
	Std. Dev.		9.861E-06	1.222E-06			
	Total Area of the Red. and Ox. / 6e-		2.411E-06		2.411E-05	2.499E-10	1.04E-09
15 min (sample 3)		1	2.969E-06	9.767E-07			
		2	4.918E-06	1.123E-06			
		3	9.650E-07				
	Total Area of Peaks		8.851E-06	2.100E-06			
	Sum of Variance		1.206E-10	9.241E-12			
	Std. Dev.		1.098E-05	3.040E-06			
	Total Area of the Red. and Ox. / 6e-		1.825E-06		1.825E-05	1.892E-10	7.88E-10
15 min (10605)		1	Added up total areas of peaks in LinkFit				
		2					
	Total Area of Peaks		7.052E-06	1.148E-06			
	Sum of Variance		1.775E-11	8.129E-12			
	Std. Dev.		4.213E-06	2.851E-06			
	Total Area of the Red. and Ox. / 6e-		1.367E-06		1.367E-05	1.416E-10	5.90E-10

20 min (sample 1)		1	4.407E-06	3.131E-07			
		2	7.896E-07	4.225E-07			
		3	3.754E-07				
	Total Area of Peaks		5.572E-06	7.356E-07			
	Sum of Variance		1.256E-11	8.062E-12			
	Std. Dev.		3.544E-06	2.839E-06			
	Total Area of the Red. and Ox. / 6e-		1.051E-06		1.051E-05	1.090E-10	4.54E-10
25 min (2605)		1	Added up total areas of peaks in LinkFit				
		2					
		3					
	Total Area		3.884E-06	3.431E-06			
	Sum of Variance		1.829E-11	7.718E-12			
	Std. Dev.		4.277E-06	2.778E-06			
	Total Area of the Red. and Ox. / 6e-		1.219E-06		1.219E-05	1.264E-10	5.27E-10

Reduction in ACN/0.1 M TBABF4, -0.5 V to -2 V

		NO2->NO2.-		NO2.- -> NO2	/ SR (0.1 Vs-1)	/ F (96485 Cmol-1)	/electrode geometric area PPF (0.24 cm2)
	Linkfit curves	Reduction Peak		Oxidation Peak	SR = scan rate	F = Faraday's constant	**NPEA surface coverage (molcm-2)**
1 min (sample 1)		1	6.236E-07	2.652E-06			
		2	2.090E-06	1.229E-06			
		3	8.018E-07				
	Total Area of Peaks		3.516E-06	3.881E-06			
	Sum of Variance		4.611E-11	1.832E-11			
	Std. Dev.		6.791E-06	4.281E-06			
	Total Area of the Red. and Ox. / 2e-		3.698E-06		3.698E-05	3.833E-10	1.60E-09
5 min (sample 1)		1	1.930E-06	5.105E-06			
		2	2.411E-06	8.487E-08			
		3	5.324E-07	1.439E-07			
	Total Area of Peaks		4.873E-06	5.334E-06			
	Sum of Variance		5.205E-11	3.125E-10			
	Std. Dev.		7.215E-06	1.768E-05			
	Total Area of the Red. and Ox. / 2e-		5.103E-06		5.103E-05	5.289E-10	2.20E-09

5 min (sample 2)		1	1.470E-06	4.326E-06			
		2	1.525E-06	2.786E-07			
		3					
	Total Area of Peaks		2.995E-06	4.604E-06			
	Sum of Variance		1.081E-10	7.089E-10			
	Std. Dev.		1.040E-05	2.662E-05			
	Total Area of the Red. and Ox. / 2e-		3.800E-06		3.800E-05	3.938E-10	1.64E-09
10 min (151204)		1 Raw data lost					
		2					
		3					
	Total Area of Peaks						
	Sum of Variance						
	Std. Dev.						
	Total Area of the Red. and Ox. / 2e-						2.44E-09
15 min (sample 1)		1	3.114E-06	5.697E-06			
		2	3.644E-06	1.225E-06			
		3	6.241E-07				
	Total Area of Peaks		7.382E-06	6.922E-06			
	Sum of Variance		1.051E-10	2.302E-10			
	Std. Dev.		1.025E-05	1.517E-05			
	Total Area of the Red. and Ox. / 2e-		7.152E-06		7.152E-05	7.412E-10	3.09E-09
20 min (sample 2)		1	2.695E-06	7.705E-06			
		2	3.237E-06	7.845E-06			
		3	6.079E-07				
	Total Area of Peaks		6.539E-06	1.555E-05			
	Sum of Variance		9.355E-11	6.041E-10			
	Std. Dev.		9.672E-06	2.458E-05			
	Total Area of the Red. and Ox. / 2e-		1.104E-05		1.104E-04	1.145E-09	4.77E-09

GC rod		0.07					
10 mins (151204)		1 Added up total areas of peaks in LinkFit					
		2					
		3					
	Total Area		1.743E-06	7.125E-07			
	Sum of Variance		5.731E-13	8.310E-13			
	Std. Dev.		7.570E-07	9.116E-07			
	Total Area of the Red. and Ox. / 2e-		1.228E-06		1.228E-05	1.272E-10	1.82E-09

Appendix 5.

Water contact angles

MP on PPF (5 mM, electrolysis time 10 minutes)

Surface 1
Drop 1
Left of drop 63 64 66
Right of drop 65 65 63

Drop 2
Left of drop 64 64 67
Right of drop 64 65 65

Surface 2
Drop 1
Left of drop 66 66 65
Right of drop 63 66 66

Drop 2
Left of drop 67 69 68
Right of drop 65 65 66 **65 ± 4**

MP on GC plate (5 mM, electrolysis time 10 minutes)

Surface 1
Drop 1
Left of drop 61 64 65
Right of drop 62 63 63

Drop 2
Left of drop 65 65 65
Right of drop 62 61 64

Surface 2
Drop 1
Left of drop 62 63 61
Right of drop 62 64 62

Drop 2
Left of drop 65 63 62
Right of drop 65 63 66 **63 ± 3**

HP on GC plate (5 mM, electrolysis time 10 minutes)

Surface 1
Drop 1
Left of drop 73 74 74
Right of drop 72 71 72

Drop 2
Left of drop 72 75
Right of drop 74 72 73

Surface 2
Drop 1
Left of drop 72 71 70
Right of drop 72 72 73

Drop 2
Left of drop 72 72 72
Right of drop 71 73 71 **72 ± 3**

MCA on PPF (5 mM, electrolysis time 10 minutes)

Surface 1
Drop 1
Left of drop 69 67 69
Right of drop 67 67 68

Drop 2
Left of drop 69 68 68
Right of drop 66 67 69

Surface 2
Drop 1
Left of drop 65 65 67
Right of drop 68 68 66

Drop 2
Left of drop 65 68 66
Right of drop 68 66 65 **67 ± 2**

NPh on PPF (0.6 mM, electrolysis time 2 minutes) **Reduced in 0.02 M benzoic acid/ ACN/0.1 M [Bu4N]BF4**

Surface 1
Drop 1
Left of drop 64 66 68
Right of drop 65 64 64

Drop 2
Left of drop 63 64 67
Right of drop 63 64 65

Surface 2 **2 scans**

Drop 1

Left of drop	62 61 64	46 45 47
Right of drop	65 64 61	42 43 43

Drop 2

Left of drop	63 66 62	50 49 48
Right of drop	61 63 62	45 48 47 **46 ± 4**

Surface 3 **10 scans**

Drop 1

Left of drop	67 65 64	46 44 46
Right of drop	66 64 68	43 42 42

Drop 2

Left of drop	65 65 61	44 48 48
Right of drop	61 61 60 **64 ± 4**	45 44 44 **45 ± 3**

NPh on GC plate (0.6 mM, electrolysis time 10 minutes)

Surface 1

Drop 1

Left of drop	58 55 56
Right of drop	55 54 55 **56 ± 2**

MP (5 mM, 10 minutes)

Sample no and date prepared, Instrument	**Scratch**	**Scan**	**File code**	**Thickness measured by section analysis** Midpoint L	Midpoint R	L of scratch	R of scratch	**Thickness measured by localised depth**	**Av. of scan minus 0.3 nm**	**Std. Dev. of scan**	**Var. of scan**	**Av. of scratch**	**Std. Dev. of scratch**	**Var. of scratch**	**Av. of sample**	**Std. Dev. or Error of sample**
MP 6504	1	1	est12051.000	3.208	3.214	3.324	3.049	3.077	2.895	0.080	0.006					
						3.257	3.169									
Scratch 8:1						3.265	3.152									
Scan with NSC 14 tip						3.208	3.222									
Scan 1:1																
Tip holder 2		2	est12051.003	3.240	3.348	3.396	3.360	3.176	3.007	0.077	0.006					
						3.267	3.201									
						3.352	3.288									
						3.396	3.351					2.951	0.111	0.012		

PEG (0.8 mM, 10 minutes)

Sample no and date prepared, Instrument	**Scratch**	**Scan**	**File code**	**Thickness measured by section analysis**				**Thickness measured by localised depth**	**Av. of scan minus 0.3 nm**	**Std. Dev. of scan**	**Var. of scan**	**Av. of scratch**	**Std. Dev. of scratch**	**Var. of scratch**	**Av. of sample**	**Std. Dev. or Error of sample**
				Midpoint L	Midpoint R	L of scratch	R of scratch									
PEG 13504	1	1	est1071.000	4.091	3.903	4.200	3.997	3.815	3.739	0.123	0.015					
						4.075	4.012									
Scratch 8:1						3.919	4.200									
Scan with NSC 14 tip						4.075	4.138									
Scan 1:1																
Tip holder 2																

NPh attached (0.6 mM, 10 minutes)

Reduction of NPh in 0.25 M H2SO4, 0.7 V to -1.0 V

Calculation of surface coverage of NPh and NPh NH2

					0.2	96485		0.07
	Linkfit curves		NO2->NH2 (6e-)/NHOH (4e-) Reduction Peak	NHOH->NO (2e-) Oxidation Peak	/ SR (0.2 Vs-1) SR = scan rate	/ F (96485 Cmol-1) F = Faraday's constant	/ electrode geometric area GC rod (0.07 cm2) **NPh or NBC surface covarage and NPh NH2 surface coverage (molcm-2)**	
1st scan/2 of NPh		1	Added up total areas of peaks in LinkFit					
(21005)		2						
Rod 15		3						
	Total Area (peak 1 and 2)		2.124E-05	9.049E-06				
	Total Area of the Red. and Ox. / 6e-		5.048E-06		2.524E-05	2.616E-10		3.74E-09
	Area for conversion to NH2		3.142E-06					
	Area for conversion to NH2 / 6e-		5.237E-07		2.618E-06	2.714E-11		3.88E-10
1st scan/2 of NPh		1	Added up total areas of peaks in LinkFit					
(21005)		2						
Rod green		3						
	Total Area (peak 1 and 2)		2.038E-05	8.070E-06				
	Total Area of the Red. and Ox. / 6e-		4.742E-06		2.371E-05	2.457E-10		3.51E-09
	Area for conversion to NH2		4.240E-06					
	Area for conversion to NH2 / 6e-		7.067E-07		3.533E-06	3.662E-11		5.23E-10
1st scan/100 of NPh		1	Added up total areas of peaks in LinkFit					
(21005)		2						
Rod 17a		3						
	Total Area (peak 1 and 2)		2.050E-05	8.730E-06				
	Total Area of the Red. and Ox. / 6e-		4.872E-06		2.436E-05	2.525E-10		3.61E-09
	Area for conversion to NH2		3.040E-06					
	Area for conversion to NH2 / 6e-		5.067E-07		2.533E-06	2.626E-11		3.75E-10

1st scan/100 of NPh		1 Added up total areas of peaks in LinkFit					
(21005)		2					
Rod 2		3					
	Total Area (peak 1 and 2)		1.413E-05	5.916E-06			
	Total Area of the Red. and Ox. / 6e-		3.341E-06		1.671E-05	1.731E-10	2.47E-09
	Area for conversion to NH2		2.298E-06				
	Area for conversion to NH2 / 6e-		3.830E-07		1.915E-06	1.985E-11	2.84E-10

Reduction of NBC coupled to NPh, in 0.25 M H2SO4, 0.7 V to -1.0 V

Calculation of surface coverage of NBC

1st scan/2 of		1 Added up total areas of peaks in LinkFit					
NBC coupled to		2					
NPh reduced with		3					
2 scans in	Total Area (peak 1 and 2)		9.449E-06	6.450E-06			
H2SO4 (21005)							
Rod 15	Total Area of the Red. and Ox. / 6e-		2.650E-06		1.325E-05	1.373E-10	1.96E-09
1st scan/2 of		1 Added up total areas of peaks in LinkFit					
NBC coupled to		2					
NPh reduced with		3					
2 scans in	Total Area (peak 1 and 2)		9.141E-06	6.058E-06			
H2SO4 (21005)							
Rod green	Total Area of the Red. and Ox. / 6e-		2.533E-06		1.267E-05	1.313E-10	1.88E-09
1st scan/2 of		1 Added up total areas of peaks in LinkFit					
NBC coupled to		2					
NPh reduced with		3					
100 scans in	Total Area (peak 1 and 2)		7.455E-06	5.305E-06			
H2SO4 (21005)							
Rod 17a	Total Area of the Red. and Ox. / 6e-		2.127E-06		1.063E-05	1.102E-10	1.57E-09
1st scan/2 of		1 Added up total areas of peaks in LinkFit					
NBC coupled to		2					
NPh reduced with		3					
100 scans in	Total Area (peak 1 and 2)		4.410E-06	2.157E-06			
H2SO4 (21005)							
Rod 2	Total Area of the Red. and Ox. / 6e-		1.095E-06		5.473E-06	5.672E-11	8.10E-10

Reduction of NPh in ethanol/water (1:9 by volume) + 0.1 M KCl, 0.5 V to -1.4 V

Calculation of surface coverage of NPh and NPh NH2

1st scan/2 of NPh (101005) Rod 17		1 Added up total areas of peaks in LinkFit 2 3					
	Total Area (peak 1 and 2)		3.786E-05	1.267E-05			
	Total Area of the Red. and Ox. / 6e-		8.422E-06		4.211E-05	4.364E-10	6.23E-09
	Area for conversion to NH2		1.252E-05				
	Area for conversion to NH2 / 6e-		2.087E-06		1.043E-05	1.081E-10	1.54E-09
1st scan/2 of NPh (101005) Rod 15		1 Added up total areas of peaks in LinkFit 2 3					
	Total Area (peak 1 and 2)		3.424E-05	1.086E-05			
	Total Area of the Red. and Ox. / 6e-		7.517E-06		3.758E-05	3.895E-10	5.56E-09
	Area for conversion to NH2		1.252E-05				
	Area for conversion to NH2 / 6e-		2.087E-06		1.043E-05	1.081E-10	1.54E-09

Reduction of NBC coupled to NPh, in ethanol/water (1:9 by volume) + 0.1 M KCl, 0.5 V to -1.4 V

Calculation of surface coverage of NBC

1st scan/2 of NBC coupled to NPh reduced with 2 scans in ethanol/ water (101005) Rod 17		1 Added up total areas of peaks in LinkFit 2 3					
	Total Area (peak 1 and 2)		1.238E-05	5.097E-06			
	Total Area of the Red. and Ox. / 6e-		2.913E-06		1.456E-05	1.509E-10	2.16E-09
1st scan/2 of NBC coupled to NPh reduced with 2 scans in ethanol/ water (101005) Rod 15		1 Added up total areas of peaks in LinkFit 2 3					
	Total Area (peak 1 and 2)		1.019E-05	7.304E-06			
	Total Area of the Red. and Ox. / 6e-		2.916E-06		1.458E-05	1.511E-10	2.16E-09

NPh attached (0.6 mM, 2 minutes)

Reduction of NPh in 0.02 M benzoic acid/ACN/0.1 M [Bu4N]BF4, 0.6 V to -1.8 V

Calculation of surface coverage of NPh and NPh NH2				0.2	96485		0.24
	Linkfit curves	NO2->NH2 (6e-)/NHOH (4e-) Reduction Peak	NHOH->NO (2e-) Oxidation Peak	/ SR (0.1 Vs-1) SR = scan rate	/ F (96485 Cmol-1) F = Faraday's constant	/ electrode geometric area PPF (0.24 cm2) **NPh or NBC surface covarage and NPh NH2 surface coverage (molcm-2)**	
1st scan/2 of NPh	1	Added up total areas of peaks in LinkFit					
(23306)	2						
PPF	3						
	Total Area (peak 1 and 2)	3.066E-05	8.178E-06				
	Total Area of the Red. and Ox. / 6e-	6.473E-06		3.237E-05	3.354E-10		1.40E-09
	Area for conversion to NH2	1.431E-05					
	Area for conversion to NH2 / 6e-	2.384E-06		1.192E-05	1.236E-10		5.15E-10
1st scan/10 of NPh	1	Added up total areas of peaks in LinkFit					
(23306)	2						
PPF	3						
	Total Area (peak 1 and 2)	3.436E-05	8.532E-06				
	Total Area of the Red. and Ox. / 6e-	7.148E-06		3.574E-05	3.704E-10		1.54E-09
	Area for conversion to NH2	1.729E-05					
	Area for conversion to NH2 / 6e-	2.882E-06		1.441E-05	1.494E-10		6.22E-10

Appendix 6.

Quantification of fluorescence of protein
All samples modified with TGD (200 mM, electrolysis time 10 minutes)

Boundary of modified/BSA-FITC : as-prepared GC/BSA-FITC regions

GC plate 3a		**Modified/BSA-FITC**	**As-prepared GC/BSA-FITC**	**Fluorescence intensity ratio**	
26104	**Image 1**	63.402	23.595	2.687	
	Image 2	71.084	27.886	2.549	
	Image 3	81.800	40.058	2.042	
	Image 4	69.161	28.048	2.466	
				Average:	2.4
				Std. Dev.:	0.3

GC plate 4b		**Modified/BSA-FITC**	**As-prepared GC/BSA-FITC**	**Fluorescence intensity ratio**	
26104	**Image 1**	249.713	92.087	2.712	
	Image 2	249.369	114.679	2.175	
				Average:	2.4
				Std. Dev.:	0.4

GC plate 5b		Modified/BSA-FITC	As-prepared GC/BSA-FITC	Fluorescence intensity ratio	
151203	**Image 1**	62.518	36.298	1.722	
	Image 2	62.214	35.602	1.747	
	Image 3	101.943	35.508	2.871	
	Image 4	87.203	53.232	1.638	
				Average:	2.0
				Std. Dev.:	0.6

GC plate 1a		Modified/BSA-FITC	As-prepared GC/BSA-FITC	Fluorescence intensity ratio	
11303	**Image 1**	14.746	9.469	1.557	
	Image 2	61.377	37.735	1.627	
				Average:	1.6
				Std. Dev.:	0.0

GC plate 2a		Modified/BSA-FITC	As-prepared GC/BSA-FITC	Fluorescence intensity ratio	
11303	**Image 1**	49.405	21.670	2.280	
	Image 2	8.978	6.940	1.294	
				Average:	1.8
				Std. Dev.:	0.7

GC plate 3a		**Modified/BSA-FITC**	**As-prepared GC/BSA-FITC**	**Fluorescence intensity ratio**	
11303	**Image 1**	16.284	10.765	1.513	
	Image 2	14.982	11.191	1.339	
				Average:	1.4
				Std. Dev.:	0.1
GC plate 1a		**Modified/BSA-FITC**	**As-prepared GC/BSA-FITC**	**Fluorescence intensity ratio**	
3403	**Image 1**	87.212	31.336	2.783	
	Image 2	167.766	58.159	2.885	
	Image 3	22.179	7.463	2.972	
	Image 4	48.155	18.892	2.549	
				Average:	2.8
				Std. Dev.:	0.2
GC plate 3a		**Modified/BSA-FITC**	**As-prepared GC/BSA-FITC**	**Fluorescence intensity ratio**	
3403	**Image 1**	40.796	28.123	1.451	
	Image 2	6.601	4.071	1.622	
				Average:	1.5
				Std. Dev.:	0.1

GC plate 2a		Modified/BSA-FITC	As-prepared GC/BSA-FITC	Fluorescence intensity ratio	
6403	**Image 1**	112.426	30.284	3.712	
	Image 2	37.461	15.151	2.472	
	Image 3	43.145	20.512	2.103	
	Image 4	32.886	16.151	2.036	
				Average:	2.6
				Std. Dev.:	0.8

Average of 9 TGD modified samples:	2.1
Average of the std. dev. of 9 TGD modified samples:	0.4

Quantification of fluorescence of protein
All samples modified with HA (5 mM, electrolysis time 10 minutes)

Boundary of modified/BSA-FITC : as-prepared GC/BSA-FITC regions

GC plate 3a		**Modified/BSA-FITC**	**As-prepared GC/BSA-FITC**	**Fluorescence intensity ratio**	
6403	**Image 1**	90.016	155.108	0.580	
	Image 2	93.427	139.783	0.668	
	Image 3	85.052	114.042	0.746	
	Image 4	13.253	22.584	0.587	
				Average:	0.6
				Std. Dev.:	0.1

GC plate 5b		**Modified/BSA-FITC**	**As-prepared GC/BSA-FITC**	**Fluorescence intensity ratio**	
6403	**Image 1**	16.332	31.445	0.519	
	Image 2	61.578	72.309	0.852	
	Image 3	24.891	30.424	0.818	
	Image 4	59.567	87.407	0.681	
				Average:	0.7
				Std. Dev.:	0.2

GC plate 2a		Modified/BSA-FITC	As-prepared GC/BSA-FITC	Fluorescence intensity ratio	
30403	**Image 1**	24.188	33.957	0.712	
	Image 2	81.721	113.078	0.723	
	Image 3	46.316	53.440	0.867	
	Image 4	55.552	71.947	0.772	
				Average:	0.8
				Std. Dev.:	0.1

GC plate 4b		Modified/BSA-FITC	As-prepared GC/BSA-FITC	Fluorescence intensity ratio	
30403	**Image 1**	17.120	20.068	0.853	
	Image 2	65.019	115.904	0.561	
	Image 3	120.185	127.296	0.944	
				Average:	0.8
				Std. Dev.:	0.2

GC plate 1a		Modified/BSA-FITC	As-prepared GC/BSA-FITC	Fluorescence intensity ratio	
28104	**Image 1**	30.599	59.374	0.515	
	Image 2	39.350	63.699	0.618	
	Image 3	28.135	44.632	0.630	
				Average:	0.6
				Std. Dev.:	0.1

GC plate 2a		Modified/BSA-FITC	As-prepared GC/BSA-FITC	Fluorescence intensity ratio	
28104	**Image 1**	25.332	39.144	0.647	
	Image 2	34.115	67.973	0.502	
	Image 3	23.463	42.229	0.556	
	Image 4	39.712	45.398	0.875	
	Image 5	32.773	43.965	0.745	
				Average:	0.7
				Std. Dev.:	0.1

GC plate 5b		Modified/BSA-FITC	As-prepared GC/BSA-FITC	Fluorescence intensity ratio	
28104	**Image 1**	51.562	83.678	0.616	
	Image 2	63.498	91.275	0.696	
	Image 3	53.851	86.840	0.620	
	Image 4	33.767	53.824	0.627	
	Image 5	26.027	46.082	0.565	
				Average:	0.6
				Std. Dev.:	0.0

Average of 7 HA modified samples:	0.7
Average of the std. dev. of 7 HA modified samples:	0.1

Quantification of fluorescence of protein
Samples modified with PGD (20 mM, electrolysis time 10 minutes)

Boundary of modified/BSA-FITC : as-prepared GC/BSA-FITC regions

GC plate 1a		Modified/BSA-FITC	As-prepared GC/BSA-FITC	Fluorescence intensity ratio	
14503	**Image 1**	23.29591	35.24059	0.661	
	Image 2	43.27908	61.5773	0.703	
	Image 3	49.14778	74.57917	0.659	
	Image 4	81.29432	123.2835	0.659	
				Average:	0.7
				Std. Dev.:	0.0

GC plate 3a		Modified/BSA-FITC	As-prepared GC/BSA-FITC	Fluorescence intensity ratio	
14503	**Image 1**	5.52134	8.67	0.637	
	Image 2	5.68662	13.60195	0.418	
	Image 3	5.63339	6.63305	0.849	
				Average:	0.6
				Std. Dev.:	0.2

GC plate 5b		Modified/BSA-FITC	As-prepared GC/BSA-FITC	Fluorescence intensity ratio	
14503	**Image 1**	68.13168	88.87501	0.767	
	Image 2	59.96157	92.34873	0.649	
	Image 3	39.81487	52.32911	0.761	
	Image 4	52.90269	66.74675	0.793	
			Average:		0.7
			Std. Dev.:		0.1

Average of 3 PGD modified samples: 0.7
Average of the std. dev. of 3 PGD modified samples: 0.1

Samples modified with PGD (50 mM, electrolysis time 10 minutes)
Boundary of modified/BSA-FITC : as-prepared GC/BSA-FITC regions

GC plate 1a		Modified/BSA-FITC	As-prepared GC/BSA-FITC	Fluorescence intensity ratio	
2903	**Image 1**	18.205	31.402	0.580	
	Image 2	31.944	46.098	0.693	
	Image 3	23.551	32.052	0.735	
	Image 4	15.780	53.778	0.293	
	Image 5	32.810	66.974	0.490	
			Average:		0.6
			Std. Dev.:		0.2

GC plate 2a		Modified/BSA-FITC	As-prepared GC/BSA-FITC	Fluorescence intensity ratio	
4903	**Image 1**	13.377	16.733	0.799	
	Image 2	13.451	17.674	0.761	
	Image 3	8.845	12.517	0.707	
	Image 4	12.945	16.896	0.766	
			Average:		0.8
			Std. Dev.:		0.0

Average of 2 PGD modified samples:	0.7
Average of the std. dev. of 2 PGD modified samples:	0.1

Quantification of fluorescence of protein
All samples modified with MP (5 mM, electrolysis time 10 minutes)

Boundary of modified/BSA-FITC : as-prepared GC/BSA-FITC regions

GC plate 20		**Modified/BSA-FITC**	**As-prepared GC/BSA-FITC**	**Fluorescence intensity ratio**	
25702	**Image 1**	196.5	109.9	1.789	
	Image 2	145.8	87.4	1.668	
	Image 3	155.4	84.0	1.850	
				Average:	1.8
				Std. Dev.:	0.1

GC plate 1a		**Modified/BSA-FITC**	**As-prepared GC/BSA-FITC**	**Fluorescence intensity ratio**	
20303	**Image 1**	215.30	180.49	1.193	
	Image 2	126.21	115.71	1.091	
	Image 3	101.47	80.36	1.263	
				Average:	1.2
				Std. Dev.:	0.1

GC plate 2a		Modified/BSA-FITC	As-prepared GC/BSA-FITC	Fluorescence intensity ratio	
20303	**Image 1**	524.66	289.98	1.809	
	Image 2	394.22	186.66	2.112	
	Image 3	362.84	228.92	1.585	
	Image 4	53.00	29.01	1.827	
				Average:	1.8
				Std. Dev.:	0.2

GC plate 3a		Modified/BSA-FITC	As-prepared GC/BSA-FITC	Fluorescence intensity ratio	
20303	**Image 1**	239.22	222.24	1.076	
	Image 2	215.96	158.10	1.366	
	Image 3	213.98	199.02	1.075	
	Image 4	612.13	504.21	1.214	
				Average:	1.2
				Std. Dev.:	0.1

GC plate 1a		Modified/BSA-FITC	As-prepared GC/BSA-FITC	Fluorescence intensity ratio	
25303	**Image 1**	250.08	207.18	1.207	
	Image 2	249.52	151.00	1.652	
	Image 3	71.18	50.34	1.414	
	Image 4	221.61	169.86	1.305	
				Average:	1.4
				Std. Dev.:	0.2

GC plate 2a		Modified/BSA-FITC	As-prepared GC/BSA-FITC	Fluorescence intensity ratio	
25303	**Image 1**	818.90	420.94	1.945	
	Image 2	482.62	280.38	1.721	
	Image 3	70.80	62.24	1.138	
	Image 4	234.43	163.51	1.434	
				Average:	1.6
				Std. Dev.:	0.4

GC plate 19		Modified/BSA-FITC	As-prepared GC/BSA-FITC	Fluorescence intensity ratio	
21802	**Image 1**	186.47	118.42	1.575	
	Image 2	138.48	100.31	1.381	
	Image 3	272.40	167.65	1.625	
				Average:	1.5
				Std. Dev.:	0.1

GC plate 5b		Modified/BSA-FITC	As-prepared GC/BSA-FITC	Fluorescence intensity ratio	
26204	**Image 1**	28.572	17.313	1.650	
	Image 2	46.687	30.720	1.520	
	Image 3	32.483	20.778	1.563	
	Image 4	35.964	22.681	1.586	
			Average:		1.6
			Std. Dev.:		0.1

Average of 8 MP modified samples:	1.5
Average of the std. dev. of 8 MP modified samples:	0.2

Quantification of fluorescence of protein
All samples modified with HP (5 mM, electrolysis time 10 minutes)

Boundary of modified/BSA-FITC : as-prepared GC/BSA-FITC regions

GC plate 1a		**Modified/BSA-FITC**	**As-prepared GC/BSA-FITC**	**Fluorescence intensity ratio**	
15303	**Image 1**	82.3979	59.45354	1.386	
			Average:		1.4
			Std. Dev.:		

GC plate 3a		**Modified/BSA-FITC**	**As-prepared GC/BSA-FITC**	**Fluorescence intensity ratio**	
21504	**Image 1**	46.9715	34.32369	1.368	
	Image 2	48.02139	38.63434	1.243	
	Image 3	50.22829	43.38004	1.158	
			Average:		1.3
			Std. Dev.:		0.1

GC plate 5b		**Modified/BSA-FITC**	**As-prepared GC/BSA-FITC**	**Fluorescence intensity ratio**	
21504	**Image 1**	52.82444	46.12686	1.145	
			Average:		1.1
			Std. Dev.:		

GC plate 5b		Modified/BSA-FITC	As-prepared GC/BSA-FITC	Fluorescence intensity ratio	
19504	**Image 1**	14.50055	10.46769	1.385	
	Image 2	58.10625	43.94852	1.322	
	Image 3	67.93955	47.60746	1.427	
	Image 4	64.79713	47.61634	1.361	
			Average:		1.4
			Std. Dev.:		0.0

Average of 4 HP modified samples:	1.3
Average of the std. dev. of 4 HP modified samples:	0.1

Quantification of fluorescence of protein
All samples modified with PEG (5 mM, electrolysis time 10 minutes)

Boundary of modified/BSA-FITC : as-prepared GC/BSA-FITC regions

GC plate		Modified/BSA-FITC	As-prepared GC/BSA-FITC	Fluorescence intensity ratio	
21802	**Image 1**	150.86	41.99	3.593	
	Image 2	165.97	69.46	2.389	
				Average:	3.0
				Std. Dev.:	0.9

GC plate		Modified/BSA-FITC	As-prepared GC/BSA-FITC	Fluorescence intensity ratio	
25504	**Image 1**	15.76207	9.778046	1.612	
	Image 2	13.75232	8.900624	1.545	
	Image 3	34.51100	26.85493	1.285	
				Average:	1.5
				Std. Dev.:	0.2

Average of 2 PEG modified samples:	2.2
Average of the std. dev. of 2 PEG modified samples:	0.5

Appendix 7.

Quantification of fluorescence of aldehyde-functionalised latex NP assemblies
All samples modified with PGD (50 mM, electrolysis time 10 minutes)

Boundary of modified/NPs : as-prepared GC/NPs regions

GC plate 1a		Modified/NPs	As-prepared GC/NPs	Fluorescence intensity ratio
19903	**Image 1**	131.017	24.451	5.358
	Image 2	95.022	29.937	3.174
	Image 3	171.037	19.601	8.726
	Image 4	168.169	58.280	2.886
			Average:	5.0
			Std. Dev.:	2.7

GC plate 5b		Modified/NPs	As-prepared GC/NPs	Fluorescence intensity ratio
19903	**Image 1**	170.456	39.046	4.366
	Image 2	171.504	23.617	7.262
	Image 3	235.890	39.316	6.000
	Image 4	155.375	17.886	8.687
			Average:	6.6
			Std. Dev.:	1.8

Boundary of as-prepared GC/NPs : as-prepared GC regions

	As-prepared GC/NPs	As-prepared GC	Fluorescence intensity ratio
Image 1	8.360	1.835	4.557
Image 2	14.831	3.754	3.951
		Average:	4.3
		Std. Dev.:	0.4

GC plate 4b		Modified/NPs	As-prepared GC/NPs	Fluorescence intensity ratio		As-prepared GC/NPs	As-prepared GC	Fluorescence intensity ratio	
23903	**Image 1**	253.958	32.536	7.806	**Image 1**	2.113	0.331	6.38	
	Image 2	253.879	37.510	6.768	**Image 2**	1.898	0.350	5.42	
	Image 3	253.928	33.562	7.566				**Average:**	5.9
				Average:	7.4			**Std. Dev.:**	0.7
				Std. Dev.:	0.5				

GC plate 5b		Modified/NPs	As-prepared GC/NPs	Fluorescence intensity ratio		As-prepared GC/NPs	As-prepared GC	Fluorescence intensity ratio	
23903	**Image 1**	104.407	23.273	4.486	**Image 1**	0.717	0.345	2.08	
	Image 2	98.231	16.740	5.868	**Image 2**	1.246	0.871	1.43	
	Image 3	136.838	23.279	5.878				**Average:**	1.8
	Image 4	144.300	25.195	5.727				**Std. Dev.:**	0.5
				Average:	5.5				
				Std. Dev.:	0.7				

GC plate 1a		Modified/NPs	As-prepared GC/NPs	Fluorescence intensity ratio		As-prepared GC/NPs	As-prepared GC	Fluorescence intensity ratio	
101003	**Image 1**	253.556	46.025	5.509	**Image 1**	12.640	4.476	2.82	
	Image 2	253.497	33.996	7.457	**Image 2**	23.282	5.967	3.90	
	Image 3	253.529	47.478	5.340				**Average:**	3.4
				Average:	6.1			**Std. Dev.:**	0.8
				Std. Dev.:	1.2				

GC plate 2a		Modified/NPs	As-prepared GC/NPs	Fluorescence intensity ratio
101003	**Image 1**	253.705	61.871	4.101
	Image 2	253.634	46.325	5.475
	Image 3	253.497	44.167	5.740
			Average:	5.1
			Std. Dev.:	0.9

	As-prepared GC/NPs	As-prepared GC	Fluorescence intensity ratio
Image 1	43.684	9.732	4.49
Image 2	50.379	15.760	3.20
		Average:	3.8
		Std. Dev.:	0.9

Control experiments: mock modification

	As-prepared GC/NPs	As-prepared GC	Fluorescence intensity ratio
Image 1	3.104	1.028	3.02
Image 2	1.337	0.722	1.85
		Average:	2.4
		Std. Dev.:	0.8

Quantification of number of citrate-capped gold NP assemblies
used as-prepared solution with unaltered pH and concentration

	Image magnification	Image 1	Adjusted to mag.	Image 2	Adjusted to mag.	Image 3	Adjusted to mag.	Average	Error
TGD (5 mM, 1 scan) 8306	200 kx	11		10		8			
time of immersion: 3 hours		11		10		13			
		8		10		12			
		10		8		10		10	± 2
Scan between 1 and -1.5 V in ACN/0.1 M [Bu4N]BF4	200 kx	11		12					
		9		11					
		11		11					
		9		12				11	± 2
TGD (5 mM, 1 scan) 5406	200 kx	11		11					
time of immersion: 3 hours		12		12					
		13		10					
		12		10				11	± 2
TGD (5 mM, 2 minutes) 8306	200 kx	12		9		12			
time of immersion: 3 hours		10		9		10			
		13		8		11			
		11		8		12		10	± 3
TGD (5 mM, 2 minutes) 9306	200 kx	11		11					
time of immersion: 3 hours		9		12					
		10		11					
		8		10				10	± 2
Scan between 1 and -1.5 V in PBS	200 kx	11		12					
		9		9					
		9		11					
		8		11				10	± 2

TGD (5 mM, 2 minutes) 1 51005	200 kx	8	8	9		
time of immersion: 3 hours		8	11	9		
		11	9	8		
		9	9	10	9	± 2
TGD (5 mM, 2 minutes) 2 51005	200 kx	11	9	8		
After soak in DMSO 2 hours		11	6	8		
time of immersion: 3 hours		14	6	11		
		9	10	9	9	± 5
TGD (5 mM, 10 minutes) 23404	200 kx	28				
time of immersion: 3 hours		24				
		24				
		23			25	± 3
Sonicate in MQ water 15 seconds	200 kx	23				
		23				
		21				
		21			22	± 1
One year later	200 kx	22	26			
		22	31			
		24	24			
		25	27		25	± 6
TGD (5 mM, 10 minutes) 5 19405	200 kx	34	29			
time of immersion: 3 hours		38	34			
		34	30			
		34	29		33	± 5
TGD (5 mM, electrolysis time 20s) 27306	200 kx	3	3	1		
time of immersion: 3 hours		4	3	4		
		3	4	3		
		2	5	2	3	± 2

TGD (5 mM, electrolysis time 150s) 27306	200 kx	11		10			
time of immersion: 3 hours		11		10			
		11		10			
		10		9		10	± 1
TGD (5 mM, electrolysis time 400s) 27306	200 kx	15		12			
time of immersion: 3 hours		14		13			
		15		13			
		14		14		14	± 2
Sonicate in 1 M HCl 15 seconds	200 kx	15		12			
		13		12			
		14		13			
		14		12		13	± 2
Control modification of TGD (1.2 V for 10 minutes) 1 24504							
time of immersion: 3 hours	100 kx	0	0	1	1		
		1	1	0	0		
		0	0	1	1		
		1	1	0	0	0	± 1
Control modification of TGD (1.2 V for 10 minutes) 2 24504							
time of immersion: 3 hours	100 kx	2	1				
		1	1				
		3	2				
		0	0			1	± 1

Quantification of number of citrate-capped gold NP assemblies
time, concentration and pH were altered as stated

	Image magnification	Image 1	Adjusted to mag.	Image 2	Adjusted to mag.	Image 3	Adjusted to mag.	Average	Error
TIME									
TGD (5 mM, 10 minutes) 1 7405									
concentration and pH were as-prepared									
time of immersion: 1 minute	200 kx	0		1					
		1		2					
		0		0					
		2		2				1	± 1
time of immersion: 22 minutes	200 kx	17		18					
		16		19					
		21		20					
		20		21				19	± 3
time of immersion: 1 hour	200 kx	30		34					
		34		38					
		34		37					
		32		36				34	± 4
time of immersion: 3 hours	200 kx	37		39					
		35		38					
		42		35					
		42		39				38	± 4
time of immersion: 26 hours	200 kx	34		31					
		36		36					
		34		34					
		33		35				34	± 3

TGD (5 mM, 10 minutes) 1 8405						
concentration and pH were as-prepared						
time of immersion: 1 minute	200 kx	1	1	0		
		1	3	3		
		1	0	1		
		2	1	1	1	± 2
time of immersion: 22 minutes	200 kx	18	20			
		23	20			
		20	22			
		22	17		20	± 3
time of immersion: 1 hour	200 kx	29	35			
		34	30			
		32	28			
		36	32		32	± 4
time of immersion: 3 hours	200 kx	42	35			
		35	37			
		38	37			
		38	39		38	± 4
time of immersion: 26 hours	200 kx	38	34			
		34	32			
		38	34			
		34	34		35	± 3
CONCENTRATION						
TGD (5 mM, 10 minutes) 2 7405						
time of immersion 3 hours and pH was as-prepared						
concentration 0.01 of as-prepared	200 kx	0	0			
		0	0			
		0	0			
		0	0		0	± 0

TGD (5 mM, 10 minutes) 2 8405					
time of immersion 3 hours and pH was as-prepared					
concentration 0.1 of as-prepared	200 kx	1	1		
		0	1		
		1	3		
		3	0	1	± 2
TGD (5 mM, 10 minutes) 3 19405					
time of immersion 3 hours and pH was as-prepared					
concentration 0.1 of as-prepared	200 kx	0	2		
		2	0		
		1	1		
		3	2	1	± 2
TGD (5 mM, 10 minutes) 4 8405					
time of immersion 3 hours and pH was as-prepared					
concentration 0.5 of as-prepared	200 kx	21	22		
		24	21		
		22	20		
		22	24	22	± 2
pH					
TGD (5 mM, 10 minutes) 3 7405					
time of immersion 3 hours and concentration was as-prepared					
pH 7	200 kx	27	31		
		29	27		
		27	25		
		26	29	28	± 3

TGD (5 mM, 10 minutes) 1 19405						
time of immersion 3 hours and concentration was as-prepared						
pH 7	200 kx	24	27			
		22	23			
		22	21			
		25	21		23	± 4
TGD (5 mM, 10 minutes) 1 16604						
time of immersion 3 hours and concentration was as-prepared						
pH 8	200 kx	9	6	6		
		9	8	8		
		7	7	5		
TGD (5 mM, 10 minutes) 2 16604		6	6	8	7	± 2
time of immersion 3 hours and concentration was as-prepared						
pH 8	200 kx	7	8			
		9	9			
		9	7			
		10	10		9	± 2
TGD (5 mM, 10 minutes) 2 19405						
time of immersion 3 hours and concentration was as-prepared						
pH 12	200 kx	0	0			
		0	1			
		1	0			
		0	2		1	± 1
TGD (5 mM, 10 minutes) 4 19405						
time of immersion 3 hours and concentration was as-prepared						
pH 12	200 kx	1	1			
		0	2			
		0	0			
		0	1		1	± 1

Quantification of number of citrate-capped gold NP assemblies used as-prepared solution with unaltered pH and concentration

	Image magnification	Image 1	Adjusted to mag.	Image 2	Adjusted to mag.	Image 3	Adjusted to mag.	Average	Error
HA (5 mM, 10 minutes) 28404	200 kx	11							
time of immersion: 3 hours		12							
		11							
		10						11	± 1
HA (5 mM, 10 minutes) 29404	200 kx	14							
time of immersion: 3 hours		11							
		11							
		11						12	± 2
HA (5 mM, 10 minutes) 30504	200 kx	12							
time of immersion: 3 hours		15							
		12							
		13						13	± 2
Sonicate in MQ water 15 seconds	200 kx	13							
		12							
		11							
		15						13	± 2
PGD (50 mM, 10 minutes) 19404	200 kx	6							
time of immersion: 3 hours		8							
		9							
		10						8	± 2
Mock modification of HA or PGD (1.3 V for 10 minutes) 20404									
time of immersion: 3 hours	200 kx	1							
		0							
		0							
		0						0	± 1

Mock modification of HA or PGD (1.3 V for 10 minutes) 1		**24504**					
time of immersion: 3 hours	100 kx	1	1				
		0	0				
		0	0				
		0	0			0	± 1
Mock modification of HA or PGD (1.3 V for 10 minutes) 2		**24504**					
time of immersion: 3 hours	100 kx	0	0	1	1		
		1	1	1	1		
		0	0	0	0		
		0	0	3	2	0	± 2

Quantification of number of citrate-capped gold NP assemblies
used as-prepared solution with unaltered pH and concentration

	Image magnification	Image 1	Adjusted to mag.	Image 2	Adjusted to mag.	Image 3	Adjusted to mag.	Average	Error
MP (5 mM, 10 minutes) 23304	200 kx	1							
time of immersion: 3 hours		0							
		0							
		0						0	± 1
MP (5 mM, 10 minutes) 6504	50 kx	6	2	9	2				
time of immersion: 3 hours		20	5	15	4				
		16	4	17	4				
		6	2	10	3			3	± 2
MP (5 mM, 10 minutes) 7504	50 kx	0	0						
time of immersion: 3 hours		8	2						
		5	1						
		5	1					1	± 1
PEG (5 mM, 10 minutes) 1 20504	100 kx	1	1						
time of immersion: 3 hours		3	2						
		2	1						
		6	3					2	± 1
PEG (5 mM, 10 minutes) 2 20504	100 kx	0	0						
time of immersion: 3 hours		6	3						
		8	4						
		1	1					2	± 2

Quantification of number of citrate-capped gold NP assemblies
used as-prepared solution with unaltered pH and concentration

	Image magnification	Image 1	Adjusted to mag.	Image 2	Adjusted to mag.	Image 3	Adjusted to mag.	Average	Error
TGD (5 mM, 2 minutes) 31005	200 kx	10		9					
NBC attached to TGD layer		8		6					
time of immersion: 3 hours		8		9					
		8		7				8	± 2
MCA (5 mM, 1 minute, Ef -1.12 V) 6905	50 kx	0	0						
time of immersion: overnight		0	0						
		0	0						
		0	0					0	± 0
NPh (0.6 mM, 2 minutes) 23306	50 kx	0	0	0	0				
time of immersion: 3 hours		0	0	0	0				
		0	0	0	0				
		0	0	0	0			0	± 0
NPh reduced (0.6 mM, 2 minutes) 23306	200 kx	8		6					
reduced in 0.02 M benzoic acid/ACN/0.1 M [Bu4N]BF4		6		7					
2 scans		6		7					
time of immersion: 3 hours		7		7				7	± 1
NPh reduced (0.6 mM, 2 minutes) 23306	200 kx	8		8					
reduced in 0.02 M benzoic acid/ACN/0.1 M [Bu4N]BF4		9		8					
10 scans		10		10					
time of immersion: 3 hours		10		9				9	± 1

Appendix 8.

Table 8.1. Procedures that produced substandard SU-8 photoresist masters.

Pattern	**Type of Si wafer**	**Period between spin coating and soft bake**	**Time for soft bake. With Al plate between hotplate and wafer?**	**Exposure time in mask aligner**	**Post bake: With Al plate between hotplate and master?**	**Resulting SU-8 photoresist master** Analysis by optical microscope (O) and profilometer (P)	**Problem and cause**
Y-shaped	*p*-type, prime grade Si(100)	Immediate	10 minutes, √	4 minutes	√	O: bits of SU-8 photoresist at edges of pattern, width 184 µm; P: height 20 µm	Width of mask 115 µm, exposure may be too long getting light spreading.
Letters	1 µm Si_3N_4, test grade Si(100)	Overnight	30 minutes, √	3 minutes	√	SU-8 photoresist lifted off in some parts after developing	Exposure time may not be long enough with large patterns
Letters	*p*-type, prime grade Si(100)	Immediate	10 minutes, √	4 minutes	√	SU-8 photoresist lifted off in some parts after developing	Heat transfer may not be good with Al plate with large patterns
Letters	*p*-type, prime grade Si(100)	Immediate	10 minutes, X	4 minutes	X	SU-8 photoresist remained in some areas. P: height 60 µm	
Plus 100	*p*-type, prime grade Si(100)	Immediate	10 minutes, X	4 minutes	X	O: edges of pattern jagged, width 152 µm; P: height 62 µm. SU-8 photoresist at corners at center of + not removed.	Mask has jagged edges. Width of mask 100 µm, exposure may be too long getting light spreading.

Plus 100 Different spin coating steps: 500 rpm, 15 seconds; 1500 rpm, 15 seconds	*p*-type, prime grade Si(100)	Immediate	30 minutes, √	4 minutes	√; after developing, master was additionally rinsed in clean developer	SU-8 photoresist at corners at centre of + not removed. Tried sonicating in SU-8 developer and SU-8 photoresist lifted off.	Exposure may be too long getting light spreading. Tried different spin coating and developing to get rid of undesired SU-8 photoresist.
Plus 100	*p*-type, prime grade Si(100)	Immediate	10 minutes, X	3½ minutes	X, developing step repeated in clean SU-8	O: edges of pattern jagged, SU-8 photoresist features larger than mask	Mask has jagged edges. Exposure may be too long getting light spreading.
Plus 100	*p*-type, prime grade Si(100)	Immediate	25 minutes, √; after soft bake wafer was left overnight then soft bake again for 5 minutes with Al plate before exposure	3 minutes	√	O: edges of pattern jagged, width 114 µm; P: height 58 µm	Mask has jagged edges. Width of mask 100 µm, exposure may be too long getting light spreading.
Plus 100	*p*-type, prime grade Si(100)	Immediate	10 minutes, X	3 minutes	X, during developing, developer was agitated by swirling	SU-8 photoresist lifted off after developing	With shorter exposure time, heat transfer may be better with Al plate
Plus 100	*p*-type, prime grade Si(100)	Immediate	10 minutes, X	2 minutes	X, during developing, developer was agitated by swirling	SU-8 photoresist lifted off after developing	With shorter exposure time, heat transfer may be better with Al plate
Plus 200	*p*-type, prime grade Si(100)	Immediate	10 minutes, X	4 minutes	X	O: edges of pattern jagged, width 256 µm; P: height 59 µm	Mask has jagged edges. Width of mask 200 µm, exposure may be too long getting light spreading.

Plus 200	1 µm Si_3N_4, test grade Si(100)	Overnight	30 minutes, X	3 minutes	√		O: edges of pattern jagged, width 222 µm; P: height 63 µm	Mask has jagged edges. Width of mask 200 µm, exposure may be too long getting light spreading.

Table 8.2. Curing procedures tried to achieve a flat piece of mechanically stable PDMS.
Note: Elastomer and curing agent were mixed in a beaker unless otherwise stated, following that vacuum applied as when stated by placing the beaker in a vacuum dessicator and then mixture transferred to curing apparatus.

Elastomer : Curing Agent (by weight)	Curing apparatus	Curing conditions	Resulting PDMS	Cause of failure
10:1	Glass petri dish	Mixed with metal spatula which introduced bubbles. 15 minutes in 150 °C oven.	Mostly solidified, however, uncured elastomer and bubbles present. PDMS was sonicated in ethanol : MQ water (1:2) for 10 minutes or ethanol for 5 minutes; and dried with $N_{2(g)}$ and in 45 °C oven but failed to remove uncured elastomer.	Elastomer : curing agent not thoroughly mixed prior to curing. Bubbles not removed prior to curing.
10:1	Si wafer with 300 µm features	Mixed with metal spatula. Applied vacuum to remove bubbles. 15 minutes on 150 °C hotplate. Followed by 50 °C overnight.	Mostly solidified, however, uncured elastomer present. PDMS cannot be peeled off master, tore and left residues on master.	Elastomer : curing agent not thoroughly mixed prior to curing.
10:1	Si wafer base with glass ring to contain mixture and increase thickness.	Thoroughly mixed in a round bottomed flask with metal spatula. Applied vacuum to remove bubbles. 15 minutes on 150 °C hotplate.	Solidified	When PDMS forms, glass ring was bound irreversibly to the wafer. Cannot use glass ring.
10:3	Si wafer with metal ring to contain mixture and give a 6 mm thick mixture.	Thoroughly mixed with metal spatula. Applied vacuum to remove bubbles. Between 60-180 °C on hotplate.	At ~180 °C, large air pockets form under PDMS.	PDMS destroyed when heat at ~180 °C.
10:1	Glass petri dish	Mixed with magnetic flea for 30 minutes. Then applied vacuum to remove bubbles. 1 hour in 100 °C oven.	Usable	None

	10:2	Si wafer on platform so mixture dripped off edge.	Mixed with metal spatula thoroughly. Applied vacuum to remove bubbles. 1 hour in 120 °C oven.	Usable	None

Appendix 9a.

Sample 1: HA (10 mM, 10 minutes)/TDA (5 mM, 2 scans)

Sample no and date prepared, Instrument	**Scratch**	**Scan**	**File code**	**Thickness measured by section analysis** Midpoint L	Midpoint R	L of scratch	R of scratch	**Thickness measured by localised depth**	**Av. of scan minus 0.3 nm**	**Std. Dev. of scan**	**Var. of scan**	**Av. of scratch**	**Std. Dev. of scratch**	**Var. of scratch**	**Av. of sample**	**Std. Dev. or Error of sample**
HA 281004	2	1	est30101a.006	2.251	2.396	2.146	2.467	2.524	2.186	0.185	0.034					
						2.425	2.738									
Scratch 4:1						2.596	2.623									
Scan with scratch tip						2.732	2.444									
Scan 4:1																
Tip holder 2	3	1	est30101a.007	3.589	3.773	3.631	4.048	3.914	3.542	0.259	0.067					
						3.434	4.008									
						4.169	3.674									
						4.260	3.762								2.864	0.318

Sample 2: TGD (5 mM, 10 minutes)

Sample no and date prepared, Instrument	Scratch	Scan	File code	Thickness measured by section analysis				Thickness measured by localised depth	Av. of scan minus 0.3 nm	Std. Dev. of scan	Var. of scan	Av. of scratch	Std. Dev. of scratch	Var. of scratch	Av. of sample	Std. Dev. or Error of sample
				Midpoint L	Midpoint R	L of scratch	R of scratch									
TGD 21205	1	1	est2421.000	3.704	3.62	3.67	3.639	3.8	3.401	0.060	0.004					
						3.717	3.647									
Scratch 8:1						3.704	3.798									
Scan with scratch tip						3.742	3.675									
Scan 8:1																
Tip holder 2		2	est2421.001	3.678	3.745	3.773	3.653	3.959	3.451	0.116	0.013					
						3.765	3.538									
						3.667	3.872									
						3.768	3.843					3.426	0.131	0.017		
	2	1	est2421.002	3.682	3.635	3.64	3.584	3.742	3.418	0.090	0.008					
						3.804	3.655									
						3.849	3.794									
						3.793										
		2	est2421.004	3.525	3.525	3.49	3.319	3.61	3.182	0.118	0.014					
						3.497	3.369									
						3.582	3.376									
						3.675	3.339					3.300	0.148	0.022	3.363	0.198

Sample 3: TGD (5 mM, 2 minutes)

Sample no and date prepared, Instrument	Scratch	Scan	File code	Thickness measured by section analysis				Thickness measured by localised depth	Av. of scan minus 0.3 nm	Std. Dev. of scan	Var. of scan	Av. of scratch	Std. Dev. of scratch	Var. of scratch	Av. of sample	Std. Dev. or Error of sample
				Midpoint L	Midpoint R	L of scratch	R of scratch									
TGD 10305		1	1 est1031a.001	3.393	3.239				3.016	0.109	0.012					
Scratch 8:1																
Scan with scratch tip																
Scan 8:1																
Tip holder 2			2 est1031a.002		3.569		3.694		3.237	0.119	0.014					
							3.457									
							3.387									
							3.577					3.126	0.161	0.026		
		2	1 est1031a.003	3.32	2.945	3.362	2.901	3.425	2.879	0.232	0.054					
						3.407	2.804									
						3.241	2.945									
						3.376	3.241								3.003	0.283

Sample 4a: TGD (5 mM, 20 scans)/*p*-NA (5 mM, 1 scan)

TGD (5 mM, 20 scans) 21305

Sample no and date prepared, Instrument	**Scratch**	**Scan**	**File code**	**Thickness measured by section analysis** Midpoint L	Midpoint R	L of scratch	R of scratch	**Thickness measured by localised depth**	**Av. of scan minus 0.3 nm**	**Std. Dev. of scan**	**Var. of scan**	**Av. of scratch**	**Std. Dev. of scratch**	**Var. of scratch**	**Av. of sample**	**Std. Dev. or Error of sample**
Scratch 8:1	1	1	1est223.001	2.583	2.610	2.605	2.657	2.633	2.296	0.036	0.001					
Scan with scratch tip						2.546	2.556									
Scan 8:1						2.622	2.610									
Tip holder 2						2.545	2.588									
	2	1	est2231a.005	3.345	2.950	3.218	2.840	3.217	2.787	0.158	0.025					
						3.009	3.009									
						3.228	3.007									
						3.191	2.943									
		2	est2231a.006	3.438	3.083	3.314	3.281	3.539	2.966	0.146	0.021	2.877	0.215	0.046		
						3.197	3.107									
						3.267	3.340									
						3.075	3.289								2.586	0.218

***p*-NA (5 mM, 1 scan) 24305**

Refind scratches	1	1	est2431a.005	2.143	1.967	2.063	2.025	2.048	1.753	0.099	0.010					
made above in TGD						2.169	1.962									
						2.183	1.853									
Scratch 8:1						2.070	2.105									
Scan with scratch tip																
Scan 8:1		2	est2431a.006	2.284	2.173	2.205	2.124	2.247	1.937	0.092	0.008					
Tip holder 2						2.260	2.072									
						2.339	2.323									
						2.372	2.214									
		3	est2431a.008	2.096	1.989	2.169	2.076	2.105	1.789	0.114	0.013					
						2.301	1.887									
						2.206	2.021									
						2.130	1.999					1.827	0.177	0.031		
	2	1	est2431a.009	2.127	2.065	2.056	2.186	2.052	1.796	0.064	0.004					

					2.037	2.003									
					2.127	2.068									
					2.210	2.125									
		2 est2431a.010	2.374	2.269	2.358	2.292	2.389	1.984	0.093	0.009					
					2.306	2.212									
					2.374	2.079									
					2.225	2.241					1.890	0.113	0.013	1.858	0.210
Rescratch in TGD	1	1 est2431a.011	3.109	3.378	3.449	3.160	3.599	3.070	0.174	0.030					
					3.490	3.174									
Scratch 8:1					3.396	3.262									
Scan with scratch tip					3.615	3.443									
Scan 8:1															
Tip holder 2		2 est2431a.013	3.587	3.263	3.500	3.384	3.606	3.137	0.147	0.022					
					3.547	3.195									
					3.360	3.441									
					3.620	3.304					3.104	0.228	0.052		
	2	1 est2431a.014	2.720	2.797	2.754	2.708	2.703	2.469	0.057	0.003					
					2.741	2.796									
					2.893	2.739									
					2.822	2.784									
		2 est2431a.015	2.941	2.952	2.938	2.942	3.104	2.665	0.090	0.008					
					2.935	2.819									
					3.097	2.896									
					3.079	2.910					2.567	0.107	0.011	2.835	0.252

Sample 4b: TGD (5 mM, 20 scans)/*p*-NA (5 mM, 1 scan)

TGD (5 mM, 20 scans) 21305

Sample no and date prepared, Instrument	**Scratch**	**Scan**	**File code**	**Thickness measured by section analysis** Midpoint L	Midpoint R	L of scratch	R of scratch	**Thickness measured by localised depth**	**Av. of scan minus 0.3 nm**	**Std. Dev. of scan**	**Var. of scan**	**Av. of scratch**	**Std. Dev. of scratch**	**Var. of scratch**	**Av. of sample**	**Std. Dev. or Error of sample**
Scratch 8:1	1	1	est2231a.014	2.777	2.712	2.969	2.596	2.592	2.418	0.122	0.015					
Scan with scratch tip						2.772	2.510									
Scan 8:1						2.769	2.725									
Tip holder 2						2.721	2.757									
	2	1	est2231a.015	2.988	2.749	2.986	2.627	2.794	2.508	0.125	0.016					
						2.814	2.653									
						2.863	2.843									
						2.899	2.671									
		2	est2231a.016	2.678	2.492		2.690	2.550	2.320	0.074	0.005					
							2.609									
							2.649									
							2.669					2.414	0.145	0.021	2.416	0.189

***p*-NA (5 mM, 1 scan) 24305**

Refind scratches made above in TGD	1	1	est2831a.008	2.392	2.271				2.032	0.086	0.007					
Scratch 8:1																
Scan with scratch tip																
Scan 8:1		2	est2831a.009	2.517	2.309				2.113	0.147	0.022					
Tip holder 2																
		3	est2831a.010	2.172	2.007				1.790	0.117	0.014					

											1.978	0.206	0.043		
	2	1 est2831a.011	2.495	2.377	2.542	2.377	2.551	2.193	0.138	0.019					
					2.454	2.441									
					2.823	2.388									
					2.616	2.362									
		2 est2831a.012	2.722	2.466	2.979	2.428	2.708	2.365	0.180	0.032					
					2.927	2.467									
					2.709	2.726									
					2.585	2.599					2.279	0.227	0.051	2.129	0.306
Rescratch in TGD	1	1 est2831a.013	3.008	2.799	3.135	2.896	2.956	2.658	0.116	0.013					
					3.158	2.801									
Scratch 8:1					2.969	2.976									
Scan with scratch tip					2.963	2.876									
Scan 8:1															
Tip holder 2		2 est2831a.014	2.908	2.580	2.890	2.639	2.827	2.480	0.120	0.014					
					2.863	2.694									
					2.879	2.705									
					2.909	2.689					2.569	0.167	0.028		
	2	1 est2831a.015	3.318	3.062	2.980	3.143	3.126	2.830	0.159	0.025					
					3.200	2.955									
					3.320	2.962									
					3.387	2.977									
		2 est2831a.016	3.249	3.048	3.214	3.005	3.182	2.833	0.134	0.018					
					3.257	3.088									
					3.297	2.941									
					3.247	2.933					2.831	0.208	0.043	2.700	0.267

Scratch in *p* -NA	1	1 est2831a.000	0.767	0.711	0.629	0.708	0.747	0.443	0.065	0.004					
					0.764	0.756									
Scratch 8:1					0.775	0.895									
Scan with scratch tip					0.702	0.720									
Scan 8:1															
Tip holder 2		2 est2831a.002	0.667	0.770		0.977		0.545	0.112	0.013					
						0.879									
						0.930									
						0.848					0.494	0.130	0.017		
	2	1 est2831a.003	1.260	1.013	1.160	1.019	0.924	0.822	0.129	0.017					
					1.347	1.086									
					1.254	1.110									
					1.155	1.010									
	3	1 est2831a.006	1.407	1.142	1.402	1.236	1.344	0.958	0.111	0.012					
					1.304	1.143									
					1.244	1.066									
					1.329	1.217									
		2 est2831a.007	1.056	0.931	1.140	1.124	0.960	0.730	0.066	0.004					
					1.031	1.030									
					1.024	0.959									
					1.065	1.012					0.844	0.129	0.017	0.720	0.224

Sample plus 200: TGD (5 mM, 10 minutes)/MP (5 mM, 1 scan)

TGD (5 mM, 10 minutes) 30605

Sample no and date prepared, Instrument	Scratch	Scan	File code	Thickness measured by section analysis				Thickness measured by localised depth	Av. of scan minus 0.3 nm	Std. Dev. of scan	Var. of scan	Av. of scratch	Std. Dev. of scratch	Var. of scratch	Av. of sample	Std. Dev. or Error of sample
				Midpoint L	Midpoint R	L of scratch	R of scratch									
Scratch 8:1	1	1	est57051a.000	2.798	2.550	2.788	2.730	2.507	2.347	0.111	0.012					
Scan with scratch tip						2.608	2.497									
Scan 8:1						2.592	2.592									
Tip holder 2						2.695	2.760									
		2	est57051a.001	2.621	2.676	2.647	2.699	2.517	2.344	0.071	0.005					
						2.705	2.577									
						2.743	2.547									
						2.664	2.682					2.345	0.132	0.017		
	2	1	est57051a.003	2.565	2.508	2.631	2.544	2.422	2.231	0.092	0.008					
						2.600	2.627									
						2.615	2.394									
						2.549	2.389									
		2	est57051a.004	2.650	2.508	2.610	2.525	2.409	2.260	0.081	0.007					
						2.612	2.618									
						2.643	2.559									
						2.589	2.439					2.246	0.122	0.015	2.296	0.180

MP (5 mM, 1 scan) 11705

Did not refind same TGD scratches made above.																
Rescratch in TGD	1	1	est127051a.001	2.582	2.486	2.582	2.338	2.484	2.256	0.152	0.023					
						2.647	2.510									
Scratch 8:1						2.710	2.303									
Scan with scratch tip						2.673	2.801									
Scan 8:1																
Tip holder 2		2	est127051a.002	2.508		2.558		2.491	2.241	0.050	0.002					

					2.500											
					2.617											
					2.573							2.249	0.160	0.026		
	2	1 est127051a.003	2.193	2.121	2.361	2.399		1.917	0.115	0.013						
					2.269	2.060										
					2.121	2.106										
					2.280	2.260										
		2 est127051a.004	2.589	2.521	2.388	2.732	2.772	2.299	0.112	0.013						
					2.707	2.511										
					2.599	2.521										
					2.645	2.604						2.108	0.161	0.026	2.178	0.227
Scratch in MP	1	1 est127051a.005	1.749	1.573	1.834	1.662	1.449	1.356	0.130	0.017						
					1.849	1.583										
Scratch 8:1					1.681	1.494										
Scan with scratch tip					1.742	1.603										
Scan 8:1																
Tip holder 2		2 est127051a.007	1.971	1.756	2.089	1.873	1.979	1.603	0.115	0.013						
					1.768	1.840										
					2.051	1.789										
					1.971	1.848						1.480	0.174	0.030		
	2	1 est127051a.008	2.125	2.037	2.169	2.018	1.877	1.763	0.086	0.007						
					2.156	1.967										
					2.047	2.101										
					2.110	2.081										
		2 est127051a.009	2.022	1.976	2.056	1.990	1.987	1.708	0.084	0.007						
					2.022	1.830										
					2.107	2.156										
					1.968	1.978						1.736	0.120	0.014	1.608	0.211

Sample 1 parallel lines: MP (20 mM, 10 minutes)/ TGD (5 mM, 1 scan)

MP (20 mM, 10 minutes) 11805

Sample no and date prepared, Instrument	**Scratch**	**Scan**	**File code**	**Thickness measured by section analysis** Midpoint L	Midpoint R	L of scratch	R of scratch	**Thickness measured by localised depth**	**Av. of scan minus 0.3 nm**	**Std. Dev. of scan**	**Var. of scan**	**Av. of scratch**	**Std. Dev. of scratch**	**Var. of scratch**	**Av. of sample**	**Std. Dev. or Error of sample**
Scratch 8:1	1	1	est318051a.000	3.187	3.192				2.889	0.003	0.000					
Scan with scratch tip	line 1 of		bowed													
Scan 8:1	pattern															
Tip holder 2																
		2	est318051a.001	3.137	3.035				2.875	0.109	0.012					
			bowed	3.344	3.173											
				3.248												
				3.110								2.882	0.109	0.012		

TGD (5 mM, 1 scan) 31805

Did not refind same MP scratches made above.																
Rescratch in MP	1	1	est318051a.005	3.374	3.190				2.982	0.130	0.017					
	line 1 of		bowed													
Scratch 8:1	pattern															
Scan with scratch tip																
Scan 8:1																
Tip holder 2		2	est318051a.006	3.310	3.048	3.337	3.173	3.345	2.902	0.132	0.017					
						3.314	3.163									
						3.210	3.126									
						3.267	2.930					2.942	0.185	0.034		
	2	1	est318051a.011	3.306	3.237	3.329	3.334	3.337	2.970	0.126	0.016					
	line 2 of					3.507	3.051									
	pattern					3.335	3.146									
						3.265	3.122									
		2	est318051a.012	3.288	3.126	3.254	3.148	3.126	2.875	0.095	0.009					

					3.234	3.160										
					3.172	2.971										
					3.311	3.140					2.923	0.158	0.025	2.932	0.243	
Scratch in TGD	1	1	est318051a.007	1.226	1.102	1.335	1.242	1.138	0.905	0.087	0.008					
in between lines						1.281	1.135									
						1.332	1.108									
Scratch 8:1						1.220	1.135									
Scan with scratch tip																
Scan 8:1		2	est318051a.008	1.250	1.027	1.198	0.952	1.179	0.840	0.100	0.010					
Tip holder 2						1.241	1.238									
						1.130	1.196									
						1.083	1.047					0.873	0.132	0.018		
	2	1	est318051a.009	1.361	1.380	1.380	1.360	1.383	1.071	0.075	0.006					
						1.578	1.324									
						1.341	1.376									
						1.300	1.299									
		2	est318051a.010	1.243	1.354	1.412	1.279	1.350	1.022	0.073	0.005					
						1.372	1.240									
						1.394	1.390									
						1.194	1.321					1.047	0.105	0.011	0.960	0.169

Sample 2 parallel lines: MP (20 mM, 10 minutes)/ TGD (5 mM, 1 scan)

MP (20 mM, 10 minutes) 11805

Sample no and date prepared, Instrument	**Scratch**	**Scan**	**File code**	**Thickness measured by section analysis** Midpoint L	Midpoint R	L of scratch	R of scratch	**Thickness measured by localised depth**	**Av. of scan minus 0.3 nm**	**Std. Dev. of scan**	**Var. of scan**	**Av. of scratch**	**Std. Dev. of scratch**	**Var. of scratch**	**Av. of sample**	**Std. Dev. or Error of sample**
Scratch 8:1	1	1	est308051a.005	2.794	2.485	2.563	2.388	2.634	2.268	0.125	0.016					
Scan with scratch tip	line 1 of					2.574	2.408									
Scan 8:1	pattern					2.682	2.452									
Tip holder 2						2.652	2.614									
		2	est308051a.006	2.422	2.641	2.403	2.464	2.432	2.166	0.082	0.007					
						2.524	2.437									
						2.585	2.425									
						2.403	2.391					2.217	0.149	0.022		
	2		est308051a.009	2.738	2.492	2.456	2.456	2.672	2.268	0.158	0.025					
	line 2 of					2.528	2.338									
	pattern					2.724	2.459									
						2.860	2.525								2.243	0.217

Sample 3 parallel lines: MP (20 mM, 10 minutes)/ TGD (5 mM, 1 scan)

MP (20 mM, 10 minutes) 11805, TGD (5 mM, 1 scan) 31805

Sample no and date prepared, Instrument	**Scratch**	**Scan**	**File code**	**Thickness measured by section analysis** Midpoint L	Midpoint R	L of scratch	R of scratch	**Thickness measured by localised depth**	**Av. of scan minus 0.3 nm**	**Std. Dev. of scan**	**Var. of scan**	**Av. of scratch**	**Std. Dev. of scratch**	**Var. of scratch**	**Av. of sample**	**Std. Dev. or Error of sample**
Scratch in TGD		1	1 est19051a.000			1.529	1.373	1.524	1.238	0.097	0.009					
in between lines						1.615	1.427									
						1.566	1.644									
Scratch 8:1						1.629										
Scan with scratch tip																
Scan 8:1			2 est19051a.001	1.610	1.476	1.477	1.305	1.474	1.189	0.098	0.010					
Tip holder 2						1.562	1.487									
						1.454	1.351									
						1.608	1.571					1.213	0.138	0.019		

Quantification of number of citrate-capped gold NP assemblies used as-prepared solution with unaltered pH and concentration

	Image magnification	Image 1	Adjusted to mag.	Image 2	Adjusted to mag.	Average	Error
Sample 4a: TGD (5 mM, 20 scans) 21305/*p*-NA (5 mM, 1 scan) 24305							
time of immersion: 3 hours							
TGD	50 kx	102	26	98	25		
		106	27	96	24		
		110	28	100	25		
		98	25	96	24	25	± 3
p-NA	50 kx	48	12	52	13		
		50	13	48	12		
		40	10	48	12		
		38	10	42	11	11	± 2
Sample 4b: TGD (5 mM, 20 scans) 21305/*p*-NA (5 mM, 1 scan) 24305							
time of immersion: 3 hours							
TGD	50 kx	104	26	106	27		
		106	27	108	26		
		108	27	110	28		
		102	26	102	26	26	± 2
p-NA	50 kx	44	11	42	11		
		48	12	42	11		
		40	10	42	11		
		44	11	38	10	11	± 1
Y-shaped: TGD (5 mM, 10 minutes) 22605							
time of immersion: 1 hour							
TGD	200 kx	15		17			
		14		15			
		17		18			
		16		16		16	± 2

Spill over	50 kx	8	2	8	2		
		2	1	4	1		
		6	2	14	4		
		6	2	10	3	2	± 2
Outside	50 kx	0	0	0	0		
		0	0	0	0		
		0	0	2	1		
		0	0	0	0	0	± 1
Sample 3 parallel lines: TGD (20 mM, 10 minutes) 11805/MP (5 mM, 1 scan) 11805 time of immersion: overnight							
TGD	200 kx	21					
		19					
		21					
		17				20	± 3
MP	200 kx	0					
		0					
		0					
		0				0	0

Sample 2 parallel lines: TGD (20 mM, 10 minutes) 11805/MP (5 mM, 1 scan) 11805					
time of immersion: 10 minutes		line 1	line 2		
TGD	200 kx	1	3		
		3	3		
		3	4		
		2	3	3	± 2
		between lines	outside		
MP	200 kx	0	0		
		0	0		
		0	0		
		0	0	0	0
Sample 1 parallel lines: MP (20 mM, 10 minutes) 11805/TGD (5 mM, 1 scan) 31805					
time of immersion: overnight					
MP	200 kx	1			
		2			
		0			
		2		1	± 1
TGD	200 kx	13			
		13			
		12			
		9		12	± 3
Sample 3 parallel lines: TGD (5 mM, 2 minutes) 111005 coupling NBC 111005-121005					
time of immersion: 3 hours		between lines	outside		
TGD	200 kx	6	9		
		9	10		
		6	11		
		10	9	9	± 3

		line 1	line 2		
TGD-NB	200 kx	0	0		
		2	1		
		0	0		
		2	0	1	± 1

```
%program read raw txt file, extending data zeroed, minimum calculated

close all
clear all

%User defined parameters

%Data set size, number of rows
L=1024;
Lf=L/2;

%Define cantilever spring constant (N/m)
k=0.56;

%Define Z sensitivity (nm/V)
sZ=12.5;

%Define X sensitivity (nm/V)
sX=0.027701;

%Define tip radius (nm)
r=15;

%Read file, deflection in V
M=dlmread('137fstm.txt','\t');

[a,b]=size(M);

for n=1:b;

rZ=M(1,n);
eZ=rZ.*sZ;
Z=linspace(0,eZ,Lf);

Dao=M(2:(Lf+1),n);
Da=sX*Dao;

Dro=M((Lf+2):a,n);
Dr=sX*Dro;

figure
plot(Z,Da,Z,Dr);
title('Raw F curve')
xlabel ('Piezo Height [nm]')
ylabel ('Deflection [nm]')

%Fit trendline to background
%Pick range
bX=ginput;

close

Da=Da-bX(1,2);
Dr=Dr-bX(1,2);

Z=Z-bX(2,1);
```

```
%Find adhesion force
Fadh=k*min(Dr);

%Store values to external matrix for final calculations
%Ranges

%Zeroed background, approach/retract
Dma(:,n)=Da;
Dmr(:,n)=Dr;

%Adhesion force
DmFad(n)=Fadh;

end

%Take average of F curves

Fav=mean(DmFad)
Fstd=std(DmFad)
```